Microscopic Investigations of the Terahertz and the Extreme Nonlinear Optical Response of Semiconductors

Dissertation

zur
Erlangung des Doktorgrades
der Naturwissenschaften
(Dr. rer. nat.)

dem Fachbereich Physik
der Philipps-Universität Marburg
vorgelegt

von
Daniel Golde
aus Frankenberg (Eder)

Marburg (Lahn), 2010

Vom Fachbereich Physik der Philipps-Universität Marburg
als Dissertation angenommen am 07.06.2010

Erstgutachter: Prof. Dr. Stephan W. Koch
Zweitgutachter: PD Dr. Sangam Chatterjee

Tag der mündlichen Prüfung: 22.06.2010

Zusammenfassung

Neben ihrer Bedeutung für technische Anwendungen sind Halbleiter von besonderem Interesse in der Grundlagenforschung. Die Möglichkeit, Halbleiter in höchster Reinheit herzustellen, macht sie zu idealen Modellsystemen für die Erforschung von Korrelationseffekten in wohldefinierten Vielteilchensystemen. Die Entwicklung moderner Wachstumstechniken hat es ermöglicht, diese Effekte sogar in Systemen reduzierter Dimensionalität zu untersuchen, von nulldimensionalen Quantenpunkten zu zweidimensionalen Quantenfilmen [1]. Werden Elektronen in einem Halbleiter aus dem Valenzband ins Leitungsband angehoben, z.B. durch optische Anregung, so erzeugt die Coulombwechselwirkung eine Vielzahl von Korrelationen unter den angeregten Teilchen. Unter anderem führt die Elektron-Elektron-Streuung zu Relaxations- und Dephasierungsprozessen, die auf einer Pikosekunden- oder sogar Femtosekunden-Zeitskala stattfinden. Diese ultraschnelle Dynamik des Vielteilchensystems kann mit Methoden der linearen und nichtlinearen optischen Spektroskopie beobachtet werden [2–6].

Ein alternativer Zugang zur Erforschung von Korrelationseffekten in Halbleitern bietet die Terahertzspektroskopie. Dabei macht man sich zunutze, dass die korrelierten Zustände typischerweise Übergangsfrequenzen von einigen Terahertz (THz) aufweisen. Dies erlaubt, Korrelationen im System zu identifizieren und zu charakterisieren, die sich der direkten Beobachtung mit optischen Methoden verschließen [7–9]. Ein wichtiges Beispiel für Korrelationseffekte in Halbleitern ist die Bildung von Exzitonen [10]. Hierbei führt die anziehende Coulombwechselwirkung zwischen einem Elektron im Leitungsband und einem Loch (ein „fehlendes Elektron“) im Valenzband zur Bildung eines gebundenen Paarzustandes ähnlich wie beim Wasserstoffatom. In vergangenen THz-Experimenten an Halbleiternanostrukturen konnte der interne $1s$-$2p$-Übergang genutzt werden, um Exzitonen nachzuweisen sowie ihren ultraschnellen Aufbau nach optischer Anregung zu untersuchen [8, 11–13]. Mithilfe starker THz-Felder ist es sogar möglich, den Zustand des Exzitons kohärent zu manipulieren [14]. Für genügend hohe Ladungsträgerkonzentrationen oder bei hohen Gittertemperaturen sind Exzitonen nicht mehr stabil, und der vorliegende Vielteilchenzustand besteht aus einem Plasma von korrelierten Elektronen und Löchern. In diesem Fall kann das System kollektive Ladungsträgerschwingungen aufweisen, sogenannte Plasmonen [1, 5, 15]. Die zugehörige Plasmafrequenz ist in Halbleitern typischerweise im Bereich von einigen THz, was die Untersuchung von Plasmonen mithilfe der THz-Spektroskopie ermöglicht [16].

Ein weiteres Anwendungsgebiet von THz-Strahlung in Halbleitern ist die Untersuchung von Übergängen zwischen quantisierten Zuständen in niederdimensionalen Systemen, sogenannte Intersubbandübergänge [17–21]. In solchen Systemen ist die Bewegung der Elektronen ein einer oder mehrere Richtungen eingeschränkt. Dabei tauchen Quantisierungseffekte in der jeweiligen Richtung auf, die dazu führen, dass die Elektronen nur noch diskrete Energiezustände besetzten können [5]. Der energetische Abstand zwischen diesen Niveaus hängt von dem tatsächlichen Potential ab, welches die Elektronen einsperrt, ist in Halbleitern aber in der Regel im Bereich von einigen zehn THz.

Eine durch einen Halbleiter propagierende THz-Welle induziert auf ihrem Weg verschiedene Übergänge, die in Resonanz mit ihr stehen, beispielsweise die oben erwähnten. Abgesehen

davon beschleunigt das relativ langsam oszillierende elektrische Feld jedoch auch die Ladungsträger gemäß des klassischen Beschleunigungstheorems, siehe z.B. Ref. [22]. Diese oszillierenden oder „wackelnden“ Elektronen strahlen ihrerseits wieder ein Feld ab und tragen somit zur THz-Antwort des Halbleiters bei. Dieser sogenannte ponderomotive Beitrag kann bei optischen Feldern für gewöhnlich vernachlässigt werden, da die Elektronen, einfach ausgedrückt, dem sich rasch ändernden elektrischen Feld nicht folgen können. Bei THz-Anregung kann der ponderomotive Beitrag jedoch signifikant die Antwort des Halbleiters beeinflussen [14, 23].

Der größte Teil der vorliegenden Arbeit beschäftigt sich mit der theoretischen Untersuchung der linearen THz-Antwort von Halbleiternanostrukturen auf Basis einer mikroskopischen Theorie [5, 10]. Dabei untersuche ich zwei verschiedene Fälle: Intersubbandübergänge in optisch angeregten Quantenfilmen sowie die THz-Antwort von zweidimensionalen korrelierten Elektron- und Elektron-Loch-Plasmen. Im zweiten Fall liefert die Bestimmung der Plasmafrequenz aus den berechneten linearen THz-Spektren signifikante Unterschiede zur allgemein bekannten Form der zweidimensionalen Plasmafrequenz [5]. Des Weiteren untersuche ich das Elektron-Loch-Systems für Bedingungen, bei denen sowohl Exzitonen vorhanden sind die THz-Antwort aber auch Einflüsse des Plasmas enthält. Ein quantitativer Exepriment-Theorie-Vergleich liefert neue Erkenntnisse über das Verhalten des Systems beim Übergang vom rein exzitonischen zum plasmaartigen Regime. Die Diskussion der Intersubbandübergänge konzentriert sich hauptsächlich auf den Einfluss der beschleunigten Ladungsträgern auf die THz-Antwort. Ich stelle eine einfache Methode vor, die es ermöglicht, die ponderomotiven Einflüsse direkt in den THz-Spektren zu identifizieren. Daneben werden auch exzitonische Effekte in den Intersubbandübergängen untersucht.

Der letzte Teil dieser Arbeit behandelt die extrem nichtlineare optische Antwort von Halbleiternanostrukturen. In diesem Regime der Licht-Materie-Wechselwirkung sind die vorhandenen Felder so stark, dass die Rabifrequenz vergleichbar oder sogar größer ist als die charakteristische Übergangsfrequenz des betrachteten Systems [24]. Dabei ist die Rabifrequenz definiert als das Produkt aus dem Dipolmatrixelement des entsprechenden Übergangs und der elektrischen Feldstärke. Bei resonanter Anregung eines Zweiniveausystems, legt die Rabifrequenz die Zeit fest, während der sich das System aus dem Grundzustand in einen komplett invertierten Zustand und wieder zurück in den Grundzustand entwickelt. Dieser Zyklus wird ein *Rabiflop* genannt. In der herkömmlichen nichtlinearen Optik beinhaltet ein Rabiflop üblicherweise viele Oszillationen des anregenden Feldes. In diesem Fall wird die Dynamik des Zweiniveausystems gut durch das sogenannte *Areatheorem* [25] der nichtlinearen Optik beschrieben, welches den Besetzungszustand des Systems mit der Einhüllenden des Laserpulses verknüpft. Die Systemdynamik wird also vielmehr durch die Einhüllende, also die Intensität, des Feldes bestimmt als durch das elektrische Feld an sich. Im Gegensatz dazu findet ein Rabiflop im extrem nichtlinearen Regime während einer einzigen Schwingung des optischen Feldes statt, so dass das elektrische Feld selbst nun den Zustand des Systems manipuliert. Man spricht hierbei von *carrier-wave Rabiflops*. Theoretische Untersuchungen [26–32] zu diesem Gebiet haben eine große Anzahl neuer nichtlinearer Effekte vorhergesagt, von denen einige auch schon in Experimenten an Halbleitern beobachtet werden konnten [33–35]. In theoretischen Arbeiten zu Halbleitern wurden diese meist als ein Ensemble von unabhängigen Zweiniveausystemen modelliert unter Vernachlässigung der Coulombwechselwirkung zwischen den angeregten Ladungsträgern. Nur in einigen wenigen Veröffentlichungen wurden Coulombeffekte im extrem nichtlinearen Regime berücksichtigt [35, 36]. Des Weiteren haben sich bisherige Untersuchungen lediglich auf Interbandübergänge konzentriert, also auf Prozesse, bei denen Elektronen aus dem Valenzband ins Leitungsband angeregt werden. Bei den hohen Feldstärken, die hier

eine Rolle spielen, kann die Intrabandbeschleunigung allerdings nicht mehr von vornherein vernachlässigt werden. Daher werden in der vorliegenden Arbeit sowohl der Einfluss der Coulombwechselwirkung als auch die Auswirkung der ponderomotiven Ladungsträgerbeschleunigung auf die extrem nichtlineare Antwort untersucht.

Die mikroskopische Theorie, die für Berechnungen der in dieser Arbeit diskutierten Resultate verwendet wurde, wird in Kapitel 2 vorgestellt. Sie basiert auf einer Bewegunsgleichungsmethode [5], bei der die auftauchende Vielteilchenhierarchie mit einer sogenannten Clusterentwicklung [10] konsistent abgebrochen wird. In Hartree-Fock-Näherung erhalte ich erweiterte Halbleiterblochgleichungen [5], die neben den üblichen Interbandübergängen auch die Intra- sowie die Intersubbaddynamik beinhalten. Des Weiteren werden die Bewegungsgleichungen für die Korrelationsfunktionen vorgestellt, die für die Beschreibung von Exzitonen bzw. korrelierten Elektron-Loch-Paaren nötig sind.

In Kapitel 3 untersuche ich Intersubbandübergänge zwischen den zwei niedrigsten Leitungssubbändern in optisch angeregten GaAs Quantenfilmen. Dabei regt das THz-Feld nicht nur Elektronen von einem Subband in das andere an, sondern kann auch an die vorhandenen kohärenten Exzitonen koppeln und somit Übergänge zwischen Exzitonen, die zu verschiedenen Subbändern gehören, induzieren. Da die exzitonischen Bindungsenergien der beiden Subbänder im hier betrachteten System leicht verschieden voneinander sind, tauchen im Absorptionsspektrum zwei Resonanzen auf, die eindeutig den exzitonischen bzw. den elektronischen Übergängen zugeordnet werden können (Paper [IX]). Interessanterweise zeigen die differentiellen THz-Transmissionsspektren eine charakteristische asymmetrische Linienform des Intersubbandübergangs, die stark an eine Fano-Resonanz [37] erinnert. Dieses Verhalten kann auf eine kohärente Überlagerung der durch Intersubbandübergänge und ponderomotive Dynamik induzierten Felder zurückgeführt werden. Folglich gibt die differentielle Transmission direkt Aufschluss über die relative Stärke der ponderomotiven Antwort in Anwesenheit eines echten THz-Übergangs: Je ausgprägter die beobachtete Fano-Signatur ist desto größer der Einfluss der ponderomotiven Ladungsträgerbeschleunigung (Paper [VII] und [VIII]). Diese Resultate sind in sehr guter Übereinstimmung mit Messungen, die kürzlich im Forschungszentrum Dresden-Rossendorf durchgeführt wurden.

Kaptitel 4 befasst sich mit der Untersuchung der Intrabanddynamik in zwei unterschiedlichen Systemen: dem Elektron-Loch-Plasma in einem optisch angeregten Quantenfilm sowie dem zweidimensionalen Elektrongas (2DEG) in einem *High-Electron Mobility Transistor* (HEMT) [38]. Für die theoretische Beschreibung des 2DEG behandle ich die Dotierungsionen, die die Elektronen für das 2DEG liefern, als Löcher mit unendlich schwerer effektiver Masse. In den konkreten Rechnungen benutze ich eine analytische Lösung der resultierenden Bewegungsgleichungen für das 2DEG. Die Antwort des Quantenfilms wird mit der THz-Elliott-Formel [10] berechnet. Mithilfe einer *Plasmon-Pol-Analyse* [16] kann die Plasmafrequenz aus der dielektrischen Funktion des Systems extrahiert werden. Für beide betrachtete zweidimensionale Systeme stellt sich heraus, dass die THz-Antwort durch eine dreidimensionale Plasmafrequenz bestimmt wird. Die Erklärung für diesen scheinbaren Widerspruch ist, dass hier die direkte lineare Antwort des Plasmas über die dielektrische Funktion untersucht wird, welche keine Rückkopplungseffekte der induzierten Felder auf die Systemdynamik enthält. Allein diese Rückkopplungseffekte sind jedoch für die Dimensionsabhängigkeit der gewöhnlichen Plasmafrequenz verantwortlich. Weiterhin wird die Antwort des Quantenfilms für Bedingungen untersucht, bei denen nahezu alle Elektronen und Löcher zu Exzitonen gebunden sind. Indem die Ladungsträgerkonzentration kontinuierlich erhöht wird, kann nun der Übergang zum korrelierten Elektron-Loch-Plasma untersucht werden. Durch einen quantitativen Ver-

gleich mit experimentellen Resultaten wird die Dichte der vorhandenen Exzitonen bestimmt. Dabei stellt sich heraus, dass das System bereits plasmaartiges Verhalten zeigt, während ein signifikanter Anteil der Ladungsträger noch zu Exzitonen gebunden ist. Die hier vorgestellten Ergebnisse sind in sehr guter Übereinstimmung mit kürzlich in Marburg durchgeführten Experimenten. Eine weiterführende theoretische Analyse der 2DEG-Daten zeigt, dass die Antwort hier sehr stark sowohl von ponderomotiven Effekten als auch von der Elektron-Ion-Streuung beeinflusst wird. Als Konsequenz der großen Streubeiträge kann die Antwort des 2DEG nicht mit einem einfachen Drude-Modell erklärt werden (Paper [V] und [VI]).

In Kapitel 5 beschäftige ich mich mit der extrem nichtlinearen Antwort von Halbleiternanostrukturen. Dazu berechne ich die kohärent emittierte Strahlung des Systems bei optischer Anregung mit Feldstärken von 50 MV/cm und mehr. In diesem Regime werden viele neuartige nichtlineare Effekte erwartet wie oben bereits diskutiert. Für reine Interbanddynamik werden hier unter anderem die *Carrier-Wave* Mollow-Aufspaltung [24] und die Erzeugung von höheren harmonischen beschrieben. Bemerkenswerterweise spielt die Coulombwechselwirkung in diesem Regime nahezu keine Rolle wie die Untersuchungen zeigen. Dies kann intuitiv damit erklärt werden, dass die für die Licht-Materie-Wechselwirkung charakteristische Energie, definiert durch die Rabifrequenz, in diesem Fall etwa zwei Größenordnungen größer ist als die typische Coulombenergie, die im Bereich der exzitonischen Bindungsenergie liegt (Paper [I] und [II]). Sobald die Intrabandbeschleunigung eingeschaltet wird, verändern sich die Emissionsspektren dramatisch. Insbesondere die Erzeugung hoher Harmonischer wird deutlich verstärkt. Es werden nun Frequenzkomponenten erzeugt, die etwa einen Faktor fünf größer sind als bei reiner Interbanddynamik. Diese starken Nichtlinearitäten kommen vor allem von der Abstrahlung über die Interbandpolarisation, die durch die Beschleunigungseffekte ultraschnell moduliert wird (Paper [III] und [IV]).

Die meisten der in dieser Arbeit vorgestellten Untersuchungen stellen keineswegs abgeschlossene Projekte dar, sondern werden momentan und in Zukunft weiter erforscht, um noch offene Fragen zu klären sowie ein tieferes Verständnis der physikalischen Prozesse zu erhalten. Beispielsweise ist die Intrabanddynamik im Grenzfall sehr kleiner Frequenzen ($\omega \to 0$) noch nicht richtig verstanden. Die hier auftretenden Probleme können auf eine ungenügende phänomenologische Behandlung diverser Streuprozesse zurückgeführt werden. Es laufen derzeit bereits Bemühungen, diese Streumodelle zu verbessern. Auf lange Sicht wird eine komplett mikroskopische Beschreibung der relevanten Streuprozesse angestrebt. Dies wird mit Sicherheit zu neuen und wertvollen Erkenntnissen der Ladungsträgerdynamik während und nach THz-Anregungen führen. Ein weiteres laufendes Projekt ist die Weiterentwicklung der 2DEG-Theorie für starke THz-Felder. Erste Untersuchungen zu einem THz-Pump-THz-Abfrage-Szenario haben bereits gezeigt, dass die lineare THz-Antwort kohärent durch den Pumppuls kontrolliert werden kann. Weiterführende Forschung auf diesem Gebiet könnte dazu beitragen, neue ultraschnelle Untersuchungsmethoden für die Intrabanddynamik zu entwickeln. Weiterhin ist geplant, die Antwort von zuvor unangeregten Halbleitern auf extrem starke THz-Pulse zu untersuchen. Vorläufige Rechnungen zeigen, dass für genügend starke Pulse signifikante Ladunsträgerkonzentrationen durch Multiphotonprozesse erzeugt werden, die dann wiederum beschleunigt werden und somit sehr hohe Harmonische erzeugen können. Die hierfür benötigten Feldstärken betragen einige 10 MV/cm und sind seit wenigen Jahren auch im THz-Bereich experimentell zugänglich [39].

Danksagung

An erster Stelle gilt mein Dank Prof. Stephan Koch und Prof. Mackillo Kira für ihre engagierte und motivierende Betreuung sowie für zahlreiche Diskussionen, Ratschläge und Tipps, ohne die diese Arbeit nicht möglich gewesen wäre.

Ebenso möchte ich mich bei Prof. Torsten Meier bedanken für die gemeinsamen Projekte auch nach seinem Fortgang aus Marburg.

Bei Dr. Sangam Chatterjee bedanke ich mich für seine Bereitschaft, das Zweitgutachten für diese Arbeit zu verfassen, sowie für die gute und erfolgreiche Zuammenarbeit beim Plasmaprojekt.

In diesem Zusammenhang gilt mein besonderer Dank auch Torben Grunwald, der die experimentellen Ergebnisse hierzu beigetragen hat. Darüber hinaus hat er mir in vielen gemeinsamen Treffen die experimentellen Details näher gebracht, was meine Arbeit erheblich erleichtert hat.

Für ihre experimentellen Beiträge zu den Intersubbandübergängen sowie für die vielen damit verbundenen fruchtbaren Diskussionen bedanke ich mich bei Martin Wagner, Dr. Harald Schneider und Prof. Manfred Helm.

Ganz besonders möchte ich mich bei Hanno Steiner bedanken für unzählige Gespräche und Diskussionen, in denen er mich an seinem Wissen über Terahertzphysik teilhaben ließ.

Mein Dank gilt auch Prof. John Sipe, der mir während seines Humboldt-Aufenthaltes in Marburg tiefe Einblicke in die Beschreibung Licht-Materie-Wechselwirkung gewährte.

Bei meinen vielen über die Jahre hinweg wechselnden Bürokollegen Eckhard, Marco, Martin, Thomas, Sebastian und Michael sowie neuerdings Christian, Alex und Uli bedanke ich mich herzlich für ein angenehmes Klima im Büro. Auch wenn sie vielleicht nicht immer den Fortschritt meine Arbeit positiv beeinflusst haben (was natürlich auf Gegenseitigkeit beruhte), so haben sie doch wesentlich dazu beigetragen, dass ich jeden Morgen gerne zur Arbeit gekommen bin.

Des Weiteren danke ich allen übrigen Gruppenmitgliedern für eine nette Arbeitsatmosphäre sowie für ihre ständige Hilfsbereitschaft bei den einen oder anderen Problemen. Ein großer Dank gilt in diesem Zusammenhang Prof. Peter Thomas für die Organisation der jährlichen gemeinsamen Wandertouren. Ebenfalls herzlich bedanken möchte ich mich bei Renate für ihre herzliche, engagierte und kompetente Hilfe bei allen bürokratischen Fragen und Problemen.

Nicht vergessen möchte ich hier meine Eltern, Schwiegereltern, Geschwister und Schwäger(innen). Vielen Dank für euren Rückhalt und eure Motivation während der letzten Jahre sowie für viele gemeinsame schöne Stunden.

Schließlich geht mein herzlichster Dank an Elvira. Danke für die unermüdliche Unterstützung und liebevolle Umsorgung gerade währed der letzten Monate. Danke, dass du immer für mich da warst und bist.

Author's Contributions

Published Papers

This Thesis consists of an introductory review part followed by nine research publications:

[I] D. Golde, T. Meier, and S. W. Koch, "Microscopic analysis of extreme nonlinear optics in semiconductor nanostructures", J. Opt. Soc. Am. B **23**, 2559 (2006).

[II] D. Golde, T. Meier, and S. W. Koch, "Modeling of the Extreme Nonlinear Optical Response of Semiconductor Nanostructures", Ultrafast Phenomena XV, Springer Series in Chemical Physics **88**, 689 (2007).

[III] D. Golde, T. Meier, and S. W. Koch, "High harmonics generated in semiconductor nanostructures by the coupled dynamics of optical inter- and intraband excitations", Phys. Rev. B **77**, 075330 (2008).

[IV] D. Golde, T. Meier, and S. W. Koch, "Microscopic analysis of high-harmonic generation in semiconductor nanostructures", phys. stat. sol. (c) **6**, 420 (2009).

[V] D. Golde, M. Kira, and S. W. Koch, "Terahertz response of a two-dimensional electron gas", Proc. SPIE **6892**, 68921F (2008).

[VI] S. Chatterjee, T. Grunwald, D. Köhler, K. Pierz, D. Golde, M. Kira, and S. W. Koch, "THz measurement of the optical response in a two-dimensional electron gas", phys. stat. sol. (c) **6**, 453 (2009).

[VII] D. Golde, M. Wagner, D. Stehr, H. Schneider, M. Helm, A. M. Andrews, T. Roch, G. Strasser, M. Kira, and S. W. Koch, "Fano Signatures in the Intersubband Terahertz Response of Optically Excited Semiconductor Quantum Wells", Phys. Rev. Lett. **102**, 127403 (2009).

[VIII] M. Wagner, D. Golde, D. Stehr, H. Schneider, M. Helm, A. M. Andrews, T. Roch, G. Strasser, M. Kira, and S. W. Koch, "Fano profile in the intersubband terahertz response of photoexcited GaAs/AlGaAs quantum wells", Journal of Physics: Conference Series **193**, 012073 (2009).

[IX] D. Golde, M. Kira, and S. W. Koch, "Ultrafast terahertz response of optically excited semiconductor heterostructures", Proc. SPIE **7600**, 76000F (2010).

Papers in Preparation

[X] D. Golde, S. Chatterjee, T. Grunwald, D. Köhler, T. Jung, K. Pierz, G. Kithrova, H. M. Gibbs, J. T. Steiner, M. Kira, and S. W. Koch, "Terahertz Signatures of Plasmons in Quasi-Two-Dimensional Semiconductor Systems", *in preparation* (2010).

Original Contributions

My first research project was to analyze the extreme nonlinear optical response of semiconductors by solving the semiconductor Bloch equations (SBE). I started this project when I was still a diploma student and continued it during my PhD time. Hence, some parts of the results have already been presented in my Diploma thesis [40]. For moderate excitation intensities, numerical solutions of the SBE usually apply the rotating-wave approximation (RWA). In extreme nonlinear optics, however, the RWA is not valid any more. Therefore, I had to write a new computer program that solves the SBE without using the RWA. This is numerically much more demanding since one has to resolve the the optical field oscillations completely in this case. In order to analyze the effect of the Coulomb interaction, I also included scattering terms in 2nd Born-Markov approximation to my RWA-free code. In the next step, I took into account the field-induced intraband acceleration. This theory was not new either and had already been used in many publications of our group. In my case, however, the exciting fields were so strong that the carriers are accelerated over the whole Brillouin zone. Consequently, I had to extend my code such that complete bands could be taken into account. The resulting numerical complexity was so high that only 1D calculations were feasible. The outcomes of this project have been published in Papers [I]–[IV]. All numerical calculations presented therein have been performed by myself. Furthermore, I have developed simplified analytical models to illustrate the observed effects on an intuitive level. I presented these results as a talk at the DPG conference in Dresden (2006), as a poster at the 15th International Conference on Ultrafast Phenomena in Pacific Grove, USA (2006), and as a poster at the NOEKS09 in Müritz (2008).

Another project discussed in this Thesis concerns the linear terahertz (THz) response of two-dimensional electron gases (2DEGs). At the time when I started this project, a theory for 2DEGs was indeed available in our group but it was rather poorly conceived. So, I derived the accordant equations again and improved the theory such that it could be applied to realistic situations. For instance, ponderomotive effects have been completely neglected before whereas I found out that they are crucial in order to describe the THz response correctly. My improved 2DEG theory could excellently reproduce corresponding measurements performed by T. Grunwald *et al.* in Marburg. I also analyzed similar experiments on optically excited quantum wells (QWs) using the THz-Elliott formula. In both cases, I was involved in detailed discussion with the experimentalists. In particular, I assisted them in extracting the susceptibility of the QW or the 2DEG from the measured transmission data using a transfer-matrix method. This approach is usually used to compute the influence of a dielectric environment on the response of the total structure, i.e., to convert the susceptibility into the complete response of the structure. In contrast, I developed a numerical method that extracts the susceptibility from the THz transmission through an almost arbitrary multi-QW structure. The corresponding experiment-theory comparison will be published in near future (Paper [X]). A purely theoretical investigation of the 2DEG theory has already been published in Paper [V].

Besides contributing the 2DEG equations here, I made the calculations and was mainly responsible for the writing. Paper [VI] presents the 2DEG measurement to which I contributed the Drude fits discussed there and, in parts, the data analysis. I presented some of the results as a talk at the DPG conference in Berlin (2008).

Additionally, I analyzed an interesting experiment performed by M. Wagner *et al.* at the Forschungszentrum Dresden-Rossendorf. They investigated intersubband transitions and found unexpected features in the THz response which they could not explain. Our first guess was that these features come from excitonic effects involving various subbands. Therefore, I extended our THz theory by including terms for the intersubband transitions and wrote a new computer program that numerically solves the intersubband response for a multisubband system. My analysis revealed that excitons indeed influence the intersubband transitions leading to additional resonances. Although this was quite a nice and interesting result, it could not explain the experimental findings. Eventually, I found that the intersubband response is superimposed by the ponderomotive contribution that directly shows up in the THz transmission. With a simplified analytical model, I could show how this superposition actually produces the observed characteristic line shape. During our collaboration, I took part in extensive discussions with the experimentalists. Again, I helped them to analyze the measured data and to extract the desired quantities. Our joint findings have been published in Papers [VII] and [VIII] while Paper [IX] presents an exclusively theoretical study on intersubband transitions. To these publications, I contributed the computed spectra and was mainly responsible for the writing of Paper [IX] and of the theory part of Paper [VII]. These results have also been presented by me in two talks at the DPG conference in Dresden (2009) and at the CLEO Europe-EQEC 2009 in Munich.

Each publication presented in this Thesis has preceded a huge amount of meetings in our group where intermediate results have been discussed and new calculations have been planned. The actual calculations and subsequent data elaborations have then been performed by myself.

Contents

1 Introduction

Besides their relevance for technical applications, semiconductors are of high interest in fundamental research. The possibility of fabricating semiconductors with highest purity makes them to ideal model systems to study correlation effects in well-defined many-particle systems. The development of modern growth techniques has even allowed for analyzing these effects in systems with reduced effective dimensionality from zero-dimensional quantum dots to two-dimensional quantum wells [1]. When the electrons in a semiconductor are transferred from the valence band to the conduction band, e.g., by optical excitation across the bandgap, the Coulomb interaction among the charge carriers induces a variety of many-body correlations. Among other things, electron-electron scattering leads to relaxation and dephasing processes on a picosecond or even femtosecond timescale. This ultrafast dynamics of the interacting many-particle system can be monitored using methods of linear and nonlinear optical spectroscopy [2–6].

An alternative approach to study correlation effects in semiconductors is the terahertz spectroscopy. Here, one takes advantage of the fact that internal transition frequencies of the correlated states are typically in the range of few terahertz (THz). This allows for identifying and characterizing correlations in the system that cannot be accessed directly using optical methods [7–9]. An important example for correlation effects in semiconductors is the formation of excitons [10]. Here, the attractive Coulomb interaction between an electron in the conduction band and a hole (i.e., a "missing electron") in the valence band causes these particles to form a bound pair state similar to the hydrogen atom. In THz experiments performed on semiconductor nanostructures, the internal $1s$-$2p$ transition has been used to detect excitons and measure their ultrafast build-up after optical excitation [8, 11–13]. Besides just detecting excitons, strong THz excitations are even able to coherently manipulate excitonic states [14]. For sufficiently high carrier concentrations or for large lattice temperatures, excitons are not stable any more and the corresponding many-body state consists of a plasma of correlated electrons and holes. In this case, the system can exhibit collective charge oscillations, the plasmons [1, 5, 15]. The corresponding plasma frequency is typically in the range of few THz in semiconductors which allows to employ the techniques of THz spectroscopy to analyze plasmons in semiconductors [16].

Another application area of THz radiation in semiconductors is the investigation of transitions between quantum confined states, so-called intersubband transitions [17–21]. Quantum confinement occurs when electrons are trapped in structures with reduced effective dimensionality. In such systems, the motion of the electrons in the confinement direction(s) is quantized such that the electrons can occupy only discrete energy levels [5]. The energetic difference between these levels depends on the actual potential that traps the electrons but is of the order of few tens of THz in typical semiconductor nanostructures.

A THz wave that propagates through a semiconductor will, of course, induce various transitions that are resonant with the THz frequency, e.g., those mentioned above. Besides that, however, its relatively slowly varying electrical field will also accelerate the carriers according

to the classical acceleration theorem (see, e.g., Ref. [22]). These oscillating or "wiggling" electrons will emit a THz field and, thus, contribute to the THz response of the semiconductor. This so-called ponderomotive contribution can usually be neglected in optics since, simply speaking, the electrons cannot follow the rapidly oscillating field. For THz fields, however, the ponderomotive contribution can significantly influence the response of the semiconductor [14, 23].

In the major part of this Thesis, we will discuss the linear THz response of semiconductor nanostructures based on a microscopic theory [5, 10]. Here, two different problems will be investigated: intersubband transitions in optically excited quantum wells and the THz plasma response of two-dimensional systems. In the latter case, we will analyze the response of correlated electron and electron-hole plasmas. Extracting the plasma frequency from the linear response, we find significant deviations from the commonly accepted two-dimensional plasma frequency [5]. Besides analyzing the pure plasma response, we will also consider an intermediate regime where the response of the electron-hole plasma consists of a mixture of plasma contributions and excitonic transitions. A quantitative experiment-theory comparison provides novel insights into the behavior of the system at the transition from one regime to the other. The discussion of the intersubband transitions will mainly focus on the coherent superposition of the responses from true THz transitions and the ponderomotively accelerated carriers. We will present a simple method to directly identify ponderomotive effects in the linear THz response. Apart from that, the excitonic contributions to intersubband transitions will be investigated.

The last part of the present Thesis deals with a completely different regime. Here, the extreme nonlinear optical response of low-dimensional semiconductor structures will be discussed. Formally, extreme nonlinear optics describes the regime of light-matter interaction where the exciting field is strong enough such that the Rabi frequency is comparable to or larger than the characteristic transition frequency of the investigated system [24]. Here, the Rabi frequency is given by the product of the electrical field strength and the dipole-matrix element of the respective transition. For resonant excitation of a two-level system, the Rabi frequency defines the time in which the population is coherently transferred from the lower state to the upper state and back again to the lower state [5, 25]. This motion is called one Rabi flop. In conventional nonlinear optics, one Rabi flop usually includes many cycles of the exciting electrical field. In this case, the dynamics of the two-level system is well described by the area theorem [25] of nonlinear optics that directly connects the occupation state of the system with the envelope of the laser pulse. So, the system dynamics is determined rather by the envelope, i.e., the intensity of the pulse than by the electrical field itself. In extreme nonlinear optics, in contrast, the Rabi flopping occurs during one single cycle of the optical field according to the definition of the extreme nonlinear regime given above. This dynamics is called carrier-wave Rabi flopping. In this regime, the electrical field itself manipulates the state of the system and, hence, the area theorem breaks down [26]. Theoretical investigations [26–32] have predicted a large number of novel nonlinear effects arising for such strong excitations. Some of them have been observed in experiments performed on semiconductors [33–35]. Previous theoretical works often modeled the semiconductor as an ensemble of independent two-level systems. Such an approach does surely not account for many-body interactions among the carriers. Only very few publications exist that include Coulomb effects in the extreme nonlinear regime [35, 36]. Furthermore, these studies concentrated exclusively on the optically induced interband transitions, i.e, processes where electrons are excited from the valence band to the conduction band. For the strong fields considered here, however,

the ponderomotive intraband acceleration of the photo-excited carriers cannot be neglected a priori. In our discussion of the extreme nonlinear optical response of semiconductors, we will analyze both the influence of the Coulomb interaction and the effect of carrier accelerations.

The Thesis is organized as follows. In Chap. 2, we will give an overview of our microscopic theory that has been used to obtain the results presented in this work. Chapter 3 discusses intersubband transitions of optically excited quantum wells. Besides a purely theoretical analysis of excitonic effects, a detailed experiment-theory comparison is presented. Chapter 4 deals with the intraband dynamics in two-dimensional semiconductor systems. Here, our results will also be compared to recent experiments. In Chap. 5, we explore the extreme nonlinear optical response of semiconductor nanostructures. Finally, we will summarize our findings and give a short outlook in Chap. 6.

2 Theoretical Approach

In this chapter, we will give an overview of the theoretical background that forms the basis of the results presented in Chaps. 3–5 and in the appended papers. The approach outlined here is based mainly on Refs. [5, 10] and shall help the reader to understand the basic concepts of our theory.

In this work, mostly quasi two-dimensional (2D) semiconductor systems, i.e., quantum wells (QWs) are considered. In contrast to bulk systems, the electrons in a quantum well can move freely only in two dimensions while they are confined in the third one (in z-direction). This leads, similar to the particle-in-a-box problem, to a splitting of the electronic bulk bands into multiple subbands [5]. The theoretical description of the optical and THz response of such 2D multisubband systems is presented here. With only minor changes, this theory can also be applied to one-dimensional quantum wires. We start start with a discussion of the Hamilton operator in Sec. 2.1 and present the formulas for the electromagnetic response in Sec. 2.2. Finally, the modeling of the microscopic dynamics using an equation-of-motion approach is presented in Sec. 2.3.

2.1 The System Hamiltonian

The Hamilton operator is the basement of each quantum mechanical investigation since it unambiguously defines the model system and its dynamics. In semiconductor optics, it is convenient to formulate the Hamiltonian within the second-quantization formalism using the Bloch basis [5]. For this purpose, one defines creation and annihilation operators $\hat{a}^\dagger_{\lambda,\mathbf{k}}$ and $\hat{a}_{\lambda,\mathbf{k}}$, respectively that create or destroy an electron in the Bloch state $|\lambda,\mathbf{k}\rangle$ with band index λ and in-plane crystal momentum $\hbar\mathbf{k}$. Here, we have defined the combined band index $\lambda = (\lambda_b, n)$ that includes both the bulk band λ_b and the subband index n. In order to keep the notation as compact as possible, the λ-notation will be used unless it is necessary to indicate subband indices explicitly. In general, the Bloch state is characterized by a third quantum number, the spin of the electron. However, since the spin does not play any role in our investigations, it is implicitly included in the momentum index $\mathbf{k}$ throughout this Thesis.

The Hamilton operator of a semiconductor QW in the presence of a classical light field is given by [5, 10]

$$\hat{H} = \sum_{\lambda,\mathbf{k}} \varepsilon^\lambda_{\mathbf{k}}\, \hat{a}^\dagger_{\lambda,\mathbf{k}}\hat{a}_{\lambda,\mathbf{k}} + \frac{1}{2} \sum_{\substack{\lambda,\lambda' \\ \mathbf{k},\mathbf{k}',\mathbf{q}\neq 0}} V^{\lambda,\lambda'}_{\mathbf{q}}\, \hat{a}^\dagger_{\lambda,\mathbf{k}}\hat{a}^\dagger_{\lambda',\mathbf{k}'}\hat{a}_{\lambda',\mathbf{k}'+\mathbf{q}}\hat{a}_{\lambda,\mathbf{k}-\mathbf{q}} + \hat{H}_{\mathrm{l-m}} + \hat{H}_{\mathrm{rest}}. \tag{2.1}$$

The first two terms describe free-particle dynamics and the many-body Coulomb interaction among the electrons, respectively. The third term, $\hat{H}_{\mathrm{l-m}}$, is the light-matter interaction that will be discussed separately below. All other contributions are formally included in $\hat{H}_{\mathrm{rest}}$ like, e.g., the coupling to lattice vibrations (phonons) or disorder-related effects. These

contributions are not taken into account microscopically but only via effective parameters or phenomenological models.

The coefficients in Eq. (2.1) are the single-particle energies $\varepsilon_{\mathbf{k}}^{\lambda}$ (i.e., the band structure) and the Coulomb-matrix element $V_{\mathbf{q}}^{\lambda,\lambda'}$ which is given by

$$V_{\mathbf{q}}^{\lambda,\lambda'} = \frac{e^2}{2\epsilon_0\epsilon_r\mathcal{S}|\mathbf{q}|}\iint_{-\infty}^{\infty} \mathrm{d}z\,\mathrm{d}z'\,|\xi_\lambda(z)|^2\,|\xi_{\lambda'}(z')|^2\,\mathrm{e}^{-|\mathbf{q}(z-z')|}. \tag{2.2}$$

Here, e is the elementary charge, ϵ_0 is the vacuum permittivity, ϵ_r is the static background dielectric constant, $\mathcal{S}$ is the quantization area of the QW, and z is the spatial component perpendicular to the quantum-well plane. The so-called confinement functions $\xi_\lambda(z)$ are the envelope part of the Bloch wave function in z-direction. They define how strongly the electrons are confined to the QW. In a simple picture, the confinement functions are the solutions of the one-dimensional particle-in-a-box problem.

For the light-matter interaction, two different approaches have been used that will be discussed in the following sections 2.1.1 and 2.1.2.

2.1.1 Light-Matter Interaction in $\mathbf{p}\cdot\mathbf{A}$ Picture

In first quantization, the light-matter interaction follows from the free-particle Hamiltonian

$$\hat{H}_0^{\mathrm{1st}} = \sum_{j=1}^{N}\left[\frac{\hat{\mathbf{p}}_j^2}{2m_0} + V_{\mathrm{L}}(\mathbf{r}_j)\right] \tag{2.3}$$

via the substitution $\hat{\mathbf{p}}_j \to \hat{\mathbf{p}}_j + |e|\mathbf{A}(\mathbf{r}_j,t)$ where $\hat{\mathbf{p}}_j$ is the momentum operator of the j-th particle and $\mathbf{A}(\mathbf{r}_j,t)$ is the (classical) vector potential at the position of the j-th particle [41]. In Eq. (2.3), m_0 is the free electron mass, N is the total number of electrons, and V_{L} is the lattice periodic potential of the ion cores. Using the Coulomb gauge, i.e., $\nabla\cdot\mathbf{A}=0$, the first quantization form of the light-matter interaction can be written as

$$\hat{H}_{\mathbf{p}\cdot\mathbf{A}}^{\mathrm{1st}} = \sum_{j=1}^{N}\left[\frac{|e|}{m_0}\mathbf{A}(\mathbf{r}_j,t)\cdot\hat{\mathbf{p}}_j + \frac{e^2}{2m_0}\mathbf{A}^2(\mathbf{r}_j,t)\right] \tag{2.4}$$

and is transformed into second quantization via

$$\hat{H}_{\mathrm{l-m}}^{\mathbf{p}\cdot\mathbf{A}} = \sum_{\lambda,\lambda',\mathbf{k},\mathbf{k}'}\hat{a}_{\lambda',\mathbf{k}'}^{\dagger}\hat{a}_{\lambda,\mathbf{k}}\left\langle\lambda',\mathbf{k}'\left|\frac{|e|}{m_0}\mathbf{A}\cdot\hat{\mathbf{p}} + \frac{e^2}{2m_0}\mathbf{A}^2\right|\lambda,\mathbf{k}\right\rangle. \tag{2.5}$$

The explicit evaluation of the matrix elements in Eq. (2.5) can be found, e.g., in Ref. [42] and is not be repeated here.

The resulting $\mathbf{p}\cdot\mathbf{A}$ -Hamiltonian in second quantization consists of four terms

$$\hat{H}_{\mathrm{l-m}}^{\mathbf{p}\cdot\mathbf{A}} = \hat{H}_{\mathrm{inter}}^{\mathbf{p}\cdot\mathbf{A}} + \hat{H}_{\mathrm{intersub}}^{\mathbf{p}\cdot\mathbf{A}} + \hat{H}_{\mathrm{intra}}^{\mathbf{p}\cdot\mathbf{A}} + \hat{H}_{A^2}^{\mathbf{p}\cdot\mathbf{A}} \tag{2.6}$$

that describe different kinds of interactions between the light-field and the crystal electrons. Assuming that the wavelength of the field is large compared to the modulation length of the

electronic wave functions (long wavelength limit), the explicit forms of the different terms are given by [10, 42, 43]

$$\hat{H}_{\text{inter}}^{\mathbf{p}\cdot\mathbf{A}} = \mathbf{A}(t)\cdot\frac{|e|}{m_0}\sum_{\lambda,\lambda',\mathbf{k}}\mathbf{p}_{\lambda,\lambda'}(\mathbf{k})\,\hat{a}^{\dagger}_{\lambda,\mathbf{k}}\hat{a}_{\lambda',\mathbf{k}}\ , \tag{2.7}$$

$$\hat{H}_{\text{intersub}}^{\mathbf{p}\cdot\mathbf{A}} = \mathbf{e}_{\text{z}}\cdot\mathbf{A}(t)\sum_{\lambda_{\text{b}},n,n',\mathbf{k}}\mu_{n,n'}^{\lambda_b}\,\hat{a}^{\dagger}_{(\lambda_b,n),\mathbf{k}}\hat{a}_{(\lambda_b,n'),\mathbf{k}}\ , \tag{2.8}$$

$$\hat{H}_{\text{intra}}^{\mathbf{p}\cdot\mathbf{A}} = -\mathbf{A}(t)\cdot\sum_{\lambda,\mathbf{k}}\mathbf{j}_{\lambda}(\mathbf{k})\,\hat{a}^{\dagger}_{\lambda,\mathbf{k}}\hat{a}_{\lambda,\mathbf{k}}\ , \tag{2.9}$$

$$\hat{H}_{\text{A}^2}^{\mathbf{p}\cdot\mathbf{A}} = A^2(t)\frac{e^2}{2m_0}\sum_{\lambda,\mathbf{k}}\hat{a}^{\dagger}_{\lambda,\mathbf{k}}\hat{a}_{\lambda,\mathbf{k}}\ . \tag{2.10}$$

Obviously, $\hat{H}_{\text{inter}}^{\mathbf{p}\cdot\mathbf{A}}$ describes interband transitions, i.e., transitions between different bands $\lambda \leftrightarrow \lambda'$. The strength of each transition is determined by the momentum-matrix element $\mathbf{p}_{\lambda,\lambda'}(\mathbf{k}) = \langle\lambda,\mathbf{k}|\hat{\mathbf{p}}|\lambda',\mathbf{k}\rangle\int \mathrm{d}z\,\xi^{*}_{\lambda}(z)\,\xi_{\lambda'}(z)$. In $\hat{H}_{\text{intersub}}^{\mathbf{p}\cdot\mathbf{A}}$, the band index has been separated into its bulk band and subband component, $\lambda = (\lambda_{\text{b}}, n)$. This part of the light-matter interaction is responsible for transitions between different subbands of the same bulk band, so-called intersubband transitions ($n \leftrightarrow n',\ \lambda_b = \text{const}$). Its strength is given by the intersubband-matrix element $\mu_{n,n'}^{\lambda_b} = -\frac{\mathrm{i}\hbar|e|}{m_{\lambda_b}}\int \mathrm{d}z\,\xi^{*}_{(\lambda_b,n)}(z)\,\frac{\mathrm{d}}{\mathrm{d}z}\xi_{(\lambda_b,n')}(z)$. Equation (2.9) describes the intraband coupling, i.e., the dynamics of the electrons within their bands. The intraband-matrix element (or current-matrix element) is given by

$$\mathbf{j}_{\lambda}(\mathbf{k}) = -\frac{|e|}{\hbar}\,\nabla_{\mathbf{k}}\varepsilon^{\lambda}_{\mathbf{k}}. \tag{2.11}$$

The last term of the light-matter interaction, $\hat{H}_{\text{A}^2}^{\mathbf{p}\cdot\mathbf{A}}$, is a trivial contribution that contains the operator of the total number of electrons in the system $\hat{N} = \sum_{\lambda,\mathbf{k}}\hat{a}^{\dagger}_{\lambda,\mathbf{k}}\hat{a}_{\lambda,\mathbf{k}}$. Consequently, it commutes with all electron operators and, thus, does not contribute to the system dynamics as long as only classical fields are taken into account.

2.1.2 Light-Matter Interaction in $\mathbf{x}\cdot\mathbf{E}$ Picture

An alternative formulation of the light-matter interaction is the $\mathbf{x}\cdot\mathbf{E}$ picture. In this picture, the Hamilton operator is written in terms of the electrical field $\mathbf{E} = -\frac{\partial\mathbf{A}}{\partial t}$ rather than the vector potential. Starting from first quantization, the transition to the $\mathbf{x}\cdot\mathbf{E}$ picture is mediated by a unitary transformation (the Göppert-Mayer Transformation) [41, 44]

$$\hat{O}' = \hat{T}\,\hat{O}\,\hat{T}^{\dagger}, \tag{2.12}$$

with the unitary operator

$$\hat{T} = \exp\left[\frac{\mathrm{i}|e|}{\hbar}\sum_{j}\mathbf{r}_j\cdot\mathbf{A}(\mathbf{r}_j,t)\right]. \tag{2.13}$$

Since $\hat{T}$ has an explicit time dependence, the dynamics of the system in the $\mathbf{x}\cdot\mathbf{E}$ picture is not governed simply by the transformed Hamiltonian but by an effective one

$$\hat{H}'_{\text{eff}} = \hat{T}\hat{H}\hat{T}^{\dagger} + |e|\sum_{j}\mathbf{r}_j\cdot\mathbf{E}(\mathbf{r}_j,t). \tag{2.14}$$

Inserting the $\mathbf{p}\cdot\mathbf{A}$ Hamiltonian in first quantization (the sum of Eqs. (2.3) and (2.4)) into Eq. (2.14) and omitting all terms proportional to a spatial derivative of $\mathbf{A}$ (dipole approximation), one finds for the effective light-matter interaction in the $\mathbf{x}\cdot\mathbf{E}$ picture

$$\hat{H}^{1st}_{\mathbf{x}\cdot\mathbf{E}} = |e| \sum_j \mathbf{r}_j \cdot \mathbf{E}(\mathbf{r}_j, t). \tag{2.15}$$

In second quantization, the light-matter interaction can again be decomposed into different contributions according to

$$\hat{H}^{\mathbf{x}\cdot\mathbf{E}}_{\mathrm{l-m}} = \hat{H}^{\mathbf{x}\cdot\mathbf{E}}_{\mathrm{inter}} + \hat{H}^{\mathbf{x}\cdot\mathbf{E}}_{\mathrm{intersub}} + \hat{H}^{\mathbf{x}\cdot\mathbf{E}}_{\mathrm{intra}} \tag{2.16}$$

with [5, 40, 45]

$$\hat{H}^{\mathbf{x}\cdot\mathbf{E}}_{\mathrm{inter}} = -\mathbf{E}(t)\cdot \sum_{\lambda,\lambda',\mathbf{k}} \mathbf{d}_{\lambda,\lambda'}(\mathbf{k})\, \hat{a}^\dagger_{\lambda,\mathbf{k}} \hat{a}_{\lambda',\mathbf{k}} \ , \tag{2.17}$$

$$\hat{H}^{\mathbf{x}\cdot\mathbf{E}}_{\mathrm{intersub}} = -\mathbf{e}_{\mathrm{z}}\cdot\mathbf{E}(t) \sum_{\lambda_{\mathrm{b}},n,n',\mathbf{k}} \bar{\mu}^{\lambda_b}_{n,n'}\, \hat{a}^\dagger_{(\lambda_b,n),\mathbf{k}} \hat{a}_{(\lambda_b,n'),\mathbf{k}} \ , \tag{2.18}$$

$$\hat{H}^{\mathbf{x}\cdot\mathbf{E}}_{\mathrm{intra}} = \mathrm{i}|e|\mathbf{E}(t)\cdot \sum_{\lambda,\mathbf{k}} \hat{a}^\dagger_{\lambda,\mathbf{k}} \left(\nabla_{\mathbf{k}} \hat{a}_{\lambda,\mathbf{k}}\right) \ . \tag{2.19}$$

The dipole-matrix element defining the strength of interband transitions in the $\mathbf{x}\cdot\mathbf{E}$ picture is defined as $\mathbf{d}_{\lambda,\lambda'}(\mathbf{k}) = -|e|\langle\lambda,\mathbf{k}|\hat{\mathbf{r}}|\lambda',\mathbf{k}\rangle \int \mathrm{d}z\, \xi^*_\lambda(z)\, \xi_{\lambda'}(z)$ with the position operator $\hat{\mathbf{r}}$. The intersubband-matrix element in Eq. (2.18) reads $\bar{\mu}^{\lambda_b}_{n,n'} = -|e| \int \mathrm{d}z\, \xi^*_{(\lambda_b,n)}(z)\, z\, \xi_{(\lambda_b,n')}(z)$ where the band index has again been split into its bulk band and subband components.

In the intraband Hamiltonian, Eq. (2.19), the k-derivative of an annihilation operator enters. This seems to be a bit odd at first sight since $\mathbf{k}$ is a discrete variable whose possible values are separated by $\Delta k = \frac{2\pi}{\sqrt{\mathcal{S}}}$. In every practical situation, however, the limit $\mathcal{S}\to\infty$ can be applied such that $\mathbf{k}$ becomes quasi continuous and the $\mathbf{k}$-sums are transferred to integrals according to $\sum_{\mathbf{k}} \to \frac{\mathcal{S}}{4\pi^2}\int \mathrm{d}^2k$ [5]. Nonetheless, we will keep the sum notation in the following since it is much shorter; in particular, once multiple $\mathbf{k}$-sums appear.

The two formulations of the light-matter interaction presented here and in Sec. (2.1.1) are, of course, completely equivalent since they are connected via a unitary transformation that does surely not change physical behavior of the system. It just turns out that for certain problems, the one or the other picture might be more suitable. However, one must be very careful if additional approximations are applied. The apparently same approximation might be good in the one picture while it leads to wrong results in the other one.

2.2 Response to Electromagnetic Fields

The propagation of an electromagnetic field through a semiconductor structure is described by the inhomogeneous wave equation

$$\left[\nabla^2 - \frac{n_{\mathrm{b}}^2}{c^2}\frac{\partial^2}{\partial t^2}\right] \mathbf{A}(\mathbf{r},t) = -\frac{1}{\epsilon_0\, c^2}\, \mathbf{J}(\mathbf{r},t), \tag{2.20}$$

where n_{b} is the background refractive index of the QW and the surrounding material (assumed to be identical), c is the speed of light in vacuum, and $\mathbf{J}(\mathbf{r},t)$ is the current density excited in the system that acts as a source for the field.

As a simple model system, we consider a single QW that is embedded in an optically inactive barrier. This means that the current density is nonzero only inside the QW. Since the wavelength of the field is typically much larger than the lateral width of the QW, the z-dependence of the current can be modeled via a δ-function. If we further assume that the incident field excites the QW homogeneously, we can write $\mathbf{J}(\mathbf{r},t) = \delta(z)\,\mathbf{J}(t)$. With this approximation, the wave equation (2.20) can be solved analytically and one finds for the electrical field at the position of the QW ($z = 0$) [10]

$$\mathbf{E}(t) = \mathbf{E}_0(t) - \frac{1}{2n_\mathrm{b}\epsilon_0\, c}\,\mathbf{J}(t), \tag{2.21}$$

where $\mathbf{E}_0(t)$ is the incident external field exciting the system. In certain situations, it is convenient to write the response of the system in terms of the macroscopic polarization $\mathbf{P}(t)$ rather than the current density. In this case, the corresponding equations follow from the simple connection $\mathbf{J}(t) = \frac{\partial \mathbf{P}}{\partial t}$.

Equation (2.21) allows for computing the optical response of a QW once the current density or the polarization in the QW is known. In the second quantization formalism, these response functions can be expressed via the following microscopic quantities

$$f_\mathbf{k}^\lambda = \langle \hat{a}^\dagger_{\lambda,\mathbf{k}} \hat{a}_{\lambda,\mathbf{k}} \rangle, \tag{2.22}$$

$$p_\mathbf{k}^{\lambda,\lambda'} = \langle \hat{a}^\dagger_{\lambda,\mathbf{k}} \hat{a}_{\lambda',\mathbf{k}} \rangle \text{ with } \lambda \neq \lambda', \tag{2.23}$$

$$p^{\lambda_b}_{nn',\mathbf{k}} = \langle \hat{a}^\dagger_{(\lambda_b,n),\mathbf{k}} \hat{a}_{(\lambda_b,n'),\mathbf{k}} \rangle \text{ with } n \neq n' \ . \tag{2.24}$$

The carrier occupations $f_\mathbf{k}^\lambda$ are the possibility distributions for finding an electron in Bloch state $|\lambda, \mathbf{k}\rangle$. The interband and intersubband polarizations $p_\mathbf{k}^{\lambda,\lambda'}$ and $p^{\lambda_b}_{nn',\mathbf{k}}$ describe the possibility for transitions between the denoted (sub-) bands. Similar as in the discussion of the Hamiltonian, Secs. 2.1.1 and 2.1.2, it is useful to split the current into three parts

$$\mathbf{J} = \frac{\partial \mathbf{P}_\mathrm{inter}}{\partial t} + \frac{\partial \mathbf{P}_\mathrm{intersub}}{\partial t} + \mathbf{J}_\mathrm{intra}, \tag{2.25}$$

that contain the response caused by the interband, the intersubband, and the intraband dynamics, respectively. The first two contributions are described via macroscopic polarizations while the intraband response is calculated in terms of the intraband-current density. The explicit expressions of the response functions depend on the choice of the light-matter interaction picture. For $\mathbf{p}\cdot\mathbf{A}$ interaction, one finds

$$\frac{\partial \mathbf{P}^{\mathbf{p}\cdot\mathbf{A}}_\mathrm{inter}}{\partial t} = -\frac{|e|}{m_0}\frac{1}{\mathcal{S}} \sum_{\lambda,\lambda',\mathbf{k}} \mathbf{p}_{\lambda,\lambda'}(\mathbf{k})\, p_\mathbf{k}^{\lambda,\lambda'} \ , \tag{2.26}$$

$$\frac{\partial \mathbf{P}^{\mathbf{p}\cdot\mathbf{A}}_\mathrm{intersub}}{\partial t} = -\mathbf{e}_z\, \frac{1}{\mathcal{S}} \sum_{\lambda_b,n,n',\mathbf{k}} \mu^{\lambda_b}_{n,n'}\, p^{\lambda_b}_{nn',\mathbf{k}} \ , \tag{2.27}$$

$$\begin{aligned} \mathbf{J}^{\mathbf{p}\cdot\mathbf{A}}_\mathrm{intra} &= \frac{1}{\mathcal{S}} \sum_{\lambda,\mathbf{k}} \mathbf{j}_\lambda(\mathbf{k})\, f_\mathbf{k}^\lambda - \frac{1}{\mathcal{S}} \sum_{\lambda,\mathbf{k}} \frac{e^2}{m_\lambda(\mathbf{k})}\, f_\mathbf{k}^\lambda\, \mathbf{A}(t) \\ &\equiv \mathbf{J}_\mathrm{THz} + \mathbf{J}_\mathrm{pond} \ . \end{aligned} \tag{2.28}$$

The intraband current consists of two terms, which we will refer to as the THz current $\mathbf{J}_\mathrm{THz}$ and the ponderomotive current $\mathbf{J}_\mathrm{pond}$, respectively, in the following. The latter one contains

the k-dependent effective mass that is defined as $\frac{1}{m_\lambda(\mathbf{k})} = \frac{1}{\hbar^2}\frac{\partial^2 \varepsilon_{\mathbf{k}}^\lambda}{\partial k^2}$. To keep the notation as compact as possible, the effective mass is assumed to be the same in all directions of the crystal. It can easily be shown that fully occupied bands do not contribute to $\mathbf{J}_{\text{pond}}$ and, thus, the λ-sum can be restricted to partially filled bands. If the charge carriers in those bands are occupying only states close to the Γ-point, i.e., with rather small k-values, the bands can often be approximated by a parabolic model such that the effective mass is constant (effective-mass approximation). In these situations, the ponderomotive term can be simplified according to

$$\mathbf{J}_{\text{pond}} = -\sum_\lambda \frac{e^2 n_\lambda}{m_\lambda}\,\mathbf{A}(t), \tag{2.29}$$

where $n_\lambda = \frac{1}{\mathcal{S}}\sum_{\mathbf{k}} f_{\mathbf{k}}^\lambda$ is the density of carriers in band λ. In this form, the λ-sum must be explicitly restricted to the partially filled bands. Physically, $\mathbf{J}_{\text{pond}}$ describes the response from the classical acceleration of the carriers due to the electrical field.

In the $\mathbf{x}\cdot\mathbf{E}$ picture, the currents and polarizations are given by

$$\mathbf{P}_{\text{inter}}^{\mathbf{x}\cdot\mathbf{E}} = \frac{1}{\mathcal{S}}\sum_{\lambda,\lambda',\mathbf{k}} \mathbf{d}_{\lambda,\lambda'}(\mathbf{k})\, p_{\mathbf{k}}^{\lambda,\lambda'}\ , \tag{2.30}$$

$$\mathbf{P}_{\text{intersub}}^{\mathbf{x}\cdot\mathbf{E}} = \mathbf{e}_z \frac{1}{\mathcal{S}}\sum_{\lambda_b,n,n',\mathbf{k}} \bar{\mu}_{n,n'}^{\lambda_b}\, p_{nn',\mathbf{k}}^{\lambda_b}\ , \tag{2.31}$$

$$\mathbf{J}_{\text{intra}}^{\mathbf{x}\cdot\mathbf{E}} = \frac{1}{\mathcal{S}}\sum_{\lambda,\mathbf{k}} \mathbf{j}_\lambda(\mathbf{k})\, f_{\mathbf{k}}^\lambda\ . \tag{2.32}$$

Whereas the expressions for the inter- and intersubband responses are significantly different in $\mathbf{p}\cdot\mathbf{A}$ and $\mathbf{x}\cdot\mathbf{E}$ pictures, the intraband current densities are quite similar. The only difference is that there is no ponderomotive current in the $\mathbf{x}\cdot\mathbf{E}$ picture as it appears in the $\mathbf{p}\cdot\mathbf{A}$ representation. Since both pictures lead to the same physical results, the absence of this term just means that the classical carrier acceleration is included implicitly via the dynamics of the occupations $f_{\mathbf{k}}^\lambda$ in the $\mathbf{x}\cdot\mathbf{E}$ picture.

2.3 Equations of Motion

In the previous section, it has been shown that the current density and the polarization determining the electromagnetic response of the semiconductor are given via expectation values of microscopic electronic operators. This allows for computing the response based on a quantum mechanical treatment. The dynamics of the expectation value of any operator $\hat{O}$ is determined by Heisenberg's equation of motion

$$\mathrm{i}\hbar\frac{\partial}{\partial t}\langle\hat{O}\rangle = \langle[\hat{O},\hat{H}]\rangle. \tag{2.33}$$

Inserting one of the quantities of Eqs. (2.22)–(2.24) into Heisenberg's equation, one immediately realizes that the commutator with the Coulomb Hamiltonian, Eq. (2.1) produces expectation values consisting of two creation and two annihilation operators. The next logical step would be to derive the equation of motion for this quantity which will then couple to quantities with six operators and so on. Eventually, one ends up with an infinite hierarchy of

equations, the well-known hierarchy problem of many-body physics which can be illustrated symbolically by

$$\frac{\partial}{\partial t}\langle N\rangle = T[\langle N\rangle] + V[\langle N+1\rangle]. \tag{2.34}$$

Here, $\langle N\rangle$ symbolizes an N-particle operator, i.e., an operator consisting of a product of N creation and N annihilation operators. The functionals T and V represent the non-interacting and the interacting part of the equation, respectively. In general, the hierarchy problem is not caused exclusively by the Coulomb interaction but by every many-body interaction like, e.g., the coupling to quantized light fields or the electron-phonon interaction [10].

In order to be able to calculate the system dynamics, the set of equations of motion has to be closed by systematically truncating the infinite hierarchy. Here, a cluster-expansion approach [10,46–48] is applied to obtain a closed set of equations. This scheme has been used successfully in different fields dealing with many-particle problems [9,47,49–54]. We will give only a brief overview of its basic idea here. A detailed discussion of the cluster expansion in semiconductors can be found, e.g., in Refs. [10,48].

As is known from the Hartree-Fock (HF) approximation, every N-particle quantity $\langle N\rangle$ (so-called N-particle cluster) contains single-particle contributions besides the true correlations. For example, a two-particle cluster (doublet) can be factorized into so-called singlets within the HF approximation according to [5]

$$\langle \hat{a}_1^\dagger \hat{a}_2^\dagger \hat{a}_3 \hat{a}_4\rangle_\mathrm{S} = \langle \hat{a}_1^\dagger \hat{a}_4\rangle \langle \hat{a}_2^\dagger \hat{a}_3\rangle - \langle \hat{a}_1^\dagger \hat{a}_3\rangle \langle \hat{a}_2^\dagger \hat{a}_4\rangle. \tag{2.35}$$

The difference between the full doublet $\langle 2\rangle$ and its factorized part $\langle 2\rangle_\mathrm{S}$ is the correlated doublet $\Delta\langle 2\rangle$ that describes truly correlated pairs of charge carriers without any single-particle contributions. In the cluster expansion, each N-particle cluster is factorized into all combinations of all correlated lower-order clusters including the fully correlated term $\Delta\langle N\rangle$. The factorization of $\langle N\rangle$ can formally be written recursively via

$$\begin{aligned}
\langle 2\rangle &= \langle 2\rangle_\mathrm{S} + \Delta\langle 2\rangle,\\
\langle 3\rangle &= \langle 3\rangle_\mathrm{S} + \langle 1\rangle\,\Delta\langle 2\rangle + \Delta\langle 3\rangle,\\
&\cdots\\
\langle N\rangle &= \langle N\rangle_\mathrm{S} + \langle N-2\rangle_\mathrm{S}\,\Delta\langle 2\rangle + \langle N-4\rangle_\mathrm{S}\,\Delta\langle 2\rangle\,\Delta\langle 2\rangle + \cdots\\
&\quad + \langle N-3\rangle_\mathrm{S}\,\Delta\langle 3\rangle + \langle N-5\rangle_\mathrm{S}\,\Delta\langle 2\rangle\,\Delta\langle 3\rangle + \cdots\\
&\quad + \langle N-6\rangle_\mathrm{S}\,\Delta\langle 3\rangle\,\Delta\langle 3\rangle + \cdots + \Delta\langle N\rangle,
\end{aligned} \tag{2.36}$$

where each term of the expansion includes a sum over all possibilities to factorize the cluster into the respective subclusters. The sign of each term has to be chosen correctly such that all clusters fulfill the fermionic symmetry principle.

The infinite hierarchy of equations can systematically be truncated at a certain order by omitting all higher-order correlated clusters in the factorization scheme, Eq. (2.36). The actual level at which the factorization can be truncated depends on the physical situation at hand. If one wants to study effects that involve M correlated particles, then at least all clusters up to $\Delta\langle M\rangle$ must be included.

In the following, we will present explicit equations of motion for the singlets and the doublets while triplets ($\Delta\langle 3\rangle$) and all higher-order clusters will be omitted. This so-called singlet-doublet approximation is able to describe correlation effects involving two particles like, e.g.,

carrier-carrier scattering or bound electron-hole pairs (excitons). But even on the pure singlet level (i.e., in HF approximation), one is able to understand many interesting effects as will be shown in Chaps. 3 and 5.

2.3.1 Singlet Dynamics

In this section, the explicit equations of motion for the relevant microscopic quantities are presented in singlet approximation. As a generalization to the well-known semiconductor Bloch equations [5, 55], we will include both the intra- and the intersubband dynamics in addition to the interband transitions. The equations are not discussed completely in both interaction pictures here but are rather given in the form in which they have been used for obtaining the results presented in this work. As usual, the interband dynamics is treated within the $\mathbf{x}\cdot\mathbf{E}$ picture. That way, one avoids possible unphysical divergencies that might appear in the $\mathbf{p}\cdot\mathbf{A}$ description of interband transitions [45, 56]. The terms describing the intraband dynamics will be presented in both pictures while the intersubband motion is treated exclusively in the $\mathbf{p}\cdot\mathbf{A}$ picture.

The complete singlet dynamics for a multiband system with an arbitrary number of subbands is given explicitly in Paper [IX]. Here, only one valence band (labeled by v) and two conduction subbands (c_1 and c_2) are taken into account. Since the amount of electrons excited from the valence band to the conduction band is typically very small compared to the total number electrons in the filled valence band, it is convenient to transform the equations into the electron-hole picture. This simply means that only the few missing electrons in the valence band, the holes, need to be considered instead of the many electrons remaining in the valence band. Formally, this is done by defining effective hole quantities via

$$f^{\mathrm{h}}_{\mathbf{k}} = 1 - f^{\mathrm{v}}_{\mathbf{k}} \,, \tag{2.37}$$

$$\varepsilon^{\mathrm{h}}_{\mathbf{k}} = -\varepsilon^{\mathrm{v}}_{\mathbf{k}} \,. \tag{2.38}$$

Because of the second relation, also the hole-effective mass $m_{\mathrm{h}} = -m_{\mathrm{v}}$ and the current-matrix element, Eq. (2.11), $\mathbf{j}_{\mathrm{h}}(\mathbf{k}) = -\mathbf{j}_{\mathrm{v}}(\mathbf{k})$ change their sign. All other valence-band related quantities are not affected by this transformation and their index v is kept in the following. With these constrictions, the equations of motion following from Eq. (2.33) in singlet approximation read

$$\begin{aligned}\mathrm{i}\hbar\frac{\partial}{\partial t}p^{\mathrm{v},\mathrm{c}_n}_{\mathbf{k}} &= (\tilde{\varepsilon}^{\mathrm{c}_n}_{\mathbf{k}} + \tilde{\varepsilon}^{\mathrm{h}}_{\mathbf{k}})\, p^{\mathrm{v},\mathrm{c}_n}_{\mathbf{k}} - (1 - f^{\mathrm{c}_n}_{\mathbf{k}} - f^{\mathrm{h}}_{\mathbf{k}})\,\Omega_{n,\mathbf{k}} + p^{\mathrm{c}}_{\bar{n}n,\mathbf{k}}\,\Omega_{\bar{n},\mathbf{k}} \\ &\quad + p^{\mathrm{v},\mathrm{c}_{\bar{n}}}_{\mathbf{k}}\left[\mu^{c}_{n,\bar{n}}\,A_z(t) - \sum_{\mathbf{q}\neq\mathbf{k}} V^{\mathrm{c}_1,\mathrm{c}_2}_{\mathbf{k}-\mathbf{q}}\, p^{\mathrm{c}}_{\bar{n}n,\mathbf{q}}\right] + \mathrm{i}\hbar\frac{\partial}{\partial t}p^{\mathrm{v},\mathrm{c}_n}_{\mathbf{k}}\bigg|_{\mathrm{intra}} \,,\end{aligned} \tag{2.39}$$

$$\begin{aligned}\mathrm{i}\hbar\frac{\partial}{\partial t}p^{\mathrm{c}}_{12,\mathbf{k}} &= (\tilde{\varepsilon}^{\mathrm{c}_2}_{\mathbf{k}} - \tilde{\varepsilon}^{\mathrm{c}_1}_{\mathbf{k}})\, p^{\mathrm{c}}_{12,\mathbf{k}} + p^{\mathrm{v},\mathrm{c}_2}_{\mathbf{k}}(\Omega_{1,\mathbf{k}})^* - (p^{\mathrm{v},\mathrm{c}_1}_{\mathbf{k}})^*\Omega_{2,\mathbf{k}} \\ &\quad + (f^{\mathrm{c}_1}_{\mathbf{k}} - f^{\mathrm{c}_2}_{\mathbf{k}})\left[\mu^{\mathrm{c}}_{21}\,A_z(t) - \sum_{\mathbf{q}\neq\mathbf{k}} V^{\mathrm{c}_1,\mathrm{c}_2}_{\mathbf{k}-\mathbf{q}}\, p^{\mathrm{c}}_{12,\mathbf{q}}\right] + \mathrm{i}\hbar\frac{\partial}{\partial t}p^{\mathrm{c}}_{12,\mathbf{k}}\bigg|_{\mathrm{intra}} \,,\end{aligned} \tag{2.40}$$

$$\begin{aligned}\hbar\frac{\partial}{\partial t}f^{\mathrm{c}_n}_{\mathbf{k}} &= -2\,\mathrm{Im}\left[(p^{\mathrm{v},\mathrm{c}_n}_{\mathbf{k}})^*\Omega_{n,\mathbf{k}}\right] - 2\,\mathrm{Im}\left[p^{\mathrm{c}}_{\bar{n}n,\mathbf{k}}\left(\mu^{\mathrm{c}}_{\bar{n}n}\,A_z(t) - \sum_{\mathbf{q}\neq\mathbf{k}} V^{\mathrm{c}_1,\mathrm{c}_2}_{\mathbf{k}-\mathbf{q}}\, p^{\mathrm{c}}_{n\bar{n},\mathbf{q}}\right)\right] \\ &\quad + \hbar\frac{\partial}{\partial t}f^{\mathrm{c}_n}_{\mathbf{k}}\bigg|_{\mathrm{intra}} \,,\end{aligned} \tag{2.41}$$

$$\hbar\frac{\partial}{\partial t}f_{\mathbf{k}}^{\mathrm{h}} = -2\,\mathrm{Im}\left[\sum_n (p_{\mathbf{k}}^{\mathrm{v,c}_n})^* \Omega_{n,\mathbf{k}}\right] + \hbar\frac{\partial}{\partial t}f_{\mathbf{k}}^{\mathrm{h}}\bigg|_{\mathrm{intra}} \ , \tag{2.42}$$

with the renormalized energies

$$\tilde{\varepsilon}_{\mathbf{k}}^{\lambda} = \varepsilon_{\mathbf{k}}^{\lambda} - \sum_{\mathbf{q}\neq\mathbf{k}} V_{\mathbf{k}-\mathbf{q}}^{\lambda,\lambda}\, f_{\mathbf{q}}^{\lambda} \ , \ \lambda \in \{\mathrm{h}, \mathrm{c}_1, \mathrm{c}_2\}, \tag{2.43}$$

and the generalized Rabi frequencies

$$\hbar\Omega_{n,\mathbf{k}} = \mathbf{d}_{\mathrm{c}_n,\mathrm{v}}(\mathbf{k})\cdot\mathbf{E}(t) + \sum_{\mathbf{q}\neq\mathbf{k}} V_{\mathbf{k}-\mathbf{q}}^{\mathrm{v,c}_n}\, p_{\mathbf{q}}^{\mathrm{v,c}_n}. \tag{2.44}$$

Here, $\bar{n}$ denotes the other subband index than n in each case and A_z is the z-component of the vector-potential.

In Eqs. (2.39)–(2.42), one can easily identify those terms which describe the different light-matter interaction processes via the appearance of the respective transition matrix elements. Terms proportional to $\mathbf{d}_{\mathrm{c}_n,\mathrm{v}}(\mathbf{k})$ are responsible for interband transitions while the intersubband motion is described by the terms containing μ_{12}^{c}. The intraband dynamics is included only formally here and will be discussed below for both interaction pictures. The many-body Coulomb interaction contributes exclusively via averaging $\mathbf{q}$-sums of the Coulomb-matrix elements $V_{\mathbf{q}}^{\lambda,\lambda'}$ and the microscopic quantities. This is a consequence of the singlet approximation that allows only for effective single-particle interactions: each electron "feels" the other electrons only via their mean field. Physically, these Coulomb sums lead to effective renormalizations of the fields and the single-particle energies.

The intraband dynamics is described in the $\mathbf{p}\cdot\mathbf{A}$ picture by the following terms [42]

$$\mathrm{i}\hbar\frac{\partial}{\partial t}p_{\mathbf{k}}^{\mathrm{v,c}_n}\bigg|_{\mathrm{intra},\mathbf{p}\cdot\mathbf{A}} = -\left(\mathbf{j}_{\mathrm{h}}(\mathbf{k}) + \mathbf{j}_{\mathrm{c}_n}(\mathbf{k})\right)\cdot\mathbf{A}(t)\ p_{\mathbf{k}}^{\mathrm{v,c}_n} \ , \tag{2.45}$$

$$\mathrm{i}\hbar\frac{\partial}{\partial t}p_{12,\mathbf{k}}^{\mathrm{c}}\bigg|_{\mathrm{intra},\mathbf{p}\cdot\mathbf{A}} = -\left(\mathbf{j}_{\mathrm{c}_2}(\mathbf{k}) - \mathbf{j}_{\mathrm{c}_1}(\mathbf{k})\right)\cdot\mathbf{A}(t)\ p_{12,\mathbf{k}}^{\mathrm{c}} \ , \tag{2.46}$$

$$\hbar\frac{\partial}{\partial t}f_{\mathbf{k}}^{\mathrm{c}_n(\mathrm{h})}\bigg|_{\mathrm{intra},\mathbf{p}\cdot\mathbf{A}} = 0 \ , \tag{2.47}$$

and in the $\mathbf{x}\cdot\mathbf{E}$ picture by [57–59]

$$\mathrm{i}\hbar\frac{\partial}{\partial t}p_{\mathbf{k}}^{\mathrm{v,c}_n}\bigg|_{\mathrm{intra},\mathbf{x}\cdot\mathbf{E}} = \mathrm{i}|e|\,\mathbf{E}(t)\cdot\nabla_{\mathbf{k}}\,p_{\mathbf{k}}^{\mathrm{v,c}_n} \ , \tag{2.48}$$

$$\mathrm{i}\hbar\frac{\partial}{\partial t}p_{12,\mathbf{k}}^{\mathrm{c}}\bigg|_{\mathrm{intra},\mathbf{x}\cdot\mathbf{E}} = \mathrm{i}|e|\,\mathbf{E}(t)\cdot\nabla_{\mathbf{k}}\,p_{12,\mathbf{k}}^{\mathrm{c}} \ , \tag{2.49}$$

$$\hbar\frac{\partial}{\partial t}f_{\mathbf{k}}^{\mathrm{c}_n(\mathrm{h})}\bigg|_{\mathrm{intra},\mathbf{x}\cdot\mathbf{E}} = |e|\,\mathbf{E}(t)\cdot\nabla_{\mathbf{k}}\,f_{\mathbf{k}}^{\mathrm{c}_n(\mathrm{h})} \ . \tag{2.50}$$

Remarkably, the intraband coupling enters the dynamics of the carrier occupations only in the $\mathbf{x}\cdot\mathbf{E}$ picture but not in the $\mathbf{p}\cdot\mathbf{A}$ picture. This asymmetry of both pictures regarding the intraband motion is exactly compensated by the asymmetry in the current densities, Eqs. (2.28) and (2.32). It is straight forward to show that Eq. (2.50) produces exactly the same response as the ponderomotive current density in Eq. (2.28).

2.3.2 Singlet-Doublet Equations for Incoherent Conditions

In this Thesis, the singlet-doublet approximation is used exclusively to study the intraband THz response of incoherent systems. This means that all interband coherences are assumed to have decayed when the THz field arrives which happens typically on a ps-timescale [2, 5]. Furthermore, all calculations including doublets are done for two bands (v, c) in effective-mass approximation. For incoherent systems, the only non-vanishing singlets are the carrier occupations that obey the following equations of motion [10, 43]

$$\hbar\frac{\partial}{\partial t}f^{\mathrm{c}}_{\mathbf{k}} = -2\,\mathrm{Im}\left[\sum_{\substack{\mathbf{k}',\mathbf{q}\\ \mathbf{q}\neq\mathbf{k}-\mathbf{k}'} } V^{\mathrm{vc}}_{\mathbf{q}-\mathbf{k}+\mathbf{k}'}\, c_{\mathrm{X}}^{\mathbf{q},\mathbf{k}',\mathbf{k}} - \sum_{\mathbf{k}',\mathbf{q}\neq\mathbf{0}} V^{\mathrm{cc}}_{\mathbf{q}} c_{\mathrm{cc}}^{\mathbf{q},\mathbf{k}',\mathbf{k}}\right], \tag{2.51}$$

$$\hbar\frac{\partial}{\partial t}f^{\mathrm{h}}_{\mathbf{k}} = 2\,\mathrm{Im}\left[\sum_{\substack{\mathbf{k}',\mathbf{q}\\ \mathbf{q}\neq\mathbf{k}-\mathbf{k}'} } V^{\mathrm{vc}}_{\mathbf{q}-\mathbf{k}+\mathbf{k}'}\, c_{\mathrm{X}}^{-\mathbf{q},\mathbf{k},\mathbf{k}'} - \sum_{\mathbf{k}',\mathbf{q}\neq\mathbf{0}} V^{\mathrm{vv}}_{\mathbf{q}} c_{\mathrm{vv}}^{\mathbf{q},\mathbf{k}',\mathbf{k}}\right]. \tag{2.52}$$

Here, the correlated doublets

$$c_{\mathrm{X}}^{\mathbf{q},\mathbf{k}',\mathbf{k}} = \Delta\langle \hat{a}^{\dagger}_{\mathrm{c},\mathbf{k}}\hat{a}^{\dagger}_{\mathrm{v},\mathbf{k}'}\hat{a}_{\mathrm{c},\mathbf{k}'+\mathbf{q}}\hat{a}_{\mathrm{v},\mathbf{k}-\mathbf{q}}\rangle \tag{2.53}$$

and

$$c_{\lambda\lambda}^{\mathbf{q},\mathbf{k}',\mathbf{k}} = \Delta\langle \hat{a}^{\dagger}_{\lambda,\mathbf{k}}\hat{a}^{\dagger}_{\lambda,\mathbf{k}'}\hat{a}_{\lambda,\mathbf{k}'+\mathbf{q}}\hat{a}_{\lambda,\mathbf{k}-\mathbf{q}}\rangle \tag{2.54}$$

have been introduced. The first one, $c_{\mathrm{X}}^{\mathbf{q},\mathbf{k}',\mathbf{k}}$, is the exciton-correlation function that describes correlations between electrons and holes and contains information about the amount of excitons in the system and their momentum distribution [10]. Equation (2.54) defines the electron-electron ($\lambda = \mathrm{c}$) and the hole-hole ($\lambda = \mathrm{v}$) correlations. These quantities do not couple to the THz field and, thus, are of minor importance in THz spectroscopy. Among other things, they describe the intraband carrier-carrier scattering which basically leads to relaxation of the electrons and holes [60]. Hence, their contribution to the dynamics of the occupations is often replaced by a phenomenological relaxation model.

The relevant quantity for the THz response, however, is the exciton-correlation function. Its equation of motion is given by [10, 43]

$$\begin{aligned}
\mathrm{i}\hbar\frac{\partial}{\partial t}c_{\mathrm{X}}^{\mathbf{q},\mathbf{k}',\mathbf{k}} &= (\tilde{\varepsilon}^{\mathrm{c}}_{\mathbf{k}'+\mathbf{q}} + \tilde{\varepsilon}^{\mathrm{h}}_{\mathbf{k}'} - \tilde{\varepsilon}^{\mathrm{c}}_{\mathbf{k}} + \tilde{\varepsilon}^{\mathrm{h}}_{\mathbf{k}-\mathbf{q}})\, c_{\mathrm{X}}^{\mathbf{q},\mathbf{k}',\mathbf{k}} \\
&\quad + V^{\mathrm{vc}}_{\mathbf{k}-\mathbf{k}'-\mathbf{q}}\left[f^{\mathrm{c}}_{\mathbf{k}'+\mathbf{q}}f^{\mathrm{h}}_{\mathbf{k}'}(1-f^{\mathrm{c}}_{\mathbf{k}})(1-f^{\mathrm{h}}_{\mathbf{k}-\mathbf{q}}) - (1-f^{\mathrm{c}}_{\mathbf{k}'+\mathbf{q}})(1-f^{\mathrm{h}}_{\mathbf{k}'})f^{\mathrm{c}}_{\mathbf{k}}f^{\mathrm{h}}_{\mathbf{k}-\mathbf{q}}\right] \\
&\quad + (1-f^{\mathrm{c}}_{\mathbf{k}}-f^{\mathrm{h}}_{\mathbf{k}-\mathbf{q}})\sum_{\mathbf{p}} V^{\mathrm{vc}}_{\mathbf{p}-\mathbf{k}}\, c_{\mathrm{X}}^{\mathbf{q},\mathbf{k}',\mathbf{p}} - (1-f^{\mathrm{c}}_{\mathbf{k}'+\mathbf{q}}-f^{\mathrm{h}}_{\mathbf{k}'})\sum_{\mathbf{p}} V^{\mathrm{vc}}_{\mathbf{p}-\mathbf{k}'}\, c_{\mathrm{X}}^{\mathbf{q},\mathbf{p},\mathbf{k}} \\
&\quad - \mathbf{j}_{\mu}(\mathbf{k}'+\mathbf{q}-\mathbf{k})\cdot\mathbf{A}(t)\, c_{\mathrm{X}}^{\mathbf{q},\mathbf{k}',\mathbf{k}} + \left[D_{\mathrm{X}}^{\mathbf{q},\mathbf{k}',\mathbf{k}}\right]_{\mathrm{rest}},
\end{aligned} \tag{2.55}$$

with $\mathbf{j}_{\mu}(\mathbf{k}) = -\frac{|e|\hbar}{\mu_{\mathrm{r}}}\mathbf{k}$ containing the reduced effective mass μ_{r} of the electrons and holes. In Eq. (2.55), only the most relevant contributions are given explicitly. All other terms are formally included in $\left[D_{\mathrm{X}}^{\mathbf{q},\mathbf{k}',\mathbf{k}}\right]_{\mathrm{rest}}$ and will be neglected in all calculations presented in this work. This *main-sum approximation* has shown to be justified for moderate excitation levels

of the semiconductor [10, 50]. The complete equation for the exciton correlations is given, e.g., in Ref. [10].

The second line of of Eq. (2.55) describes the microscopic scattering of electrons and holes. This process is clearly responsible for the build-up of the correlations since it is the only source term for $c_{\mathrm{X}}^{\mathbf{q},\mathbf{k}',\mathbf{k}}$. All other terms contain $c_{\mathrm{X}}^{\mathbf{q},\mathbf{k}',\mathbf{k}}$ itself and, thus, cannot generate but only modify the correlations. The contributions in the third line are important for the description of excitons [10] while the first term in line four represents the THz coupling.

Equations (2.51), (2.52), and (2.55) reveal an important feature of THz spectroscopy: For incoherent conditions, the THz field affects the system dynamics only via $c_{\mathrm{X}}^{\mathbf{q},\mathbf{k}',\mathbf{k}}$ and does not enter the singlet equations directly. This means that the THz response directly detects correlations in the system [9, 10].

3 Intersubband Transitions in Optically Excited Quantum Wells

When electrons are confined in a quasi two-dimensional structure, e.g., in a semiconductor QW, the quantization of their motion perpendicular to this plain leads to a splitting of the energy bands into so-called subbands [5]. In typical GaAs type QWs, electronic transitions between these subbands can be analyzed and manipulated using the techniques of THz spectroscopy [17–21].

Here, we present a theoretical study of the linear THz intersubband response of an optically excited GaAs QW. In order to analyze the basic principles of the intersubband dynamics, we concentrate on transitions between the two lowest conduction subbands (c1 and c2) and omit all higher subbands. Moreover, only one valence band is taken into account. The excitation scheme that is considered here is illustrated in Fig. 3.1. An optical pump beam excites the system across the bandgap and creates carriers in the c1 band as well as interband coherences (microscopic polarizations) between the c1 and the hole states. After a certain delay time, the excited system is probed by a weak THz pulse tuned to the c1-c2 intersubband transition.

In Sec. 3.1, the ultrafast THz response within the first few ps after the optical excitation is analyzed. In this regime, the optical interband coherences are still present and contribute to the intersubband response. It is shown that they lead to additional resonances in the THz absorption spectrum that can be attributed to excitonic intersubband transitions (Paper [IX]).

Section 3.2 deals with the interplay of intersubband transitions and the classical field-induced intraband carrier accelerations. Due to the coherent superposition of these contributions, characteristic Fano-like line shapes are observed in the transmission spectra. The results are in excellent agreement with recent experiments (Papers [VII] and [VIII]). Since the interband polarizations play no role in this analysis, only the incoherent case for large delay times is considered here.

In both investigations presented in this chapter, the THz intersubband response is computed by solving Eqs. (2.39)–(2.42) numerically without including the intraband dynamics, i.e., for $j_\lambda(\mathbf{k}) = 0$. These terms can be neglected since the typical intraband transitions in GaAs have frequencies of about 2 THz [10, 43] while the relevant frequency range for intersubband transitions is around 25 THz here. Furthermore, a phenomenological damping term $\mathrm{i}\hbar\frac{\partial}{\partial t}p_\mathbf{k}\big|_\mathrm{deph} = -\mathrm{i}\gamma p_\mathbf{k}$ has been added to the polarization equations in order to account for the dephasing of the coherences.

3.1 Coherent Excitonic Effects

For short delay times ($\sim$ few ps) between the optical pump pulse and the THz probe beam, the system is still in a coherent state when the THz pulse arrives. This means that the excitation state of the system is characterized by the incoherent charge carriers (electrons and holes)

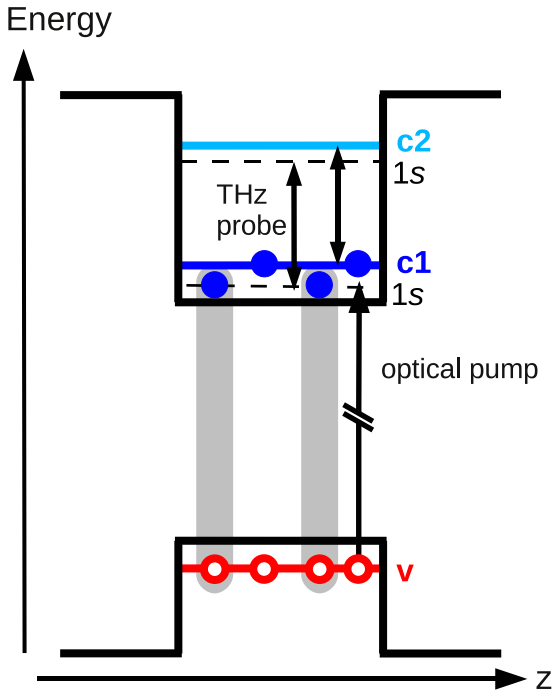

Figure 3.1: Excitation scheme considered in this chapter. First, an optical pump pulse excites the QW at the 1s resonance of the first conduction band (c1). Then, a weak THz pulse probes the c1-c2 intersubband transition probability of the excited system. The gray connections between the electrons (blue filled circles) and the holes (red open circles) symbolize the excitonic interband coherences in contrast to the incoherent electrons in the c1 band.

$f_{\mathbf{k}}^{\mathrm{c1(h)}}$ and the microscopic interband polarizations $p_{\mathbf{k}}^{\mathrm{v,c1}}$. Here, the influence of these interband polarizations on the THz intersubband response is analyzed.

It is known from the optical spectroscopy of semiconductors [5] that the interband transitions are dominated by the 1s excitonic resonance due to its strong oscillator strength compared to the free-particle transitions. In other words, the optical pulse generates basically polarizations in the 1s state, so-called coherent excitons, whose energy is reduced with respect to the bandgap. The energy levels of the 1s states for both subbands are denoted by the dashed lines in Fig. 3.1.

A detailed discussion of the polarization equations (2.39) and (2.40) reveals that there are two sources for intersubband transitions (see Paper [IX]) which are illustrated in Fig. 3.1. Besides exciting band-to-band transitions of the incoherent electrons, the THz field also couples to the v-c1 interband polarization and transfers it to a v-c2 polarization. According to the discussion above, the latter process describes transitions between coherent excitons that belong to different subbands. If the binding energies of the excitons in both subbands are sufficiently different from each other, both transitions should show up in the absorption spectrum.

To compute the linear THz absorption, we introduce the susceptibility via

$$\chi(\omega) = \frac{J_{\mathrm{intersub}}(\omega)}{\epsilon_0\,\omega^2 A(\omega)}, \tag{3.1}$$

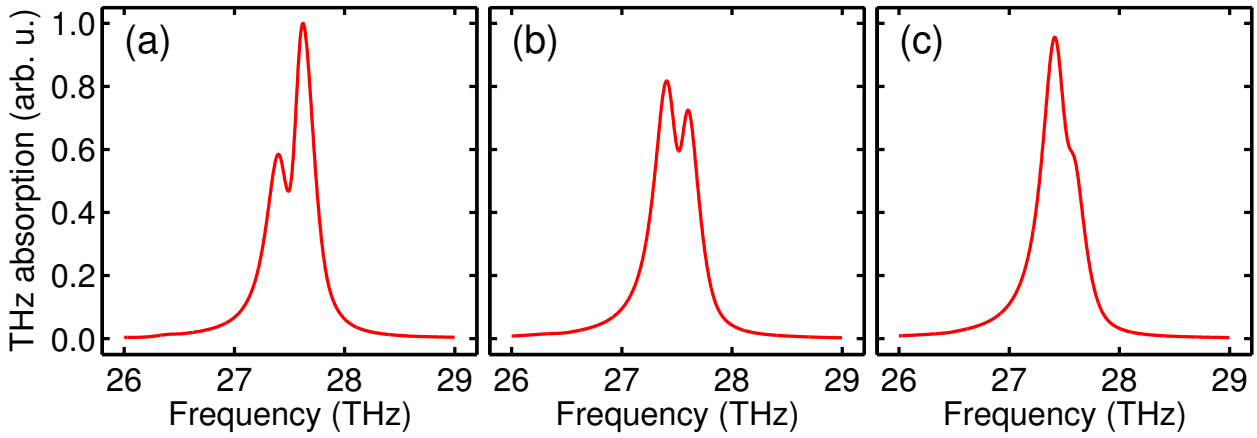

Figure 3.2: THz absorption spectra after optical excitation with a 100 fs pulse at the 1s resonance of the c1 subband. The figure illustrates the dependence on the time delay τ between the optical and the THz beams: (a) shows the absorption for $\tau = 1$ ps, (b) for $\tau = 2$ ps, and (c) for $\tau = 3$ ps. A phenomenological dephasing constant of $\gamma = 0.2$ meV has been used which corresponds to a decay time of about 3 ps of the coherences.

where $J_{\text{intersub}}(\omega)$ is the Fourier transform of the intersubband current, see Eq. (2.27). The absorption follows from $\alpha(\omega) \propto \omega \,\text{Im}[\chi(\omega)]$ [10]. More details, e.g., about the actual parameters used in the calculations are given in Paper [IX].

Figure 3.2 shows the THz absorption spectra for different values of the delay time τ between the optical and the THz excitation. For a time delay of $\tau = 1$ ps (Fig. 3.2(a)), two absorption peaks are obtained with a spectral splitting of 0.22 THz or 0.9 meV. The origin of these peaks can be revealed by switching off the terms responsible for the two transitions in the equations of motion one after another (Paper [IX]). One finds that the low-energy peak comes from the free-particle band-to-band transition while the high-energy peak is caused by 1s-to-1s transition of the coherent excitons between the subbands. In principle, also transitions to higher excitons like 1s-to-2s are possible. However, they cannot be seen here since their oscillator strengths are much smaller than that of the dominant 1s-to-1s resonance. With increasing time delay (Figs. 3.2(b) and (c)), the excitonic peak decays due to the dephasing of the v-c1 interband polarizations such that only the incoherent band-to-band resonance survives for long delay times.

As a result, we have shown that the ultrafast THz response is influenced by coherent excitonic effects. However, the splitting between the excitonic and the free-particle transitions is rather small in GaAs QWs and, thus, can only be observed for sufficiently small spectral line widths.

3.2 Fano Signatures

A THz wave that propagates through an optically excited or doped semiconductor can, under certain conditions, excite the system by inducing internal transitions. Apart from that, however, the electrical field also accelerates the charge carriers according to the acceleration theorem [22, 61, 62] leading to a wiggling motion of the electrons with the frequency of the

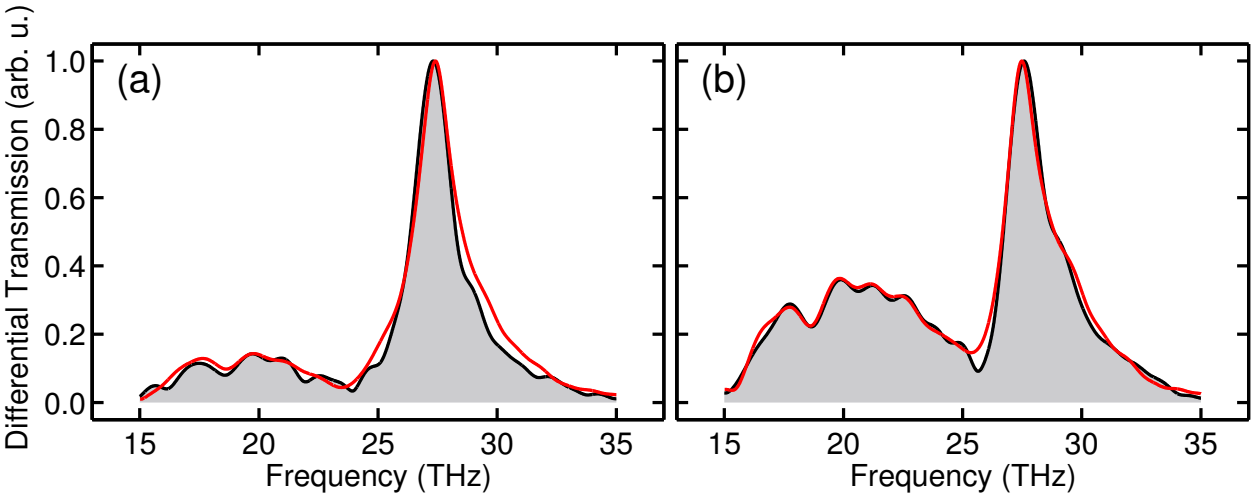

Figure 3.3: (taken from Paper [VII]) Measured (gray shaded area) and computed (red line) spectral amplitudes of the differential THz transmission $|\Delta E(\omega)|$. (a) and (b) show the result for optical ps- and fs-excitation, respectively. In (b), the ponderomotive current has been enhanced by a factor of 1.85 in the calculation in order to account for substrate excitations (see main text). To obtain the best experiment-theory agreement, the experimental THz pulse has been used as input for the theory. The phenomenological dephasing constant of $\gamma = 1.6\,\mathrm{meV}$ has been chosen to match the experimental line width.

THz field. Hence, the THz response consists of a mixture of true internal transitions and the emission from the accelerated carriers, i.e., the ponderomotive response. In many cases, this mixture shows up rather indirectly in the actual THz spectra and a careful theoretical analysis is required in order to expose the influence of the ponderomotive response [14, 23], see also Sec. 4.3.

In this section, we show that the interplay of true THz transitions and the ponderomotive motion of the carriers can directly be observed in linear THz transmission spectra. Similar to the previous section, we investigate intersubband transitions of an optically excited GaAs QW. The ponderomotive response, however, is completely non-absorptive (Paper [VII]) and can consequently not be studied with THz absorption spectroscopy. We rather analyze the differential transmission spectrum $\Delta E(\omega) = E_\mathrm{T}(\omega) - E_0(\omega)$ that is the difference between the transmitted field E_T and the incoming field E_0. According to Eq. (2.21), ΔE is proportional to the total current density

$$\Delta E(\omega) \propto J_\mathrm{tot}(\omega) = J_\mathrm{intersub}(\omega) + J_\mathrm{pond}(\omega), \tag{3.2}$$

where J_intersub and J_pond are defined in Eqs. (2.27) and (2.28), respectively. The other contributions to the current are omitted since they are strongly off-resonant with the exciting THz pulse.

Our theoretical findings (Paper [VII]) are compared to a recent experiment done by M. Wagner *et al.* at the *Forschungszentrum Dresden-Rossendorf*. They analyzed the intersubband transitions in a GaAs multi-QW structure. Detailed information about this experiment is given in Papers [VII] and [VIII]. Figure 3.3 shows the measured (gray shaded area) and the computed (red line) spectral amplitudes of the differential transmission $|\Delta E(\omega)|$ for two different optical excitation conditions. Besides the expected intersubband resonance at roughly

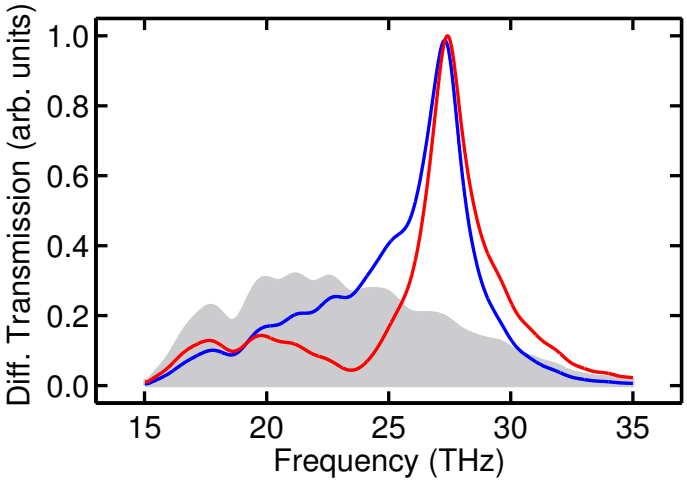

Figure 3.4: (taken from Paper [VII]) Analysis of the contributions to the differential THz transmission (ps excitation). The total result (red line) is shown together with its two components the intersubband response J_{intersub} (blue line) and the ponderomotive current J_{pond} (gray shaded area).

27 THz, we find a second broad feature centered at about 20 THz. Interestingly, the intersubband peak resembles a typical Fano resonance [37, 63–66] with an asymmetric line shape and an undershoot at its low-frequency side. To reveal the origin of the Fano signature in the THz response, we separate J_{pond} and J_{intersub} from the total current in Fig. 3.4 for the case of ps excitation. The ponderomotive current (gray shaded area) just reflects the vector potential of the THz pulse and is obviously responsible for the broad feature in the total response. Moreover, we see that the Fano-like line shape is a result of the phase-sensitive superposition of J_{intersub} and J_{pond}. Figure 3.4 clearly shows that the two contributions interfere constructively or destructively depending on the frequency.

In order to gain more insight into the interference effects that lead to the Fano signatures, a simplified analytical solution for the current density is presented here. Before the THz pulse arrives, the system is assumed to be in an incoherent excited state with no carriers in the second subband. Neglecting renormalization effects, the intersubband current takes the simple form

$$J_{\mathrm{intersub}}(\omega) = \frac{|\mu^{\mathrm{c}}_{1,2}|^2}{S} A(\omega) \sum_{\mathbf{k}} \frac{f^{\mathrm{c1}}_{\mathbf{k}}}{\varepsilon^{\mathrm{c2}}_{\mathbf{k}} - \varepsilon^{\mathrm{c1}}_{\mathbf{k}} - \hbar\omega - \mathrm{i}\gamma}. \tag{3.3}$$

To reveal the essential mechanisms, we further assume that the conduction subbands have the same dispersion (i.e., $\varepsilon^{\mathrm{c2}}_{\mathbf{k}} - \varepsilon^{\mathrm{c1}}_{\mathbf{k}} = \Delta\varepsilon = \text{const.}$) and that the THz pulse is δ-like in time space, i.e., $A(\omega) = A_0 \in \mathbb{R}$. In this case, the total current casts into

$$J_{\mathrm{tot}}(\omega) = A_0 \left(|\mu^{\mathrm{c}}_{1,2}|^2 \, n_{\mathrm{e}} \, \frac{\Delta\varepsilon - \hbar\omega}{(\Delta\varepsilon - \hbar\omega)^2 + \gamma^2} - \varepsilon_0 \, \omega^2_{\mathrm{pl}} \right) + \mathrm{i} \, \frac{A_0 |\mu^{\mathrm{c}}_{1,2}|^2 \, n_{\mathrm{e}} \, \gamma}{(\Delta\varepsilon - \hbar\omega)^2 + \gamma^2}, \tag{3.4}$$

where n_{e} is the density of the excited electrons in the c1 band. The second term in the brackets containing the plasma frequency ω_{pl} represents the ponderomotive current while all other terms follow from the intersubband current. For frequencies below the intersubband resonance ($\hbar\omega < \Delta\varepsilon$), the two terms in the brackets, i.e., J_{pond} and $\mathrm{Re}[J_{\mathrm{intersub}}]$ have an opposite sign and, thus, partially compensate each other. This leads to a reduction of the

intersubband transmission directly below the resonance frequency. At the resonance, the real part of J_{intersub} changes its sign such that J_{pond} and J_{intersub} interfere constructively for higher frequencies. Altogether, this analysis explains the Fano-typical narrowing of the resonance at the low-frequency side and the broadening above the resonance leading to an asymmetric line shape. Due to the general form of J_{intersub} in Eq. (3.4), the same argumentation holds, of course, for any transition resonance and is not restricted to intersubband transitions alone.

The Fano feature is even more pronounced if the system is excited with a broadband fs-laser pulse, see Fig. 3.3(b). In this case, the optical pulse is spectrally much broader than the line width of the $1s$ resonance. Consequently, some frequency components are not absorbed by the QWs and enter the substrate. The charge carriers excited in the bulk material effectively enhance the ponderomotive contribution with respect to the intersubband response. A quantitative analysis of the pulse propagation through the QWs (Paper [VII]) predicts an enhancement factor of 1.85 due to the bulk excitations which is in excellent agreement with the experiment (Fig. 3.3(b)).

The discussion in this section shows that the interplay of carrier accelerations and true THz transitions produces a Fano-like resonance in the spectral amplitude of the linear differential transmission. Moreover, the relative importance of the ponderomotive contribution is directly reflected by the strength of the Fano signature. Thus, the linear THz transmission provides a tool for directly identifying ponderomotive effects and determining their importance.

4 Intraband Terahertz Response of Two-Dimensional Systems

In the previous chapter, we discussed the QW response in the spectral region around 20 THz where the dynamics is dominated by intersubband transitions while intraband effects contribute only via the ponderomotive carrier acceleration. The investigations presented in this Chapter focus on the frequency range below 3 THz where true intraband effects become important in GaAs-based semiconductors. As has been verified experimentally in recent years, the major contributions to the intraband dynamics are plasmonic effects [16] and intra excitonic transitions [8, 12].

In Sec. 4.2, we study both effects for two different systems: a single-component two dimensional electron gas (2DEG) and an optically excited GaAs QW. We analyze the linear THz response for incoherent conditions and extract the plasma frequency from the obtained spectra using a plasmon-pole analysis according to Huber *et al.* [16]. Although it is well-known that the two-dimensional (2D) and three-dimensional (3D) plasma frequencies are qualitatively different from each other [5], we find that the direct THz response is characterized by a 3D-like plasma frequency for both 2D systems studied here. Besides the plasmonic features, the response of the QW is also determined by excitonic effects. By changing the carrier density, we study the transition from the purely excitonic to the plasma-like regime. This section presents a detailed experiment-theory comparison of our theoretical findings with recently measured results from T. Grunwald, S. Chatterjee *et al.* The results discussed here have not been published yet but will be part of a paper that is in preparation (Paper [X]).

In Sec. 4.3, the influence of the many-body effects on the THz response is briefly analyzed. It is shown that the response of the 2DEG consists of a strong competition between the ponderomotive response and the Coulomb correlations. As a consequence, the obtained results cannot be explained by means of a simple Drude model [1].

To compute the THz response, we have to solve the equations of motion in singlet-doublet approximation, see Sec. 2.3.2. In contrast to the previous section, however, we use analytical solutions here instead of solving the equations numerically. The analytical formulas for the THz response of the 2DEG and the QW are presented Sec. 4.1.

4.1 Analytical Solutions

The total response of the system is determined by the intraband-current density in Eq. (2.28), i.e., $J_{\mathrm{tot}} = J_{\mathrm{THz}} + J_{\mathrm{pond}}$. For the investigation presented in this chapter, we assume parabolic bands such that the ponderomotive current takes the simple form in Eq. (2.29). Hence, only the dynamics of J_{THz} remains to be solved. With few approximations, the singlet-doublet equations (2.51), (2.52), and (2.55) can be solved analytically. We first derive the response for the 2DEG in Sec. 4.1.1 and then give the result for the QW in Sec. 4.1.2.

4.1.1 Two-Dimensional Electron Gas

In a semiconductor-based 2DEG structure, the electrons forming the 2DEG are provided by a nearby n-doped layer. The remaining dopants are positively charged such that various many-body correlations will emerge between the 2DEG electrons and the dopants. This is a similar situation as in an optically excited QW with the dopants playing the role of the holes. An important difference, of course, is that the holes in a QW can move freely while the dopants are fixed at their lattice site. The analogy to the electron-hole gas allows us to formulate a theory for the 2DEG electrons based on the QW theory discussed in Chap. 2. To account for the immobility of the doping ions, we simply regard them as holes with an infinite effective mass, $m_{\mathrm{ion}} \to \infty$ and consequently $\varepsilon_{\mathbf{k}}^{\mathrm{ion}} = 0$. The distribution function of the ions is constant $f_{\mathbf{k}}^{\mathrm{ion}} = f_0^{\mathrm{ion}} \ll 1$ but still satisfies $\frac{1}{\mathcal{S}} \sum_{\mathbf{k}} f_{\mathbf{k}}^{\mathrm{ion}} = n_{\mathrm{ion}}$ where n_{ion} is the 2D density of the dopants.

The 2DEG system which we consider in this chapter is a high-electron-mobility transistor (HEMT) described in Ref. [38] and in Paper [VI]. Here, the dopant are located in a thin sheet separated from the 2DEG electrons by a spacer layer with thickness $d_{\mathrm{sp}} = 10\,\mathrm{nm}$. The 2DEG theory presented here is, of course, not only applicable for this particular structure but can be used to describe any semiconductor-based 2DEG. However, some of the approximations made in the following are adapted for this HEMT and might fail in some other structures.

Before we apply the 2DEG transformations to the equations of motion, we first introduce some approximations. As mentioned already in Sec. 2.3.2, we include the electron-electron correlations only via a phenomenological relaxation of the electron distribution. Second, we neglect the main-sum terms in Eq. (2.55), i.e., those terms including a sum over the correlations. These terms describe bound pairs of electrons and holes/ions. In our case, however, the electrons and ions are located in spatially separated layers which makes it very unlikely for them to form bound pairs.

With these approximations, the 2DEG equations following from Eqs. (2.51) and (2.55) read

$$\hbar \frac{\partial}{\partial t} f_{\mathbf{k}} = -2\,\mathrm{Im}\left[\sum_{\mathbf{q}\neq\mathbf{k}} V_{\mathbf{q}-\mathbf{k}}^{\mathrm{vc}}\, \bar{c}_{\mathrm{X}}^{\mathbf{q},\mathbf{k}}\right] - \Gamma(f_{\mathbf{k}} - f_{\mathbf{k}}^{\mathrm{FD}}), \tag{4.1}$$

$$\begin{aligned} \mathrm{i}\hbar \frac{\partial}{\partial t} \bar{c}_{\mathrm{X}}^{\mathbf{q},\mathbf{k}} = {} & (\tilde{\varepsilon}_{\mathbf{q}} - \tilde{\varepsilon}_{\mathbf{k}} - \mathrm{i}\gamma)\, \bar{c}_{\mathrm{X}}^{\mathbf{q},\mathbf{k}} + V_{\mathbf{q}-\mathbf{k}}^{\mathrm{vc}}\, (f_{\mathbf{q}} - f_{\mathbf{k}})\, \mathcal{S}\, n_{\mathrm{ion}} \\ & - \mathbf{j}(\mathbf{q}-\mathbf{k}) \cdot \mathbf{A}(t)\; \bar{c}_{\mathrm{X}}^{\mathbf{q},\mathbf{k}}, \end{aligned} \tag{4.2}$$

where we have defined the reduced correlation function

$$\bar{c}_{\mathrm{X}}^{\mathbf{q},\mathbf{k}} = \sum_{\mathbf{k}'} c_{\mathrm{X}}^{\mathbf{q}-\mathbf{k}',\mathbf{k}',\mathbf{k}}. \tag{4.3}$$

Since we describe only electrons in one band, the band indices of the energies and the occupations have been omitted here. The second term of Eq. (4.1) describes the phenomenological relaxation of the electrons towards a Fermi-Dirac distribution $f_{\mathbf{k}}^{\mathrm{FD}}$ at lattice temperature. This term includes formally all kinds of scattering processes except for the electron-ion scattering that is taken into account microscopically. In Eq. (4.2), we have defined a damping constant γ for the correlations to account for higher-order scattering processes. A more general form of Eq. (4.2) including the complete doublet dynamics can be found in Paper [V].

In order to solve Eqs. (4.1) and (4.2), we assume that the system in a steady-state with

$f_{\mathbf{k}}^{(0)} = f_{\mathbf{k}}^{\mathrm{FD}}$ before the THz pulse arrives. The corresponding correlation function is given by

$$\bar{c}_{\mathrm{X},(0)}^{\mathbf{q},\mathbf{k}} = \frac{V_{\mathbf{q}-\mathbf{k}}^{\mathrm{vc}} \left(f_{\mathbf{k}}^{\mathrm{FD}} - f_{\mathbf{q}}^{\mathrm{FD}}\right) \mathcal{S} n_{\mathrm{ion}}}{\tilde{\varepsilon}_{\mathbf{q}} - \tilde{\varepsilon}_{\mathbf{k}} - \mathrm{i}\gamma}. \tag{4.4}$$

As a next step, we apply a perturbation expansion of the occupations and correlations in orders of the vector potential: $f_{\mathbf{k}} = f_{\mathbf{k}}^{(0)} + f_{\mathbf{k}}^{(1)} + \mathcal{O}(A^2)$ and $\bar{c}_{\mathrm{X}}^{\mathbf{q},\mathbf{k}} = \bar{c}_{\mathrm{X},(0)}^{\mathbf{q},\mathbf{k}} + \bar{c}_{\mathrm{X},(1)}^{\mathbf{q},\mathbf{k}} + \mathcal{O}(A^2)$. We truncate the expansion after the first order since we are only interested in the linear response. When neglecting scattering and renormalization effects of the first-order quantities, their equations of motion can be easily solved using a Fourier transformation. Inserting the solution into Eq. (2.28) yields the THz-current density for the 2DEG

$$J_{\mathrm{THz}}(\omega) = \frac{e^2\hbar^2\, n_{\mathrm{ion}}\, A(\omega)}{m_e^2\left(\hbar\omega + \mathrm{i}\Gamma\right)} \sum_{\mathbf{k},\mathbf{q}} (V_{\mathbf{q}-\mathbf{k}}^{\mathrm{vc}})^2 \, \frac{f_{\mathbf{q}}^{\mathrm{FD}} - f_{\mathbf{k}}^{\mathrm{FD}}}{\tilde{\varepsilon}_{\mathbf{q}} - \tilde{\varepsilon}_{\mathbf{k}} - \mathrm{i}\gamma} \, \frac{(k_x - q_x)^2}{\hbar\omega - \tilde{\varepsilon}_{\mathbf{q}} + \tilde{\varepsilon}_{\mathbf{k}} + \mathrm{i}\gamma}. \tag{4.5}$$

Without loss of generality, we have assumed that the THz field is polarized in x-direction.

4.1.2 Terahertz-Elliott Formula

We compute the THz response of a QW using the analytical result presented in Ref. [10]. The singlet-doublet equations are solved within the exciton basis that is defined via the Wannier Equation

$$(\tilde{\varepsilon}_{\mathbf{k}}^{\mathrm{c}} + \tilde{\varepsilon}_{\mathbf{k}}^{\mathrm{h}})\, \phi_{\lambda}^{\mathrm{R}}(\mathbf{k}) - (1 - f_{\mathbf{k}}^{\mathrm{c}} - f_{\mathbf{k}}^{\mathrm{h}}) \sum_{\mathbf{q}} V_{\mathbf{k}-\mathbf{q}}^{\mathrm{vc}}\, \phi_{\lambda}^{\mathrm{R}}(\mathbf{q}) = E_{\lambda}\, \phi_{\lambda}^{\mathrm{R}}(\mathbf{k}). \tag{4.6}$$

Here, $\phi_{\lambda}^{\mathrm{R}}(\mathbf{k})$ is the right-handed wave function of an exciton in state λ and E_{λ} is the corresponding eigenenergy. In this basis, the THz current can be written as [10]

$$J_{\mathrm{THz}}(\omega) = \frac{A(\omega)}{\hbar\omega + \mathrm{i}\Gamma} \sum_{\nu,\lambda} (S^{\nu,\lambda}(\omega)\Delta n_{\nu,\lambda} - [S^{\nu,\lambda}(-\omega)\Delta n_{\nu,\lambda}]^*), \tag{4.7}$$

where

$$S^{\nu,\lambda}(\omega) = \sum_{\beta} \frac{(E_{\beta} - E_{\nu}) J_{\nu,\beta} J_{\beta,\lambda}}{E_{\beta} - E_{\nu} - \hbar\omega - \mathrm{i}\gamma} \tag{4.8}$$

is the generic THz response function and

$$J_{\alpha,\beta} = \sum_{\mathbf{k}} \phi_{\alpha}^{\mathrm{L}}(\mathbf{k})\, j_{\mu}(\mathbf{k})\, \phi_{\beta}^{\mathrm{R}}(\mathbf{k}) \tag{4.9}$$

is the transition matrix element between pair states α and β containing the left-handed solution of the Wannier Equation $\phi_{\lambda}^{\mathrm{L}}(\mathbf{k})$. In this description, we fully include pair-wise electron-hole correlations while electron-electron and hole-hole as well as higher order correlations are included via the phenomenological damping constants γ and Γ. The THz current, Eq. (4.7), depends on the initial many-body state $\Delta n_{\nu,\lambda}$ which includes the population of true (bound or unbound) excitons for $\nu = \lambda$ as well as a correlated electron-hole plasma for $\nu \neq \lambda$. The steady-state for the off-diagonal correlations reads [10]

$$\Delta n_{\nu,\lambda} = \frac{E_{\nu} - E_{\lambda}}{E_{\lambda} - E_{\nu} - \mathrm{i}\gamma} \frac{1}{\mathcal{S}} \sum_{\mathbf{k},\mathbf{q}} \phi_{\nu}^{\mathrm{L}}(\mathbf{k})\, f_{\mathbf{k}+\mathbf{q}}^{\mathrm{c}} f_{\mathbf{k}-\mathbf{q}}^{\mathrm{h}}\, \phi_{\lambda}^{\mathrm{L}}(\mathbf{k}). \tag{4.10}$$

Since we do not include exciton formation [9, 50, 51] microscopically here, the diagonal populations $\Delta n_{\lambda,\lambda}$ are a free parameter of our theory.

4.2 2D Plasmons

The fundamental excitations of an electron gas are the plasmons, i.e., collective oscillations of the charges with the plasma frequency ω_{pl} [67–70]. They serve as an important model system for many-particle interactions [15] and are currently widely employed in plasmonics [71–73] and metamaterial research [74–76]. Moreover, the plasmon contribution to screening determines the effective Coulomb interaction among the charge carriers, showing a strong dependence on the effective dimensionality of the interacting many-body system [5,15,77–81].

One identifies the plasma frequency in a 3D system as $\omega^2_{\mathrm{pl,3D}} = \frac{n_{\mathrm{3D}}e^2}{\epsilon_0\epsilon_{\mathrm{b}}m_e}$ when analyzing, e.g., the long-wavelength limit of the dielectric function in random phase approximation (RPA) [5]. Here, n_{3D} is the 3D electron density, m_e is the effective mass of the electrons, and ϵ_{b} is the background dielectric constant. A similar analysis of a 2D electron gas yields $\omega^2_{\mathrm{pl,2D}}(\mathbf{q}_\parallel) = \frac{n_{\mathrm{2D}}e^2}{2\epsilon_0\epsilon_{\mathrm{b}}m_e}\ |\mathbf{q}_\parallel|$ with the sheet electron density n_{2D} and the in-plane wave vector $\mathbf{q}_\parallel$. In contrast to the three dimensional case, the 2D plasma frequency vanishes in the long-wavelength limit ($\mathbf{q}_\parallel \to 0$) and, in particular, for a homogeneous excitation of the 2D plasmon.

This dimension dependence of the plasma frequency is well-known and commonly accepted. In fact, the characteristic dispersion properties of the 2D plasma frequency have been verified experimentally already more that thirty years ago [82–85]. In these works, the plasma frequency was measured in different 2D systems like image-potential surface states on liquid helium [82], a 2DEG embedded in a field-effect transistor [83, 84], and in GaAs-AlGaAs heterostructures [85]. In contrast to our analysis presented in this section, the plasma frequency has been extracted directly from transmission spectra in those investigations. Consequently, it contains mixed information about both the pure response of the respective 2D system and the electrodynamical back coupling of the emitted fields to the matter.

The ultrafast build-up of the plasmonic response of a 3D carrier plasma was investigated in a femtosecond-pump and THz-probe experiment by Huber *et al.* [16]. The authors identified the plasmons by extracting the inverse dielectric function $1/\epsilon$ from the measured THz spectra.

Similar to this approach, we study the plasmonic response of two different 2D systems, i.e., the electron-hole plasma in an optically excited QW and the 2DEG in a HEMT that is described in Ref. [38] and in Paper [VI]. To apply the plasmon-pole analysis of Ref. [16], we have to compute the linear dielectric function ϵ that is defined via $D(\mathbf{q}_\parallel,\omega) = \epsilon_0\,\epsilon_b\,\epsilon(\mathbf{q}_\parallel,\omega)\,E(\mathbf{q}_\parallel,\omega)$ [15, 86–89] where $D(\mathbf{q}_\parallel,\omega)$ is the displacement field and $E(\mathbf{q}_\parallel,\omega)$ the electrical field. This relation leads to a simple connection between the dielectric function and the susceptibility: $\epsilon = \epsilon_b + \chi$. In the long-wavelength limit ($\mathbf{q}_\parallel = 0$), the dielectric function can be written as

$$\epsilon(\omega) = \epsilon_{\mathrm{b}}\left(1 - \frac{\omega^2_{\mathrm{pl}}}{\omega^2}\right) + \frac{J_{\mathrm{THz}}(\omega)}{\epsilon_0 L_{\mathrm{QW}}\,\omega^2 A(\omega)}, \tag{4.11}$$

with the generic plasma frequency $\omega^2_{\mathrm{pl}} = \frac{ne^2}{\epsilon_0\epsilon_{\mathrm{b}}\mu_r}$, the reduced mass of electrons and holes/ions μ_r, the quantum-well/2DEG width L_{QW}, and the vector potential of the THz field $A(\omega)$. The density n entering the plasma frequency is the 3D carrier density, i.e., $n = n_{\mathrm{2D}}/L_{\mathrm{QW}}$. The term containing ω_{pl} in Eq. (4.11) represents the ponderomotive contribution while the last term includes the response from the many-body correlations which are computed with the analytical formulas given in Sec. 4.1. Our results are compared to a recent experiment performed by T. Grunwald *et al.* Detailed information about the 2DEG measurements can be found in Paper [VI].

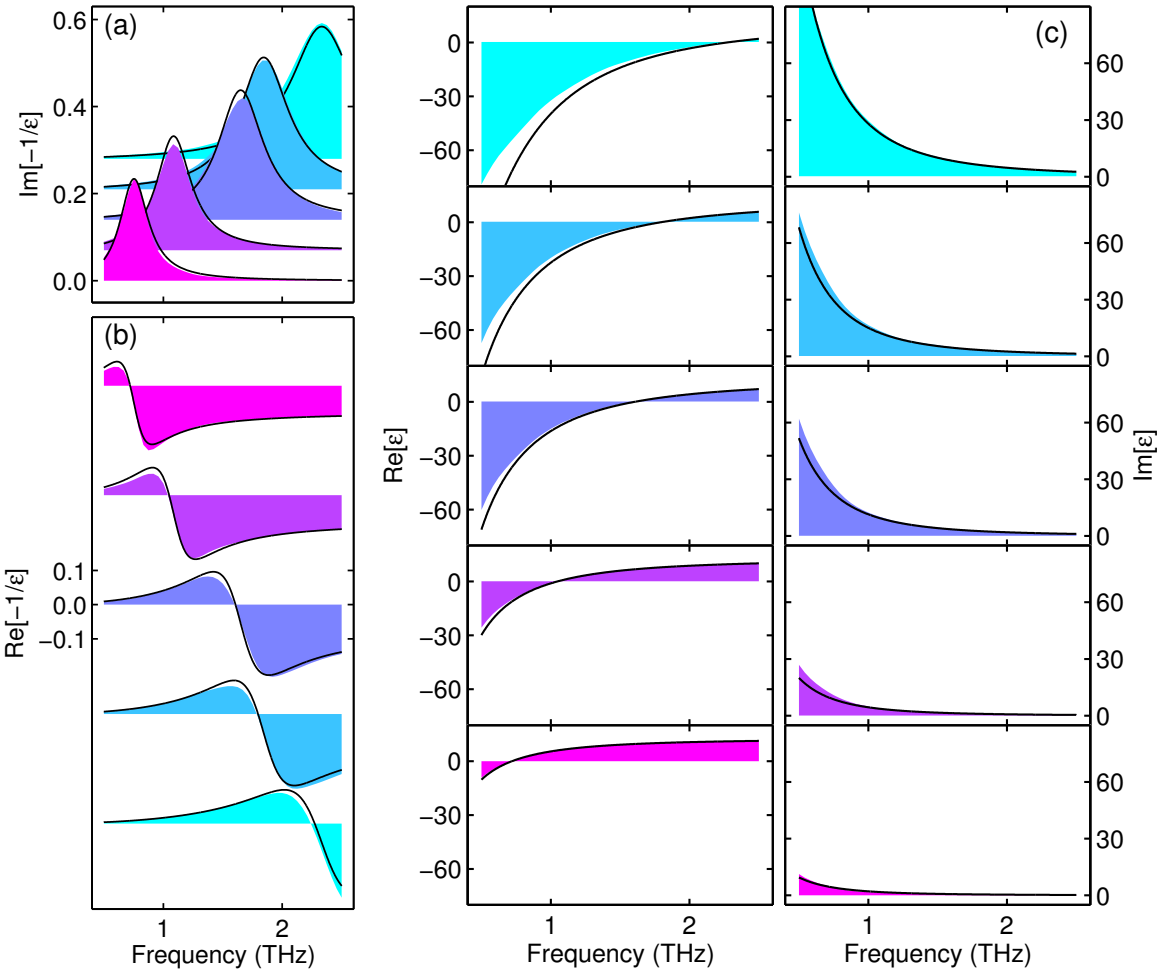

Figure 4.1: Quantum well THz response for plasma conditions with a lattice temperature of 100 K. (a), Measured (shaded areas) and calculated (solid lines) $\mathrm{Im}[-1/\varepsilon]$ spectra for different carrier densities (4.4, 8.5, 18.5, 22.8, and 35.5 $\times 10^9\,\mathrm{cm}^{-2}$ from bottom to top). (b), Experiment-theory comparison of $\mathrm{Re}[-1/\varepsilon]$ for the same excitation conditions as in (a). Here, the excitation density increases from top to bottom. (c), The corresponding $\epsilon(\omega)$ spectra.

First, we discuss the THz response of the QW at a lattice temperature of 100 K after optical excitation in the band continuum. In our plasmon-pole analysis, we characterize the plasma frequency via a resonance peak in $\mathrm{Im}[-1/\epsilon]$ and an accompanying dispersive feature in $\mathrm{Re}[-1/\epsilon]$. Figure 4.1(a) shows $\mathrm{Im}[-1/\varepsilon]$ as function of the THz frequency for various carrier densities. The experimental results are represented by the shaded areas and the theoretical findings are plotted as black lines. In the calculations, we included a thermal distribution of ionized excitons besides the steady-state solution for the correlated electron-hole plasma, Eq. (4.10). As in all investigations presented in this chapter, the experimental carrier densities are obtained via the experiment-theory comparison. We clearly identify a well-defined plasmon pole at finite frequencies for all excitation levels. The corresponding graphs of $\mathrm{Re}\,[-1/\varepsilon]$ are shown in Fig. 4.1(b). Here, the typical dispersive behavior is found confirming the presence of plasma resonances at the respective frequencies. The corresponding ϵ-spectra (Fig. 4.1(c)) also display a plasma-like response, i.e., a ω^{-1}-decay of the imaginary

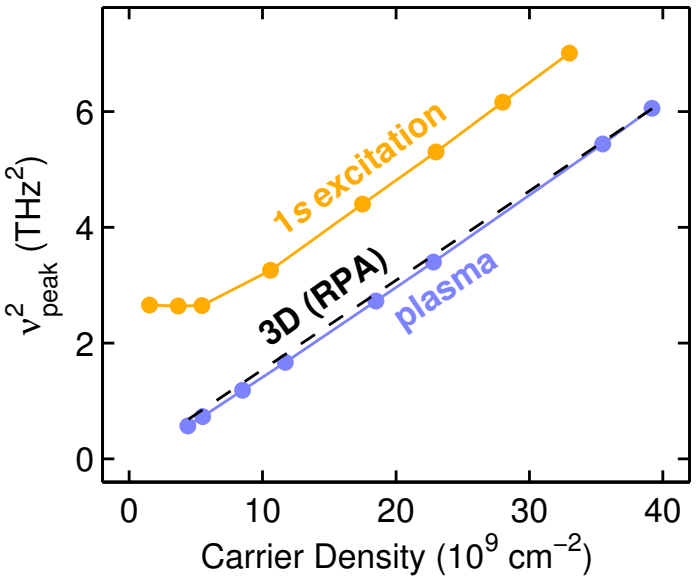

Figure 4.2: Squared peak frequency of $\mathrm{Im}[-1/\varepsilon]$ as a function of the carrier density extracted from the QW results. The blue curve shows the result for plasma conditions (see Fig. 4.1(a)) and the orange curve for resonant $1s$ excitation (see Fig. 4.4(a)). For comparison, we also show the RPA result for the 3D plasma frequency (black dashed line).

part and a zero-crossing of the real part at the plasma frequency.

A quantitative analysis of the density dependence of the plasma frequency is presented as the blue line in Fig. 4.2. We find a linear increase of ω_{pl}^2 with the carrier density as expected for the plasma frequency. Moreover, the 2D result almost perfectly coincides with the usual 3D plasma frequency for all densities. The slight deviations from the 3D result are a consequence of many-body effects included in our theory.

Next, we investigate the THz response of the 2DEG as a representative of a single-component electron plasma in contrast to the two-component electron-hole plasma that we studied above. Experimentally, the electron density of the 2DEG can be controlled via an external bias voltage applied to the HEMT. This allows us to perform a similar experiment-theory study as for the QW. Figure 4.3(a) displays the resulting $\mathrm{Im}[-1/\epsilon]$ spectra for different electron densities. We again find pronounced plasma peaks that shift to higher frequencies when the density is increased. A quantitative analysis verifies the expected linear density dependence of ω_{pl}^2 (Fig. 4.3(b)). The dielectric function, Figs. 4.3(c) and (d), also shows the typical plasma behavior with a zero crossing of the real part both in our calculations (red lines) and in the measurement (shaded areas). Notably, the plasma peaks of the 2DEG are much broader than those of the QW, cp. Fig. 4.1(a). This is caused by the electron-ion correlations that turn out to be very strong in this system as will be shown in Sec. 4.3.

The observation of a dimension-independent plasma-frequency ω_{pl} in our investigations is a consequence of the direct analysis of the dielectric function $\epsilon(\omega)$. This quantity describes the pure material response without any electrodynamic modifications due to back coupling of the induced fields to the matter. Indeed, the direct response of a plasma system is independent of its dimension as was already noted by F. Stern [90] in 1967. The response and, thus, the plasma

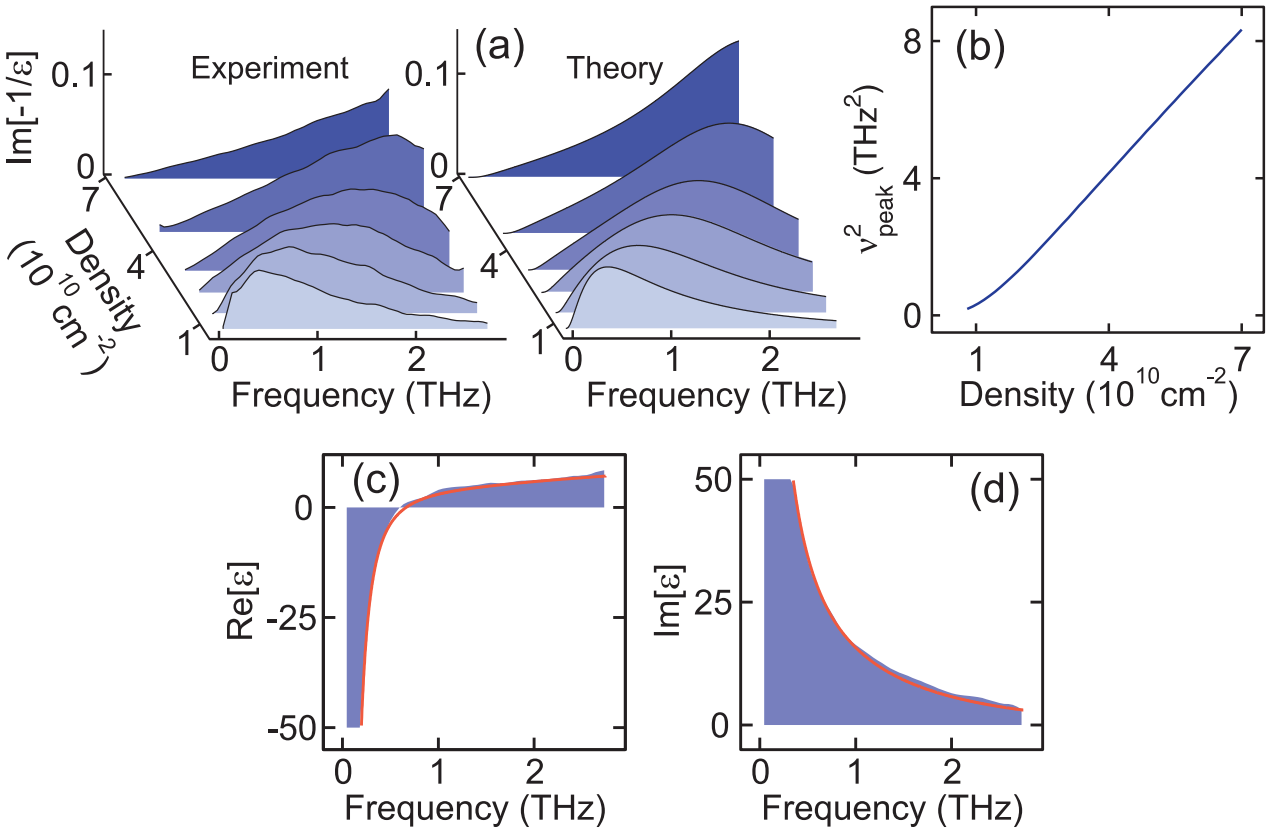

Figure 4.3: Plasmon pole analysis of the THz response of the 2DEG embedded in a HEMT. (a), Experimental (left) and theoretical (right) Im$[-1/\varepsilon]$ spectra for carrier densities of 0.8, 1.45, 2.3, 3.2, 4.8, and 7.0 $\times 10^{10}\,\mathrm{cm}^{-2}$ from bottom to top. (b), Density dependence of the plasma frequency. (c) and (d), Real and imaginary part of $\epsilon(\omega)$ for a carrier density of $3.2{\times}10^{10}\,\mathrm{cm}^{-2}$. The blue shaded areas show the experimental results while the red solid lines represent the calculations. The doping concentration of the HEMT is $4{\times}10^{12}\mathrm{cm}^{-2}$.

frequency ($\tilde{\omega}_{\mathrm{pl}}$) become strongly dimension dependent if and only if back-coupling effects are included, as reported, e.g., in Refs. [82–85]. The reason for this dimension dependence is that the actual electromagnetic field that the electrons respond to depends on the arrangement of the electrons. A 2D sheet of electrons surely induces a field that is significantly different from that induced by the electrons in a 3D system. Furthermore, the induced field from a 2D plasma is fully 3D and consequently extends into the surrounding material. This means that the system dynamics and, thus, the plasma frequency $\tilde{\omega}_{\mathrm{pl}}$ obtained from such a back-coupling sensitive analysis is also affected by the environment of the plasma. In contrast, the dielectric function $\epsilon(\omega)$ contains the pure response of the 2D plasma and does not depend on the plasma's surroundings.

Coming back to the QW, we now study the THz response in a regime where bound electron-hole pairs, i.e., excitons exist. In the experiment, this is done by pumping resonantly at the $1s$ exciton energy for a lattice temperature of 4 K. Figure 4.4(a) shows the experimental and theoretical plasmon-pole analysis for different carrier densities. We find a clear resonance even for the lowest excitation levels where a cold exciton gas with a $1s$ fraction of nearly 100% is

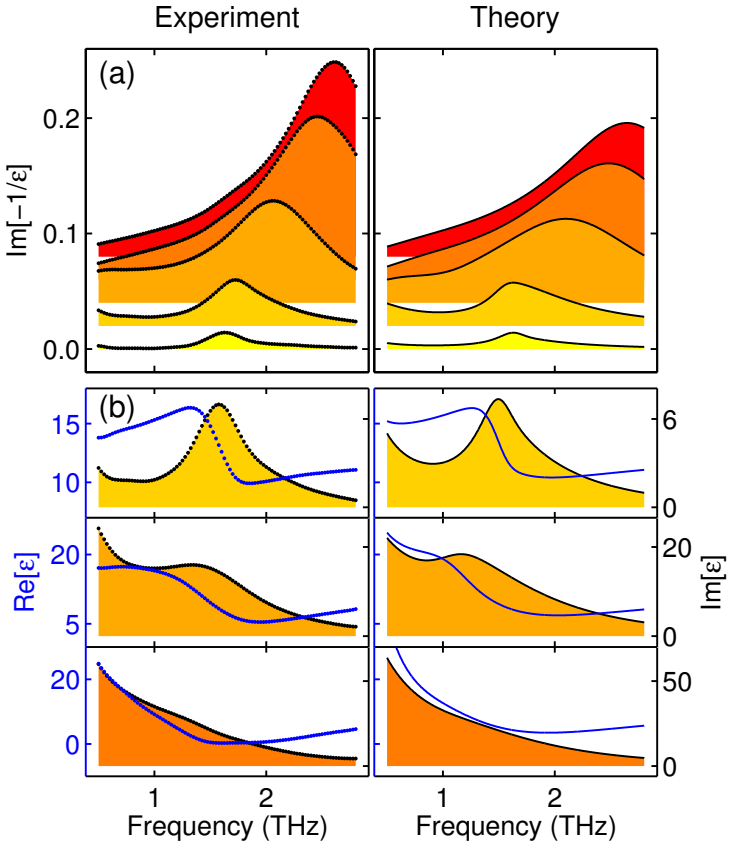

Figure 4.4: THz response after resonant excitation at the 1s exciton with a lattice temperature of 4 K. (a), Plasmon-pole analysis according to Fig. 4.1(a). The experimental results are compared to the model calculations with sheet densities of 1.52, 5.45, 17.5, 28.0, and 33.0 $\times 10^9\,\mathrm{cm}^{-2}$. (b), Dielectric function $\epsilon(\omega)$ for three different excitation densities (increasing from top to bottom). The blue lines show the real part of $\epsilon(\omega)$ while the imaginary part is presented as the shaded areas. We scaled Re[ϵ] to the left y-axes and Im[ϵ] to the right y-axes.

excited, i.e., almost all carriers are bound to 1s excitons. Under these condition, the response is dominantly determined by the excitons and not by the plasma contributions. Hence, the definition of a plasma frequency becomes questionable here. In fact, our quantitative analysis of the density dependence of the peak frequencies reveals a completely different behavior at small densities than expected for a plasma frequency (orange curve in Fig. 4.2).

To clarify the origin of the peaks in Im[$-1/\epsilon$], we look at the dielectric function instead of its inverse. The real (blue lines) and imaginary parts (shaded areas) of $\epsilon(\omega)$ are shown in Fig. 4.4(b) for three different excitation densities increasing from top to bottom. A response typical for a 1s exciton gas is obtained for the smallest density. Here, the peak of Im[ϵ] mainly results from transitions from the 1s to 2p exciton state with additional contributions from transitions to higher p-states. The real part of ε shows the typical dispersive shape at the 1s-to-2p transition.

Obviously, the peak position of the low-density Im[$-1/\epsilon$] spectrum coincides with the 1s-to-2p transition frequency. Hence, the resonance in Im[$-1/\epsilon$] is actually a signature of intra-

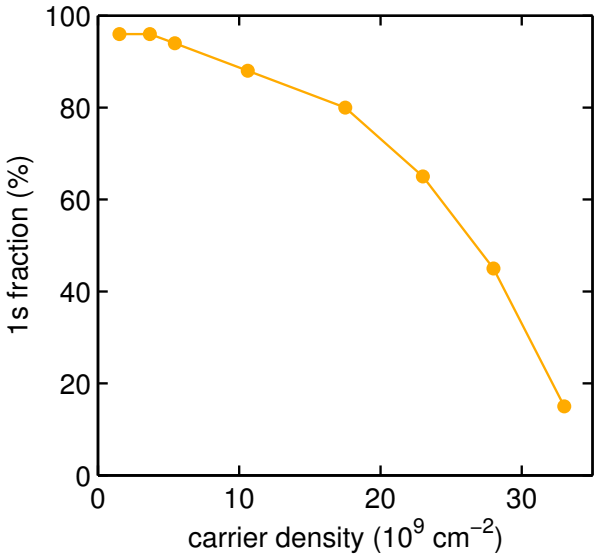

Figure 4.5: Fraction of electron-hole pairs that are bound to 1s excitons as function of carrier density for resonant 1s excitation. The exciton fractions have been extracted from the experiment-theory comparison.

excitonic transitions and is not related to the plasma frequency. This is easily confirmed by the straight-forward identity $\mathrm{Im}[-1/\epsilon] = \frac{\mathrm{Im}[\epsilon]}{|\epsilon|^2}$. In fact, a resonance in $\mathrm{Im}[-1/\epsilon]$ is observed even if $|\epsilon|^2$ is spectrally flat. The resonance then originates from a peak in $\mathrm{Im}[\epsilon]$, e.g., at the 1s-to-2p frequency. Consequently, the plasma frequency cannot be determined from the $\mathrm{Im}[-1/\varepsilon]$ spectrum alone but additional analysis is necessary, e.g., information about the density dependence of the peak frequency is required. Moreover, a true plasma resonance is necessarily accompanied by a zero crossing of $\mathrm{Re}[\epsilon]$ and, thus, by a dispersive line shape of $\mathrm{Re}[-1/\epsilon]$.

As the carrier density is increased, the response becomes more plasma-like. Most importantly, $\mathrm{Im}[\epsilon]$ diverges towards zero frequency as expected for a simple Drude response of an electron gas. However, no zero crossing is observed in $\mathrm{Re}[\epsilon]$ even for the highest experimentally accessible carrier densities. Thus, no pure plasma response is found and the resonance in $\mathrm{Im}[-1/\varepsilon]$ is a mixture of both exciton and plasma contributions. The detailed experiment-theory comparison provides information about the exciton densities in the QW when the system evolves from the excitonic towards the plasma-like regime. As shown in Fig. 4.5, the total 1s exciton fraction drops from 96 % to 15 % for the lowest and highest carrier densities, respectively. Comparing this result with Fig. 4.2, we find that the resonance in $\mathrm{Im}[-1/\epsilon]$ already shows the typical dependence of a plasmon pole as a significant amount of 1s excitons is still present in the system.

Our investigations show that the THz response of 2D electron or electron-hole plasmas exhibit plasmon poles that behave essentially the same way as in 3D. In particular, we observe non-vanishing plasma frequencies for vanishing in-plane wave vector. Since we analyze the dielectric function, we obtain the direct response of the plasma without any modifications due to the self consistent back coupling of the induced fields to the system dynamics. Only these back-coupling effects are responsible for the dimension dependence of the self consistent plasma frequency. Consequently, our THz response contains only information about the

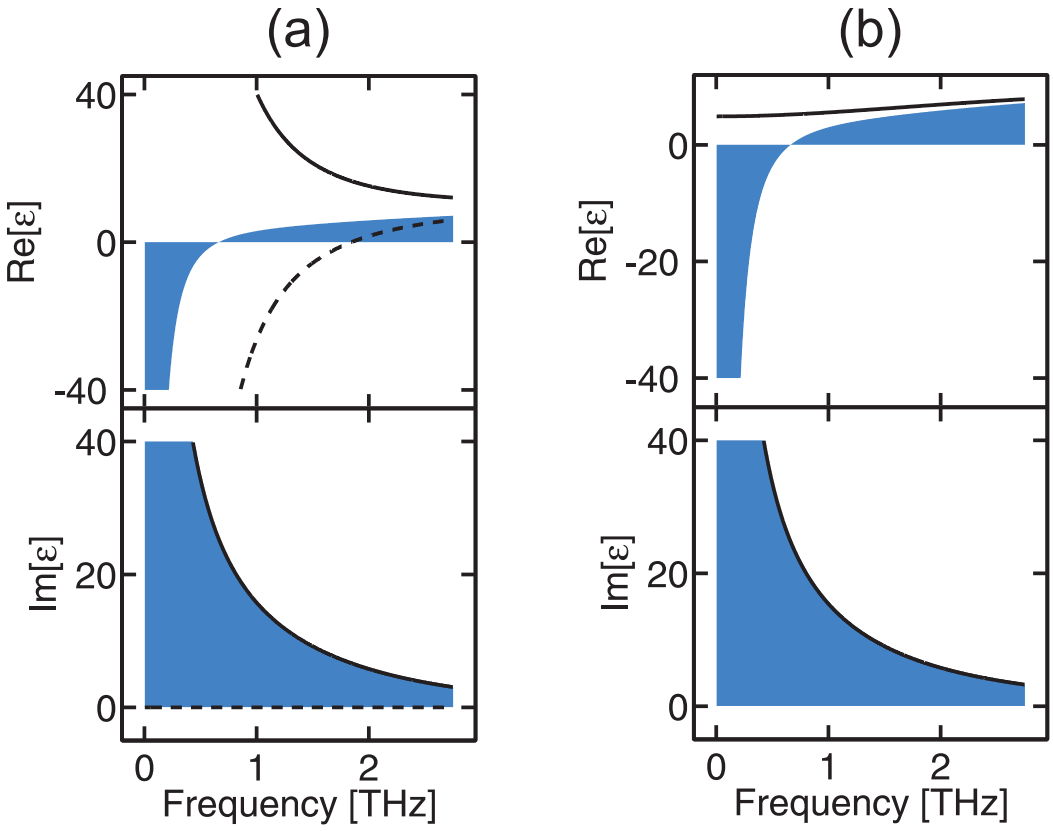

Figure 4.6: (Taken from Paper [V]) Computed dielectric function of the 2DEG for an electron density of $3.2 \times 10^{10}\,\mathrm{cm}^{-2}$ and a doping concentration of $4 \times 10^{12}\,\mathrm{cm}^{-2}$. (a) The full calculation (blue shaded area) is shown together with the contributions from J_{THz} (solid lines) and from J_{pond} (dashed lines). (b) Comparison of the Drude model (black line) with the full result (blue shaded area). The Drude parameters have been chosen to match the imaginary part.

plasma and is not affected by its environment. In all cases studied here, we obtain an excellent agreement with corresponding experiments. This allows us to extract detailed information about the behavior of the electron-hole system at the transition from the excitonic to the plasma regime.

4.3 Many-Body Effects

In order to identify the influence of many-body effects in the response of the 2DEG, we perform a switch-off analysis with our theory. Figure 4.6(a) shows the full dielectric function (blue shaded area) of the 2DEG together with the result from purely ponderomotive motion (dashed lines) and from the electron-ion correlations (solid lines). First of all, we see that the imaginary part and, thus, the absorption follows exclusively from the many-body interactions. This is, of course, not surprising since non-interacting particles cannot absorb light. The real part, however, consists of a strong competition between both effects. Since J_{pond} and J_{THz} have a similar magnitude but a different sign, they partially compensate each other leading

to a total response that is much smaller than any of its contributions. Hence, the Coulomb correlations between the electrons in the 2DEG and the doping ions play an important role in the THz response. This might seem surprising since the electrons and ions are in different layers in the HEMT such that the Coulomb interaction among the charges is significantly reduced. However, for the experimentally relevant conditions, the doping concentration, i.e., the density of ions is about two orders of magnitude larger than the electron density. This enhances the many-body contributions with respect to the ponderomotive response since the ion density enters only J_{THz} but not J_{pond}, see Eqs. (4.5) and (4.11). From a physical point of view, the electron-ion scattering probability is strongly increased due to the huge amount of available scattering partners for the electrons. In contrast, the ponderomotive contribution accelerates only the 2DEG electrons regardless of the ion concentration.

A simple model that is often used to describe the response of an electron plasma is the Drude model [1]. It basically adds a phenomenological damping to the ponderomotive current leading to the dielectric function

$$\epsilon_{\mathrm{Drude}}(\omega) = \epsilon_b \left(1 - \frac{\omega_{\mathrm{pl}}^2}{\omega\left(\omega + \mathrm{i}\Gamma_{\mathrm{D}}\right)}\right), \tag{4.12}$$

were Γ_{D} is the phenomenological damping constant. In Fig. 4.6(b), we compare this model with our full calculation (solid lines: Drude model, blue shaded areas: microscopic theory). The parameters of the Drude model are chosen such that the best fit with the imaginary part of $\epsilon(\omega)$ is obtained. In this case, the model predicts a completely wrong real part. An alternative fit to $\mathrm{Re}[\epsilon]$ would produce a wrong imaginary part. In Paper [VI], a similar Drude fit is applied to the measured response of the 2DEG leading to the same result. Obviously, the strong many-body effects in the 2DEG produce a THz response that cannot be explained by means of a simple Drude model.

We want to close this chapter with a short remark about the validity of the intraband theory used here. As shown in Sec. 4.2, our theory explains the measured spectra very well in the experimentally accessible frequency range, i.e., down to roughly 0.2 THz. As ω approaches zero, however, we find a ω^{-2} divergence of the real part of the susceptibility χ, see, e.g., Eqs. (4.5) and (4.7). This causes a divergent conductivity $\sigma = -\mathrm{i}\epsilon_0\omega\chi$ at zero frequency. In semiconductors, however, scattering processes should lead to a constant current density for a constant electric field according to Ohm's law. Consequently we should expect a real-valued finite conductivity in this case, i.e., a saturation of $\mathrm{Re}[\chi]$ for $\omega \to 0$ as predicted, e.g, by the Drude model. Obviously, our theory fails at very small frequencies. The divergencies, by the way, are not an artifact of the approximations that we applied to derive the analytical formulas. They are rather a consequence of the phenomenological scattering models in the equations of motion for the occupations and the correlations. In fact, it is known [10] that such simple models violate fundamental conservation laws of the actual scattering processes. Therefore, it is not surprising that we find the wrong behavior for $\omega \to 0$ where the response is dominantly determined by scattering effects.

5 Extreme Nonlinear Optics

We now want to discuss a completely different regime than in the previous chapters where we investigated the *linear THz* response. In contrast, the discussion in this chapter focuses on the *extreme nonlinear* regime, i.e., the response to extremely strong fields. Furthermore, we leave the field of THz physics here and study the response to optical fields.

In general, extreme nonlinear optics describes the regime where the Rabi frequency, i.e., the field strength times the dipole-matrix element, becomes comparable to or even larger than the transition frequencies in the investigated system [24]. In GaAs-type semiconductor structures peak-field strengths of several tens of MV/cm are required to reach this regime. Such high field strengths can nowadays be achieved using ultrashort laser pulses [91] which allows for accessing the extreme nonlinear optical response experimentally. Theoretical investigations [26–32] predicted many novel effects including carrier-wave Rabi flopping, high-harmonic generation (HHG), and carrier-wave Mollow splitting. Some of these effects have also been observed experimentally in semiconductors [33–35]. Theoretically, the extreme nonlinear regime can be characterized by the failure of the rotating-wave approximation (RWA) [5, 24] that is usually applied in nonlinear optics. In short, this approximation neglects the non-resonant negative frequency components of the exciting pulse. For very strong fields, however, these contributions become important and produce new effects as is shown below. Hence, we define the extreme nonlinear effects as those effects that cannot be explained within the RWA.

In this chapter, we review our theoretical studies on the extreme nonlinear optical response of semiconductor nanostructures presented in Papers [I]–[IV]. Among other things, it is shown that Coulomb effects are negligibly small in this regime in contrast to linear or conventional nonlinear optics where the Coulomb interaction dominates the response [5]. We start our investigations in Sec. 5.1 discussing the response from pure interband transitions. In Sec. 5.2, we demonstrate that the intraband acceleration plays an important role leading to even stronger nonlinearities than the pure interband dynamics.

We compute the extreme nonlinear response by numerically solving Eqs. (2.39)–(2.42) in two-band approximation, i.e., without the terms describing intersubband transitions. The intraband dynamics is treated in the $\mathbf{x} \cdot \mathbf{E}$ picture here, see Eqs. (2.48)–(2.50). The emission follows from the total current density $J_{\mathrm{tot}} = \frac{\partial}{\partial t} P_{\mathrm{inter}} + J_{\mathrm{intra}}$ according to Eqs. (2.30) and (2.32). More information about the theoretical treatment is given in Papers [I] and [III].

5.1 Interband Transitions

To get an overview of the extreme nonlinear effects in the semiconductor, we compute the intensity of the coherently emitted radiation $I_{\mathrm{rad}}(\omega)$ for many different peak field strengths E_0 of the exciting laser pulse. As a starting point, we omit the intraband terms and include only interband transitions in this section. Figure 5.1(a) shows such an excitation dependent emission spectrum of a GaAs quantum wire. Similar results are obtained for QWs, see Paper [I]. Each cross section parallel to the x-axis corresponds to a simple $I_{\mathrm{rad}}(\omega)$ spectrum

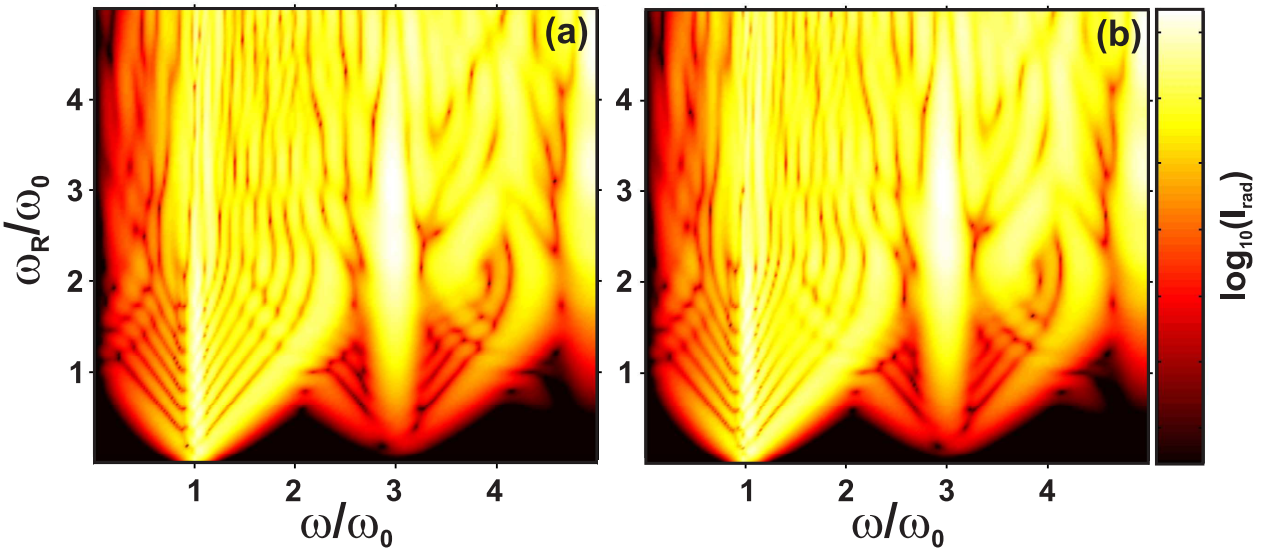

Figure 5.1: (taken from Paper [I]) Excitation dependent emission spectra of a quantum wire for pure interband dynamics. The x-axis labels the spectrometer frequency ω in units of the excitation frequency ω_0. Here, the system is excited resonantly at the bandgap by a Gaussian pulse with a duration of 10 ps. The y-axis shows the dependence on the excitation strength scaled via the Rabi frequency ω_R. The emission intensity is illustrated by the logarithmic color encoding that covers seven orders of magnitude. In (a), the result for the free-particle dynamics is shown while (b) includes the Coulomb interaction on Hartree-Fock level.

for the respective excitation level. The field strength of the exciting pulse is scaled via the peak Rabi frequency $\omega_R = \hbar^{-1} d_{vc}(0) E_0$ where $d_{vc}(0)$ is the dipole-matrix element at $k = 0$. The system is excited resonantly at the bandgap, i.e., $\hbar\omega_0 = E_g = 1.43\,\text{meV}$. Assuming $d_{vc}(0) = 3\,e\text{Å}$ in GaAs, a Rabi frequency of $\omega_R = \omega_0$ corresponds to a field strength of $E_0 = 48\,\text{MV/cm}$. For not too strong excitation, $\omega_R < \omega_0$, we see that the fundamental emission at $\omega = \omega_0$ is accompanied by the so-called Mollow sidebands [92] at frequencies $\omega_0 \pm \omega_R$. A similar structure is found around the third harmonic, $\omega = 3\omega_0$, where additional sidebands arise at $3\omega_0 \pm \omega_R$. Whereas the fundamental Mollow triplet is a well-known nonlinear effect, the splitting of the third harmonic as well as the emergence of the third harmonic itself are true extreme nonlinear effects beyond the RWA. In analogy to the conventional Mollow splitting that arises due to the Rabi flopping of the Bloch vector [5], the splitting of the higher harmonics is called carrier-wave Mollow splitting since it results from carrier-wave Rabi flopping [26]. Further extreme nonlinear effects that can be seen here are discussed in Paper [I].

In order to study the influence of the Coulomb interaction among the carriers on the extreme nonlinear response, we include the many-body effects on different levels to our theory. As a reference, Fig. 5.1(a) shows the result of a free-particle calculation. In Fig. 5.1(b), the Coulomb interaction has been included in Hartree-Fock approximation. One can hardly identify any differences between these two figures. Even if one plots the cross sections on top of each other, only minute Coulomb effects are visible (Paper [I]). In the next step, we include the carrier-carrier scattering microscopically in second-Born Markov approximation [5, 55].

It turns out that the scattering has almost no effect on the response (see Paper [I]). Consequently, we can conclude that Coulomb effects play only a minor role in the extreme nonlinear response of semiconductor nanostructures while the dominant contribution follows from the free-particle dynamics. This is the complete opposite of what is known from linear and conventional nonlinear optics where excitonic effects as well as scattering processes dominate the optical response [5]. As an intuitive explanation, we note that in extreme nonlinear optics, the energy scale describing the light-matter interaction ($\hbar\omega_\mathrm{R} \approx E_\mathrm{g}$) is about two orders of magnitude larger than the typical Coulomb energies, i.e., the exciton binding energy $E_\mathrm{B} \approx 10\,\mathrm{meV}$. Consequently, the system dynamics is mainly governed by light-matter interaction processes and not by carrier-carrier interactions. This argumentation is supported by further investigations (Paper [I]) that show a strong dependence of the spectra on the details of the exciting pulse. In contrast, changing, e.g., the dephasing times has almost no effect on the results.

5.2 Coupled Inter- and Intraband Dynamics

Up to now, only the extreme nonlinear effects that arise due to interband transitions have been studied. In semiconductors, however, the electrons also experience a ponderomotive intraband acceleration as has already been discussed in previous chapters. In conventional optics, the amplitudes of the resulting wiggling motion of the electrons are negligibly small due to the large frequencies of the optical pulses. For elevated excitation, these rapid oscillations become stronger and might influence the optical response for sufficiently high field strengths. With a simple estimation, we can identify the regime where significant modifications due to the ponderomotive motion can be expected. In the $\mathbf{x}\cdot\mathbf{E}$ picture, the intraband dynamics is described via Eqs. (2.48)–(2.50) which lead effectively to a time-dependent electron wave vector k according to the acceleration theorem [22, 61, 62]

$$\frac{\mathrm{d}k}{\mathrm{d}t} = -\frac{|e|}{\hbar}\,E(t). \tag{5.1}$$

The solution is given by $k(t) = k_0 + \frac{|e|}{\hbar}\,A(t)$ where k_0 is the wave vector before the excitation and $A(t) = -\int_{-\infty}^{t}\mathrm{d}t' E(t')$ is the vector potential of the optical pulse. We see that the electrons are transiently shifted in k-space directly following the vector potential. Hence, the largest shift Δk_max the electrons experience during the excitation is defined by the peak value of the vector potential $A_0 \approx \omega_0^{-1} E_0$:

$$\Delta k_\mathrm{max} \approx \frac{|e|E_0}{\hbar\omega_0}. \tag{5.2}$$

As soon as Δk_max becomes comparable to the extent of the Brillouin zone, we might expect significant nonlinear contributions from the carrier acceleration. For the extreme nonlinear conditions discussed in Sec. 5.1 with $\omega_\mathrm{R} = \omega_0$, we find a shift of roughly one third of the Brillouin zone indicating strong ponderomotive effects in the extreme nonlinear response.

In fact, Fig. 5.2(b) shows a strong enhancement of the HHG once the intraband terms are included. For comparison, we also plot the result for pure interband dynamics in Fig. 5.2(a). In both cases, we find a linear increase of the highest generated frequency with the excitation strength. Without carrier accelerations, significant emission for frequencies $\omega \lesssim 2\,\omega_\mathrm{R}$ is obtained while the full calculation predicts strong emission even up to $\omega \approx 10\,\omega_\mathrm{R}$. Apart

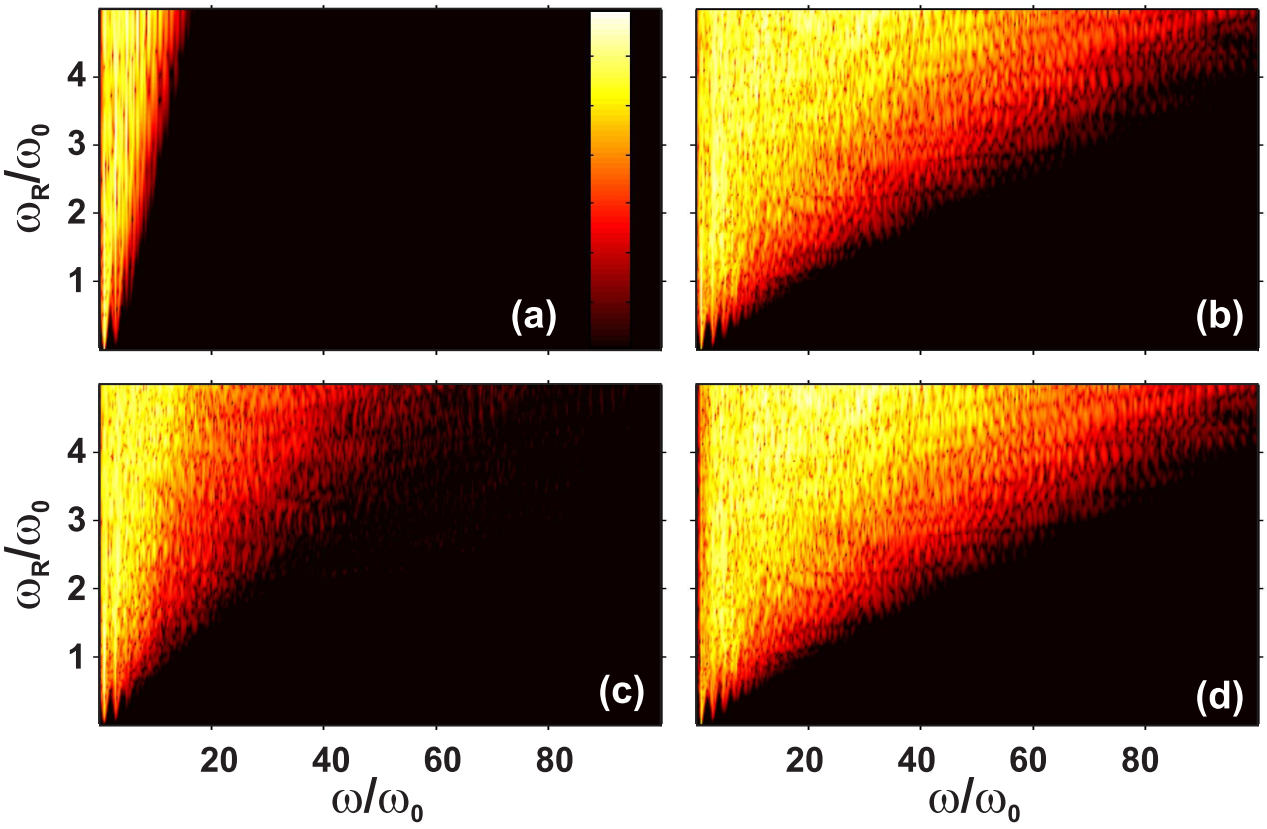

Figure 5.2: (taken from Paper [III]) The emission spectra from the coupled inter- and intraband dynamics, (b)–(d), are compared to the result for pure interband coupling, (a). The total result, (b), is separated into the emission via the intraband current, (c), and via the interband polarization, (d). The excitation conditions are the same as in Fig. 5.1.

from the HHG, it is hardly possible to assign any of the spectral features to certain extreme nonlinear effects in Fig. 5.2(b) due to the high complexity of the emission spectra.

In paper [IV], it is shown that the pure intraband acceleration of an excited carrier distribution would lead to the emergence of odd harmonics at frequencies obeying roughly $\omega \lesssim 0.5\,\omega_{\mathrm{R}}$, i.e., even less HHG than for pure interband dynamics. Hence, it is clearly the nontrivial coupling of inter- and intraband dynamics that is responsible for both the strong enhancement of the HHG and the high spectral complexity. To gain more insight into these coupling effects, we separate the total emission into its contributions from the intraband current J_{intra} and from the interband polarization P_{inter}. The resulting spectra are shown in Fig. 5.2(c) and (d), respectively. Obviously, the emission is mainly governed by the interband polarization. In fact, a more careful analysis of the different contributions (see Paper [III]) reveals that the emission via J_{intra} is about two orders of magnitude smaller than the polarization emission. Consequently, the strong broadening of the emission spectra is caused by the acceleration induced modifications of the interband transitions. In other words, the optically excited microscopic interband polarizations $p_{\mathbf{k}}^{\mathrm{vc}}$ are accelerated in k-space leading to rapid modulations of their phases. Each microscopic polarization oscillates with $\exp\left(-\frac{\mathrm{i}}{\hbar}\varepsilon_{k(t)}\right)$ where $\varepsilon_k = \varepsilon_k^{\mathrm{c}} + \varepsilon_k^{\mathrm{h}}$ is the interband-transition energy and $k(t)$ is given by Eq. (5.1). This nontrivial time depen-

dence of the phases induces additional strong nonlinearities in the interband dynamics leading to the observed broad emission in Figs. 5.2(b) and (d).

Additionally, we analyze the influence of the effective band structure parameters on the response, see Paper [III]. Due to the huge transient shifts of the carriers in k-space, we need to model the band structure in the whole Brillouin zone. In the calculations presented in Fig. 5.2, we used simple tight-binding bands [5] proportional to $\cos(ka)$ where a is the lattice constant of GaAs. The parameters of this model are chosen such that the correct effective masses for GaAs at the Γ-point are obtained. This model, however, predicts a too large band width of the conduction band ($\Delta_c = 6.9\,\mathrm{eV}$). Computing the response with an artificially decreased band width, we found significant narrower emission spectra, i.e., less high-harmonic generation. Within the tight-binding model, the decrease of the band width is accompanied by an unphysical increase of the effective mass. Consequently, it is not clear which of the band parameters is responsible for the narrowing of the transmission. To overcome this problem, we introduce an improved band structure resulting from a linear combination of $\cos(ka)$ and $\cos(2ka)$. This allows us to vary the band width and the effective mass separately. Corresponding calculations show that the emission is much more sensitive to the effective mass than to the band width. In particular, we obtain equally efficient HHG as in Fig. 5.2(b) when the band width is decreased to a physical meaningful value while the effective mass is kept constant. Obviously, a smaller effective mass increases the broadness of the emission, i.e, produces higher harmonics. This is understandable since a decrease of the effective mass automatically produces an increase of the maximum steepness of the band structure. For steeper bands, the transition energies ε_k change more rapidly due to the time-dependent wave vector $k(t)$ as discussed above. Consequently, the phase factor $\exp\left(-\frac{\mathrm{i}}{\hbar}\varepsilon_{k(t)}\right)$ of the polarizations contains higher frequency components leading to more efficient HHG in the emission.

6 Conclusion and Outlook

In this Thesis, we studied the linear THz and the extreme nonlinear optical response of low-dimensional semiconductor structures. Besides purely theoretical investigations, detailed experiment-theory comparisons have been presented that showed excellent agreement of our calculations with recent state-of-the-art measurements.

Our microscopic theory is based on an equation-of-motion approach where the infinite many-body hierarchy is truncated using a cluster-expansion scheme. We presented extended semiconductor Bloch equations in singlet approximation including inter- intra- and intersubband dynamics. It has been shown that for incoherent conditions, the inclusion of doublets, i.e., two-particle correlations, is crucial in order to describe true intraband transitions apart from the ponderomotive motion. The latter contribution to the intraband dynamics describes the classical free-particle accelerations of the electrons induced by the electrical field. This part of the intraband coupling can usually be neglected when only the absorption is studied. However, we showed that it significantly contributes to the complete response of semiconductors both for weak THz fields and for sufficiently strong optical excitation.

As a first application of our theory, we investigated intersubband transitions between the two lowest conduction subbands in optically excited QWs. We showed that the THz field does not only excite electrons from one subband to another but it can also couple to the coherent excitons and induce excitonic intersubband transitions. This means that the THz field generates transitions between excitonic states that belong to different subbands. In GaAs, the excitonic binding energies of the first and the second conduction subbands are slightly different from each other such that we found two distinct resonances in the absorption spectrum resulting from the excitonic and the band-to-band transitions. Inspired by a recent measurement of intersubband transitions in GaAs QWs, we also analyzed the differential THz transmission and obtained a characteristic Fano-like line shape of the intersubband resonance. This Fano resonance could unambiguously be attributed to the phase sensitive superposition of the responses due to the intersubband transitions and the ponderomotive carrier accelerations. In other words, the differential transmission provides direct information about the relative importance of ponderomotive effects in the presence of a true transition resonance: The stronger the observed Fano features are the larger is the contribution from the carrier accelerations to the response of the investigated system.

Next, we studied the THz response from the intraband dynamics in two different 2D systems: the electron-hole plasma in an optically excited QW and the 2DEG in a HEMT. We derived effective equations of motion for the 2DEG by treating the doping ions that provide the electrons for the 2DEG as holes with infinite effective masses. For the actual calculations, we used an analytical solution of the resulting 2DEG equations. The response of the QW has been computed with the THz-Elliott formula. First, we investigated the responses of the 2DEG and the QW under plasma conditions. Using a plasmon pole analysis, i.e., plotting the inverse dielectric function, we found that the THz response of both 2D systems is determined by a 3D-like plasma frequency. These findings are in great agreement with recent experi-

ments. As an explanation for this seeming contradiction, we noted that we analyze the direct plasma response via the dielectric function that does not include self-consistent back coupling effects which are responsible for the dimension dependence of the usual plasma frequency. Additionally, we analyzed the QW response for conditions where almost all electrons and holes are bound to excitons. By increasing the density, we followed the transition from the exciton dominated to the plasma-like regime. A quantitative experiment-theory comparison allowed us to extract the actual exciton fractions for each density. We found that the QW already starts to shows plasma-like response while a significant amount of carriers is still bound to excitons. Furthermore, a theoretical switch-off analysis of the 2DEG response revealed a strong competition between ponderomotive dynamics and the many-body contributions. As a consequence, the response of the 2DEG cannot be explained by the simple Drude model.

In the last part of this Thesis, we discussed the extreme nonlinear optical response of GaAs nanostructures. Here, we computed the emission intensity after extremely strong optical excitation with peak field strengths exceeding 50 MV/cm. For such strong fields, the rotating-wave approximation fails producing novel extreme nonlinear features. For pure interband dynamics, interesting effects were found like the generation of higher harmonics and the carrier-wave Mollow splitting. Remarkably, the Coulomb interaction has almost no influence on the extreme nonlinear response since the light-matter interaction defines the dominating energy scale in this regime. As soon as the intraband acceleration has been included, the emission spectra broadened drastically indicating a strong enhancement of the high-harmonic generation. We could assign this broadening to the emission via the interband polarization that is rapidly modulated by the intraband acceleration.

Most of the studies discussed in this Thesis do not represent completed projects but are currently still under investigation in order to clarify open questions and to gain a deeper understanding of the physical processes. For instance, the intraband dynamics is not entirely understood for the limit of small frequencies, see comment at the end of Chap. 4. We are currently working on improved scattering models to overcome these problems at $\omega \to 0$. In the long term, it is, of course, desirable to include all relevant scattering processes fully microscopically. Besides reducing the number of free parameters of our theory, this would surely provide novel and valuable insights into the fundamental carrier dynamics during and after THz excitations. As another promising project, we started to extend our 2DEG theory for nonlinear THz excitations. Analyzing a THz-pump-THz-probe scenario, we could already show that the linear THz transmission can be coherently controlled by the pump pulse. Further investigations of these coherent-coupling effects could possibly provide novel techniques to study the intraband dynamics on an ultrafast time scale. Besides that, one could also think of applications as ultrafast switches for the THz response. In connection with the extreme nonlinear optical response discussed in Chap. 5, we also plan to analyze the response of initially unexcited semiconductors to extremely intense THz fields. First preliminary calculations show that for sufficiently strong fields, multiphoton processes lead to carrier excitations across the bandgap. The combined dynamics of these off-resonant interband transitions and the intraband carrier accelerations produces high harmonics of the THz pulse in the visible spectral region and beyond. The THz-field strengths needed to generate such high nonlinearities are in the range of 10 MV/cm and have recently become available experimentally [39].

Bibliography

[1] P. Y. Yu and M. Cardona. *Fundamentals of Semiconductors*. Springer, Berlin, 1999.

[2] S. W. Koch, M. Kira, and T. Meier. Correlation effects in the excitonic optical properties of semiconductors. *J. Opt. B: Quantum and Semiclass. Opt.*, **3**:R29, 2001.

[3] H. Wang, K. Ferrio, D. G. Steel, Y. Z. Hu, R. Binder, and S. W. Koch. Transient nonlinear optical response from excitation induced dephasing in GaAs. *Phys. Rev. Lett.*, **71**:1261–1264, 1993.

[4] K. Leo, M. Wegener, J. Shah, D. S. Chemla, E. O. Göbel, T. C. Damen, S. Schmitt-Rink, and W. Schäfer. Effects of coherent polarization interactions on time-resolved degenerate four-wave mixing. *Phys. Rev. Lett.*, **65**:1340–1343, 1990.

[5] H. Haug and S. W. Koch. *Quantum Theory of the Optical and Electronic Properties of Semiconductors*. World Scientific, Singapore, fifth edition, 2009.

[6] T. Meier, P. Thomas, and S. W. Koch. *Coherent Semiconductor Optics: From Basic Concepts to Nanostructure Applications*. Springer, Berlin, 2007.

[7] S. W. Koch, M. Kira, G. Khitrova, and H. M. Gibbs. Semiconductor excitons in new light. *Nature Mat.*, **5**:523–531, 2006.

[8] I. Galbraith, R. Chari, S. Pellegrini, P. J. Phillips, C. J. Dent, A. F. G. van der Meer, D. G. Clarke, A. K. Kar, G. S. Buller, C. R. Pidgeon, B. N. Murdin, J. Allam, and G. Strasser. Excitonic signatures in the photoluminescence and terahertz absorption of a GaAs/$Al_xGa_{1-x}As$ multiple quantum well. *Phys. Rev. B*, **71**:073302, 2005.

[9] M. Kira, W. Hoyer, T. Stroucken, and S. W. Koch. Exciton formation in semiconductors and the influence of a photonic environment. *Phys. Rev. Lett.*, **87**:176401, 2001.

[10] M. Kira and S. W. Koch. Many-body correlations and excitonic effects in semiconductor spectroscopy. *Prog. Quantum Electron.*, **30**:155–296, 2006.

[11] R. H. M. Groeneveld and D. Grischkowsky. Picosecond time-resolved far-infrared experiments on carriers and excitons in GaAs-AlGaAs multiple quantum wells. *J. Opt. Soc. Am. B*, **11**:2502–2507, 1994.

[12] R. A. Kaindl, M. A. Carnahan, D. Hägele, R. Lövenich, and D. S. Chemla. Ultrafast terahertz probes of transient conducting and insulating phases in an electronhole gas. *Nature*, **423**:734–738, 2003.

[13] R. Huber, R. A. Kaindl, B. A. Schmid, and D. S. Chemla. Broadband terahertz study of excitonic resonances in the high-density regime in $GaAs/Al_xGa_{1-x}As$ quantum wells. *Phys. Rev. B*, **72**:161314, 2005.

[14] S. Leinß, T. Kampfrath, K. v. Volkmann, M. Wolf, J. T. Steiner, M. Kira, S. W. Koch, A. Leitenstorfer, and R. Huber. Terahertz coherent control of optically dark para excitons in. *Phys. Rev. Lett.*, **101**:246401, 2008.

[15] D. Pines and P. Nozières. *The Theory of Quantum Liquids*. Benjamin Reading Mass., 1966.

[16] R. Huber, F. Tauser, A. Brodschelm, M. Bichler, G. Abstreiter, and A. Leitenstorfer. How many-particle interactions develop after ultrafast excitation of an electronhole plasma. *Nature*, **414**:286–289, 2001.

[17] A. Bonvalet, J. Nagle, V. Berger, A. Migus, J.-L. Martin, and M. Joffre. Femtosecond infrared emission resulting from coherent charge oscillations in quantum wells. *Phys. Rev. Lett.*, **76**:4392, 1996.

[18] J. N. Heyman, R. Kersting, and K. Unterrainer. Time-domain measurement of intersubband oscillations in a quantum well. *Appl. Phys. Lett.*, **72**:644–646, 1998.

[19] R. Kersting, R. Bratschitsch, G. Strasser, K. Unterrainer, and J. N. Heyman. Sampling a terahertz dipole transition with subcycle time resolution. *Opt. Lett.*, **25**:272, 2000.

[20] T. Müller, W. Parz, G. Strasser, and K. Unterrainer. Influence of carrier-carrier interaction on time-dependent intersubband absorption in a semiconductor quantum well. *Phys. Rev. B*, **70**:155324, 2004.

[21] C. W. Luo, K. Reimann, M. Woerner, T. Elsaesser, R. Hey, and K. H. Ploog. Phase-resolved nonlinear response of a two-dimensional electron gas under femtosecond intersubband excitation. *Phys. Rev. Lett.*, **92**:047402, 2004.

[22] C. Kittel. *Quantum Theory of Solids*. Wiley, New York, 1963.

[23] J. R. Danielson, Y.-S. Lee, J. P. Prineas, J. T. Steiner, M. Kira, and S. W. Koch. Interaction of strong single-cycle terahertz pulses with semiconductor quantum wells. *Phys. Rev. Lett.*, **99**:237401, 2007.

[24] M. Wegener. *Extreme Nonlinear Optics*. Springer, Berlin, 2005.

[25] L. Allen and J. H. Eberly. *Optical Resonance and Two-Level Atoms*. Wiley, New York, 1975.

[26] S. Hughes. Breakdown of the area theorem: Carrier-wave rabi flopping of femtosecond optical pulses. *Phys. Rev. Lett.*, **81**:3363–3366, 1998.

[27] T. Tritschler, O. D. Mücke, and M. Wegener. Extreme nonlinear optics of two-level systems. *Phys. Rev. A*, **68**:033404, 2003.

[28] R. W. Ziolkowski, J. M. Arnold, and Daniel M. G. Ultrafast pulse interactions with two-level atoms. *Phys. Rev. A*, **52**:3082–3094, 1995.

[29] V. P. Kalosha and J. Herrmann. Formation of optical subcycle pulses and full Maxwell-Bloch solitary waves by coherent propagation effects. *Phys. Rev. Lett.*, **83**:544–547, 1999.

[30] S. Hughes. Subfemtosecond soft-x-ray generation from a two-level atom: Extreme carrier-wave rabi flopping. *Phys. Rev. A*, **62**:055401, 2000.

[31] X. Song, S. Gong, W. Yang, and Z. Xu. Propagation of an attosecond pulse in a dense two-level medium. *Phys. Rev. A*, **70**:013817, 2004.

[32] O. D. Mücke, T. Tritschler, M. Wegener, U. Morgner, and F. X. Kärtner. Role of the carrier-envelope offset phase of few-cycle pulses in nonperturbative resonant nonlinear optics. *Phys. Rev. Lett.*, **89**:127401, 2002.

[33] O. D. Mücke, T. Tritschler, M. Wegener, U. Morgner, and F. X. Kärtner. Signatures of carrier-wave rabi flopping in GaAs. *Phys. Rev. Lett.*, **87**:057401, 2001.

[34] T. Tritschler, O. D. Mücke, M. Wegener, U. Morgner, and F. X. Kärtner. Evidence for third-harmonic generation in disguise of second-harmonic generation in extreme nonlinear optics. *Phys. Rev. Lett.*, **90**:217404, 2003.

[35] Q. T. Vu, H. Haug, O. D. Mücke, T. Tritschler, M. Wegener, G. Khitrova, and H. M. Gibbs. Light-induced gaps in semiconductor band-to-band transitions. *Phys. Rev. Lett.*, **92**:217403, 2004.

[36] Q. T. Vu and H. Haug. Detection of light-induced band gaps by ultrafast femtosecond pump and probe spectroscopy. *Phys. Rev. B*, **71**:035305, 2005.

[37] U. Fano. Effects of configuration interaction on intensities and phase shifts. *Phys. Rev.*, **124**:1866, 1961.

[38] T. Kleine-Ostmann, K. Pierz, G. Hein, P. Dawson, and M. Koch. Room-temperature semiconductor modulators for free-space signal transmission with THz waves. *Proc. SPIE Int. Soc. Opt. Eng.*, **5593**:521–532, 2004.

[39] A. Sell, A. Leitenstorfer, and R. Huber. Phase-locked generation and field-resolved detection of widely tunable terahertz pulses with amplitudes exceeding 100 MV/cm. *Opt. Lett.*, **33**:2767–2769, 2008.

[40] D. Golde. Theoretische Untersuchungen zur extrem nichtlinearen Optik von Halbleiternanostrukturen. Diploma thesis, Philipps-University Marburg, 2006.

[41] C. Cohen-Tannoudji, J. Dupont-Roc, and G. Grynberg. *Photons and Atoms - Introduction to Quantum Electrodynamics*. Wiley, third edition, 1989.

[42] J. T. Steiner. *Microscopic Theory of Linear and Nonlinear Terahertz Spectroscopy of Semiconductors*. PhD thesis, Philipps-University Marburg, 2008.

[43] M.Kira, W. Hoyer, and S. W. Koch. Microscopic theory of the semiconductor terahertz response. *phys. stat. sol. (b)*, **238**:443–450, 2003.

[44] M. Kira, F. Jahnke, W. Hoyer, and S. W. Koch. Quantum theory of spontaneous emission and coherent effects in semiconductor microstructures. *Progress in Quantum Electronics*, **23**:189 – 279, 1999.

[45] J. E. Sipe and A. I. Shkrebtii. Second-order optical response in semiconductors. *Phys. Rev. B*, **61**:5337–5352, 2000.

[46] H. W. Wyld and B. D. Fried. Quantum mechanical kinetic equations. *Annals of Physics*, **23**:374 – 389, 1963.

[47] J. Fricke. Transport equations including many-particle correlations for an arbitrary quantum system: A general formalism. *Annals of Physics*, **252**:479 – 498, 1996.

[48] M. Kira and S. W. Koch. Microscopic theory of optical excitations, photoluminescence, and terahertz response in semiconductors. *Eur. J. Phys. D*, **36**:143–157, 2005.

[49] G. D. Purvis and R. J. Bartlett. A full coupledcluster singles and doubles model: The inclusion of disconnected triples. *J. Chem. Phys.*, **76**:1910, 1982.

[50] W. Hoyer, M. Kira, and S. W. Koch. Influence of coulomb and phonon interaction on the exciton formation dynamics in semiconductor heterostructures. *Phys. Rev. B*, **67**:155113, 2003.

[51] M. Kira, W. Hoyer, and S. W. Koch. Terahertz signatures of the exciton formation dynamics in non-resonantly excited semiconductors. *Sol. Stat. Comm.*, **129**:733–736, 2004.

[52] M. Kira and S. W. Koch. Exciton-population inversion and terahertz gain in semiconductors excited to resonance. *Phys. Rev. Lett.*, **93**:076402, 2004.

[53] M. Kira and S. W. Koch. Quantum-optical spectroscopy of semiconductors. *Phys. Rev. A*, **73**:013813, 2006.

[54] M. Kira and S. W. Koch. Cluster-expansion representation in quantum optics. *Phys. Rev. A*, **78**:022102, 2008.

[55] M. Lindberg and S. W. Koch. Effective bloch equations for semiconductors. *Phys. Rev. B*, **38**:3342–3350, 1988.

[56] J. E. Sipe and E. Ghahramani. Nonlinear optical response of semiconductors in the independent-particle approximation. *Phys. Rev. B*, **48**:11705–11722, 1993.

[57] T. Meier, G. von Plessen, P. Thomas, and S. W. Koch. Coherent electric-field effects in semiconductors. *Phys. Rev. Lett.*, **73**:902–905, 1994.

[58] H. T. Duc, T. Meier, and S. W. Koch. Microscopic analysis of the coherent optical generation and the decay of charge and spin currents in semiconductor heterostructures. *Phys. Rev. Lett.*, **95**:086606, 2005.

[59] H. T. Duc, Q. T. Vu, T. Meier, H. Haug, and S. W. Koch. Temporal decay of coherently optically injected charge and spin currents due to carrier–lo-phonon and carrier-carrier scattering. *Phys. Rev. B*, **74**:165328, 2006.

[60] R. Binder, D. Scott, A. E. Paul, M. Lindberg, K. Henneberger, and S. W. Koch. Carrier-carrier scattering and optical dephasing in highly excited semiconductors. *Phys. Rev. B*, **45**:1107–1115, 1992.

[61] J. B. Krieger and G. J. Iafrate. Time evolution of bloch electrons in a homogeneous electric field. *Phys. Rev. B*, **33**:5494–5500, 1986.

[62] F. Bloch. Über die Quantenmechanik der Elektronen in Kristallgittern. *Z. Phys.*, **52**:555, 1929.

[63] J. Faist, C. Sirtori, F. Capasso, S.-N. G. Chu, L. N. Pfeiffer, and K. W. West. Tunable fano interference in intersubband absorption. *Opt. Lett.*, **21**:985, 1996.

[64] J. Faist, F. Capasso, C. Sirtori, K. W. West, and L. N. Pfeiffer. Controlling the sign of quantum interference by tunneling from quantum wells. *Nature*, **390**:589–591, 1997.

[65] H. Schmidt, K. L. Campman, A. C. Gossard, and A. Imamoğlu. Tunneling induced transparency: Fano interference in intersubband transitions. *Appl. Phys. Lett.*, **70**:3455–3457, 1997.

[66] H. C. Liu, C. Y. Song, Z. R. Wasilewski, J. A. Gupta, and M. Buchanan. Fano resonance mediated by intersubband-phonon coupling. *Appl. Phys. Lett.*, **91**:131121, 2007.

[67] L. Tonks and I. Langmuir. Oscillations in ionized gases. *Phys. Rev.*, **33**:195–210, 1929.

[68] D. Bohm and E. P. Gross. Theory of plasma oscillations. A. Origin of medium-like behavior. *Phys. Rev.*, **75**:1851–1864, 1949.

[69] D. Bohm and D. Pines. A collective description of electron interactions. I. Magnetic interactions. *Phys. Rev.*, **82**:625–634, 1951.

[70] P. Nozières and D. Pines. Electron interaction in solids. General formulation. *Phys. Rev.*, **109**:741–761, 1958.

[71] S. I. Bozhevolnyi, V. S. Volkov, E. Devaux, J.-Y. Laluet, and T. W. Ebbesen. Channel plasmon subwavelength waveguide components including interferometers and ring resonators. *Nature*, **440**:508–511, 2006.

[72] S. A. Maier, P. G. Kik, H. A. Atwater, S. Meltzer, E. Harel, B. E. Koel, and A. A.G. Requicha. Local detection of electromagnetic energy transport below the diffraction limit in metal nanoparticle plasmon waveguides. *Nature Mater.*, **2**:229–232, 2003.

[73] M. Quinten, A. Leitner, J. R. Krenn, and F. R. Aussenegg. Electromagnetic energy transport via linear chains of silver nanoparticles. *Opt. Lett.*, **23**:1331–1333, 1998.

[74] J. B. Pendry. Negative refraction makes a perfect lens. *Phys. Rev. Lett.*, **85**:3966–3969, 2000.

[75] R. A. Shelby, D. R. Smith, and S. Schultz. Experimental Verification of a Negative Index of Refraction. *Science*, **292**:77–79, 2001.

[76] S. Linden, C. Enkrich, M. Wegener, J. Zhou, T. Koschny, and C. M. Soukoulis. Magnetic Response of Metamaterials at 100 Terahertz. *Science*, **306**:1351–1353, 2004.

[77] B. I. Lundqvist. Single-particle spectrum of the degenerate electron gas. *Z. Phys. B: Condens. Matter*, **6**:193–205, 1967.

[78] G. D. Mahan. *Many Particle Physics*. Plenum Press, New York, 1981.

[79] K. El Sayed, S. Schuster, H. Haug, F. Herzel, and K. Henneberger. Subpicosecond plasmon response: Buildup of screening. *Phys. Rev. B*, **49**:7337–7344, 1994.

[80] L. Bányai, Q. T. Vu, B. Mieck, and H. Haug. Ultrafast quantum kinetics of time-dependent RPA-screened coulomb scattering. *Phys. Rev. Lett.*, **81**:882–885, 1998.

[81] Q. T. Vu, H. Haug, W. A. Hügel, S. Chatterjee, and M. Wegener. Signature of electron-plasmon quantum kinetics in GaAs. *Phys. Rev. Lett.*, **85**:3508–3511, 2000.

[82] C. C. Grimes and G. Adams. Observation of two-dimensional plasmons and electron-ripplon scattering in a sheet of electrons on liquid helium. *Phys. Rev. Lett.*, **36**:145–148, 1976.

[83] S. J. Allen, D. C. Tsui, and R. A. Logan. Observation of the two-dimensional plasmon in silicon inversion layers. *Phys. Rev. Lett.*, **38**:980–983, 1977.

[84] T. N. Theis, J. P. Kotthaus, and P. J. Stiles. Wavevector dependence of the two-dimensional plasmon dispersion relationship in the (100) silicon inversion layer. *Solid State Commun.*, **26**:603 – 606, 1978.

[85] D. Olego, A. Pinczuk, A. C. Gossard, and W. Wiegmann. Plasma dispersion in a layered electron gas: A determination in GaAs-(AlGa)As heterostructures. *Phys. Rev. B*, **25**:7867–7870, 1982.

[86] H. A. Kramers. The stopping power of a metal for alpha-particles. *Physica*, **13**:401 – 412, 1947.

[87] J. Lindhard. On the properties of a gas of charged particles. *K. Dan. Vidensk. Selsk. Mat. Fys. Medd.*, **28**:8, 1954.

[88] J. Hubbard. The dielectric theory of electronic interactions in solids. *Proceedings of the Physical Society. Section A*, **68**:976, 1955.

[89] H. Ehrenreich and M. H. Cohen. Self-consistent field approach to the many-electron problem. *Phys. Rev.*, **115**:786–790, 1959.

[90] F. Stern. Polarizability of a two-dimensional electron gas. *Phys. Rev. Lett.*, **18**:546–548, 1967.

[91] T. Brabec and F. Krausz. Intense few-cycle laser fields: Frontiers of nonlinear optics. *Rev. Mod. Phys.*, **72**:545–591, 2000.

[92] B. R. Mollow. Power spectrum of light scattered by two-level systems. *Phys. Rev.*, **188**:1969–1975, 1969.

Paper I:
J. Opt. Soc. Am. B 23, 2559 (2006)

Microscopic analysis of extreme nonlinear optics in semiconductor nanostructures

Daniel Golde, Torsten Meier, and Stephan W. Koch

Department of Physics and Material Sciences Center, Philipps University, Renthof 5, D-35032 Marburg, Germany

Received July 13, 2006; accepted August 15, 2006; posted August 29, 2006 (Doc. ID 72931)

A microscopic analysis is presented for the extreme nonlinear optical response of semiconductor quantum wells and wires after intense excitation with femtosecond laser pulses. In this regime, the light–matter interaction is the dominant energy scale, leading to a number of interesting effects such as carrier-wave Rabi flopping, Mollow splitting, and the creation of higher harmonics. The results presented here were obtained by evaluating the semiconductor Bloch equations without the rotating wave approximation. The electronic dispersion of semiconductor nanostructures is shown to have a characteristic influence on the extreme nonlinear optical response, whereas the relative importance of the carrier Coulomb interaction decreases with increasing excitation intensities.

OCIS codes: 190.7110, 320.7110, 190.5970.

1. INTRODUCTION

For optical interband transitions, the regime where the Rabi energy, i.e., the electric field times the dipole matrix element, becomes comparable to, or even larger than, the transition energies of the investigated system is called extreme nonlinear optics.[1] This regime has become accessible experimentally in the past few years by using intense ultrashort laser pulses containing just a few optical cycles.[2] Compared to the extensive knowledge that exists for ordinary nonlinear optics where the Rabi frequency is much smaller than the transition frequencies, and therefore a perturbative treatment of the light–matter interaction is often useful, see, e.g., Refs. 3 and 4, the available information about the dynamics of optical excitations in the regime of extreme nonlinear optics is rather limited. Obviously, the rotating wave approximation (RWA) that is often applied in nonlinear optics is no longer valid in the extreme nonlinear regime. The nonresonant contributions of the exciting light field are relevant and may lead to so-called carrier-wave Rabi flopping[5,6] of the Bloch vector. This dynamics results in many interesting new effects such as the creation of higher harmonics and carrier-wave Mollow splitting.[1,7] Some of the predicted effects have already been observed in experiments performed on semiconductors.[6,8,9]

In theoretical investigations, the nonlinear optical response of (atomic) two-level systems to intense ultrashort pulses has been analyzed by solving Bloch or Maxwell–Bloch equations.[7,10–14] It has also been studied how an additional level[15] and field-induced ionization[16] modify the results. The extreme nonlinear optical response of semiconductors with a continuous band structure has been modeled by an ensemble of inhomogeneously broadened two-level systems.[8,17] Although it is well known that the many-body Coulomb interaction between the photoexcited electrons and holes strongly influences the linear and nonlinear optical response of semiconductors in the regime where the light–matter interaction is not the dominating energy scale,[18,19] only very few publications exist that have investigated these effects in the regime of extreme nonlinear optics.[9,20]

In this paper we analyze the extreme nonlinear optical response of direct semiconductor quantum wells and wires by numerically solving the semiconductor Bloch equations (SBEs) without employing the RWA. Thus we focus on optical interband transitions alone; the influence of intraband contributions to the response will be discussed in a future paper. The many-body Coulomb interaction is investigated on both the Hartree–Fock level and on the second-Born level. We start in Section 2 by describing our theoretical approach, and then we present and discuss results in Section 3. It is shown that due to the band dispersion, the optical response of semiconductor nanostructures differs characteristically from that of a single two-level system. Furthermore, the role of the Coulomb interaction in the extreme nonlinear regime as well as the dependence of the optical response on the excitation conditions and material properties is investigated. Our most important results are briefly summarized in Section 4.

2. THEORY

The linear and nonlinear optical response of semiconductors and semiconductor nanostructures can be computed on a microscopic level by evaluating the SBE.[18,19,21] This set of coupled equations of motion for the interband coherences and the electronic occupations includes, in particular, the continuous electronic dispersion, the light–matter interaction, and the many-body Coulomb interaction among the photoexcited carriers. For a two-band model the SBEs read[18,19,21]

$$\frac{\partial}{\partial t}p_{\mathbf{k}} = -\frac{i}{\hbar}(\epsilon^{e}_{\mathbf{k}} + \epsilon^{h}_{\mathbf{k}})p_{\mathbf{k}} + i(1 - n^{e}_{\mathbf{k}} - n^{h}_{\mathbf{k}})\omega_{R,\mathbf{k}} + \left.\frac{\partial}{\partial t}p_{\mathbf{k}}\right|_{\text{corr}}, \tag{1}$$

$$\frac{\partial}{\partial t} n_{\mathbf{k}}^{e} = -2\,\mathrm{Im}[\omega_{R,\mathbf{k}} p_{\mathbf{k}}^{*}] + \left.\frac{\partial}{\partial t} n_{\mathbf{k}}^{e}\right|_{\mathrm{corr}}, \tag{2}$$

$$\frac{\partial}{\partial t} n_{\mathbf{k}}^{h} = -2\,\mathrm{Im}[\omega_{R,\mathbf{k}} p_{\mathbf{k}}^{*}] + \left.\frac{\partial}{\partial t} n_{\mathbf{k}}^{h}\right|_{\mathrm{corr}}. \tag{3}$$

Here, $p_{\mathbf{k}} = \langle \hat{a}_{v,\mathbf{k}}^{\dagger} \hat{a}_{c,\mathbf{k}} \rangle$ is the interband coherence or microscopic polarization, $n_{\mathbf{k}}^{e} = \langle \hat{a}_{c,\mathbf{k}}^{\dagger} \hat{a}_{c,\mathbf{k}} \rangle$ is the occupation of electrons in the conduction band c, and $n_{\mathbf{k}}^{h} = 1 - \langle \hat{a}_{v,\mathbf{k}}^{\dagger} \hat{a}_{v,\mathbf{k}} \rangle$ is the occupation of holes in the valence band v. The operators $\hat{a}_{\nu,\mathbf{k}}^{\dagger}(\hat{a}_{\nu,\mathbf{k}})$ that appear in the expectation values create (destroy) an electron with wave vector $\mathbf{k}$ in band $\nu = c, v$.

The terms given explicitely in Eqs. (1)–(3) are the ones that arise in the time-dependent Hartree–Fock approximation.[18,19,21] All many-body terms beyond this level are formally contained in the correlation contributions which are denoted by $|_{\mathrm{corr}}$. The quantities $\omega_{R,\mathbf{k}}$ and $\epsilon_{\mathbf{k}}^{e,h}$ are the Hartree–Fock renormalized Rabi frequency and electronic energies, respectively, and given by[18,19]

$$\omega_{R,\mathbf{k}} = \frac{1}{\hbar}\left(\mathbf{d}_{\mathbf{k}} \cdot \mathbf{E}(t) + \sum_{q \neq \mathbf{k}} V_{\mathbf{k}-\mathbf{q}} p_{\mathbf{q}}\right), \tag{4}$$

$$\epsilon_{\mathbf{k}}^{e,h} = E_{\mathbf{k}}^{e,h} - \sum_{\mathbf{q} \neq \mathbf{k}} V_{\mathbf{k}-\mathbf{q}} n_{\mathbf{q}}^{e,h}. \tag{5}$$

In Eq. (4), $\mathbf{d}_{\mathbf{k}}$ is the dipole matrix element, and $\mathbf{E}(t)$ is the electric field of the exciting laser pulse. The $\mathbf{k}$ dependence of $\mathbf{d}_{\mathbf{k}}$ is in first-order $\mathbf{k} \cdot \mathbf{p}$ theory given by[18]

$$\mathbf{d}_{\mathbf{k}} = \mathbf{d}_0 \frac{E_G}{E_{\mathbf{k}}^{e} + E_{\mathbf{k}}^{h}}, \tag{6}$$

where E_G is the bandgap energy, and $E_{\mathbf{k}}^{e,h}$ are the single-particle band structures of the electrons and holes. Here, the electronic dispersion is treated in effective mass approximation, i.e., $E_{\mathbf{k}}^{e,h} = (E_G/2) + (\hbar^2 k^2 / 2m_{e,h})$. Our calculations show, however, that more realistic band shapes do not alter the results significantly.

In Eqs. (4) and (5), $V_{\mathbf{q}}$ is the Coulomb matrix element in $\mathbf{k}$ space. Since in effective mass approximation the electronic eigenfunctions are plane waves, $V_{\mathbf{q}}$ is the Fourier transform of the Coulomb potential in real space. For ideal 2D quantum wells it is given by[18]

$$V_{\mathbf{q}}^{2D} = \frac{e^2}{2\epsilon_0 \epsilon_r A} \frac{1}{q}, \tag{7}$$

with the quantization area A of the quantum well. The quasi-one-dimensional Coulomb potential is approximated by the regularized potential in real space[18,22]

$$V^{q1D}(z) = \frac{e^2}{4\pi\epsilon_0 \epsilon_r} \frac{1}{|z| + \alpha R}, \tag{8}$$

where $\alpha = 0.3$ is a fitting parameter, and R is the radius of the quantum wire that has been chosen as 6 nm. It has been shown that this 1D potential describes excitons in quantum wires in very good agreement with much more involved 3D calculations that include the finite width of the wires.[22] The Fourier transform of Eq. (8), which is required for the solution of Eqs. (1)–(3), is computed numerically.

The simplest way to treat the correlation terms in Eqs. (1)–(3) is to introduce a phenomenological damping of the polarization

$$\left.\frac{\partial}{\partial t} p_{\mathbf{k}}\right|_{\mathrm{corr}} = -\frac{p_{\mathbf{k}}}{T_2}, \tag{9}$$

where T_2 is the dephasing time. Additionally, the thermalization of the carrier occupations that relax toward quasi-equilibrium Fermi–Dirac distributions in the respective bands can be modeled by a T_1 time. However, this process is not relevant for the calculations presented below, and therefore is not considered in this paper. The solutions of Eqs. (1)–(3) with a phenomenological dephasing described by Eq. (9) are denoted by Hartree–Fock results in Section 3.

For a more realistic description of many-body correlations, we also perform calculations on the second-Born level, which includes the scattering among the carrier occupations and the polarizations, see, e.g., Refs. 18, 19, 21, and 23. In this approach, the correlations describe on a microscopic level the relaxation of the carrier distributions as well as the excitation-dependent dephasing of the polarizations. As we are interested in extreme nonlinear optics and thus deal with very strong exciting fields that induce high occupations, the Coulomb scattering processes are expected to provide the dominant contributions for relaxation and dephasing. Therefore electron–phonon scattering is not considered here.

The macroscopic time-dependent polarization $\mathbf{P}(t)$ is given by

$$\mathbf{P}(t) = \sum_{\mathbf{k}} (\mathbf{d}_{\mathbf{k}} p_{\mathbf{k}} + \mathrm{c.c.}). \tag{10}$$

The time dependence of the interband coherence $p_{\mathbf{k}}$ is computed by solving Eqs. (1)–(3). The dipole matrix elements $\mathbf{d}_{\mathbf{k}}$ are taken to be linearly polarized parallel to the polarization direction of the incident laser field, i.e., the vector character of $\mathbf{P}$ is ignored here.

To investigate the optical response of the system, we compute the intensity of the radiation emitted by the photoexcited system according to $I_{\mathrm{rad}}(\omega) \propto |\omega^2 P(\omega)|^2$, where ω is the spectrometer frequency, and $P(\omega)$ is the Fourier transform of $P(t)$.

The exciting laser field $\mathbf{E}(t)$ is modeled as a Gaussian-shaped pulse

$$\mathbf{E}(t) = \mathbf{E}_0 \exp\left[\frac{-2\ln(2)t^2}{\tau^2}\right] \cos(\omega_0 t), \tag{11}$$

where τ is the pulse duration, i.e., the FWHM of the envelope of the pulse intensity, ω_0 is the central frequency, and $\mathbf{E}_0$ defines the polarization direction and the amplitude of the pulse. In all calculations, we use material parameters corresponding to GaAs, i.e., $E_G = 1.43$ eV, $m_e = 0.069 m_0$, $m_h = 0.5 m_0$, $\epsilon_r = 13.74$, and $d_0 = 3$ eÅ, which is the component of the dipole matrix element that is parallel to the linearly polarized incident laser pulse.

3. NUMERICAL RESULTS AND DISCUSSION

As an introduction to our analysis of the extreme nonlinear optical response of semiconductor systems, we start in Subsection 3.A with a brief summary of results for the much simpler two-level system. As shown in Ref. 7, the response of a two-level system already contains a great variety of interesting effects that arise in the presence of extremely intense laser fields. In Subsection 3.B, we then discuss the optical properties of semiconductor nanostructures in the high excitation regime. We investigate both 1D quantum wires and 2D quantum wells. Besides neglecting the many-body Coulomb interaction, we analyze results that have been computed on both the Hartree–Fock and the second-Born levels. It is shown that some of the signatures present in the response of a two-level system also show up for semiconductor nanostructures. However, mainly the continuous electronic dispersion leads to distinct differences between both systems. In Subsection 3.C, we present an analytical solution of the two-level problem in the RWA for box-shaped pulses and analyze a number of effects that can be understood already on this level.

A. Two-Level Systems

A comprehensive survey of the response of two-level systems in the extreme nonlinear regime is given in Ref. 7. To compare the two-level results with those described below for semiconductor nonostructures, we evaluated the optical response of a resonantly excited ($\hbar\omega_0 = E_{2LS}$) two-level system (see Fig. 1). The duration of the exciting pulse is $\tau = 10$ fs, and the polarization is damped with $T_2 = 50$ fs. The peak Rabi frequency ω_R that is denoted on the y axis is defined as $\hbar\omega_R \equiv d_0 E_0$. For Rabi frequencies smaller than the transition frequency ($\omega_R/\omega_0 < 1$), the well-known Mollow sidebands[24] are visible at spectrometer frequencies $\omega = \omega_0 \pm \omega_R$ in Fig. 1. Besides these Mollow sidebands, additional parallel lines are visible, and a detailed analysis of the response at the fundamental frequency ($\omega = \omega_0$) shows that several minima at different Rabi frequencies occur. The origin of these effects is discussed in Subsection 3.C where it is shown that the minima at $\omega \approx \omega_0$ and small ω_R are related to the Rabi flopping of the Bloch vector and that the additional lines depend on the pulse duration.

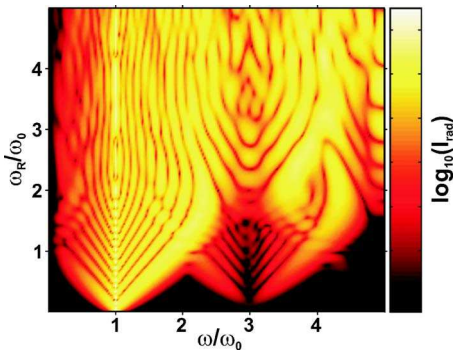

Fig. 1. (Color online) Intensity of the emitted radiation I_{rad} of a two-level system as a function of the spectrometer frequency ω and the peak Rabi frequency ω_R. I_{rad} is plotted on a logarithmic scale that spans 7 orders of magnitude. The system is excited resonantly by a Gaussian laser pulse with a duration of $\tau = 10$ fs. The transition energy of the system is $E_{2LS} = \hbar\omega_0 = 1.43$ eV.

For interband transitions, a characteristic feature of extreme nonlinear optics is the splitting of the higher harmonics that can be seen, at approximately $\omega/\omega_0 = 3$ in Fig. 1 for the case of the third harmonic. It is remarkable that the third harmonic itself is strongly suppressed. The two sidebands at positions $3\omega_0 \pm \omega_R$ are called carrier-wave Mollow sidebands because of their analogy to the fundamental Mollow sidebands. At $\omega_R \approx \omega_0$, the sidebands of the fundamental and the third harmonic meet and create a peak at $\omega \approx 2\omega_0$, i.e., twice the laser frequency. The same happens whenever ω/ω_0 is equal to an even integer; however, for $\omega_R \approx \omega_0$ the intensity of the higher harmonics decreases rapidly. As is discussed in Ref. 8 these peaks should not be confused with even-harmonic generation since the considered system has full spatial inversion symmetry, and therefore even harmonics are forbidden even in the presence of extremely high fields. For larger Rabi frequencies, the emission spectra shown in Fig. 1 become increasingly complex. It is difficult to interpret all the details, in particular, since they sensitively depend on the pulse characteristics, e.g., duration and shape.[7]

B. Semiconductor Nanostructures

The simplest way to model the optical properties of semiconductor nonostructures with continuous electronic dispersion, is to perform a so-called free-carrier calculation. This means that one neglects the Coulomb interaction among the photoexcited carriers, i.e., one sets $V_{\mathbf{k}} = 0$ in the SBE, Eqs. (1)–(3). In this approximation, the semiconductor is modeled as a set of uncoupled two-level systems with transition energies $E_{\mathbf{k}} = E^e_{\mathbf{k}} + E^h_{\mathbf{k}}$ and matrix elements $\mathbf{d}_{\mathbf{k}}$. The contributions of each two-level system are summed up according to Eq. (10) to obtain the overall response of the system. If the $\mathbf{k}$ dependence of the dipole matrix element is weak, the linear absorption spectra obtained from the free-carrier model are proportional to the joint density of the states of the valence to conduction band transitions. Since this approximation does not include many-body effects it does not provide an adequate description of the linear optical spectra of semiconductors that are dominated by excitonic effects.[18,19]

The extreme nonlinear optical response of a 1D semiconductor quantum wire in free-carrier approximation is shown in Fig. 2(a). The laser frequency is resonant with the bandgap and all the parameters are the same as those used for the two-level calculations of Fig. 1. Many of the features that appear in Fig. 1, e.g., the carrier-wave Mollow splitting and the peaks at even harmonics, are also present in Fig. 2(a). Thus besides quantitative changes, the quantum wire response is qualitatively quite similar to the two-level result. The main differences between the results of the two-level system and those of the quantum wire are the strong peaks that appear in Fig. 2(a) at odd harmonics of the laser frequency, in particular at $\omega/\omega_0 = 3$ and 5. To understand this difference between Figs. 1 and 2(a), one has to keep in mind that the free-carrier semiconductor model is nothing but an ensemble of inhomogeneously broadened two-level systems. This suggests that the strong enhancement of the odd harmonics in the semiconductor spectrum could be due to contributions

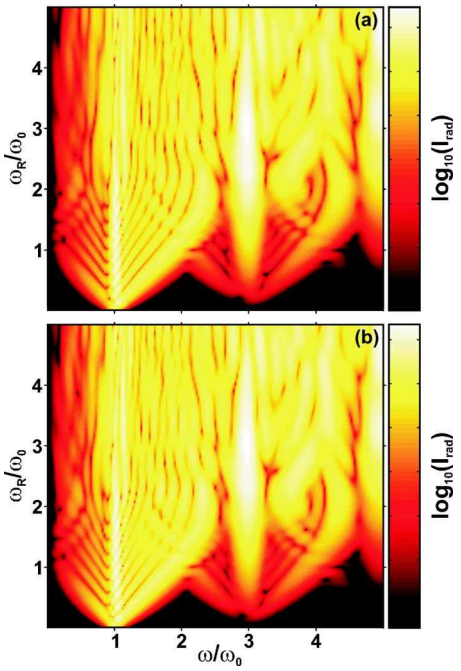

Fig. 2. (Color online) Intensity of the emitted radiation I_{rad} of a 1D semiconductor quantum wire described by a two-band effective mass model with an energy gap of $E_G=\hbar\omega_0=1.43$ eV. (a) Free-carrier result, i.e., the many-body Coulomb interaction is neglected, (b) the Coulomb interaction is treated on the Hartree–Fock level. The excitation parameters are the same as in Fig. 1.

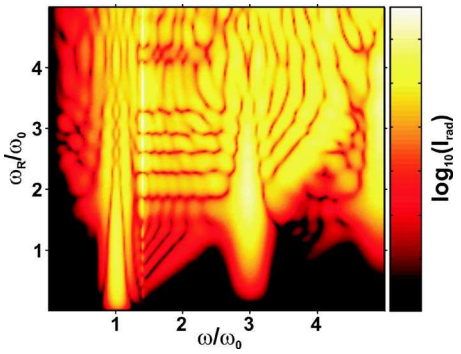

Fig. 3. (Color online) Same as Fig. 1 but for nonresonant excitation of a two-level system with a transition energy of $E_{2\mathrm{LS}}=1.4\hbar\omega_0\approx 2$ eV.

from nonresonantly excited transitions. Figure 3 where the response of the nonresonantly excited two-level system ($E_{2LS}=1.4\hbar\omega_0$) is shown, confirms this expectation. Hence, it is the band dispersion of the semiconductor that leads to the appearance of strong odd harmonics in the emission spectra.

Figure 4 shows the response computed for a 2D quantum well in the free-carrier model. Comparing it with the quantum wire result, Fig. 2(a), we find that the 1D and the 2D spectra are qualitatively very similar. The strongest differences between Figs. 4 and 2(a) appear for $\omega<\omega_0$ and $\omega_R\leq 2\omega_0$ where the relative 2D response is reduced in comparison to the 1D result. In the free-carrier model, the only difference between the 1D and 2D calculations is the modified joint density of states. Whereas in one dimension the density of states has a maximum at the bandedge and then continuously decreases with increasing energy, the density of states is constant in two dimensions.[18] Therefore the 1D response is in the vicinity of $\omega=\omega_0$ very similar to the two-level results, whereas in two dimensions the relatively enhanced contributions of energetically higher transitions somewhat reduce the response for $\omega<\omega_0$ and not too high ω_R.

Now we analyze the influence of the Coulomb interaction among the photoexcited carriers on the extreme nonlinear optical response of semiconductor nanostructures. Figure 2(b) shows the result of a Hartree–Fock calculation. In fact, there are hardly any differences between Figs. 2(a) and 2(b), which means that the Coulomb interaction on the Hartree–Fock level does not significantly influence the system response in this regime. In Fig. 5, we compare the emission spectra obtained within the free-particle model with those computed on the Hartree–Fock level for two Rabi frequencies. The comparison shows (i) that the overall structure of the spectra is due to the light–matter interaction and (ii) that the Hartree–Fock contributions do not vanish but lead to only small changes. This result may seem surprising since it is well

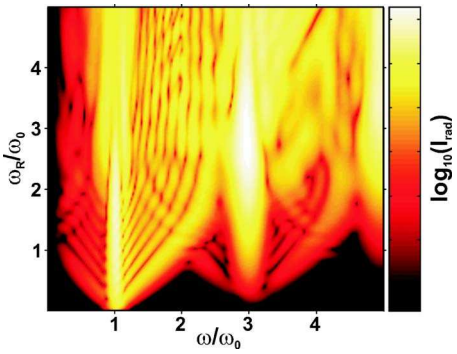

Fig. 4. (Color online) Same as Fig. 2(a) computed for a 2D semiconductor quantum well.

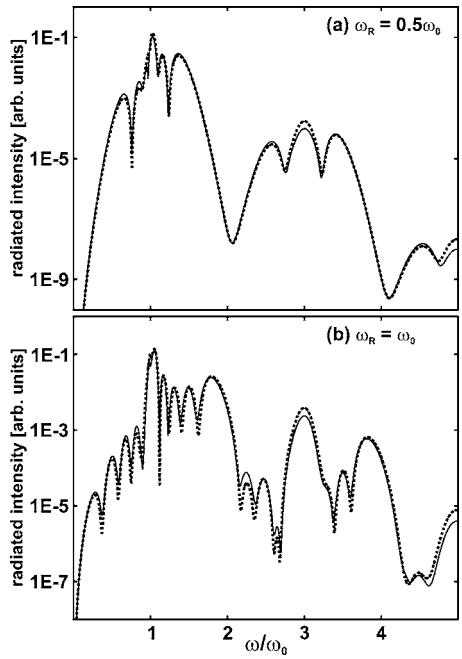

Fig. 5. Cross sections through Fig. 2(a) (dotted curves, free-carrier calculation) and Fig. 2(b) (solid curves, Hartree–Fock calculation) for two different Rabi frequencies.

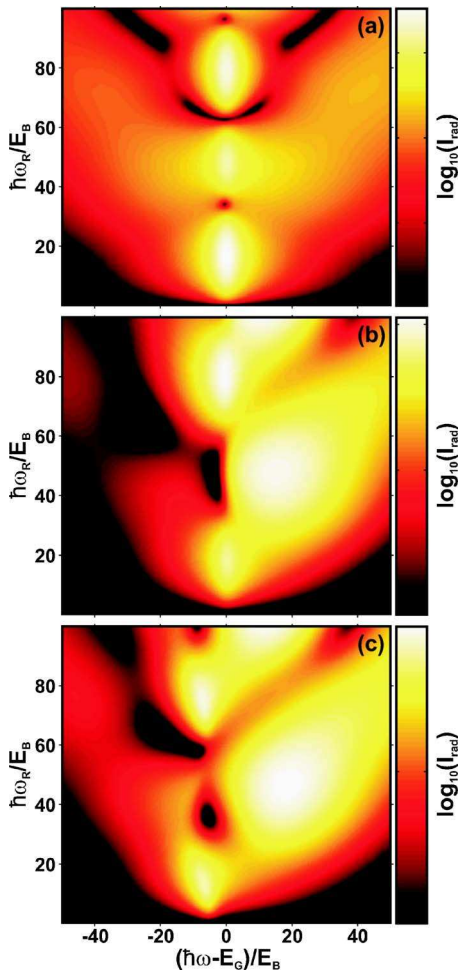

Fig. 6. (Color online) Intensity of the emitted radiation I_{rad} for smaller Rabi frequencies at approximately $\omega/\omega_0=1$ for (a) two-level system, (b) free-carrier, and (c) Hartree–Fock calculation. The excitation conditions are the same as in Figs. 1 and 2. Note that the axes are scaled in units of the 3D exciton binding energy $E_B \approx 4.37$ meV, which is approximately 327 times smaller than the transition energy of the two-level system, and the bandgap $\hbar\omega_0=E_G=1.43$ eV.

known that excitonic and further many-body effects dominate the optical response for weak and moderate excitation intensities.[18,19] However, when the Rabi frequency is comparable to the bandgap frequency the energy scale describing the light–matter coupling is much larger than the typical Coulomb energy, i.e., the exciton binding energy that is only a small fraction of the bandgap. Therefore this regime is dominated by the light–matter interaction, and the Hartree–Fock terms result in only weak modifications of the response.

Figure 6 compares the emission spectra of a two-level system [Fig. 6(a)] with those obtained for a free-carrier [Fig. 6(b)], and Hartree–Fock calculations [Fig. 6(c)]. In Fig. 6 we concentrate on the spectra in the vicinity of $\omega=\omega_0=E_G/\hbar$ for rather small Rabi frequencies. In this region, the two-level response is symmetric with respect to $\omega=\omega_0$, whereas the semiconductor models are not symmetric and have a large response at $\omega>E_G/\hbar$. Thus Figs. 6(b) and 6(c) differ significantly from Fig. 6(a). Furthermore, one can clearly identify strong differences between Figs. 6(b) and 6(c). Thus in the region of not too strong Rabi frequencies the Hartree–Fock terms are relevant and cannot be neglected. By comparing Figs. 6(b) and 6(c), we notice that the importance of the Coulomb interaction decreases with increasing excitation intensity.

Furthermore, we have investigated the influence of Coulomb many-body correlations on the extreme nonlinear optical response by treating the correlation terms of Eqs. (1)–(3) on the second-Born level. On this level, the correlations describe on a microscopic level the relaxation of the carrier distributions as well as the excitation-dependent dephasing of the polarizations attributable to Coulomb scattering. A comparison between the Hartree–Fock and the second-Born results for two different excitation intensities is shown in Fig. 7. One clearly sees that unlike the case of moderate excitation intensities[18,19] the correlation terms do not alter the spectra in the extreme nonlinear regime. Therefore we conclude that in 1D and 2D semiconductor nanostructures the Coulomb interaction can be regarded as a small correction of the dominating free-particle dynamics in the regime of extreme nonlinear optics.

It is well known that Coulomb scattering leads to a damping of the microscopic polarization $p_{\mathbf{k}}$ which depends on the excitation conditions. However, for our Hartree–Fock and free-carrier calculations we have used a constant dephasing time T_2. Figure 7 shows that our results are not altered by a microscopic treatment of the dephasing. This leads to the question of whether the extreme nonlinear optical response depends on the dephasing time at all. The spectra computed from Hartree–Fock calculations performed for two different dephasing times are shown in Fig. 8(a). These results demonstrate that, in fact, the emission spectra, and, in particular, the linewidths do not depend on the damping of the polarization as long as T_2 is significantly longer than τ. Figure 8(b) shows the computed emission spectra for two different

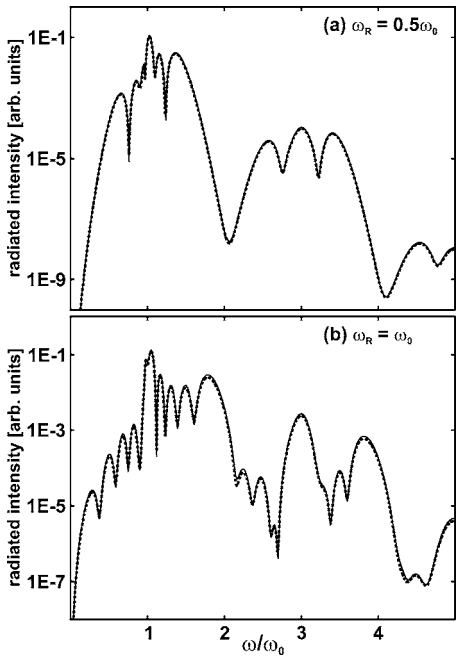

Fig. 7. Same as Fig. 5 but the calculations are performed on the Hartree–Fock level (dotted curve) and on the second-Born level (solid curve).

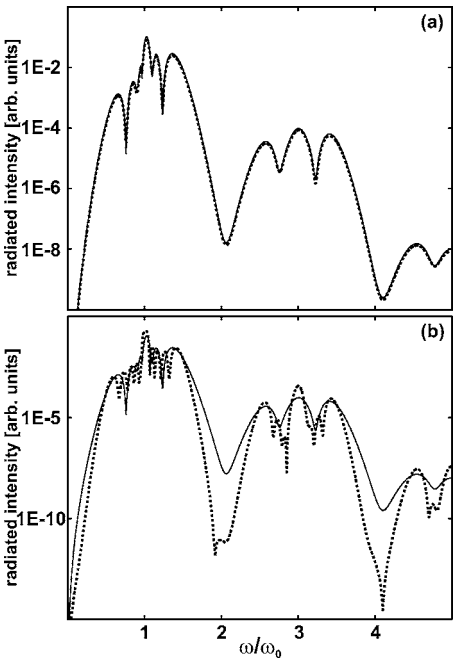

Fig. 8. Spectra of the emitted radiation I_{rad} computed on the Hartree–Fock level for $\omega_R=0.5\omega_0$. (a) Results for the dephasing times of $T_2=50$ fs (solid curve) and $T_2=30$ fs (dotted curve) are shown. The pulse duration is fixed at $\tau=10$ fs here. (b) Spectra for different pulse durations, i.e., $\tau=20$ fs (dotted curve), and $\tau=10$ fs (solid curve).

durations of the exciting pulse. Obviously, the linewidths of the emission spectra reflect the spectral width of the incident laser pulse. The results of Fig. 8 demonstrate that the structure of the emission spectra is determined by the ultrafast dynamics that take place during the excitation. The decay of the polarization after the excitation has basically no influence on the spectra (at least as long as the dephasing time is significantly longer than the pulse duration).

C. Simplified Analytical Results for a Two-Level System

To understand some features of the emission spectra in more detail, we have performed a simplified analytical solution for a two-level system within the RWA by using box-shaped pulses. These results help us to understand the spectra near the fundamental resonance for small Rabi frequencies. As shown in Fig. 6(a), minima for certain Rabi frequencies are present near the fundamental resonance. The most obvious explanation for the origin of these minima would be Rabi flopping of the Bloch vector, i.e., the minima arise at those Rabi frequencies where the system is either completely inverted or in the ground state after the excitation is over. For both cases, the polarization is zero after the pulse. This means that the pulse area has to fulfill the condition $d\int\tilde{E}(t)\mathrm{d}t/\hbar=\int\omega_R(t)\mathrm{d}t=n\pi$ with integer n, where $\tilde{E}(t)$ is the envelope of the exciting field. A detailed analysis shows, however, that the minima in Fig. 6(a) appear at slightly different Rabi frequencies than predicted by the Rabi oscillation model. Assuming a box-shaped pulse and applying the RWA, which is valid for small Rabi frequencies, Eqs. (1)–(3) can be solved analytically for a resonantly excited two-level system. One obtains for the time-dependent polarization:

$$P(t,\omega_R)=\begin{cases}\dfrac{i}{2}\sin(\omega_R t)e^{-i\omega_0 t}e^{-(t/T_2)}, & t\le\tau\\ \dfrac{i}{2}\sin(\omega_R\tau)e^{-i\omega_0 t}e^{-(t/T_2)}, & t\ge\tau\end{cases}. \tag{12}$$

A Fourier transformation of Eq. (12) with respect to t yields

$$\begin{aligned}P(\Delta\omega,\omega_R)=&\frac{i}{2}\frac{1}{(i\Delta\omega-T_2^{-1})^2+\omega_R^2}\{e^{(i\Delta\omega-T_2^{-1})\tau}\\&\times[(i\Delta\omega-T_2^{-1})\sin(\omega_R\tau)-\omega_R\cos(\omega_R\tau)]+\omega_R\}\\&-\frac{i}{2}\frac{\sin(\omega_R\tau)}{i\Delta\omega-T_2^{-1}}e^{(i\Delta\omega-T_2^{-1})\tau},\end{aligned} \tag{13}$$

with $\Delta\omega\equiv\omega-\omega_0$. To obtain an explanation for the positions of the minima in Fig. 6(a) at $\omega=\omega_0$, we analyze Eq. (13) at $\Delta\omega=0$:

$$\begin{aligned}P(0,\omega_R)=&\frac{i}{2}\frac{\omega_R T_2^2}{(\omega_R T_2)^2+1}\{1-e^{-\tau/T_2}[\cos(\omega_R\tau)\\&-\omega_R T_2\sin(\omega_R\tau)]\}.\end{aligned} \tag{14}$$

In the limit of slow dephasing, i.e., $T_2\to\infty$, the roots of Eq. (14) appear at $\omega_R\tau=n\pi$, which is exactly the condition for the Rabi flopping mentioned above. However, according to Eq. (14) the $(2n-1)$th roots shift to larger, and the $2n$th roots shift to smaller, Rabi frequencies with decreasing dephasing time. Thus, Rabi flopping is the origin of the minima in Fig. 6(a) whose exact position is modified by dephasing. However, as long the dephasing rate T_2^{-1} is much smaller than the Rabi frequency ω_R (for $T_2=50$ fs

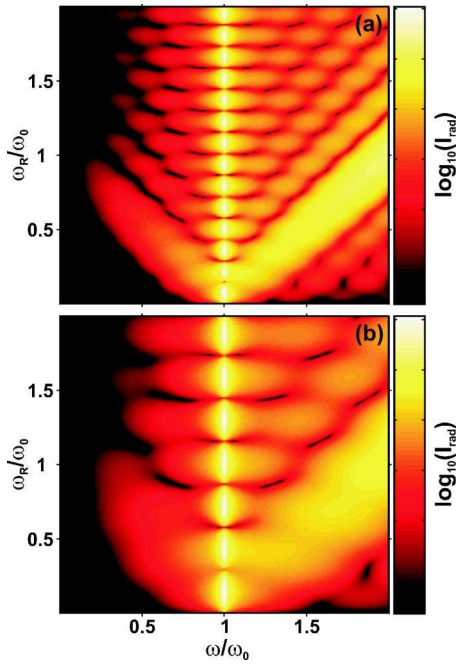

Fig. 9. (Color online) Intensity of the emitted radiation I_{rad} of a resonantly excited two-level system obtained from the analytical solution of Eq. (13) for a box-shaped pulse and in RWA. The dephasing time is $T_2=50$ fs, and the pulse duration is (a) $\tau=10$ fs and (b) $\tau=5$ fs.

this condition is already fulfilled for $\hbar\omega_R > 10E_B$) these modifications are very small.

To get further information from the analytical solution, the response of a resonantly excited two-level system as described by Eq. (13) is plotted in Fig. 9 for extreme nonlinear excitation conditions, although the RWA is valid only for small Rabi frequencies, i.e., $\hbar\omega_R \ll E_G$. Figure 9 shows that the additional sidebands mentioned in Subsection 3.A when discussing Fig. 1 appear also in RWA calculations. A comparison between Figs. 9(a) and 9(b) shows that the number and position of the additional sidebands scale with the pulse duration in the same way as the minima at the fundamental resonance. This suggests that these sidebands are also connected to the Rabi flopping of the Bloch vector.

4. CONCLUSIONS

We have analyzed the extreme nonlinear optical response of direct bandgap semiconductor quantum wells and wires by numerically solving the semiconductor Bloch equations beyond the rotating wave approximation. Our results demonstrate that mostly because of electronic dispersion the optical response of semiconductor nonostructures differs characteristically from that of a single two-level system. When the excitation pulse is tuned to the bandgap, optical transitions with higher resonance frequencies are also excited and contribute significantly to the response. It is shown that compared to a two-level system the enhanced generation of odd harmonics in semiconductor nonostructures can be understood to be the result of off-resonantly driven transitions.

The many-body Coulomb interaction is investigated on both the Hartree–Fock and the second-Born level. The Coulombic terms are known to dominate the optical response at weak and moderate excitation intensities. However, when the Rabi frequency becomes comparable to the bandgap frequency this energy scale is much larger than the typical Coulomb energy, i.e., the exciton binding energy that is only a small fraction of the bandgap. Therefore the optical response in this regime is dominated by the light–matter interaction, and the Coulomb interaction only weakly modifies the response.

It is possible to describe certain features of the emission spectra by simplified analytical solutions. Signatures related to Rabi flopping and dephasing have been analyzed. In future studies we plan to incorporate further bands into our approach. Additionally, the influence of the field-induced acceleration of the photoexcited carriers within a band will be investigated.

ACKNOWLEDGMENTS

This work was supported by the Deutsche Forschungsgemeinschaft (DFG), by the Center for Optodynamics of the Philipps University, Marburg by Air Force Office of Scientific Research through the Multidisciplinary Research Initiative Program F49620-02-1-0380, and by the John von Neumann Institut für Computing (NIC) of the Forschungszentrum Jülich, Germany. T. Meier thanks the DFG for support under a Heisenberg fellowship (ME 1916/1).

The corresponding author's e-mail address is torsten.meier@physik.uni-marburg.de.

REFERENCES

1. M. Wegener, *Extreme Nonlinear Optics* (Springer, 2005).
2. T. Brabec and F. Krausz, "Intense few-cycle laser fields: frontiers of nonlinear optics," Rev. Mod. Phys. **72**, 545–591 (2000).
3. N. Bloembergen, *Nonlinear Optics* (Benjamin, 1965).
4. L. Allen and J. H. Eberly, *Optical Resonance and Two-Level Atoms* (Wiley, 1975).
5. S. Hughes, "Breakdown of the area theorem: carrier-wave Rabi flopping of femtosecond optical pulses," Phys. Rev. Lett. **81**, 3363–3366 (1998).
6. O. D. Mücke, T. Tritschler, M. Wegener, U. Morgner, and F. X. Kärtner, "Signatures of carrier-wave Rabi flopping in GaAs," Phys. Rev. Lett. **87**, 057401 (2001).
7. T. Tritschler, O. D. Mücke, and M. Wegener, "Extreme nonlinear optics of two-level systems," Phys. Rev. A **68**, 033404 (2003).
8. T. Tritschler, O. D. Mücke, M. Wegener, U. Morgner, and F. X. Kärtner, "Evidence of third-harmonic generation in disguise of second-harmonic generation in extreme nonlinear optics," Phys. Rev. Lett. **90**, 217404 (2003).
9. Q. T. Vu, H. Haug, O. D. Mücke, T. Tritschler, M. Wegener, G. Khitrova, and H. M. Gibbs, "Light-induced gaps in semiconductor band-to-band transitions," Phys. Rev. Lett. **92**, 217403 (2004).
10. R. W. Ziolkowski, J. M. Arnold, and D. M. Gogny, "Ultrafast pulse interactions with two-level atoms," Phys. Rev. A **52**, 3082–3094 (1995).
11. V. P. Kalosha and J. Herrmann, "Formation of optical subcycle pulses and full Maxwell–Bloch solitary waves by coherent propagation effects," Phys. Rev. Lett. **83**, 544–547 (1999).
12. S. Hughes, "Subfemtosecond soft-x-ray generation from a two-level atom: extreme carrier-wave Rabi flopping," Phys. Rev. A **62**, 055401 (2000).
13. X. Song, S. Gong, W. Yang, and Z. Hu, "Propagation of an attosecond pulse in a dense two-level medium," Phys. Rev. A **70**, 013817 (2004).
14. R. Parzyński and M. Sobczak, "Analytical calculation of atomic response to a few-cycle optical pulse," J. Phys. B **37**, 743–751 (2004).
15. J. Cheng and J. Zhou, "Validity of the two-level approximation in the interaction of few-cycle light pulses with atoms," Phys. Rev. A **67**, 041404 (2003).
16. X. Song, S. Gong, R. Li, and Z. Hu, "Effect of time-dependent ionization on the propagation of a few-cycle laser pulse in a two-level medium," Phys. Rev. A **72**, 043820 (2005).
17. O. D. Mücke, T. Tritschler, M. Wegener, U. Morgner, and F. X. Kärtner, "Role of the carrier-envelope offset phase of few-cycle pulses in nonperturbative resonant nonlinear optics," Phys. Rev. Lett. **89**, 127401 (2002).
18. H. Haug and S. W. Koch, *Quantum Theory of the Optical and Electronic Properties of Semiconductors*, 4th ed. (World Scientific, 2004).
19. W. Schäfer and M. Wegener, *Semiconductor Optics and Transport Phenomena* (Springer, 2002).
20. Q. T. Vu and H. Haug, "Detection of light-induced band gaps by ultrafast femtosecond pump and probe spectroscopy," Phys. Rev. B **71**, 035305 (2005).
21. M. Lindberg and S. W. Koch, "Effective Bloch equations for semiconductors," Phys. Rev. B **38**, 3342–3350 (1988).
22. L. Bányai, I. Galbraith, C. Ell, and H. Haug, "Excitons and biexcitons in semiconductor quantum wires," Phys. Rev. B **36**, 6099–6104 (1987).
23. W. Schäfer, "Influence of electron–electron scattering on femtosecond four-wave mixing in semiconductors," J. Opt. Soc. Am. B **13**, 1291–1297 (1996).
24. B. R. Mollow, "Power spectrum of light scattered by two-level systems," Phys. Rev. **188**, 1969–1975 (1969).

Paper II:
Ultrafast Phenomena XV, Springer Series in Chemical Physics 88, 689 (2007)

Modeling of the Extreme Nonlinear Optical Response of Semiconductor Nanostructures

D. Golde, T. Meier, and S. W. Koch
Department of Physics and Materials Sciences Center, Philipps University, Renthof 5, D-35032 Marburg, Germany
phone: ++49 6421 2824221, fax: ++49 6421 2827076
torsten.meier@physik.uni-marburg.de

Abstract: In extreme nonlinear optics the Rabi and transition frequencies are on the same order of magnitude. In this highly nonperturbative regime, the band dispersion characteristically modifies the response of semiconductor quantum wells and wires.

OCIS codes: (190.5970) Semiconductor nonlinear optics including MQW; (190.7110) Ultrafast nonlinear optics

1. Introduction

Compared to the vast amount of information about nonlinear optical processes that is available in the perturbative regime and for cases in which the Rabi energy, i.e., the light-matter coupling, is not the dominating energy scale, presently, only little knowledge in the regime of extreme nonlinear optics exists [1]. This regime is, however, accessible experimentally using intense ultrashort laser pulses that excite optical transitions in, e.g., semiconductors [2,3]. Furthermore, in extreme nonlinear optics one expects a multitude of interesting effects, as has been shown in [4] where a two-level system has been considered. Therefore, systematic theoretical investigations can provide an important step forward in gaining a better understanding of the ultrafast nonlinear optical response in this high-intensity regime.

In the following, we present results of a number of model calculations. In Sec. 2, we start by showing computed intensity-dependent emission spectra of a simple two-level system. Next, we extend the analysis and consider a three-level system, where the upper level is supposed to describe the onset of the vacuum states above which photoemission is possible. The results of the model calculations in Sec. 2 are presented in order to highlight the variety of fundamental and for characterizing the full scenario of effects arising in extreme nonlinear optics. In Sec. 3, we consider optical excitations in semiconductor nanostructures which are described by the semiconductor Bloch equations [5]. These equations include besides the band dispersions also many-body Coulomb effects, e.g., excitonic resonances. It is shown that in quantum wells and quantum wires, in particular, the band dispersion characteristically modifies the extreme nonlinear optical response [6].

2. Two- and three-level systems

When exciting a two-level system with an intense square wave, one can clearly identify the generation of odd higher harmonics and Mollow sidebands. These sidebands can couple to the emission at the fundamental transition frequency and the odd harmonics and may lead to an interesting emission near the even harmonics [1,4]. When using pulses with smooth envelopes, the computed intensity-dependent emission spectra include additional structure, see Fig. 1, which depend sensitively on the pulse duration and to a certain extend also on the chosen shape of the envelope.

For Rabi energies on the order of or even above the fundamental transition frequency, it becomes questionable whether the two-level approximation can be used to properly describe the optical response of atomic systems and nanostructures. For example, in intense laser pulses photoemission is possible which can only be described if additional levels or bands are incorporated into the analysis. The simplest extension in this direction is considered in Fig. 2. Here, we use a three-level system with an upper level which describes the onset of the vacuum states. By comparing Figs. 1 and 2, we find that on the one hand the additional level leads to some signatures in the emission at the new transition frequency which corresponds to about $1.5\omega_0$ in Fig. 2. On the other hand, it also significantly modifies the generation of the higher harmonics, in particular, at elevated excitation intensities.

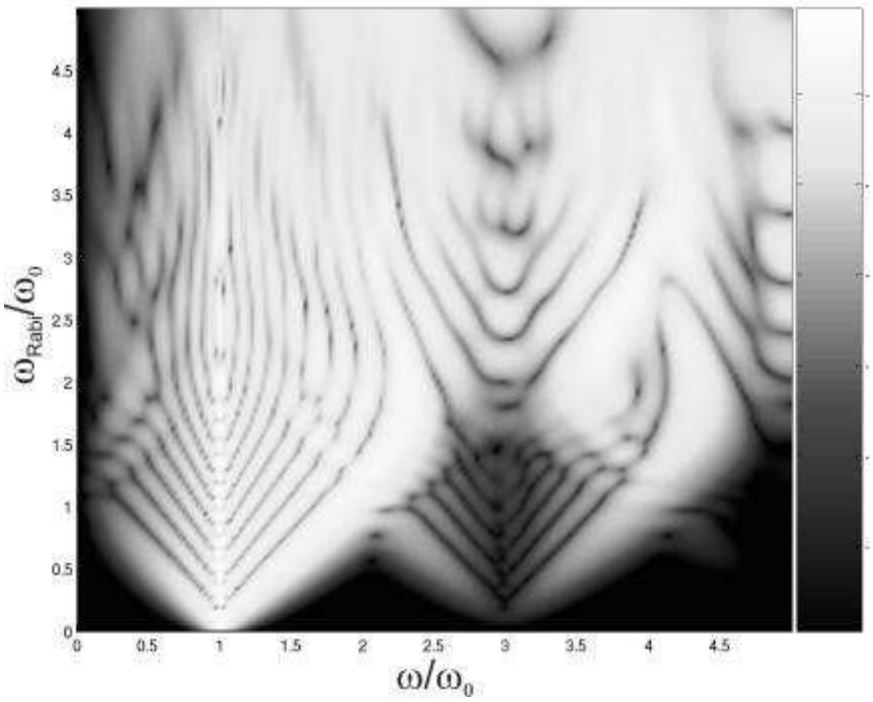

Fig. 1. Contour plot of the emitted intensity of a two-level system with transition frequency ω_0 driven resonantly by a 10fs intense Gaussian laser pulse. The x-axis denotes the emitted frequency ω_0 and the y-axis the Rabi frequency ω_{Rabi} which are both given in units of ω_0.

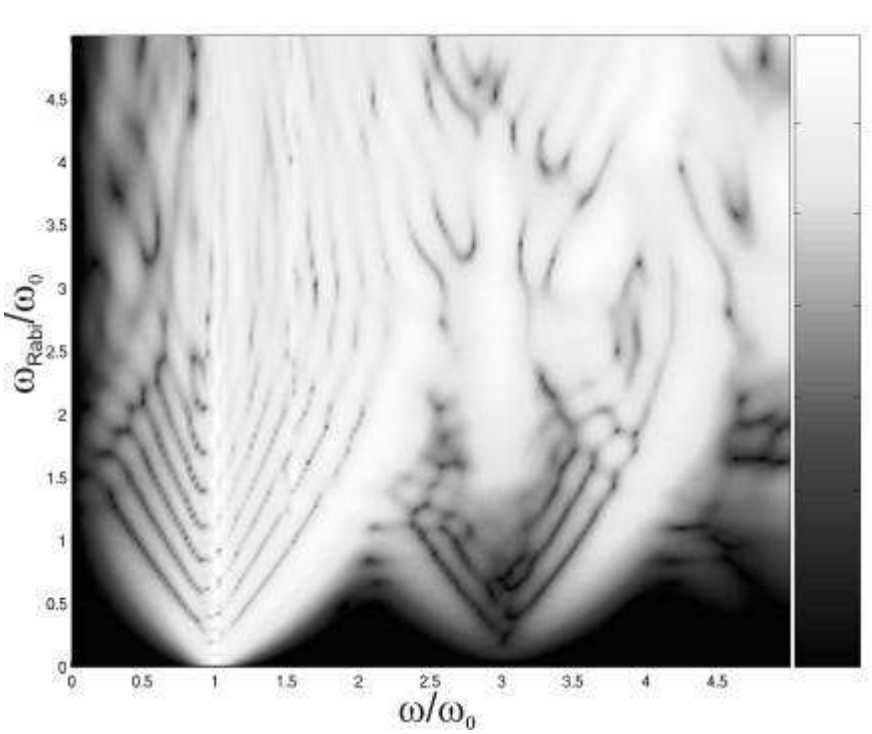

Fig. 2. Same as Fig. 1, considering a three-level system with an upper level situated about $1.5\omega_0$ above the intermediate level. The two transition dipoles are chosen to be equal.

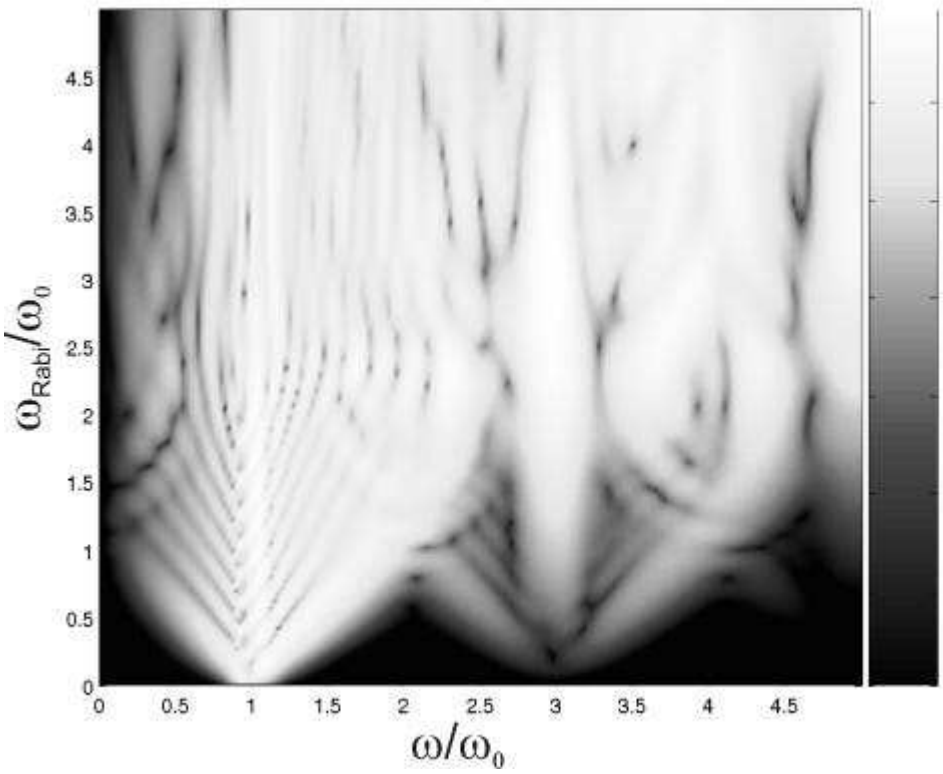

Fig. 3. Same as Fig. 1, for a semiconductor nanostructure which is excited by an intense 10fs Gaussian laser pulse resonantly at the fundamental band edge (ω_0). Compared to Fig. 1 characteristic changes are observable which are basically a consequence of the band dispersion. Qualitatively similar results are obtained for both quantum wells and quantum wires.

3. Semiconductor nanostructures

When comparing Fig. 3 to Fig. 1 one notices characteristic differences between the response of a two-level system and that of a semiconductor nanostructure. In Fig. 3, in particular, the third harmonic but also the fifth harmonic are stronger than in Fig. 1 and start to become significant at lower Rabi frequencies. Additional calculations (not shown in figure) allow us to identify that these signatures arise basically from the band dispersion. Due to this dispersion, the optical transitions in the semiconductor nanostructures are intrinsically inhomogeneously broadened. Thus besides the resonant excitation near the band edge always also off-resonant excitation contribute to a certain extend to the optical response. It has been verified that such off-resonant excitations are responsible for most of the differences between Fig. 1 and Fig. 3.

It is well known that in semiconductor nanostructures Coulomb many-body effects dominate the nonlinear optical response close to the fundamental band edge if the Rabi energy is much smaller than the band gap [5]. It, however, turns out that these effects are of less importance in the regime where the light-matter interaction is the dominating energy scale. Presently, work is in progress concerning the inclusion of energetically higher bands and the field-induced electronic acceleration.

4. References

[1] M. Wegener, "Extreme Nonlinear Optics," (Springer, New York, 2005).
[2] T. Tritschler, O. D. Mücke, M. Wegener, U. Morgner, and F. X. Kärtner, „Evidence for Third-Harmonic Generation in Disguise of Second-Harmonic Generation in Extreme Nonlinear Optics", Phys. Rev. Lett. **90**, 217404 (2003).
[3] Q. T. Vu, H. Haug, O. D. Mücke, T. Tritschler, M. Wegener, G. Khitrova, and H. M. Gibbs,.,,Light-Induced Gaps in Semiconductor Band-to-Band Transitions," Phys. Rev. Lett. **92**, 217403 (2004).
[4] T. Tritschler, O. D. Mücke, and M. Wegener, "Extreme nonlinear optics of two-level systems," Phys. Rev. A **68**, 033404 (2003).
[5] H. Haug and S. W. Koch, "Quantum Theory of the Optical and Electronic Properties of Semiconductors," 4th ed. (World Scientific, Singapore, 2004).
[6] D. Golde, T. Meier, and S. W. Koch, to be published.

Paper III:
Phys. Rev. B 77, 075330 (2008)

High harmonics generated in semiconductor nanostructures by the coupled dynamics of optical inter- and intraband excitations

D. Golde,[1] T. Meier,[2] and S. W. Koch[1]
[1]*Department of Physics and Material Sciences Center, Philipps University, Renthof 5, D-35032 Marburg, Germany*
[2]*Department Physik, Fakultät für Naturwissenschaften, Universität Paderborn, Warburger Strasse 100, D-33098 Paderborn, Germany*
(Received 10 October 2007; revised manuscript received 21 December 2007; published 27 February 2008)

The emitted radiation from semiconductor nanostructures due to the excitation with intense ultrashort optical laser pulses is analyzed. Semiconductor Bloch equations that consistently describe the coupled light-field-induced interband and intraband dynamics are solved numerically. It is demonstrated that the intraband dynamics considerably influences the light emission in the regime of extreme nonlinear optics. In particular, the intraband acceleration significantly modifies the dynamics of the interband polarization which results in a strong enhancement of high-harmonic generation.

DOI: 10.1103/PhysRevB.77.075330 PACS number(s): 42.65.Ky, 42.50.Hz, 78.47.−p

I. INTRODUCTION

The study of light-matter interactions with intense ultrafast laser pulses is a rapidly advancing research field yielding novel informations on fundamental light-matter interaction processes with significant application potential. Employing high-harmonic generation (HHG)[1,2] it became possible to initiate, observe, and control transient processes in atomic and molecular systems on attosecond time scales, see, e.g., Refs. 3–5. The fascinating regime of extreme nonlinear optics in which the Rabi frequency is comparable to or larger than the transition frequency can also be reached in semiconductors, see, e.g., Refs. 6. Interesting effects that have been predicted and observed in semiconductors include carrier-wave Rabi flopping,[7–9] HHG,[10–14] and the Mollow triplet.[15]

Theoretically the nonlinear optical response of two-level systems to intense ultrashort pulses has been studied by solving Bloch or Maxwell-Bloch equations.[7,10,11,14,16–18] In Refs. 12 and 19 the extreme nonlinear optical response of semiconductors with a continuous band structure has been modeled by an ensemble of inhomogeneously broadened two-level systems. The influence of the many-body Coulomb interaction among the photoexcited electrons and holes, which strongly influences the linear and nonlinear optical response of semiconductors in the regime where the light-matter interaction is not the dominating energy scale,[20,21] has been analyzed in a few investigations.[13,15,22] In Ref. 13 it has been shown that in two-dimensional semiconductor quantum wells and in one-dimensional semiconductor quantum wires the Coulomb interaction affects the light emission only weakly in the regime where the light-matter interaction dominates the energy scale. However, characteristic differences between the emission of a two-level system and extended semiconductors with a continuous dispersion have been demonstrated.[13]

Previous studies of the light emission of semiconductor nanostructures after excitation with intense femtosecond laser pulses have focused on light-field-induced interband transitions that give rise to carrier-wave Rabi flopping and HHG. Here, we extend the theoretical approach by additionally considering intraband excitations, i.e., the light-field-induced carrier acceleration. Such terms are well known to be relevant for descriptions of phototransport effects, e.g., optically detected Bloch oscillations[23] and dynamic localization[24] and the coherent generation of photocurrents by two-color excitation.[25–27] Here, a theory that consistently includes both interband and intraband excitations[23,24,26–28] is used to analyze the light emission of semiconductor nanostructures in the extreme nonlinear optical regime. Numerical solutions of the extended semiconductor Bloch equations (SBE) demonstrate that surprisingly the intraband acceleration strongly enhances the HHG compared to the case when only interband excitations are considered.

Our theoretical approach, i.e., SBE that describe the dynamics of the polarizations and the occupations due to interband and intraband excitation, is introduced in Sec. II. Numerical results on the emission in the regime of extreme nonlinear optics are presented and discussed in Sec. III. The intraband excitations lead to an additional radiation source via the light-field-induced current and also significantly modify the dynamics of the optical polarization. Altogether, the emission spectra are strongly enhanced towards high frequencies by the intraband acceleration. Furthermore, the influence of the band width and the effective mass on the emission is analyzed. Our most important results are summarized in Sec. IV.

II. THEORETICAL APPROACH

The coupled interband and intraband dynamics of semiconductor nanostructures is described by the SBE within a two-band model.[23,24,28] Since Ref. 13 showed no strong influence of the dimensionality on the light emission in the extreme nonlinear optical regime, we consider here a one-dimensional quantum wire and linearly polarized light fields, which allows us to ignore the vector character of the wave vector, the electric field, etc. Furthermore, we omit here the Coulomb interaction among the photoexcited carriers which influences the emission in the regime of extreme nonlinear optics only very weakly.[13] To understand this issue, one has to keep in mind that in semiconductors the Coulomb energy is typically of the order of the exciton binding energy. Thus, in extreme nonlinear optics, the energy scale describing the

light-matter interaction dominates the system response and the Coulomb interaction can in this case be regarded as a small perturbation. The equations of motion of the interband coherence (polarization) p_k and the occupation $n_k^{e(h)}$ of electrons (holes) read

$$i\hbar\frac{\partial}{\partial t}p_k = \left(\varepsilon_k^e + \varepsilon_k^h - i\frac{\hbar}{T_2}\right)p_k - (1 - n_k^e - n_k^h)d_k E(t) + ieE(t)\cdot\nabla_k p_k, \tag{1}$$

$$\hbar\frac{\partial}{\partial t}n_k^{e(h)} = -2\,\mathrm{Im}[d_k E(t)p_k^*] + eE(t)\cdot\nabla_k n_k^{e(h)}. \tag{2}$$

Here, $\varepsilon_k^{e(h)}$ are the single particle energies of the electrons (holes), T_2 is the dephasing time of the polarization, d_k is the (k-dependent) dipole matrix element, and $E(t)$ denotes the the electric field of the exciting laser pulse. While the terms proportional to $d_k E(t)$ in Eqs. (1) and (2) represent optical interband transitions, the intraband excitations are described by the terms proportional to $E(t)\cdot\nabla_k$. These terms lead to a time-dependent wave vector k which changes according to the acceleration theorem at a rate that is proportional to $E(t)$[29–31]

$$\frac{d}{dt}k(t) = -\frac{e}{\hbar}E(t). \tag{3}$$

In conventional optics, the rapidly oscillating changes of the wave vector that are induced by the optical fields are very small compared to typical wave vectors in a semiconductor. Therefore, the intraband dynamics usually does not modify the optical response significantly and consequently the intraband effects can often be neglected. In extreme nonlinear optics, however, the exciting fields are strong enough to cause very large transient shifts of the wave vector which can exceed the width of the Brillouin zone.[6] The results presented below demonstrate that in this regime the intraband effects cannot be neglected but play a major role for the optically-induced dynamics of the system and its emission.

Due to the motion of the carriers within the bands, a macroscopic current J arises which contributes to the light emission of the nanostructure in addition to the macroscopic polarization P. In the time domain these quantities are given by

$$P(t) = \sum_k [d_k p_k(t) + \text{c.c.}] \tag{4}$$

and

$$J(t) = \sum_{\lambda,k} e v_k^\lambda n_k^\lambda(t), \tag{5}$$

where d_k is the interband dipole matrix element, v_k^λ is the group velocity, i.e., proportional to the derivative of the dispersion with respect to k, and $\lambda = e, h$ is a band index. The time-dependent occupations $n_k^\lambda(t)$ and polarizations $p_k(t)$ which determine P and J are obtained by numerical solutions of the SBE, Eqs. (1) and (2).

The spectrum of the emitted radiation is given by

$$I_{\text{rad}}(\omega) \propto |\omega^2 P(\omega) + i\omega J(\omega)|^2. \tag{6}$$

Below, we distinguish between the total emission given by Eq. (6), the emission due to the interband polarization $I_{\text{rad}}^{\text{pol}} = |\omega^2 P(\omega)|^2$ and that due to the intraband current $I_{\text{rad}}^{\text{curr}} = |\omega J(\omega)|^2$. Eq. (6) shows that I_{rad} is not just given by the sum of the interband and intraband emission intensities, but also depends on the interference of $P(\omega)$ and $J(\omega)$. In addition to the numerical results that are presented and discussed in the following section, simplified analytical solutions of the SBE and of the polarization and current dynamics are provided in the Appendix.

III. NUMERICAL RESULTS

In order to keep the numerics as simple as possible, we consider a one-dimensional GaAs quantum wire in two-band approximation. However, as shown by our earlier comparisons,[13] the results presented should be qualitatively similar to those of quantum wells. The electron and heavy-hole dispersions are modeled as tight-binding bands that are proportional to $-\frac{\Delta_\lambda}{2}\cos(ka)$, where a is the lattice constant and Δ_λ is the width of band λ. If the curvature of the dispersion is chosen to coincide with that of a parabolic effective mass model, one has to use a band width that is inversely proportional to the effective mass m_λ[15,22,28]

$$\Delta_\lambda = \frac{2\hbar^2}{m_\lambda a^2}. \tag{7}$$

Using Γ-point effective masses of $m_e = 0.069 m_0$ and $m_{hh} = 0.5 m_0$ for the electron and heavy-hole bands, respectively, and the GaAs lattice constant of $a = 5.65$ Å results in band widths of $\Delta_e = 6.9$ eV for the conduction and $\Delta_h = 0.96$ eV for the valence band. In all calculations we consider an exciting laser pulse with Gaussian shape, a duration of $\tau = 10$ fs, and a central frequency that is resonant with the band gap, i.e., $E_G = \hbar\omega_0 = 1.43$ eV. The decay of the polarization is modeled by a dephasing time of $T_2 = 50$ fs.

Figure 1(a) shows the excitation dependent spectra if as in previous studies intraband excitations, i.e., the terms proportional to ∇_k in Eqs. (1) and (2) are neglected. In this case, the current J and thus $I_{\text{rad}}^{\text{curr}}(\omega)$ vanish and the total emission is due to the optical polarization, i.e., $I_{\text{rad}}(\omega) = I_{\text{rad}}^{\text{pol}}(\omega)$ and one obtains significant emission for frequencies $\omega \leqslant \alpha\omega_R$ with $\alpha \approx 2$. Incorporating the intraband acceleration into the theory strongly increases the width of the emission spectra, see Fig. 1(d), and the region of significant emission corresponds to $\alpha \approx 10$. Surprisingly, Figs. 1(b) and 1(c) show that the interband polarization $I_{\text{rad}}^{\text{pol}}$ and not the current $I_{\text{rad}}^{\text{curr}}$ is mainly responsible for the strong broadening of the emission spectra. It is thus the modification of the dynamics of the optical polarization $P(t)$ via the intraband acceleration that largely increases the HHG compared to calculations that consider only interband excitations. In the Appendix, this effect is analyzed qualitatively on the basis of simplified analytic investigations.

To analyze the different terms more precisely, the emission spectra for $\omega_R = 3\omega_0$ of the contour plot Fig. 1 are shown

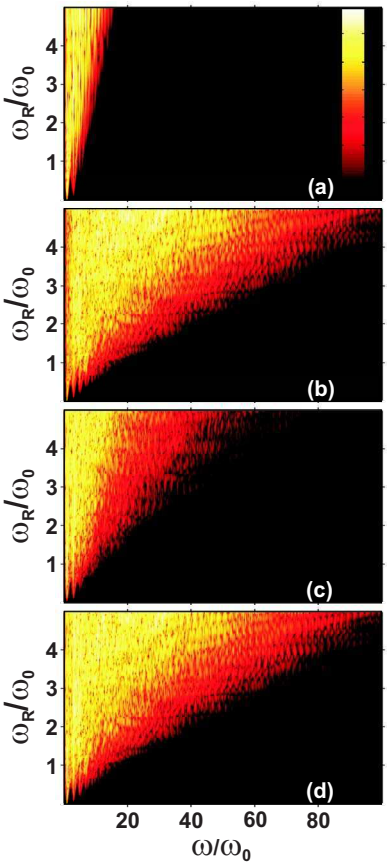

FIG. 1. (Color online) Excitation dependent emission of a GaAs quantum wire with a tight-binding band structure. ω is the spectrometer frequency, ω_R the peak Rabi frequency, and ω_0 the excitation frequency. The logarithmic color encoding covers seven orders of magnitude, see (a). In (a), the emission for pure interband dynamics is shown, i.e., $I_{\mathrm{rad}}(\omega)=I_{\mathrm{rad}}^{\mathrm{pol}}(\omega)$. (b), (c), and (d) show the spectra for coupled interband and intraband dynamics due to the polarization $I_{\mathrm{rad}}^{\mathrm{pol}}(\omega)$, the current $I_{\mathrm{rad}}^{\mathrm{curr}}(\omega)$, and the total emission $I_{\mathrm{rad}}(\omega)$, respectively.

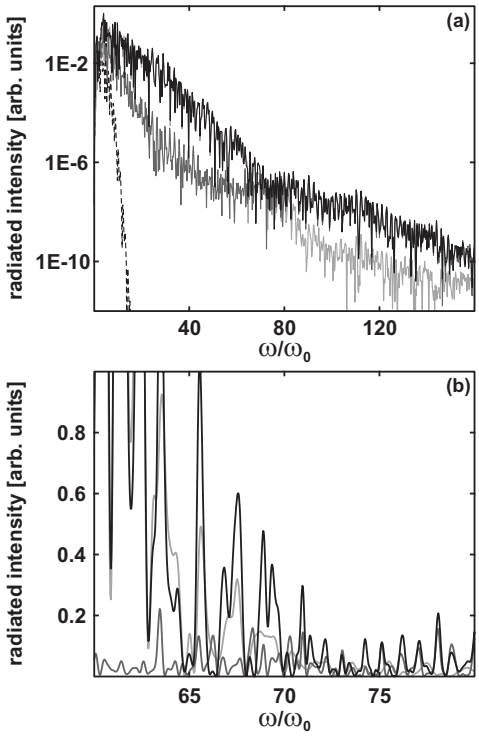

FIG. 2. Cross section through Fig. 1 at $\omega_R=3\omega_0$ for pure interband dynamics (dashed curve) and the coupled interband and intraband dynamics showing $I_{\mathrm{rad}}^{\mathrm{pol}}(\omega)$ (light gray curve), $I_{\mathrm{rad}}^{\mathrm{curr}}(\omega)$ (dark gray curve), and $I_{\mathrm{rad}}(\omega)$ (solid black curve). (a) The emission spectra on a logarithmic scale for a wide ω range, whereas in (b) the emission in the transition region, where $I_{\mathrm{rad}}^{\mathrm{pol}}(\omega)$ and $I_{\mathrm{rad}}^{\mathrm{curr}}(\omega)$ are comparable, is shown on a linear scale.

as lines in Fig. 2(a). For pure interband dynamics the emission intensity falls off rapidly with increasing frequency. When the coupled interband and intraband dynamics is considered, significant emission appears over a broader range and the decrease for large frequencies becomes much slower. The total emission intensity I_{rad} is basically given by the current-induced emission $I_{\mathrm{rad}}^{\mathrm{curr}}$ for $\omega \leqslant 60\omega_0$, whereas the polarization-induced emission $I_{\mathrm{rad}}^{\mathrm{pol}}$ dominates for $\omega \geqslant 80\omega_0$. Figure 2(b) shows I_{rad}, $I_{\mathrm{rad}}^{\mathrm{curr}}$, and $I_{\mathrm{rad}}^{\mathrm{pol}}$ in the transition region where the polarization- and the current-induced emission intensities are of comparable strength and interference effects are significant.

Clearly, the width of the conduction band $\Delta_e=6.9$ eV is unrealistic since such a wide conduction band would extend into the vacuum region where only unbound states exist. If one, however, reduces the bandwidth within the tight-binding model one, according to Eq. (7), simultaneously increases the effective mass. The total emission for a conduction band of width $\Delta_e=2.5$ eV which corresponds to a concomitant increase of the electron effective mass to $m_e=0.19m_0$ is shown in Fig. 3(a). Comparing to Fig. 1(d) demonstrates that the region of strong emission is smaller when the bandwidth is decreased.

To be able to vary bandwidth and effective mass separately, we use a model that includes nearest and second nearest neighbor interactions. In this case, the dispersion is pro-

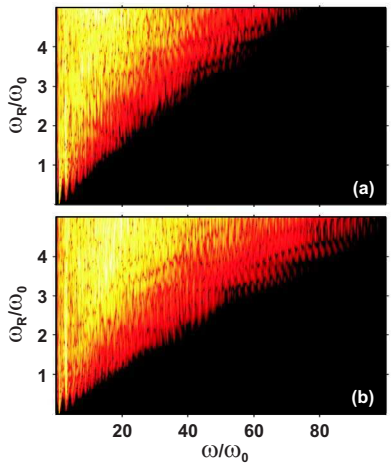

FIG. 3. (Color online) Total emission spectra $I_{\mathrm{rad}}(\omega)$ for coupled interband and intraband dynamics. In (a) a tight-binding model with a bandwidth of $\Delta_e=2.5$ eV and an effective mass of $m_e=0.19m_0$ is used. (b) is for a dispersion that includes also second-nearest neighbor interactions with $\Delta_e=2.5$ eV and $m_e=0.069m_0$.

portional to $A\cos(ka)+B\cos(2ka)$ and the two parameters A and B can be chosen to obtain the desired bandwidth and effective mass. In Fig. 3(b) we have evaluated such a model which has the same band width as in Fig. 3(a) of $\Delta_e = 2.5$ eV and the GaAs effective masses of $m_e = 0.069 m_0$. Comparing Figs. 3(a) and 3(b) demonstrates that for constant bandwidth the emission depends significantly on the effective mass or one could say on the details of the dispersion. In fact, the range of emission seen in Fig. 3(b) is not very different from that of Fig. 1(d), i.e., the width of the emission spectra depends much more strongly on the effective mass than on the band width. Alternatively, one can conclude that the maximum steepness of the band dispersion and not the bandwidth determines the broadness of the emission. This is understandable since for a steeper dispersion the intraband acceleration leads to a more rapid variation of the electron and hole energies $\varepsilon_k^{e/h}$ through the time-dependent wave vector. In order to obtain an improved physical understanding of this phenomenon, analytical solutions of Eqs. (1) and (2) for realistic excitation conditions are required which are presently not available.

IV. SUMMARY

The radiation emitted from a semiconductor quantum wire after extreme nonlinear optical excitation has been computed. Whereas most previous studies concentrate on interband excitations, we present and evaluate a theory that consistently describes the coupled light-field-induced interband and intraband dynamics. It is demonstrated that in the regime of extreme nonlinear optics the intraband acceleration significantly influences the light-field-induced dynamics and the emission. In particular, the intraband acceleration modifies the dynamics of the interband polarization. This results in a strongly enhanced generation of high harmonics as compared to the case when only interband excitations are considered.

ACKNOWLEDGMENTS

This work is supported by the Deutsche Forschungsgemeinschaft (DFG) and by the John von Neumann Institut für Computing (NIC), Forschungszentrum Jülich, Germany.

APPENDIX: SIMPLIFIED QUALITATIVE ANALYSIS

Already in the regime of ordinary nonlinear optics, i.e., for a Rabi frequency that is much smaller than the band gap, analytical solutions of the SBE, Eqs. (1) and (2), are only available for certain pulse shapes, e.g., ultrashort δ pulses or pulses with a constant envelope, for the cases of resonant or near-resonant excitation, which allows one to use the rotating-wave approximation to simplify the calculations.[20,21,28] When analyzing the generation of higher-harmonics in the regime of extreme nonlinear optics such simplifications are not possible[6,11,13] and consequently no analytical solutions for realistic pulse shapes are available.

In order to support our numerical findings, we therefore present in the following a number of simplified analytical results. We start with a two-level system whose polarization is given by

$$P(t) = d[p(t) + \text{c.c.}], \tag{A1}$$

which corresponds to Eq. (4) without the k summation. For excitation with an ultrashort pulse of the form

$$E(t) = \hat{E}(t)(e^{i\omega_0 t} + e^{-i\omega_0 t}), \tag{A2}$$

where $\hat{E}(t)$ is the envelope, we write the the time-dependent polarization as

$$P(t) = H(t)\Phi(t) = H(t)e^{i\varphi(t)}. \tag{A3}$$

Its Fourier transform is thus given by the convolution

$$P(\omega) = \int d\omega' H(\omega')\Phi(\omega - \omega'). \tag{A4}$$

During the excitation, $H(t)$ and $\Phi(t)$ are oscillating rapidly and due to coherent nonlinear dynamics of the two-level system, in particular, carrier-envelope Rabi flopping, this dynamics leads to the generation of higher harmonics $n\omega_0$ which are visible in the emission spectrum $I_{\text{rad}}^{\text{pol}}(\omega) = |\omega^2 P(\omega)|^2$.[6,11]

For the analysis of a two-band semiconductor, we incorporate the band dispersion into the equations given above and write

$$P(t) = \sum_k P_k(t) = \sum_k H_k(t)e^{i\varphi_k(t)} \tag{A5}$$

and

$$P(\omega) = \sum_k P_k(\omega) = \sum_k \int d\omega' H_k(\omega')\Phi_k(\omega - \omega'). \tag{A6}$$

Due to interferences among the complex $P_k(\omega)$'s which include resonantly and off-resonantly excited transitions, this inhomogeneous broadening modifies $I_{\text{rad}}^{\text{pol}}(\omega)$ compared to a two-level system.[13]

As discussed in Sec. II, the intraband acceleration that is described via the terms proportional to $ieE(t)\cdot\nabla_k$ in Eqs. (1) and (2), leads to a time-dependence of the wave vector $k(t)$ which varies with a rate that is proportional to the field amplitude $E(t)$. This means that the transition frequency $\omega_k^{eh} = (\varepsilon_k^e + \varepsilon_k^h)/\hbar$ becomes a function that through $k(t)$ acquires a rapid time dependence. For tight-binding dispersions we have

$$\omega_k^{eh}(t) = \omega_{\text{gap}} + \frac{\Delta_e + \Delta_h}{2\hbar}\{1 - \cos[k(t)a]\}. \tag{A7}$$

The time dependence of the wave vector is given by $k(t) = k_0 - \frac{e}{\hbar}\int_{-\infty}^{t} dt' E(t')$, i.e., for a constant field envelope $\hat{E}$, it oscillates as $\sin(\omega_0 t)$. Thus, in this case the explicit time evolution of the transition frequencies follows from

$$\omega_{k_0}^{eh}(t) = (\omega_{\text{gap}} + \omega_\Delta) - \omega_\Delta \cos\left(k_0 a + \frac{\omega_B}{\omega_0}\sin(\omega_0 t)\right)$$
$$= (\omega_{\text{gap}} + \omega_\Delta) - \omega_\Delta \cos(k_0 a)\cos\left(\frac{\omega_B}{\omega_0}\sin(\omega_0 t)\right)$$
$$- \omega_\Delta \sin(k_0 a)\sin\left(\frac{\omega_B}{\omega_0}\sin(\omega_0 t)\right) \tag{A8}$$

with $\omega_\Delta = \frac{\Delta_e + \Delta_h}{2\hbar}$ and the Bloch frequency $\omega_B = \frac{ea\hat{E}}{\hbar}$. In order to gain more insight into the actual temporal behavior of the transition frequencies, we rewrite the nontrivial contributions of Eq. (A8) as:

$$\cos\left(\frac{\omega_B}{\omega_0}\sin(\omega_0 t)\right) = \mathcal{J}_0\left(\frac{\omega_B}{\omega_0}\right) + 2\sum_{N=0}^{\infty}\mathcal{J}_{2N}\left(\frac{\omega_B}{\omega_0}\right)\cos(2N\omega_0 t) \tag{A9}$$

and

$$\sin\left(\frac{\omega_B}{\omega_0}\sin(\omega_0 t)\right) = 2\sum_{N=0}^{\infty}\mathcal{J}_{2N+1}\left(\frac{\omega_B}{\omega_0}\right)\cos[(2N+1)\omega_0 t], \tag{A10}$$

where $\mathcal{J}_N$ is the Nth order Bessel function of first kind. Obviously, the transition frequencies oscillate with multiple integers of the exciting field frequency ω_0. The intraband dynamics leads therefore, in particular, to an additional rapid oscillatory behavior of the phase $\varphi_k(t)$ that causes a broadening of $\Phi_k(\omega)$ and thus a broadening of $P(\omega)$ as compared to considering only interband excitations. This reasoning qualitatively explains the difference between Figs. 1(a) and 1(b), i.e., that the intraband excitations modify the interband dynamics and emission.

So far, we have dealt with the emission due to the polarization only. However, similar arguments explain the generation of higher harmonics in the emission due to the current $I_{\text{rad}}^{\text{curr}}(\omega)$. Surely, the current would vanish without intraband contributions since pure interband excitations create carrier occupations n_k^λ that are symmetric in k while the group velocity v_k^λ in Eq. (5) is an odd function of k.

The intraband motion leads to unsymmetric distribution functions and thus, to a finite current. For tight-binding bands, the group velocity is given by $v_k^\lambda = \frac{ea\Delta_\lambda}{2\hbar}\sin(ka)$. Inserting this into Eq. (5) and taking into account the time dependence of the wave vector for constant field envelopes yields

$$J(t) = -ea\omega_\Delta \sin\left(\frac{\omega_B}{\omega_0}\sin(\omega_0 t)\right)\sum_{k_0} n_{k_0}(t)\cos(k_0 a). \tag{A11}$$

Again, this expression can be expanded in terms of Bessel functions which unravels the high-harmonic oscillations

$$J(t) = -ea\omega_\Delta 2\sum_{N=0}^{\infty}\mathcal{J}_{2N+1}\left(\frac{\omega_B}{\omega_0}\right)\sin[(2N+1)\omega_0 t]$$
$$\times\sum_{k_0} n_{k_0}(t)\cos(k_0 a). \tag{A12}$$

The interband dynamics leads to a time dependence of $n_{k_0}(t)$ via carrier-wave Rabi flopping and thus, modifies the current in addition to the intraband contributions. Hence, the actual dynamics of the current, similarly to the polarization dynamics, results from a nontrivial coupling of interband and intraband excitations each producing high Fourier components that leads to the broad emission spectrum of Fig. 1(c).

The simplified analysis presented in this appendix qualitatively explains the high harmonic generation due to coupled interband and intraband dynamics. However, if one wants to obtain quantitative analytical results, e.g., unravel the relative importance of both contributions, see, e.g., Figs. 1 and 2, it is required to solve Eqs. (1) and (2) analytically for realistic pulse shapes and excitation conditions. Unfortunately, such solutions are not available.

[1] P. B. Corkum, Phys. Rev. Lett. **71**, 1994 (1993).
[2] M. Lewenstein, P. Balcou, M. Y. Ivanov, A. L'Huillier, and P. B. Corkum, Phys. Rev. A **49**, 2117 (1994).
[3] T. Brabec and F. Krausz, Rev. Mod. Phys. **72**, 545 (2000).
[4] *Few-Cycle Laser Pulse Generation and Its Applications*, edited by F. X. Kärtner, Vol. 95 of *Topics in Applied Physics* (Springer, Berlin, 2004).
[5] P. B. Corkum and F. Krausz, Nat. Phys. **3**, 381 (2007).
[6] M. Wegener, *Extreme Nonlinear Optics* (Springer, Berlin, 2005).
[7] S. Hughes, Phys. Rev. Lett. **81**, 3363 (1998).
[8] O. D. Mücke, T. Tritschler, M. Wegener, U. Morgner, and F. X. Kärtner, Phys. Rev. Lett. **87**, 057401 (2001).
[9] O. D. Mücke, T. Tritschler, and M. Wegener, in *Few-Cycle Laser Pulse Generation and Its Applications*, (Ref. 4), pp. 379–410.
[10] S. Hughes, Phys. Rev. A **62**, 055401 (2000).
[11] T. Tritschler, O. D. Mücke, and M. Wegener, Phys. Rev. A **68**, 033404 (2003).
[12] T. Tritschler, O. D. Mücke, M. Wegener, U. Morgner, and F. X. Kärtner, Phys. Rev. Lett. **90**, 217404 (2003).
[13] D. Golde, T. Meier, and S. W. Koch, J. Opt. Soc. Am. B **23**, 2559 (2006).
[14] C. Van Vlack and S. Hughes, Opt. Lett. **32**, 187 (2006).
[15] Q. T. Vu, H. Haug, O. D. Mücke, T. Tritschler, M. Wegener, G. Khitrova, and H. M. Gibbs, Phys. Rev. Lett. **92**, 217403 (2004).
[16] R. W. Ziolkowski, J. M. Arnold, and D. M. Gogny, Phys. Rev. A **52**, 3082 (1995).
[17] V. P. Kalosha and J. Herrmann, Phys. Rev. Lett. **83**, 544 (1999).
[18] X. Song, S. Gong, W. Yang, and Z. Xu, Phys. Rev. A **70**, 013817 (2004).
[19] O. D. Mücke, T. Tritschler, M. Wegener, U. Morgner, and F. X. Kärtner, Phys. Rev. Lett. **89**, 127401 (2002).
[20] H. Haug and S. W. Koch, *Quantum Theory of the Optical and Electronic Properties of Semiconductors*, 4th ed. (World Scientific, Singapore, 2004).

[21] W. Schäfer and M. Wegener, *Semiconductor Optics and Transport Phenomena* (Springer, Berlin, 2002).
[22] Q. T. Vu and H. Haug, Phys. Rev. B **71**, 035305 (2005).
[23] T. Meier, G. von Plessen, P. Thomas, and S. W. Koch, Phys. Rev. Lett. **73**, 902 (1994).
[24] T. Meier, F. Rossi, P. Thomas, and S. W. Koch, Phys. Rev. Lett. **75**, 2558 (1995).
[25] R. Atanasov, A. Haché, J. L. P. Hughes, H. M. van Driel, and J. E. Sipe, Phys. Rev. Lett. **76**, 1703 (1996).
[26] H. T. Duc, T. Meier, and S. W. Koch, Phys. Rev. Lett. **95**, 086606 (2005).
[27] H. T. Duc, Q. T. Vu, T. Meier, H. Haug, and S. W. Koch, Phys. Rev. B **74**, 165328 (2006).
[28] T. Meier, P. Thomas, and S. W. Koch, *Coherent Semiconductor Optics: From Basic Concepts to Nanostructure Applications* (Springer, Berlin, 2007).
[29] C. Kittel, *Quantum Theory of Solids* (Wiley, New York, 1963).
[30] A. Nenciu and G. Nenciu, Phys. Lett. **78A**, 101 (1980).
[31] J. B. Krieger and G. J. Iafrate, Phys. Rev. B **33**, 5494 (1986).

Paper IV:
phys. stat. sol. (c) 6, 420 (2009)

Phys. Status Solidi C **6**, No. 2, 420–423 (2009) / **DOI** 10.1002/pssc.200880309

physica status solidi c
www.pss-c.com
current topics in solid state physics

Microscopic analysis of high-harmonic generation in semiconductor nanostructures

Daniel Golde[1,*], Torsten Meier[2], and Stephan W. Koch[1]

[1] Department of Physics and Material Sciences Center, Philipps University, Renthof 5, 35032 Marburg, Germany
[2] Department Physik, Fakultät für Physik und Naturwissenschaften, Universität Paderborn, Warburger Straße 100, 33098 Paderborn, Germany

Received 23 May 2008, accepted 20 June 2008
Published online 21 October 2008

PACS 42.50.Hz, 42.65.Ky, 78.47.-p, 78.67.Lt

* Corresponding author: e-mail daniel.golde@physik.uni-marburg.de, Phone: +49-6421-2824117, Fax: +49-6421-2827076

A microscopic analysis of the emitted radiation of a semiconductor nanostructure after excitation with an extremely intense ultrashort laser pulse is presented. It is shown that the extreme nonlinear optical response is not sufficiently described by pure interband transitions but one has to include intraband effects as well. Numerical solutions of extended Bloch equations that include the coupled inter- and intraband dynamics are presented. For large excitation intensities, the intraband effects strongly modify the polarization dynamics and lead to a strong enhancement of high-harmonic generation compared to pure interband dynamics.

1 Introduction In the recent years, the high-harmonic generation (HHG) [1,2] via the interaction of strong optical fields with matter allowed for studying ultrafast transient processes in atoms and molecules on an attosecond time scale [3]. Due to the development of few-cycle intense laser sources [4,5], the regime of extreme nonlinear optics, i.e., the regime where the Rabi frequency is comparable to or larger than the band gap became accessible in semiconductors [6]. For such strong fields, a huge amount of novel interesting effects arises like carrier-wave Rabi flopping [7,8], HHG [9,10], and carrier-wave Mollow triplets [11] that have been predicted theoretically as well as observed experimentally.

When modeling the the extreme nonlinear optical response theoretically, previous studies [8–13] mainly focused on the interband transitions induced by the light field while the intraband excitations have not been included. However, these intraband contributions lead to a rapid periodic acceleration of the photoexcited carriers due to the electric field of the laser [6]. For moderate laser intensities, i.e., in conventional nonlinear optics, these changes of the carrier momentums are very small and, thus, the intraband dynamics can often be neglected. However, if the laser intensity is increased such that extreme nonlinear effects dominate the response, the intraband acceleration can cause very large shifts of the carrier momenta within half a period of the electric field. These shifts can even exceed the width of the Brillouin zone. Hence, the intraband contributions cannot be assumed to be small any more. In this paper, we analyze the extreme nonlinear optical response of semiconductor nanostructures due to the coupled inter- and intraband dynamics. It is demonstrated that the intraband motion of the photo-excited carriers leads to a strong broadening of the emission spectra and, thus, to a strong enhancement of HHG.

We start our analysis in Sec. 2.1 with presenting our microscopic theory for the extreme nonlinear optical response. In Sec. 2.2, we discuss the equations with regard to the pure intraband effects. The full numerical results including both inter- and intraband dynamics are presented and discussed in Sec. 3 before we briefly summarize our most important results in Sec. 4.

2 Theory

2.1 Equations of motion In order to keep the theoretical description as simple as possible, we focus on the optical response of a one-dimensional quantum wire within a two-band model. We assume the electrical field to be po-

larized linearly along the wire axis. Thus, we can omit the vector character of all vectorial quantities in our calculations. Another reason for considering only quantum wires is to reduce the numerical complexity of the problem since due to the intraband dynamics, the problem is not rotationally symmetric any more.

In extreme nonlinear optics, the energy scale describing the light-matter interaction ($\sim$ band gap energy) is much larger than the energy scale of the Coulomb interaction ($\sim$ exciton binding energy). Thus, the many-body Coulomb interaction among the carriers is only a small perturbation to the extreme nonlinear response and we can omit it in this analysis. A detailed study of this matter is provided by Ref. [10].

We compute the coupled inter- and intraband dynamics of the semiconductor nanostructure using an equation-of-motion approach. For this purpose, we solve the dynamics of the microscopic interband coherence (polarization) $p_k = \langle a^\dagger_{v,k} a_{c,k}\rangle$ and the carrier occupations $f^e_k = \langle a^\dagger_{c,k} a_{c,k}\rangle$ and $f^h_k = 1 - \langle a^\dagger_{v,k} a_{v,k}\rangle$ for electrons and holes, respectively. Here, $a^{(\dagger)}_{\lambda,k}$ are destruction (creation) operators for electrons in band λ with lattice momentum k. With the assumptions mentioned above, the equations of motion are given by [14–16]

$$i\hbar\frac{\partial}{\partial t}p_k = (\varepsilon^e_k + \varepsilon^h_k - i\frac{\hbar}{T_2})p_k - (1 - f^e_k - f^h_k)d_k E(t) + ieE(t)\cdot\nabla_k p_k, \quad (1)$$

$$\hbar\frac{\partial}{\partial t}f^{e(h)}_k = -2\,\mathrm{Im}\left[d_k E(t) p^*_k\right] + eE(t)\cdot\nabla_k f^{e(h)}_k \quad (2)$$

with the band dispersion for electrons (holes) $\varepsilon^{e(h)}_k$, the electric field of the exciting laser pulse $E(t)$, the k-dependent dipole-matrix element d_k, and the dephasing time of the polarization T_2. The terms containing the dipole-matrix element represent the interband transitions and the terms containing ∇_k describe the intraband acceleration. We will show in Sec. 2.2 that these gradient terms give rise to a ponderomotive motion of the photoexcited carriers due to the laser field.

The incoming electrical field induces a macroscopic polarization $P(t)$ due to the interband transitions of the electrons as well as a macroscopic current $J(t)$ along the quantum wire axis due to the acceleration of the carriers within their bands. These quantities determine the optical response of the semiconductor and can be computed via the solutions of Eqs. (1) and (2):

$$P(t) = \sum_k \left(d_k p_k(t) + \mathrm{c.c.}\right), \quad (3)$$

$$J(t) = \sum_{\lambda,k} e v^\lambda_k\, f^\lambda_k(t). \quad (4)$$

Here, $v^\lambda_k = \frac{1}{\hbar}\frac{\partial\varepsilon^\lambda_k}{\partial k}$ is the group velocity of the electrons (holes) and e is the elementary charge. Since the single particle energies are even functions of k, the group velocity is odd in k: $v^\lambda_{-k} = -v^\lambda_k$. This means that the current vanishes for any even carrier distribution and, in particular, for equilibrium conditions. Thus, $J(t)$ follows entirely from the odd part of the light-field induced non-equilibrium distributions.

The intensity of the radiation that is coherently emitted by the excited quantum wire is given by

$$I_{\mathrm{rad}}(\omega) \propto \left|\omega^2 P(\omega) + i\omega J(\omega)\right|^2 \quad (5)$$

in the Fourier domain. Obviously, the total emission follows from a coherent superposition of the two emission sources, i.e., the emission via the polarization and via the current.

Before we present and discuss numerical solutions of the emission according to Eq. (5) in Sec. 3, we start with a simplified discussion of Eqs. (1) and (2). This qualitative analysis improves the understanding of the numerical results.

2.2 Discussion of the equations We start to consider the artificial situation of pure interband dynamics. In this case, the gradient terms in Eqs. (1) and (2) vanish and the ordinary optical Bloch equations for an ensemble of inhomogeneously broadened two-level systems are obtained. A detailed analysis of the interband dynamics of semiconductor nanostructures in the extreme nonlinear optical regime can be found, e.g., in Refs. [6,10]. For strong excitation intensities where the Rabi energy $\hbar\omega_{\mathrm{R}} \equiv d_0 E_0$ is not small compared to the bandgap energy, the system dynamics is dominated by so-called carrier-wave Rabi flopping [7] that leads to novel effects in the emission spectra like high-harmonic generation (HHG) and carrier-wave Mollow triplets.

In order to gain more insight into the intraband motion of the carriers, we now assume that the system is in an excited, incoherent state, i.e., $p_k = 0 \neq f^\lambda_k$ for times before the laser pulse. For the sake of simplicity, we consider only the conduction-band electrons whose distribution function $f^{(0)}_k$ shall be in quasi-equilibrium before the pulse ($t \leq 0$). In this case, Eq. (2) simplifies to

$$\frac{\partial}{\partial t}f_k(t) = \frac{e}{\hbar}E(t)\frac{\partial}{\partial k}f_k(t). \quad (6)$$

By introducing a time dependent wave vector according to the acceleration theorem [17,18]

$$\frac{d}{dt}k(t) = -\frac{e}{\hbar}E(t), \quad (7)$$

the total derivative of the electron occupation vanishes

$$\frac{d}{dt}f_{k(t)} = 0 \quad (8)$$

where $k(t) = k(0) - \frac{e}{\hbar}\int_0^t \mathrm{d}t' E(t')$. This means that the entire distribution function is shifted in k-space according to Eq. (7) due to the electrical field of the laser. In general, we can conclude that the intraband terms in Eqs. (1)

and (2) lead to a time-dependent wave vector and, thus, to a ponderomotive intraband motion of the carriers and the polarization.

With help of Eq. (8), the dynamics of the current, Eq. (4), can be solved analytically:

$$J(t) = \frac{e}{\hbar}\sum_k \varepsilon'(k - \frac{e}{\hbar}\int_0^t \mathrm{d}t' E(t'))f_k^{(0)} \qquad (9)$$

where the definition of the group velocity has been used and $\varepsilon'(k)$ denotes the derivative of the single-particle energy with respect to k. Equation (9) shows directly that emission due to the intraband acceleration depends strongly on the band structure. For parabolic bands (free electrons), for example, ε' is a linear function of k and, thus, the current is linear in the electric field. This means that there is no nonlinearity and no HHG for free electrons. High-harmonic generation via pure intraband dynamics is a direct consequence of the non-parabolicity of the band structure. For illustration, the current following from a tight-binding dispersion can be written as

$$J(t) = -\frac{ea\Delta}{2\hbar}\sin\left(\frac{ea}{\hbar}\int_0^t \mathrm{d}t' E(t')\right) C\{f_k^{(0)}\} \qquad (10)$$

where a is the lattice constant, Δ is the band width, and $C\{f_k^{(0)}\} \equiv \sum_k f_k^{(0)}\cos(ka)$ is a prefactor depending on the initial carrier distribution. Obviously, the current contains highly nonlinear contributions now that lead to HHG. This can be seen explicitly by assuming a continuous-wave laser field, $E(t) = E_0\cos(\omega_0 t)$:

$$J(t) = -\frac{ea\Delta}{\hbar}C\{f_k^{(0)}\} \times \sum_{N=0}^{\infty}\mathcal{J}_{2N+1}\left(\frac{\omega_B}{\omega_0}\right)\sin((2N+1)\,\omega_0 t). \qquad (11)$$

Here, $\omega_B = eaE_0/\hbar$ is the Bloch frequency and $\mathcal{J}_M$ is the Mth order Bessel function of first kind. We see that the current oscillates with odd integers of the laser frequency weighted with the corresponding Bessel function at ω_B/ω_0. This clearly leads to odd harmonics in the emission spectrum. From the properties of the Bessel function follows that the highest frequency emerging in the emission spectrum is roughly equal to the Bloch frequency. Thus, one finds as the condition for HHG from pure interband dynamics that the Bloch frequency must be larger than the excitation frequency, $\omega_B > \omega_0$. For such strong fields, the intraband acceleration according to Eq. (7) causes large transient shifts of the wave vector that are comparable to or even larger than the width of the Brillouin zone.

In GaAs structures, the Bloch frequency is very similar to the Rabi frequency. Thus, one has to expect that both inter- and intraband dynamics are important for the extreme nonlinear ($\hbar\omega_R \gtrsim E_G$) optical response of a GaAs quantum wire when the sample is excited resonantly ($\hbar\omega_0 = E_G$). However, the structure of Eqs. (1) and (2) implies that both effects are not just additive in a realistic situation but are non-trivially coupled. The resulting emission spectra following from the coupled inter- and intraband dynamics are presented in Sec. 3.

3 Numerical results In order to compute the emission spectra of a GaAs quantum wire due to the coupled inter- and intraband dynamics, we solve Eqs. (1) and (2) numerically. Since the intraband motion can produce coherences and occupations at arbitrarily large k-values, the band structure needs to be modeled for all wave vectors within the Brillouin zone. Therefore, we assume tight-binding bands for the electron and hole dispersion

$$\varepsilon_k^\lambda = \frac{\Delta_\lambda}{2}(1 - \cos(ka)) + \frac{E_G}{2} \qquad (12)$$

where $\Delta_\lambda = \frac{2\hbar^2}{m_\lambda a^2}$ is the band width, $a = 5.65\,\text{Å}$ is the lattice constant of GaAs, and $m_{e(h)}$ is the effective mass of the electrons (holes) at the Γ-point. With the GaAs masses ($m_e = 0.069\,m_0$ and $m_h = 0.5\,m_0$), the resulting band widths are $\Delta_e = 6.9\,\text{eV}$ and $\Delta_h = 0.96\,\text{eV}$. In all calculations presented in this paper, the exciting laser pulse has a Gaussian shape with a duration of $\tau = 10\,\text{fs}$ (FWHM) and a central frequency ω_0 that is resonant with the band gap, $\hbar\omega_0 = E_G = 1.43\,\text{eV}$. Due to the strong excitations, the polarization decays on an ultrafast time scale that has been modeled by a constant dephasing time $T_2 = 50\,\text{fs}$.

The emission spectrum for pure interband dynamics is shown in Fig. 1(a). In order to characterize the HHG, we introduce the maximum frequency $\omega_{\max}$ at which significant emission arises for each Rabi frequency. From Fig. 1(a), we extract a maximum emission of $\omega_{\max} \approx 2\,\omega_R$ due to the interband transitions, i.e., due to carrier-wave Rabi flopping. Once the intraband acceleration is included (Fig. 1(d)), the HHG is strongly enhanced. Now, we have $\omega_{\max} \approx 10\,\omega_R$ which is much larger than the maximum emission from pure interband as well as from pure intraband ($\omega_{\max} \approx \omega_R$) dynamics. Thus, the strong broadening of the emission spectra follows from the non-trivial coupling of both effects. This coupling can be qualitatively illustrated as follows. The intraband current, Eq. (4), is modified by the interband transitions that lead to a rapid oscillation of the carrier occupations due to carrier-wave Rabi flopping additionally to the intraband acceleration in k-space. This clearly causes additional nonlinearities in the current. On the other hand, the time dependence of the wave vectors (see Eq. (7)) due to the intraband acceleration leads to a rapid oscillation of the transition frequencies $\omega_{k(t)}^\lambda = \varepsilon_{k(t)}^\lambda/\hbar$ with multiple integers of the laser frequency due to the non-parabolicity of the band structure. Since the interband coherences p_k in Eq. (3) rotate with these transition frequencies, there are additional highly nonlinear contributions to the macroscopic interband polarization and, thus, to the emission.

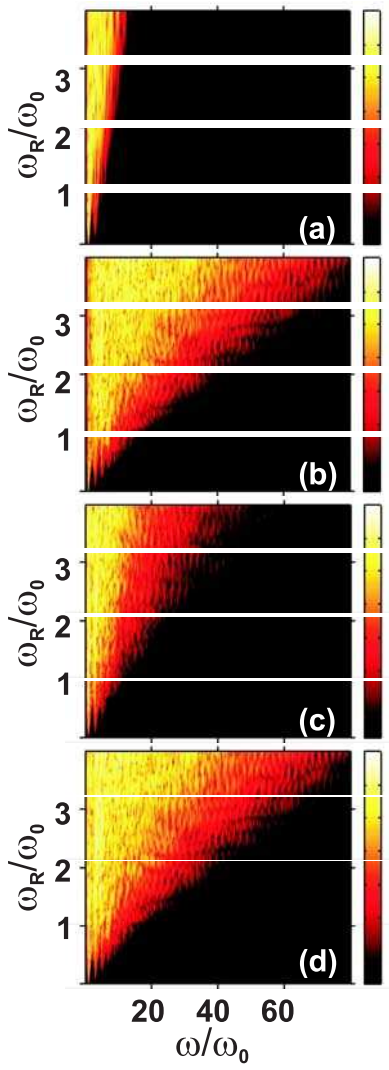

Figure 1 Calculated excitation dependent emission spectra of a GaAs quantum wire. The x-axis denotes the spectrometer frequency ω in units of the central excitation frequency ω_0. On the y-axis, the peak Rabi frequency ω_R in units of ω_0 is plotted. The intensity of the coherently emitted radiation is represented by the logarithmic color encoding that covers seven orders of magnitude. In (a), the result for pure interband dynamics is shown. The other frames present the emission due to the polarization (b), the current (c), and the total emission (d) due to coupled inter- and intraband dynamics.

In order to find out which of these effects dominates the coherent emission, we calculated the emission from the polarization $I_{\mathrm{rad}}^{\mathrm{pol}}(\omega) = |\omega^2 P(\omega)|^2$ and from the current $I_{\mathrm{rad}}^{\mathrm{curr}}(\omega) = |\omega J(\omega)|^2$ separately (see Figs. 1(b) and 1(c)). Evidently, the emission from the polarization is much broader than that from the current. Additionally, Fig. 1(b) looks very similar to the total emission spectrum (Fig. 1(d)). Hence, we can conclude that the modifications of the polarization due to the intraband acceleration are mainly responsible for the strong enhancement of the HHG.

4 Summary The extreme nonlinear optical response of a GaAs quantum wire following from the coupled inter- and intraband dynamics has been computed by solving extended Bloch equations. The intraband acceleration of the carriers leads to emission at very high harmonics of the laser frequency. We have demonstrated that neither pure interband transitions nor pure intraband motion can explain such high frequency components but they follow from the intricate coupling of both effects. In particular, the intraband-modified polarization dynamics is responsible for the strong enhancement of the HHG.

Acknowledgements This work has been supported by the Deutsche Forschungsgemeinschaft (DFG) and by the John von Neumann-Institut für Computing (NIC), Forschungszentrum Jülich, Germany.

References

[1] P. B. Corkum, Phys. Rev. Lett. **71**(13), 1994–1997 (1993).
[2] M. Lewenstein, P. Balcou, M. Y. Ivanov, A. L'Huillier, and P. B. Corkum, Phys. Rev. A **49**(3), 2117–2132 (1994).
[3] P. B. Corkum and F. Krausz, Nature Phys. **3**(6), 381–387 (2007).
[4] T. Brabec and F. Krausz, Rev. Mod. Phys. **72**(2), 545–591 (2000).
[5] F. X. Kärtner (ed.), Few-Cycle Laser Pulse Generation and Its Applications, Topics in Applied Physics, Vol. 95 (Springer, Berlin, 2004).
[6] M. Wegener, Extreme Nonlinear Optics (Springer, Berlin, 2005).
[7] S. Hughes, Phys. Rev. Lett. **81**(16), 3363–3366 (1998).
[8] O. D. Mücke, T. Tritschler, M. Wegener, U. Morgner, and F. X. Kärtner, Phys. Rev. Lett. **87**(5), 057401 (2001).
[9] T. Tritschler, O. D. Mücke, M. Wegener, U. Morgner, and F. X. Kärtner, Phys. Rev. Lett. **90**(21), 217404 (2003).
[10] D. Golde, T. Meier, and S. W. Koch, J. Opt. Soc. Am. B **23**(12), 2559–2565 (2006).
[11] Q. T. Vu, H. Haug, O. D. Mücke, T. Tritschler, M. Wegener, G. Khitrova, and H. M. Gibbs, Phys. Rev. Lett. **92**(21), 217403 (2004).
[12] O. D. Mücke, T. Tritschler, M. Wegener, U. Morgner, and F. X. Kärtner, Phys. Rev. Lett. **89**(12), 127401 (2002).
[13] Q. T. Vu and H. Haug, Phys. Rev. B **71**(3), 035305 (2005).
[14] T. Meier, G. von Plessen, P. Thomas, and S. W. Koch, Phys. Rev. Lett. **73**(6), 902–905 (1994).
[15] H. T. Duc, T. Meier, and S. W. Koch, Phys. Rev. Lett. **95**(8), 086606 (2005).
[16] D. Golde, T. Meier, and S. W. Koch, Phys. Rev. B **77**(7), 075330 (2008).
[17] C. Kittel, Quantum Theory of Solids (Wiley, New York, 1963).
[18] J. B. Krieger and G. J. Iafrate, Phys. Rev. B **33**(8), 5494–5500 (1986).

Paper V:
Proc. SPIE 6892, 68921F (2006)

Terahertz response of a two-dimensional electron gas

D. Golde, M. Kira, and S. W. Koch

Department of Physics and Material Sciences Center, Philipps University, Renthof 5, D-35032 Marburg, Germany

ABSTRACT

The terahertz response of a two-dimensional electron gas (2DEG) is investigated theoretically. The developed microscopic model shows that the terahertz absorption sensitively detects Coulomb-induced many-body correlations within the entire 2DEG system. In particular, the resulting response follows from a nontrivial competition between the ponderomotive and the Coulomb-correlation contributions. The result is in good agreement with recent experiments while the response cannot be explained with a simple Drude-model analysis.

Keywords: semiconductors, terahertz excitation, optical properties, two-dimensional electron gas

1. INTRODUCTION

Optical spectroscopy provides a sensitive method to detect small concentrations of a particular species of atoms or molecules via the related transitions between the eigenstates. If the characteristic absorption resonances are observed in the probe spectrum, the atoms or molecules must be present; one can even deduce their relative concentration when the respective transition strengths are known. The same idea can be applied to characterize quasi-particle states, such as plasma, plasmons, and excitons, in solids. However, the transition between different quasi-particle excitations typically correspond to terahertz (THz) fields for solids, which poses new requirements for THz laser sources. With this respect, recent experimental efforts[1–10] have extended semiconductor optics toward the regime where transitions between quasi-particle states can be probed directly with THz frequencies which are orders of magnitude lower than the usual band-to-band transitions. At the same time, recently developed microscopic THz theory for solids[11–16] has shown that THz spectroscopy is indeed uniquely qualified to detect non-trivial quasi-particle states.

In this paper, we investigate theoretically the THz response of a two-dimensional electron gas (2DEG) embedded in a GaAs-based high electron mobility transistor (HEMT) as described in Ref. 17. In particular, we describe the Coulomb-induced many-body correlations microscopically in order to explain the related quasi-particle state and its THz response. We show that the 2DEG response has features beyond the simple Drude response of a plasma. In particular, the 2DEG response is a combination of the so-called ponderomotive contribution and true many-body correlations. For the investigated 2DEG, the essential response features lie within THz to far-infrared regime such that experimental realization must employ THz techniques to detect the proposed effects. Indeed, the presented numerical results are in excellent agreement with state-of-the-art THz experiments[18] performed on 2DEG systems.

In Sec. 2, we present a detailed description of the 2DEG theory. In particular, we extend the generic semiconductor theory[15] to obtain formalism applicable for the 2DEG systems. After the proper system Hamiltonian is found, we solve the linear dielectric function using an equation of motion approach. In Sec. 3, we use the developed theory to numerically evaluate the THz response using realistic material parameters. These examples illustrate that the THz response of the 2DEG consists of a non-trivial combination of ponderomotive contribution and a many-body Coulomb contribution. The competition between these two contributions leads to an overall system response well beyond the simple Drude model.

Further author information: D. Golde: E-mail: daniel.golde@physik.uni-marburg.de

2. THEORY

In principle, the THz-sensitive part of the 2DEG consists mainly of the high-mobility electrons. Thus, we carefully need to investigate how the semiconductor-based THz theory[12,14,15] has to be applied for this situation. In particular, we aim to determine which many-body correlations and quasi-particle states couple to THz light. As a starting point, the 2DEG structure consists of a GaAs/AlGaAs interface with a thin (quasi two-dimensional) n-doped layer separated from the interface by a undoped AlGaAs spacer layer of thickness d_{sp}. Due to band-bowing effects, the donator atoms are ionized and the electrons are transferred into the GaAs/AlGaAs interface where they form the 2DEG. Within the 2DEG, the motion of the electrons is determined by the band dispersion of the two-dimensional GaAs conduction band. Thus, we can model the 2DEG electrons as quasi-free electrons with an effective mass m_e whose motion is confined to two dimensions.

Although the doping layer is spatially separated from the 2DEG, the electrons still see the long-range Coulomb potential of the positively charged doping ions. This means that all kinds of many-body correlations will emerge between the electrons and the ions. As will be shown in Sec. 3, these many-body effects strongly influence the response of the system to an external electromagnetic field. Thus, we cannot restrict our theoretical investigations to the 2DEG alone but we need to incorporate the ions in the doping layer, too. First, we point out that our system can be regarded as an ordinary electron-hole system with the ions playing the role of the holes. This observation connects the 2DEG investigations to "ordinary" semiconductors with well-defined electron and hole bands.

When we apply this connection, we obviously have to take into account the much higher mass of the ions compared to that of the electrons, i.e., $m_{\mathrm{ion}} \gg m_e$ as well as the spatial separation of electrons and ions. Thus, in order to develop a theory for the 2DEG, we apply the existing semiconductor THz theory[12,14,15] to derive the equations of motion of an interacting electron-hole plasma with spatially separated electrons and holes. In the last step, we will take the limit $m_{\mathrm{ion}} \to \infty$ to obtain the 2DEG equations. Surely, such an approach will, in principle, allow for including all correlations between electrons and ions.

2.1 The system Hamiltonian

The microscopic theory for the 2DEG can be systematically anchored by determining the relevant the Hamilton operator. As discussed above, we start from a general semiconductor Hamiltonian.[19] For the sake of clarity, we separate the total Hamilton operator into three contributions

$$H = H_{\mathrm{kin}} + H_{\mathrm{C}} + H_{\mathrm{LM}} \tag{1}$$

where H_{kin} is the kinetic energy of the crystal electrons, H_{C} describes the Coulombic many-body interaction, and H_{LM} determines the interaction with the classical THz field. Since we want to study the THz response and its modifications due to Coulomb interactions, we omit all additional contributions such as coupling to phonons and disorder landscape.

In second quantization formalism, the kinetic part reads

$$H_{\mathrm{kin}} = \sum_{\lambda,\mathbf{k}} \varepsilon^{\lambda}_{\mathbf{k}}\, a^{\dagger}_{\lambda,\mathbf{k}} a_{\lambda,\mathbf{k}} \tag{2}$$

in the Bloch basis where $a^{(\dagger)}_{\lambda,\mathbf{k}}$ is an annihilation (creation) operator of an electron in Bloch state $|\lambda\,\mathbf{k}\rangle$ with band index λ and (in-plane) crystal momentum $\mathbf{k}$. The coefficients $\varepsilon^{\lambda}_{\mathbf{k}}$ are the single-particle energies of the electrons in the crystal lattice. At this point, λ denotes both the electrons within the 2DEG as well as the holes (i.e. the n-doped ions).

The corresponding Coulomb interaction is given by

$$H_{\mathrm{C}} = \frac{1}{2} \sum_{\substack{\mathbf{k},\mathbf{k}',\mathbf{q}\neq 0 \\ \lambda,\lambda'}} V^{\lambda\lambda'}_{\mathbf{q}}\, a^{\dagger}_{\lambda\mathbf{k}} a^{\dagger}_{\lambda'\mathbf{k}'} a_{\lambda',\mathbf{k}'+\mathbf{q}} a_{\lambda,\mathbf{k}-\mathbf{q}} \tag{3}$$

which describes a real many-body interaction because it contains combinations of two annihilation and creation operators. As a result of this two-particle interaction, it is impossible to solve the problem exactly and thus, consistent approximation schemes need to be applied. We will address this problem below when discussing the equations of motion. The strength of the Coulomb interaction is given by the Coulomb-matrix element in Eq. (3) which follows from

$$V_{\mathbf{q}}^{\lambda\lambda'} = \frac{e^2}{2\epsilon_0\epsilon_r S}\frac{1}{|\mathbf{q}|}\iint_{-\infty}^{\infty} \mathrm{d}z\,\mathrm{d}z'\,|\xi_\lambda(z)|^2\,|\xi_{\lambda'}(z')|^2 e^{-|\mathbf{q}||z-z'|} \tag{4}$$

where $\xi_\lambda(z)$ is the confinement function of carriers in band λ, ϵ_r is the background dielectric constant, and S a normalization area. The confinement functions simply indicate how strong the carriers are confined in z-direction, i.e., perpendicular to the 2D layers.

At this point, we have to bear in mind that electrons and holes are spatially separated from each other for the 2DEG system investigated. This separation leads to an effective reduction of the electron-hole Coulomb interaction as can be seen explicitly when assuming δ like confinement, i.e., $|\xi_e(z)|^2 = \delta(z)$ and $|\xi_h(z)|^2 = \delta(z - d_{\mathrm{sp}})$. In this case, the electron-hole Coulomb-matrix element is given by

$$V_{\mathbf{q}}^{eh} = \frac{e^2}{2\epsilon_0\epsilon_r S}\frac{1}{|\mathbf{q}|}e^{-|\mathbf{q}|d_{sp}} \tag{5}$$

where, again, d_{sp} is the thickness of the spacer layer between the 2DEG and the doping layer. Obviously, the interaction strength decays exponentially with increasing spacer thickness. The interaction matrix elements for electron-electron and hole-hole interaction follow from Eq. (5) by setting $d_{\mathrm{sp}} = 0$.

As a last contribution to the Hamiltonian, we discuss the light-matter interaction. Since we are interested in the THz response of the system, we include only the intraband excitations since possible interband transitions are strongly non-resonant with respct to the THz field. In this situation, we obtain the light-matter Hamiltonian from

$$H_{\mathrm{LM}} = \sum_{\lambda,\mathbf{k}}\left[-j_\lambda(\mathbf{k})A_{\mathrm{THz}}(t) + \frac{e^2}{2m_0}A_{\mathrm{THz}}^2(t)\right]a_{\lambda\mathbf{k}}^\dagger a_{\lambda\mathbf{k}} \tag{6}$$

where A_{THz} is the vector potential of the exciting THz field. The current-matrix element in the first term is defined as $j_\lambda(\mathbf{k}) = -\frac{e\hbar}{m_\lambda}\mathbf{k}\cdot\mathbf{e_p}$ where m_λ is the effective mass of band λ and $\mathbf{e_p}$ is the polarization vector of the THz field. It is notable that the A_{THz}^2 contribution contains the free-electron mass.

2.2 Calculation of the linear THz response

The linear response of a system to an external electromagnetic field is given by the dielectric function $\epsilon(\omega)$ and the susceptibility χ respectively. These two quantities are connected via

$$\epsilon(\omega) = \epsilon_\infty + \chi(\omega) \tag{7}$$

where ϵ_∞ is the background dielectric constant for high frequencies. For linear response, the susceptibility is defined as

$$\chi(\omega) = \frac{P(\omega)}{\epsilon_0 E_{\mathrm{THz}}(\omega)} = \frac{J(\omega)}{\epsilon_0\,\omega^2 A_{\mathrm{THz}}(\omega)} \tag{8}$$

where P is the total polarization density induced by the THz field and J the total current density averaged over the thickness of the 2DEG. In Eq. (8), we have used the relations $J(t) = \frac{\partial}{\partial t}P(t)$ and $E_{\mathrm{THz}}(t) = -\frac{\partial}{\partial t}A_{\mathrm{THz}}(t)$. Thus, we need to compute J in first order in the THz field.

The total response of the 2DEG system follows from the wave equation for the vector potential; for homogeneous excitation and perpendicularly incident fields, we find

$$\left[\frac{\partial^2}{\partial t^2} - \frac{\epsilon_\infty(z)}{c^2}\frac{\partial^2}{\partial t^2}\right]A_{\mathrm{THz}}(z,t) = -\mu_0\left(J_{\mathrm{intra}}(z,t) + \frac{\partial}{\partial t}P_{\mathrm{inter}}(z,t)\right). \tag{9}$$

Here, J_{intra} is the intraband current density

$$J_{\mathrm{intra}}(z,t) = \sum_{\lambda} |\xi_\lambda(z)|^2 \left(\frac{1}{S} \sum_{\mathbf{k}} j_\lambda(\mathbf{k}) f_{\mathbf{k}}^\lambda(t) - \frac{e^2 n_\lambda}{m_0} A_{\mathrm{THz}}(t) \right) , \tag{10}$$

while P_{inter} is the interband polarization, $f_{\mathbf{k}}^\lambda \equiv \langle a_{\lambda,\mathbf{k}}^\dagger a_{\lambda,\mathbf{k}} \rangle$ is the occupation propability of the Bloch state $|\lambda \mathbf{k}\rangle$, and n_λ is the total density of carriers in band λ. The first term of Eq. (10) describes a current due to non-symmetric carrier distributions $f_{\mathbf{k}}^\lambda \neq f_{-\mathbf{k}}^\lambda$ generated by the THz field. Since $j_\lambda(\mathbf{k})$ is an odd function of the momentum, this term vanishes for symmetric distribution functions in particular for equilibrium Fermi-Dirac distributions. The second term is the so-called ponderomotive contribution; it follows from the term proportional to A^2 in the light-matter Hamiltonian, Eq. (6). It is notable that the free electron mass and not an effective mass appears here. Thus, if we assume the same confinement for all bands, this term is independent of the excitation conditions of the system since only the total electron density including all filled valence bands enters. However, it can be shown[12,20,21] that m_0 becomes replaced by m_λ once the nonresonantly excited interband polarization is taken into account. Thus, for small values of $\mathbf{k}$, the total current density entering the susceptibility, Eq. (8), takes the form

$$\begin{aligned} J(t) &\equiv J_{\mathrm{intra}} + \frac{\partial}{\partial t} P_{\mathrm{inter}} \\ &= \frac{1}{S\,L} \sum_{\lambda,\mathbf{k}} j_\lambda(\mathbf{k}) f_{\mathbf{k}}^\lambda(t) - \sum_{\lambda} \frac{e^2 n_\lambda}{m_\lambda\, L} A_{\mathrm{THz}}(t) \\ &\equiv J_{\mathrm{THz}}(t) + J_{A^2}(t)\,. \end{aligned} \tag{11}$$

Here, only partly filled bands contribute to the A^2 term. Obviously, the dynamics for the carrier distributions $f_{\mathbf{k}}^\lambda$ has to be solved in order to compute the susceptibility.

2.3 Equations of motion

To compute the dynamics of the relevant quantities, we use the equation of motion approach. The dynamics of the expectation value of any operator $\hat{O}$ is given by

$$i\hbar \frac{\partial}{\partial t} \langle \hat{\mathcal{O}} \rangle = \langle [\hat{\mathcal{O}}, H]_- \rangle\,. \tag{12}$$

Due to the Coulomb interaction, the equation of motion of an arbitrary N-particle quantity couples to $(N+1)$-particle quantities. Thus, one obtains an infinite hierarchy of equations that needs to be truncated consistently. In the following, we will apply the so-called cluster expansion[15] to treat this problem.

For the investigated 2DEG, we need to compute the dynamics of $f_{\mathbf{k}}^e = \langle a_{c\mathbf{k}}^\dagger a_{c\mathbf{k}} \rangle$ and $f_{\mathbf{k}}^h = 1 - \langle a_{v\mathbf{k}}^\dagger a_{v\mathbf{k}} \rangle$ to solve the THz-induced currents. The equations of motion of these quantities are not directly influenced by the THz field. Instead, the Coulomb interaction introduces coupling of $f_{\mathbf{k}}^\lambda$ to two-particle quantities of the form

$$C_{eh}^{\mathbf{q}\mathbf{k}'\mathbf{k}} = \Delta \langle a_{c\mathbf{k}}^\dagger a_{v\mathbf{k}'}^\dagger a_{v\mathbf{k}'+\mathbf{q}} a_{c\mathbf{k}-\mathbf{q}} \rangle \equiv \langle a_{c\mathbf{k}}^\dagger a_{v\mathbf{k}'}^\dagger a_{v\mathbf{k}'+\mathbf{q}} a_{c\mathbf{k}-\mathbf{q}} \rangle - \langle a_{c\mathbf{k}}^\dagger a_{v\mathbf{k}'}^\dagger a_{v\mathbf{k}'+\mathbf{q}} a_{c\mathbf{k}-\mathbf{q}} \rangle_{\mathrm{S}} \tag{13}$$

where $\langle \ldots \rangle_{\mathrm{S}}$ denotes the single-particle factorization which is identical to the Hartree-Fock approximation for fermionic particles. Since $f_{\mathbf{k}}^\lambda$ does not couple to the THz field, we derive the equation of motion for the two-particle correlations. The hierarchy is truncated at this level by factorizing the emerging three-particle expectation values into all combinations of one- and two-particle quantities. The remaining true three-particle correlations are treated as a phenomenological damping of the two-particle quantities.

As the next step, we apply the 2DEG property, $m_h \to \infty$, discussed earlier at the beginning of this section. Consequently, the holes remain stationary such that we only need to solve the dynamics of the electrons within the 2DEG. Furthermore, the equation for $f_{\mathbf{k}}^e$ does not couple to the full correlation, Eq. (13), but we can introduce a reduced correlation function

$$C_{eh}^{\mathbf{q},\mathbf{k}} \equiv \sum_{\mathbf{k}'} C_{eh}^{\mathbf{q},\mathbf{k}',\mathbf{k}} \,. \tag{14}$$

Since the electron-electron correlations do not couple to the THz field, we treat them in relaxation time approximation, i.e., we introduce a phenomenological relaxation constant Γ for the electron distribution. Assuming incoherent conditions in the 2DEG, the equations of motion read

$$\hbar \frac{\partial}{\partial t} f_{\mathbf{k}}^{e} = 2\mathrm{Im}\left[\sum_{\mathbf{q}} V_{\mathbf{q}}^{eh} C_{eh}^{\mathbf{qk}}\right] - \Gamma(f_{\mathbf{k}}^{e} - f_{\mathbf{k}}^{FD}) \,, \tag{15}$$

$$\begin{aligned} i\hbar \frac{\partial}{\partial t} C_{eh}^{\mathbf{qk}} = {} & (\tilde{\varepsilon}_{\mathbf{k}-\mathbf{q}} - \tilde{\varepsilon}_{\mathbf{k}} - i\gamma) C_{eh}^{\mathbf{qk}} + V_{\mathbf{q}}^{eh}(f_{\mathbf{k}}^{e} - f_{\mathbf{k}-\mathbf{q}}^{e}) N_{\mathrm{ion}} \\ & + V_{\mathbf{q}}^{ee}(f_{\mathbf{k}}^{e} - f_{\mathbf{k}-\mathbf{q}}^{e}) \sum_{\mathbf{k}'} C_{eh}^{\mathbf{q},\mathbf{k}'+\mathbf{k}} \\ & - (f_{\mathbf{k}}^{e} - f_{\mathbf{k}-\mathbf{q}}^{e}) \sum_{\mathbf{k}'} V_{\mathbf{k}'}^{ee} C_{eh}^{\mathbf{q},\mathbf{k}'+\mathbf{k}} \\ & + \sum_{\mathbf{k}'} V_{\mathbf{k}'}^{eh} \left[C_{eh}^{\mathbf{k}'+\mathbf{q},\mathbf{k}'+\mathbf{k}} - C_{eh}^{\mathbf{q}-\mathbf{k}',\mathbf{k}}\right] \\ & + j_e(\mathbf{q})\, C_{eh}^{\mathbf{qk}} A_{\mathrm{THz}}(t) \end{aligned} \tag{16}$$

where $\tilde{\varepsilon}_{\mathbf{k}}$ are Coulomb renormalized single particle energies, $f_{\mathbf{k}}^{FD}$ the Fermi-Dirac distribution, N_{ion} the number of doping ions, and γ a phenomenological damping constant due to three-particle correlations. In order to obtain the linear THz response, it is convenient to separate all dynamical quantities into even (E) and odd (O) parts:

$$\begin{aligned} \mathcal{F}^{O}(\mathbf{k}) &\equiv \frac{1}{2}(\mathcal{F}(\mathbf{k}) - \mathcal{F}(-\mathbf{k})), \\ \mathcal{F}^{E}(\mathbf{k}) &\equiv \frac{1}{2}(\mathcal{F}(\mathbf{k}) + \mathcal{F}(-\mathbf{k})). \end{aligned} \tag{17}$$

One immediately realizes that in the linear response regime, the THz field couples only to the odd correlation function which generates an odd distribution leading to a finite THz current J_{THz} via Eq. (11). Already at this stage, we see that the coupling of the THz field to the carrier distributions is a direct consequence of the electron-ion interaction. This means, in particular, that the THz term in Eq. (11) is completely due to many-body interactions whereas the A^2 term is obviously a pure free-particle contribution.

Equations (15)–(16) can be solved numerically. Inserting the solution for $f_{\mathbf{k}}^{e}$ into Eq. (11) and using Eqs. (8) and (7) yields the resulting dielectric function

$$\epsilon(\omega) = \epsilon_{\infty}\left(1 - \frac{\omega_{\mathrm{PL}}^2}{\omega^2}\right) + \frac{J_{\mathrm{THz}}(\omega)}{\epsilon_0 \omega^2 A_{\mathrm{THz}}(\omega)} \,. \tag{18}$$

Here, we have identified the the 3D plasma frequency

$$\omega_{\mathrm{PL}}^2 = \frac{(n_{\mathrm{2D}}/L)e^2}{\epsilon_0 \epsilon_{\infty} m_e} \tag{19}$$

where n_{2D} is the two-dimensional density of electrons in the 2DEG. Clearly, the A^2 term leads to the typical plasma response of non-interacting 3D electron gases. However, this response is modified by many-body effects via the THz term as discussed above. Furthemore, it can be seen that the A^2 term produces a purely real-valued response. Thus, the entire THz absorption follows from the many-body THz term only since the absorption is essentially given by the imaginary part of $\epsilon(\omega)$.

If the system can assumed to be in a steady-state and only dominant terms are included, the equations of motion (15)–(16) can be solved quasi analytically. The THz current J_{THz} then takes a Lindhard-type form leaving three integrals that need to be evaluated numerically.

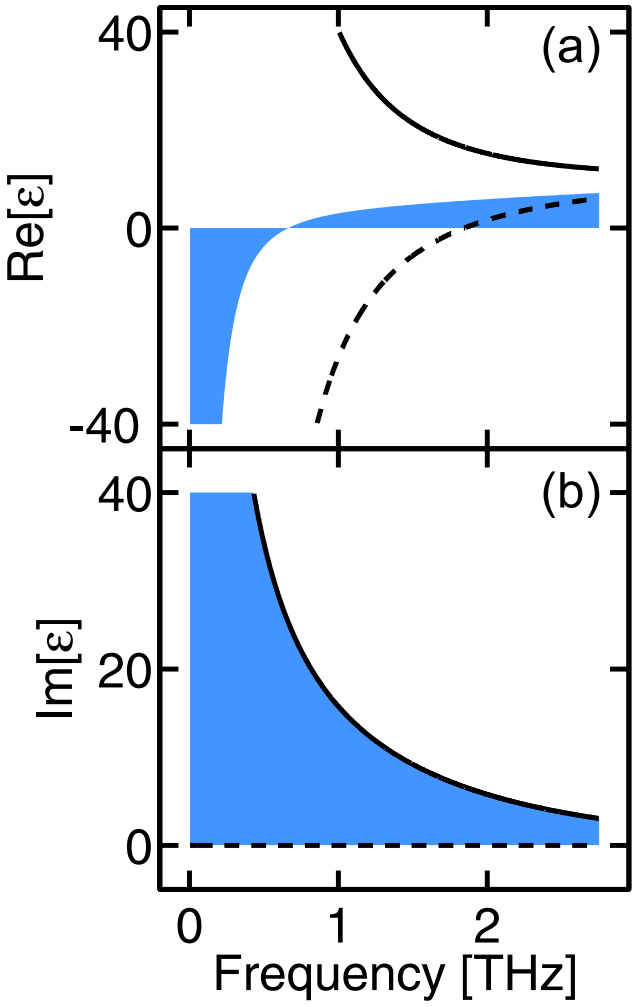

Figure 1. Computed dielectric function according to Eq. (18). In (a), the real part of ϵ is presented while (b) contains the imaginary part. The shaded area shows the full calculation whereas the solid line shows the THz contribution and the dashed line the A^2 contribution to the dielectric function. The density of doping ions is $n_{\mathrm{ion}} = 4 \cdot 10^{12}\,\mathrm{cm}^{-2}$ and the density of the 2DEG electrons is $n_{\mathrm{2D}} = 3.2 \cdot 10^{10}\,\mathrm{cm}^{-2}$. The damping constants are $\Gamma = \gamma = 16.7\,\mathrm{meV}$.

3. RESULTS

To illustrate the generic 2DEG-response features, we numerically solve Eqs. (15)–(16). The considered 2DEG structure has a doping concentration of $n_{\mathrm{ion}} = 4 \cdot 10^{12}\,\mathrm{cm}^{-2}$ and a spacer-layer thickness of $d_{\mathrm{sp}} = 10\,\mathrm{nm}$. These parameters have been used in our calculations. The density of the 2DEG electrons can be tuned by applying a bias voltage to the HEMT. As a realistic value, we use $n_{\mathrm{2D}} = 3.2 \cdot 10^{10}\,\mathrm{cm}^{-2}$.

The shaded area in Figure 1 presents the real and the imaginary part of the resulting dielectric function according to Eq. (18). It shows the typical behavior of the plasma response of an electron gas. The imaginary part diverges for low frequencies and decays roughly as ω^{-1} for larger frequencies. The real part of ϵ converges towards ϵ_∞ for large frequencies but diverges to negative values for $\omega \to 0$. The zero crossing of $\mathrm{Re}[\epsilon]$ is also a typical signature for plasma response. The presented theoretical results are in excellent agreement with recent THz transmission experiments performed on the 2DEG.[18]

In order to give evidence about the quantitative importance of the different contributions, Fig. 1 also shows the dielectric function due to the THz term $\epsilon_{\mathrm{THz}}(\omega) = \epsilon_\infty + \frac{J_{\mathrm{THz}}(\omega)}{\epsilon_0 \omega^2 A_{\mathrm{THz}}(\omega)}$ (solid line) and that due to the A^2

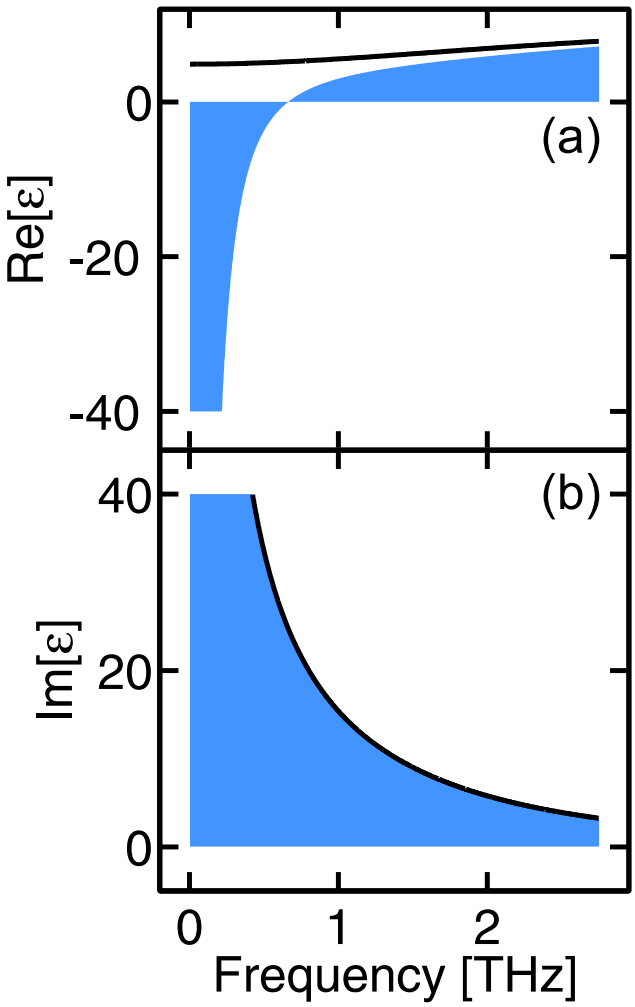

Figure 2. Comparison of computed (a) real and (b) imaginary part of the dielectric function with a Drude model (see Eq. (20)). The microscopic calculation (shaded area) is the same as the full calculation presented in Fig. 1. The parameters in the Drude model are $n_{\mathrm{Drude}} = 4.2 \cdot 10^{10}\,\mathrm{cm}^{-2}$ and $\Gamma_{\mathrm{Drude}} = 11.7\,\mathrm{meV}$. These parameters have been chosen to match the imaginary parts.

term $\epsilon_{A^2}(\omega) = \epsilon_\infty \left(1 - \frac{\omega_{\mathrm{PL}}^2}{\omega^2}\right)$ (dashed line). Apparently, these two contributions show a qualitatively completely different behavior. As already discussed above, the imaginary part follows entirely from from the THz term whereas the real part cannot be explained with a single contribution. In fact, both contributions strongly compensate each other to produce the correct dielectric function. Thus, we have found that the plasma response of the 2DEG is strongly influenced by both free plasma oscillations and many-body effects.

Often, the response of an electron gas to external electromagnetic fields is modeled by a simple Drude model which essentially follows from ϵ_{A^2} with introducing a phenomenological damping

$$\epsilon_{\mathrm{Drude}} = \epsilon_\infty \left(1 - \frac{\omega_{\mathrm{PL}}^2}{\omega(\omega + i\Gamma_{\mathrm{Drude}})}\right). \tag{20}$$

In Fig. 2, a comparison of the Drude result with the microscopic calculation is shown. The density and the damping of the Drude model have been fitted to match the imaginary parts of ϵ and $\epsilon_{\mathrm{Drude}}$. However, this Drude model produces a completely wrong real part. Of course, it is also possible to find a parameter set for the Drude

model that describes the real part well but then the imaginary part is wrong. Thus, the Drude model is not suited to describe the THz response of the 2DEG.

4. SUMMARY

Our analysis show that the 2DEG system can be analyzed on the basis of interacting electron-hole plasma. In this approach, the high-mobility electrons couple to the doping ions via the Coulomb interaction, which eventually produces correlations that can be detected with THz spectroscopy. In this description, the ions can be considered as immobile holes that attract electrons to create the Coulombic correlations. We show that the resulting 2DEG response consists of a non-trivial competition between the ponderomotive and Coulomb-correlation contributions. The results explain the THz-response observed in recent experiments. At the same time, we find out that these results cannot be attributed to a simple Drude response. Thus, the THz response of 2DEG systems consists of an intriguing combination of many-body and single-particle effects.

ACKNOWLEDGMENTS

This work has been supported by the Deutsche Forschungsgemeinschaft, the Bundesministerium für Bildung und Forschung, and the Optodynamics Research Center. We thank Sangam Chatterjee, Torben Grunwald, David Köhler, and Klaus Pierz for fruitful discussions and collaborations.

REFERENCES

1. R. H. M. Groeneveld and D. Grischkowsky, "Picosecond time-resolved far-infrared experiments on carriers and excitons in GaAs-AlGaAs multiple quantum wells," *J. Opt. Soc. Am. B* **11**, pp. 2502–2507, 1994.
2. J. Černe, J. Kono, M. S. Sherwin, M. Sundaram, A. C. Gossard, and G. E. W. Bauer, "Terahertz dynamics of excitons in GaAs/AlGaAs quantum wells," *Phys. Rev. Lett.* **77**, pp. 1131–1134, 1996.
3. M. C. Beard, G. M. Turner, and C. A. Schmuttenmaer, "Transient photoconductivity in GaAs as measured by time-resolved terahertz spectroscopy," *Phys. Rev. B* **62**, pp. 15764–15777, 2000.
4. R. Huber, F. Tauser, A. Brodschelm, M. Bichler, G. Abstreiter, and A. Leitenstorfer, "How many-particle interactions develop after ultrafast excitation of an electron-hole plasma," *Nature* **414**, pp. 286–289, 2001.
5. R. A. Kaindl, M. A. Carnahan, D. Hägele, R. Lövenich, and D. S. Chemla, "Ultrafast terahertz probes of transient conducting and insulating phases in an electron-hole gas," *Nature* **423**, pp. 734–738, 2003.
6. R. Huber, C. Kübler, S. Tübel, A. Leitenstorfer, Q. T. Vu, H. Haug, F. Köhler, and M.-C. Amann, "Femtosecond formation of coupled phonon-plasmon modes in InP: Ultrabroadband THz experiment and quantum kinetic theory," *Phys. Rev. Lett.* **94**, p. 027401, 2005.
7. J. R. Danielson, Y.-S. Lee, J. P. Prineas, J. T. Steiner, M. Kira, and S. W. Koch, "Interaction of strong single-cycle terahertz pulses with semiconductor quantum wells," *Phys. Rev. Lett.* **99**, p. 237401, 2007.
8. I. Galbraith, R. Chari, S. Pellegrini, P. J. Phillips, C. J. Dent, A. F. G. van der Meer, D. G. Clarke, A. K. Kar, G. S. Buller, C. R. Pidgeon, B. N. Murdin, J. Allam, and G. Strasser, "Excitonic signatures in the photoluminescence and terahertz absorption of a $GaAs/Al_xGa_{1-x}As$ multiple quantum well," *Phys. Rev. B* **71**, p. 073302, 2005.
9. C. Kübler, R. Huber, and A. Leitenstorfer, "Ultrabroadband terahertz pulses: generation and field-resolved detection," *Semicond. Sci. Technol.* **20**, pp. S128–S133, 2005.
10. M. Tonouchi, "Cutting-edge terahertz technology," *Nature Photonics* **1**, pp. 97–105, 2007.
11. M. Kira, W. Hoyer, T. Stroucken, and S. W. Koch, "Exciton formation in semiconductors and the influence of a photonic environment," *Phys. Rev. Lett.* **87**, p. 176401, 2001.
12. M. Kira, W. Hoyer, and S. W. Koch, "Microscopic theory of the semiconductor terahertz response," *phys. stat. sol. (b)* **238**, pp. 443–450, 2003.
13. M. Kira and S. W. Koch, "Exciton-population inversion and terahertz gain in semiconductors excited to resonance," *Phys. Rev. Lett.* **93**, p. 076402, 2004.
14. M. Kira, W. Hoyer, and S. W. Koch, "Terahertz signatures of the exciton formation dynamics in non-resonantly excited semiconductors," *Sol. Stat. Comm.* **129**, pp. 733–736, 2004.

15. M. Kira and S. W. Koch, "Many-body correlations and excitonic effects in semiconductor spectroscopy," *Prog. Quantum Electron.* **30**, pp. 155–296, 2006.
16. S. W. Koch, M. Kira, G. Khitrova, and H. M. Gibbs, "Semiconductor excitons in new light," *Nature Mat.* **5**, pp. 523–531, 2006.
17. T. Kleine-Ostmann, K. Pierz, G. Hein, P. Dawson, and M. Koch, "Room-temperature semiconductor modulators for free-space signal transmission with THz waves," in *Nanosensing: Materials and Devices*, M. S. Islam and A. K. Dutta, eds., *Proc. SPIE Int. Soc. Opt. Eng.* **5593**, pp. 521–532, 2004.
18. S. Chatterjee, T. Grunwald, D. Köhler, K. Pierz, D. Golde, M. Kira, and S. W. Koch, "Terahertz detection of plasmons and their many-body signatures in a two-dimensional electron gas." to be published.
19. H. Haug and S. W. Koch, *Quantum Theory of the Optical and Electronic Properties of Semiconductors*, World Scientific, Singapore, fourth ed., 2004.
20. J. E. Sipe and E. Ghahramani, "Nonlinear optical response of semiconductors in the independent-particle approximation," *Phys. Rev. B* **48**, pp. 11705–11722, 1993.
21. J. E. Sipe and A. I. Shkrebtii, "Second-order optical response in semiconductors," *Phys. Rev. B* **61**, pp. 5337–5352, 2000.

Paper VI:
phys. stat. sol. (c) 6, 453 (2009)

Phys. Status Solidi C **6**, No. 2, 453–456 (2009) / **DOI** 10.1002/pssc.200880337

physica status solidi c
www.pss-c.com
current topics in solid state physics

THz measurements of the optical response in a two-dimensional electron gas

S. Chatterjee[1,*], T. Grunwald[1], D. Köhler[1], K. Pierz[2], D. Golde[1], M. Kira[1], and S. W. Koch[1]

[1] Faculty of Physics, Philipps-Universität,Renthof 5, 35032 Marburg, Germany
[2] Physikalisch-Technische Bundesanstalt, Bundesallee 100, 38116 Braunschweig, Germany

Received 26 May 2008, revised 16 June 2008, accepted 17 June 2008
Published online 21 October 2008

PACS 73.21.Ac, 78.30.Fs, 78.47.-p, 78.67.Pt

* Corresponding author: e-mail sangam.chatterjee@physik.uni-marburg.de, Phone: +49-6421-2822115, Fax: +49-6421-2827036

We present an experimental study of the THz transmission through a two dimensional electron gas embedded in a high electron-mobility transistor-like structure. Similar to previous experiments in a three-dimensional system, a clear resonance is observed in the imaginary part of the inverse dielectric function $\Im\{1/\varepsilon(\omega)\}$. A detailed analysis using a Drude-like response cannot explain all experimental findings. These significant deviations make a more detailed microscopic analysis necessary.

1 Introduction High electron-mobility transistors are well-established in today's world of electronics. The technical properties are well understood and can be found in many standard textbooks on semiconductor devices, see e.g. [1]. The main underlying physical component is a two-dimensional electron gas (2DEG) which is formed due to band-bowing. Its two-dimensionality is well established and has even been used as a model system, including the quantum hall effect [2].

The fundamental excitation of an electron gas is the plasmon. It describes a collective charge oscillation in response to an electro-magnetic field [3–6]. Its light dispersion is well established, see e.g. [7–10], as is its dimension dependence. A vanishing response is expected for an excitation normal to the two-dimensional system, i.e. with an in-plane momentum $q_{\|} = 0$ [11].

In this paper, we present experimental study showing that the terahertz (THz) response of such a 2DEG embedded in a high electron-mobility transistor-like structure. Its dielectric function is extracted from the measured transmitted complex THz-field. A clear plasmon pole is observed, similar to [12] in bulk material. The experimental response is analyzed using a Drude response. While real or imaginary part can be fitted, the complete details of the experimentally determined response cannot be described in this way [13].

2 Experimental detail and sample The investigation is a standard transmission experiment in a THz time-

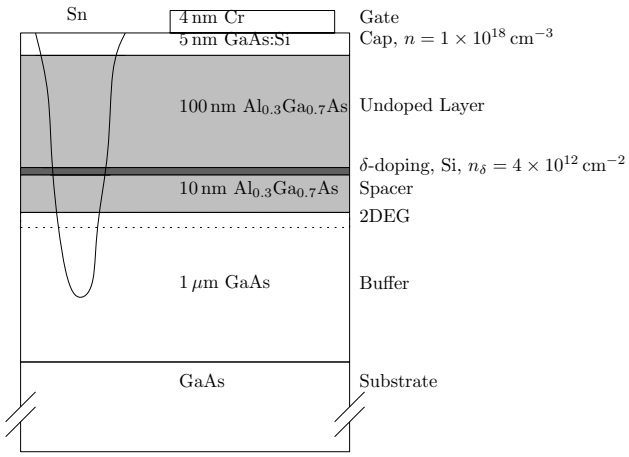

Figure 1 Schematic cross-section of the investigated sample structure.

domain setup. The THz-pulses are generated in a biased photoconductive antenna using a Ti:Sapphire laser oscillator emitting 30 fs pulses at 80 MHz repetition rate centered at 780 nm. The generated THz radiation is focused to a spot of about 400 µm diameter full width at half maximum on the sample. The transmitted THz field is subsequently detected by electro-optic sampling using a 1 mm (110)-cut ZnTe crystal. The setup yields a spectral bandwidth of more than 2.5 THz and a signal-to-noise ratio grater than four orders of magnitude in the electric field. The sample is kept at 10 K inside a helium cold finger cryostat equipped with TPX windows and electrical feed-through.

The carriers are injected electrically into the structure by applying a bias voltage between the four source / drain contacts and the top gate shown in Fig. 1. Both, amplitude and phase of the transmitted THz-field are measured.

The reference signal $E(t)$ is recorded for a constant bias of -1 V. Here, the 2DEG is empty, as capacitance-considerations and Hall-measurements reveal. The electrons are injected by applying a square waveform varying between -1 V and -0.85 V at a frequency of 1.71 kHz. The carrier density in the sample leads to characteristic signatures in the transmitted THz-signal $\Delta E(t)$. This is then recorded using standard lock-in technique in an optical bridge. Figure 2 shows typical experimental time traces. The reference signal $E(t)$ is plotted in black (left-hand y-scale) and an exemplary differential signal $\Delta E(t)$ is shown in red (right-hand y-scale, area under curve is filled). The time-domain signals $E(t)$ and $\Delta E(t)$ are numerically converted into frequency space by using a standard fast-Fourier transform (FFT) algorithm. The complex dielectric function is then evaluated according to

$$\varepsilon(\omega) = \varepsilon_\infty - \frac{i2c\sqrt{\varepsilon_{\mathrm{GaAs}}(\omega)}}{\omega L}\,\frac{\Delta E(\omega)}{E(\omega)} \quad . \qquad (1)$$

3 Results and analysis Exemplary experimental results are plotted as blue curves in Fig. 3. For completeness, the imaginary and real part of ε is shown in the topmost row and the imaginary and real part of $1/\varepsilon$ below. The set of four graphs is shown again for comparison with a Drude-like response of varying parameters (see below). Similar to [12], a clear resonance is observed at 1.3 THz. The electron densities considered in our experiment, however, are considerably lower, explaining the energetically low position of the resonance. Also, the zero-crossing in $\Re(\varepsilon)$ should be noted.

The experimental data are analyzed using a classical Drude model. The dielectric function ε for this case is given by

$$\varepsilon(\omega) = \varepsilon_\infty \left(1 - \frac{\omega_{\mathrm{pl}}^2}{\omega^2 + i2\frac{e}{\mu_{\mathrm{e}} m^*}\omega}\right) \quad . \qquad (2)$$

where $\varepsilon_\infty = 10.9$ is the GaAs background dielectric constant, ε_0 the vacuum dielectric constant, and e the elementary charge of an electron. An effective electron mass in the GaAs conduction band of $m^* = 0.06 \cdot m_0$, using the electron rest mass m_0, and a mobility $\mu_{\mathrm{e}} = 8000\,\mathrm{cm}^2/(\mathrm{V\,s})$ were used. Here, the plasma frequency ω_{pl} enters. Obviously, the two-dimensional form needs to be considered for a 2DEG. In this case, it is given by

$$\omega_{\mathrm{pl(2d)}} = \sqrt{\frac{e^2 n_{\mathrm{e}}}{2\varepsilon_0 \varepsilon_\infty m} q_\parallel} \quad , \qquad (3)$$

where $q_\parallel$ is the momentum in the plane of the 2DEG. This yields a vanishing plasmon pole for THz-frequencies and does not fit the experimental findings at all.

Although obviously unphysical in case of a 2DEG, the three-dimensional plasma-frequency

$$\omega_{\mathrm{pl(3d)}} = \sqrt{\frac{n_{\mathrm{e}} e^2}{\varepsilon_0 \varepsilon_\infty m}} \qquad (4)$$

yields a decent fit to the experiment. Here, a homogeneous carrier distribution $n_{\mathrm{e}}^{\mathrm{3d}} = n_{\mathrm{e}}^{\mathrm{2d}}/L$ is assumed across the "thickness" of the 2DEG $L = 10$ nm.

The calculated cures are shown in red in Fig. 3. For the top set of four graphs, the Drude response is fit to the experimental value of $\Im(\varepsilon)$ by adjusting carrier density n_{e} and damping γ. Hereby, good agreement is found for $\Re(1/\varepsilon)$ and $\Im(1/\varepsilon)$. However, the zero-crossings in the real-parts of ε and $1/\varepsilon$ are not reproduced while the response for larger frequencies agrees rather well.

The Drude response for the bottom set of graphs is fitted to $\Re(\varepsilon)$. In this case, the zero-crossings in the real-parts of ε are reproduced, however all other features, i.e., the whole line shape is not. Especially, the resonance in $\Im(1/\varepsilon)$ is strongly shifted to lower energies.

In summary, even though the response of a two-dimensional electron gas was measured, the experimental

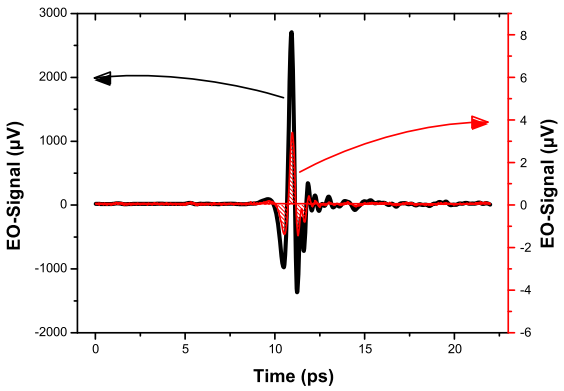

Figure 2 Time traces of the reference signal $E(t)$ shown in black (left-hand y-scale) and exemplary differential signal $\Delta E(t)$ shown in red (right-hand y-scale, area under curve is filled).

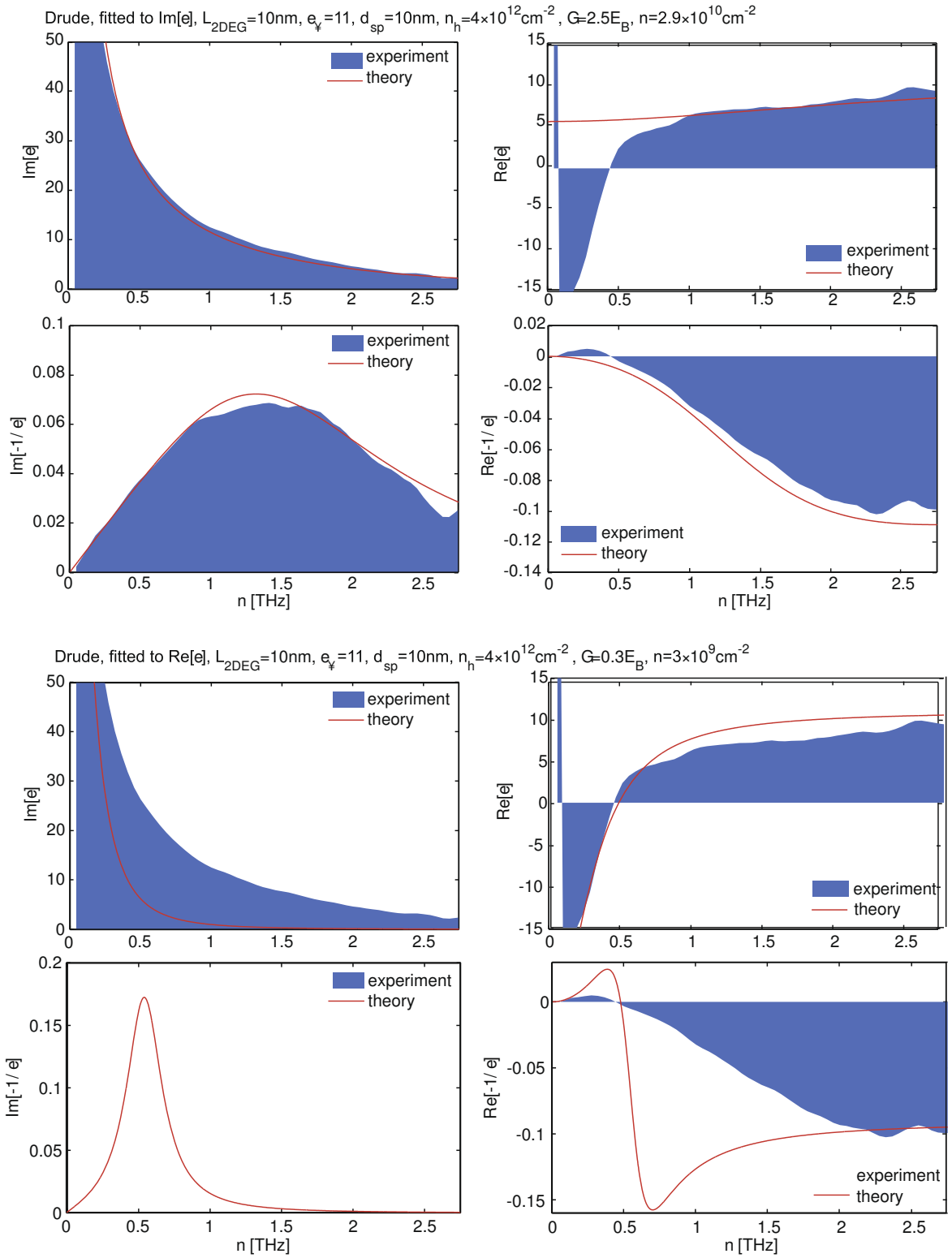

Figure 3 Dielectric function of the 2DEG for an applied bias voltage of -0.85V. The response calculated according to a Drude model (red) is fitted to the $\Im(\varepsilon)$ (top) and $\Re(\varepsilon)$ (bottom) of the experimental data shown in blue. A single set of parameters, i.e. carrier density and damping is used for each fit.

results cannot be fitted using a two-dimensional Drude model. The three-dimensional plasma frequency yields a decent approximation of the observation. It should be noted, that the mismatch of real and imaginary part are not a violation of the Kramers-Kronig relation [14] since only a very limited spectral range is considered here. Clearly, the presented analysis is only a first step and a more detailed microscopic description of the *two-dimensional* case is required.

Acknowledgements The authors want to thank the German ministry of education and research (Bundesministerium für Bildung und Forschung, BMBF) under contract number 13N9405 and the Optodynamics research center for financial support. Technical discussions with Martin Koch and Thomas Kleine-Ostmann are gratefully acknowledged.

References

[1] K. K. N. Simon and M. Sze, Physics of Semiconductor Devices, 3rd ed. (John Wiley and Sons, Hoboken, NJ, USA, 2006).
[2] K. v. Klitzing, G. Dorda, and M. Pepper, Phys. Rev. Lett. **45**(6), 494–497 (1980).
[3] L. Tonks and I. Langmuir, Phys. Rev. **33**(2), 195–210 (1929).
[4] D. Bohm and E. P. Gross, Phys. Rev. **75**(12), 1851–1864 (1949).
[5] D. Bohm and D. Pines, Phys. Rev. **82**(5), 625–634 (1951).
[6] P. Nozières and D. Pines, Phys. Rev. **109**(3), 741–761 (1958).
[7] M. Quinten, A. Leitner, J. R. Krenn, and F. R. Aussenegg, Opt. Lett. **23**(17), 1331–1333 (1998).
[8] J. B. Pendry, Phys. Rev. Lett. **85**(18), 3966–3969 (2000).
[9] R. A. Shelby, D. R. Smith, and S. Schultz, Science **292**(5514), 77–79 (2001).
[10] S. Linden, C. Enkrich, M. Wegener, J. Zhou, T. Koschny, and C. M. Soukoulis, Science **306**(5700), 1351–1353 (2004).
[11] M. C. Peter P. Yu, Fundamentals of Semiconductors: Physics and Materials Properties , 3rd ed. (Springer, Berlin, Germany, 2005).
[12] R. Huber, F. Tauser, A. Brodschelm, M. Bichler, G. Abstreiter, and A. Leitenstorfer, Nature **414**(6961), 286–289 (2001).
[13] F. Stern, Phys. Rev. Lett. **18**(14), 546–548 (1967).
[14] H. Haug and S. W. Koch, Quantum Theory of the Optical and Electronic Properties of Semiconductors (World Scientific Publishing, London, 2004).

Paper VII:
Phys. Rev. Lett. 102, 127403 (2009)

Fano Signatures in the Intersubband Terahertz Response of Optically Excited Semiconductor Quantum Wells

D. Golde,[1,*] M. Wagner,[2] D. Stehr,[2] H. Schneider,[2] M. Helm,[2] A. M. Andrews,[3] T. Roch,[3] G. Strasser,[3] M. Kira,[1] and S. W. Koch[1]

[1]*Department of Physics and Materials Sciences Center, Philipps-University, Renthof 5, 35032 Marburg, Germany*
[2]*Institute of Ion Beam Physics and Materials Research, Forschungszentrum Dresden-Rossendorf, P.O. Box 510119, 01314 Dresden, Germany*
[3]*Solid State Electronics Institute, Micro- & Nanostructure Center, TU Wien, Floragasse 7, 1040 Vienna, Austria*

(Received 12 December 2008; published 24 March 2009)

Absorption and transmission spectra of broadband terahertz pulses are measured to probe the intersubband response of an optically excited quantum-well heterostructure. While the terahertz absorption shows the single peak of the resonant intersubband transition, the transmission spectra display strong Fano signatures due to the phase sensitive superposition of ponderomotive and terahertz currents as predicted by our microscopic theory.

DOI: 10.1103/PhysRevLett.102.127403 PACS numbers: 78.67.De, 42.25.Bs, 73.21.Fg

Terahertz (THz) experiments on optically excited or doped semiconductors provide unique opportunities to analyze and manipulate low-energy excitations or quasiparticle states, like intersubband transitions between quantum confined states [1–5], excitons, or plasmons, and monitor their dynamical evolution [6–10]. With sufficiently strong THz pulses, one can even reach the regime of ''extreme nonlinear optics'' leading to effects such as Rabi flopping [5,11,12], ac-Stark splitting [13], or the dynamical Franz-Keldysh effect [14,15]. The microscopic analysis of these experiments shows that the THz wave propagating through the semiconductor is determined by the combined response of the so-called ponderomotive current and the true THz transitions. Here, the ponderomotive contribution refers to the charge current generated by the classical field that causes a wiggling motion of the carriers according to the acceleration theorem $\hbar\dot{\mathbf{k}} = -e\mathbf{E}_{\mathrm{THz}}$ [16,17]. This part of the light-matter interaction, often thought to be relevant only at high intensities [15], produces the simple response $\chi(\omega) = -\frac{\omega_{\mathrm{PL}}^2}{\omega^2}$ with the plasma frequency ω_{PL}. Because of the factor ω^{-2}, the ponderomotive contribution can usually be neglected in the analysis of interband optical excitation; however, it is of relevance in the THz regime even at the lowest intensities. Thus, the THz response of an excited semiconductor is influenced by ponderomotive effects plus the true THz transitions. When both contributions are of equal strength, one expects a strong interplay. In the experiments reported in Refs. [12,18] the evidences for the role of the ponderomotive current are rather indirect. Their influence could only be seen by virtue of a theoretical switch-off analysis.

To clearly expose the interplay of ponderomotive and true THz response, one needs an experimental method that makes it possible to observe both effects directly. In this Letter, we study the intersubband transition of photoexcited semiconductor quantum wells using linear THz spectroscopy. Monitoring the transmission of a broadband THz pulse, we directly observe signatures of the ponderomotive motion of the excited carriers. We show that interference of ponderomotive and resonant contributions produces a characteristic Fano-like line shape in the differential transmission spectrum.

Asymmetric Fano line shapes are known to result from quantum interference of discrete energy levels coupled to a nearby continuum [19] and have been observed in semiconductor heterostructures under various conditions [20–23]. Whereas the relevant continuum in typical Fano configurations is an integral part of the probed quantum object, in our system an effective continuum is provided by the light-matter interaction through the ponderomotive contribution.

Figure 1(a) shows the basic concept of our experiment where spectrally broadband THz pulses probe the sample's intersubband transition after resonant photoexcitation. The THz pulses are generated in a 55 μm thin z-cut GaSe crystal by phase-matched difference frequency mixing [24] within the broad spectrum of 12 fs optical pulses, delivered by a 78 MHz Ti:sapphire oscillator (Femtolasers: Femtosource Scientific sPro). The THz beam is focused by off-axis parabolic mirrors on the multi-quantum-well (MQW) sample, with the THz field having a strong component perpendicular to the MQW plane to couple effectively to the intersubband transition [25]. For THz-field-resolved detection, phase-matched electro-optic sampling [26,27] is applied. To this end, a weak component of the 12 fs laser beam goes through a delay stage and samples the THz-field induced polarization change in a second 30 μm thin z-cut GaSe crystal as a function of the time delay between THz pulse and sampling pulse [Fig. 1(c)].

The sample studied consists of 60 periods of 8.2-nm-thick undoped GaAs quantum wells, separated by 19.6-nm-thick barriers of $Al_{0.34}Ga_{0.66}As$. The sample was prepared

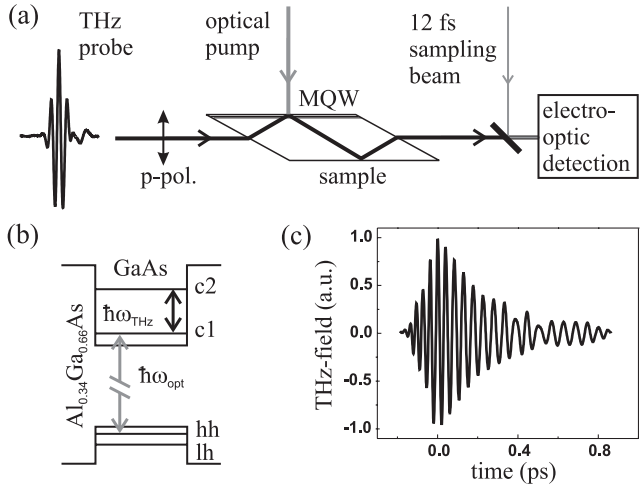

FIG. 1. (a) Optical interband pump intersubband THz probe experiment. (b) The transition from the heavy-hole (hh) state to the first conduction state (c1) in the $Al_{0.34}Ga_{0.66}As/GaAs$ multiquantum-well (MQW) sample is resonantly excited, either by a ps or a fs laser. THz pulses probe the c1-to-c2 transition 25 ps after photoexcitation. (c) The field transients of the transmitted THz pulses are detected by phase-matched electro-optic sampling with a sampling beam. The reference without photoexcitation is shown.

in a 38-degree wedged-waveguide geometry, as shown in Fig. 1(a). To ensure optimized overlap between MQW region and THz standing wave [25], an additional $Al_{0.34}Ga_{0.66}As$ spacer layer of 300 nm thickness was grown on top of the sample. The experiments are performed at a temperature of 6 K.

The photoexcitation scheme is illustrated in Fig. 1(b). An optical interband pump pulse excites the MQW resonantly at the 1*s* heavy-hole exciton and creates carriers in the first conduction band. We choose either spectrally narrow 2.5 ps or broadband 100 fs optical excitation centered at $\hbar\omega_{opt} = 1.56$ eV. Both lasers are 78 MHz Ti:sapphire oscillators (Spectra Physics: Tsunami), locked to the repetition rate of the THz generating laser. In each case, only the first conduction subband of the MQW is populated. After a time delay of 25 ps during which the optically induced interband coherences disappear, the weak broadband THz-pulse probes the c1-to-c2 intersubband transition. In all the experiments, the photoexcited carrier density is 2×10^{10} cm^{-2} per quantum well.

A two-lock-in technique is employed to measure the transmitted THz transients with and without excitation. The visible pump and THz probe beams are chopped simultaneously at different frequencies around 2 kHz. The first lock-in amplifier locks on the modulation of the optical pump beam. Since the THz beam is also chopped at the same time, twice the signal obtained by the first lock-in amplifier yields the differential transmission $\Delta E(t)$, i.e., the pump-induced change in the transmitted THz field. The second lock-in amplifier detects the mean value between transmission with and without photoexcitation, leading to the reference $E_{ref}(t)$ without excitation by subtracting the signal of the first lock-in amplifier. This allows us to record $\Delta E(t)$ and $E_{ref}(t)$ simultaneously under the same conditions, preventing a drift in the relative phase between them. Such a phase drift would strongly affect the computed total THz absorption of the quantum wells $\alpha(\omega)$, where the complex valued Fourier transforms of $\Delta E(t)$ and $E_{ref}(t)$ enter in the following way: $\alpha(\omega) = 2\mathrm{Im}[-i\Delta E(\omega)/E_{ref}(\omega)]$. This relation follows from Maxwell's equations and the assumptions that (i) $|\Delta E| \ll |E_{ref}|$, (ii) the unexcited sample is nonabsorptive in the investigated frequency range, and (iii) only the single-pass signal is measured.

Figure 1(c) shows the reference transient $E_{ref}(t)$. Compared with the incident THz transient [Fig. 1(a)], the field oscillations last longer in time due to dispersion in the sample. The differential THz transmission transients $\Delta E(t)$ are presented in Figs. 2(a) and 2(b) for ps and fs excitation, respectively. First, one observes that the signal has 440 fs

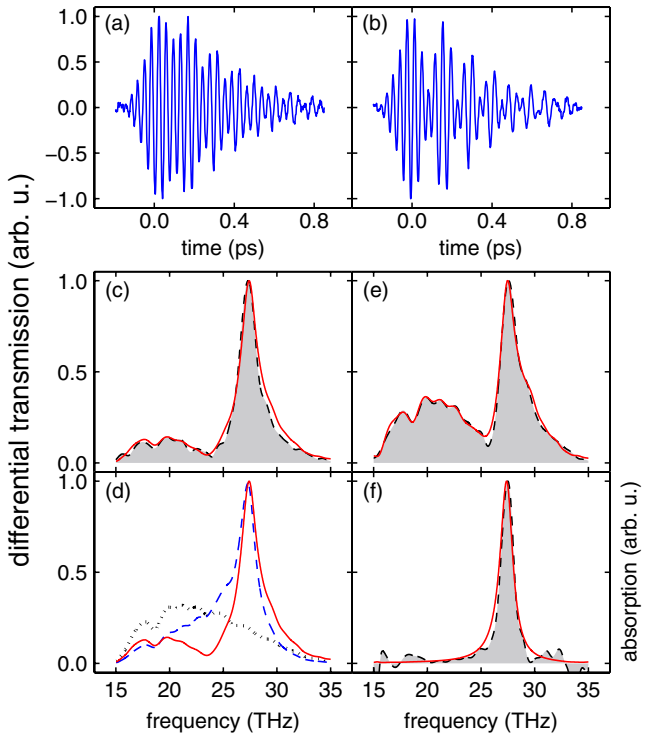

FIG. 2 (color online). Experiment-theory comparison of the THz intersubband response. (a),(b) Measured time-resolved differential transmission signals $\Delta E(t)$ for ps and fs excitation, respectively. (c) Measured spectral amplitude of differential transmission $|\Delta E(\omega)|$ (shaded area) and calculated current density $|J_{tot}(\omega)|$ (red solid line) after optical ps excitation. (d) shows the decomposition of the computed total current density (red solid line) into the ponderomotive contribution $|J_A|$ (black dotted line) and the intersubband current $|J_{THz}|$ (blue dashed line). (e), (f) Measured (shaded area) and computed (red solid line) differential transmission and THz absorption, respectively, after fs excitation. Here, J_A has been enhanced by 1.85 in order to account for substrate excitations.

decay constant for both ps and fs excitation, whereas a decay of 240 fs is observed for the reference $E_{\mathrm{ref}}(t)$ [see Fig. 1(c)]. This reveals the dephasing of the reradiated THz-induced intersubband polarization [2,3,28]. Second and more interesting, one observes a clear beating compared to the reference $E_{\mathrm{ref}}(t)$, superimposed on the dephasing and being more pronounced for fs photoexcitation.

We first address the ps excitation to analyze the origin of the observed beating. Figure 2(c) shows the spectral amplitude of the measured differential THz transmission $|\Delta E(\omega)|$ after optical excitation at the $1s$ position of the heavy-hole exciton resonance. We see that the spectrum consists of two major contributions: (i) a sharp resonance peak at the transition frequency of the conduction subbands $\nu_{1,2} = 27.3$ THz and (ii) a broad contribution centered at roughly 20 THz, being responsible for the beating in the time domain. These features remind us of a typical Fano spectrum, i.e., an undershoot at the low-frequency side of the peak followed by an asymmetric line shape.

When the system is excited with a 100 fs pulse, the broad contribution and the Fano signatures are more pronounced than in the ps case [Fig. 2(e)]. To check whether the broad feature in the differential transmission is caused by an additional carrier transition besides the intersubband resonance, we measure the THz absorption. Figure 2(f) shows that the absorption is single peaked; i.e., only the intersubband resonance appears and no Fano-like signature is observed.

In order to explain the experimental findings, we compute the THz transmission of a quantum well positioned at $z = 0$ (where z is the growth direction of the quantum well). The THz response follows from the wave equation

$$\left(\nabla^2 - \frac{n_b^2}{c^2}\frac{\partial^2}{\partial t^2}\right)E(\mathbf{r}, t) = \mu_0 \delta(z)\frac{\partial}{\partial t}(J_{\mathrm{A}}(t) + J_{\mathrm{THz}}(t)), \quad (1)$$

where n_b is the background refractive index, c is the speed of light, and μ_0 is the permeability of free space. The delta function arises due to the fact that the quantum-well width is much smaller than the wavelength of the THz field. The induced current density appearing as source term on the right-hand side of Eq. (1) consists of two terms: J_{THz} is the current due to the intersubband transitions and J_{A} describes the ponderomotive motion of the excited carriers due to the THz field. Solving Eq. (1), one finds that the differential transmission, i.e., the field that is reemitted by the current density, is directly proportional to the induced current [29]: $\Delta E \propto J_{\mathrm{A}} + J_{\mathrm{THz}}$.

The ponderomotive contribution to the current density is given by $J_{\mathrm{A}} = -\sum_\lambda \frac{e^2 n_\lambda}{m_\lambda} A_{\mathrm{THz}}$ [30] where n_λ is the carrier density in band λ and m_λ is the effective mass. The vector potential A_{THz} of the THz pulse is defined via $E_{\mathrm{THz}} = -\frac{\partial}{\partial t}A_{\mathrm{THz}}$. Here, λ includes both bulk-band index and subband index. Obviously, the ponderomotive current directly follows A_{THz} with an opposite phase due to the minus sign in J_{A}. The linear susceptibility $\chi_{\mathrm{A}}(\omega) = -\frac{\omega_{\mathrm{PL}}^2}{\omega^2}$ following from the ponderomotive current is a real-valued quantity. Consequently, J_{A} does not contribute to the absorption $\alpha(\omega) \propto \omega \mathrm{Im}[\chi(\omega)]$, but simply introduces a refractive index change to the excited material.

The THz current is computed via $J_{\mathrm{THz}} = \frac{1}{S}\sum_{\lambda,l,l',\mathbf{k}} j^\lambda_{l',l} p^\lambda_{l,l',\mathbf{k}}$ with the quantization area S and the matrix elements $j^\lambda_{l,l'}$. The quantity $p^\lambda_{l,l',\mathbf{k}}$ represents the microscopic intersubband polarization between subbands l and l' of bulk-band λ. The intersubband matrix element is given by $j^\lambda_{l,l'} = -\frac{i\hbar e}{m_\lambda}\int dz \xi^*_{\lambda,l}(z)\frac{\partial}{\partial z}\xi_{\lambda,l'}(z)$ where $\xi_{\lambda,l}(z)$ is the confinement wave function of the carriers.

The intersubband polarization $p^\lambda_{l,l',\mathbf{k}}$ in J_{THz} is computed microscopically with an equation-of-motion approach. Since we are interested only in the c1-to-c2 transition, we can restrict the sum to $\lambda = c$ and $l, l' \in \{1, 2\}$. In analogy to the semiconductor Bloch equations [31], one finds for the time evolution of the intersubband polarization

$$\begin{aligned} i\hbar\frac{\partial}{\partial t}p^c_{1,2,\mathbf{k}} = {} & (\tilde{\varepsilon}^c_{2,\mathbf{k}} - \tilde{\varepsilon}^c_{1,\mathbf{k}})p^c_{1,2,\mathbf{k}} + \frac{\partial}{\partial t}p^c_{1,2,\mathbf{k}}\Big|_{\mathrm{scatt}} \\ & + (f^{c1}_{\mathbf{k}} - f^{c2}_{\mathbf{k}})\Big[j^c_{2,1}A_{\mathrm{THz}} - \sum_{\mathbf{q}\neq\mathbf{k}} V_{\mathbf{k}-\mathbf{q}}p^c_{1,2,\mathbf{q}}\Big] \\ & + S^{\mathrm{coh}}_{\mathbf{k}}, \end{aligned} \quad (2)$$

where $\tilde{\varepsilon}^c_{l,\mathbf{k}}$ are the renormalized single-particle energies, $f^{c,l}_{\mathbf{k}}$ are the optically excited carrier distributions in the conduction bands, and $V_{\mathbf{q}}$ is the Coulomb matrix element. The term $\frac{\partial}{\partial t}p^c_{1,2,\mathbf{k}}|_{\mathrm{scatt}}$ formally contains all scattering effects and $S^{\mathrm{coh}}_{\mathbf{k}}$ includes the coupling to optically excited interband coherences via the Coulomb interaction. The scattering terms are modeled by a phenomenological dephasing constant γ to match the measured 440 fs decay, i.e., $\frac{\partial}{\partial t}p^c_{1,2,\mathbf{k}}|_{\mathrm{scatt}} \approx -i\gamma p^c_{1,2,\mathbf{k}}$. This approximation is justified since in our case, the intersubband transitions are not affected by excitonic effects due to large experimental linewidths (roughly 3.3 meV). For large time delays of optical pump and THz probe pulses, the optically excited coherences have decayed such that $S^{\mathrm{coh}}_{\mathbf{k}}$ does not contribute.

In our numerical evaluations, we compute the single-particle energies of the quantum-well system using standard $\mathbf{k}\cdot\mathbf{p}$ perturbation theory. For the THz response, we include the first two conduction subbands and the first heavy-hole and light-hole subband [Fig. 1(b)]. As input for the time-dependent fields, we use the experimental THz-pulse shapes of the reference pulse.

The theoretical results are superimposed to the experimental results in Fig. 2. The (red) solid line in Figs. 2(c) and 2(e) represents the absolute value of the computed current density, i.e., the differential transmission for the ps (c) and fs excitation (e). Figure 2(d) separates the two contributions J_{A} (dotted line) and J_{THz} (blue dashed line) to the total current for the case of ps excitation. The solid line in Fig. 2(f) shows the computed absorption spectrum.

In all cases, an excellent experiment-theory agreement is obtained.

As in the measurement, we clearly notice the double peaked Fano-like feature in the transmission spectra, whereas the absorption is only single peaked. In our theory, the origin of the Fano-like feature can be investigated looking at the individual contributions separately. J_A directly reflects the vector potential of the THz probe pulse while J_{THz} consists of the intersubband resonance weighted with the pulse spectrum. The broad feature in the transmission spectrum is a direct consequence of the broad probe pulse. The Fano-like line shape is caused by the phase sensitive superposition of the broad ponderomotive and the sharp intersubband contribution, $|J_{tot}| = |J_A + J_{THz}|$. A further analysis reveals that for frequencies smaller than $\nu_{1,2}$, both contributions partially compensate each other while they interfere constructively for larger frequencies. As for typical Fano situations, this kind of superposition leads to narrowing of the resonance at the low-frequency side and a broadening at the high-frequency side, resulting in the characteristic asymmetric Fano line shape. Since the ponderomotive current leads to a real-valued susceptibility, there is no Fano-like behavior in the THz absorption [Fig. 2(f)].

In order to explain the more pronounced ponderomotive feature in the fs experiment, we had to extend our model beyond the single-quantum-well response. Since the fs pump pulse is spectrally significantly broader than the line width of the 1s exciton resonance (18.2 meV vs 3.3 meV), some frequency components are transmitted through the quantum wells and excite carriers in the substrate. These carriers contribute to J_A but not to J_{THz}, since there are no subbands in bulk material. A quantitative investigation of the interband optical excitation shows that 46% of the pump pulse is transmitted through the quantum wells and absorbed by the substrate. Hence, the total carrier density (in the wells plus substrate) is 1.85 times larger than the density in the quantum wells alone. Since J_A is proportional to the carrier density, we can model the substrate contribution to the THz response simply by enhancing J_A relative to J_{THz} by 1.85. The resulting current density is shown as the red solid line in Fig. 2(e). In the ps experiment, substrate excitations can be neglected since only 1.4% of the pump pulse reaches the substrate.

In summary, we have shown how the emission by the ponderomotive motion of the excited carriers can directly be identified in the linear THz response. Using a microscopic theory for the THz response, the observed Fano-like features in the transmission spectrum can unambiguously be attributed to the phase sensitive superposition of the intersubband resonance and the ponderomotive carrier dynamics. Our results are connected to the typical Fano situation because the system has a sharp discrete intersubband resonance that interferes with a broad continuous contribution, i.e., the ponderomotive current density. However, one of the contributions in our case is nonabsorptive such that we do not observe the Fano resonance in the absorption spectrum but in the differential transmission spectrum only.

The authors from Forschungszentrum Dresden-Rossendorf are grateful to Dr. Stephan Winnerl for critical discussions. The Marburg work is supported by the Quantum Optics in Semiconductors DFG Research Group. The Vienna group is supported by the Austrian FWF.

*daniel.golde@physik.uni-marburg.de

[1] A. Bonvalet *et al.*, Phys. Rev. Lett. **76**, 4392 (1996).
[2] J. N. Heyman, R. Kersting, and K. Unterrainer, Appl. Phys. Lett. **72**, 644 (1998).
[3] R. Kersting *et al.*, Opt. Lett. **25**, 272 (2000).
[4] T. Müller *et al.*, Phys. Rev. B **70**, 155324 (2004).
[5] C. W. Luo *et al.*, Phys. Rev. Lett. **92**, 047402 (2004).
[6] R. H. M. Groeneveld and D. Grischkowsky, J. Opt. Soc. Am. B **11**, 2502 (1994).
[7] J. Cerne *et al.*, Phys. Rev. Lett. **77**, 1131 (1996).
[8] R. Huber *et al.*, Nature (London) **414**, 286 (2001).
[9] R. A. Kaindl *et al.*, Nature (London) **423**, 734 (2003).
[10] I. Galbraith *et al.*, Phys. Rev. B **71**, 073302 (2005).
[11] B. E. Cole *et al.*, Nature (London) **410**, 60 (2001).
[12] S. Leinß *et al.*, Phys. Rev. Lett. **101**, 246401 (2008).
[13] J. F. Dynes *et al.*, Phys. Rev. Lett. **94**, 157403 (2005).
[14] K. B. Nordstrom *et al.*, Phys. Rev. Lett. **81**, 457 (1998).
[15] A. H. Chin, J. M. Bakker, and J. Kono, Phys. Rev. Lett. **85**, 3293 (2000).
[16] J. B. Krieger and G. J. Iafrate, Phys. Rev. B **33**, 5494 (1986).
[17] F. Bloch, Z. Phys. **52**, 555 (1929).
[18] J. R. Danielson *et al.*, Phys. Rev. Lett. **99**, 237401 (2007).
[19] U. Fano, Phys. Rev. **124**, 1866 (1961).
[20] J. Faist *et al.*, Opt. Lett. **21**, 985 (1996).
[21] J. Faist *et al.*, Nature (London) **390**, 589 (1997).
[22] H. Schmidt *et al.*, Appl. Phys. Lett. **70**, 3455 (1997).
[23] H. C. Liu *et al.*, Appl. Phys. Lett. **91**, 131121 (2007).
[24] R. A. Kaindl *et al.*, Opt. Lett. **23**, 861 (1998).
[25] M. Helm, in *Semiconductors and Semimetals*, edited by H. C. Liu and F. Capasso (Academic Press, San Diego, 2000), Vol. 62, Chap. 1.
[26] K. Liu, J. Xu, and X.-C. Zhang, Appl. Phys. Lett. **85**, 863 (2004).
[27] C. Kübler *et al.*, Appl. Phys. Lett. **85**, 3360 (2004).
[28] R. A. Kaindl *et al.*, Phys. Rev. B **63**, 161308(R) (2001).
[29] M. Kira and S. W. Koch, Prog. Quantum Electron. **30**, 155 (2006).
[30] The electrons experience a wiggling motion also in the growth direction due to the tilting of the confinement potential.
[31] H. Haug and S. W. Koch, *Quantum Theory of the Optical and Electronic Properties of Semiconductors* (World Scientific, Singapore, 2009), 5th ed.

Paper VIII:
Journal of Physics: Coference Series 193, 012073 (2009)

Journal of Physics: Conference Series **193** (2009) 012073 doi:10.1088/1742-6596/193/1/012073

Fano profile in the intersubband terahertz response of photoexcited GaAs/AlGaAs quantum wells

M. Wagner[1], D. Golde[2], D. Stehr[1], H. Schneider[1], M. Helm[1], A. M. Andrews[3], T. Roch[3], G. Strasser[3], M. Kira[2], and S. W. Koch[2]

[1]Institute of Ion Beam Physics and Materials Research, Forschungszentrum Dresden-Rossendorf, P.O. Box 510119, 01314 Dresden, Germany
[2]Department of Physics and Material Sciences Center, Philipps-University, 35032 Marburg, Germany
[3]Micro- & Nanostructure Center, TU Wien, Floragasse 7, 1040 Vienna, Austria

E-mail: m.wagner@fzd.de

Abstract. In our work we probe the conduction intersubband transition of an undoped $GaAs/Al_{0.34}Ga_{0.66}As$ multiple quantum well via broadband terahertz pulses after resonant photoexcitation at the 1s heavy-hole exciton. The pump-induced change in the transmitted terahertz field shows a strong beating. In the frequency domain this results in an asymmetric Fano-like line shape for the intersubband resonance and an additional broad low-frequency peak. However, the total THz absorption shows only the single symmetric peak of the intersubband transition. In our microscopic theory these signatures unambiguously originate from the phase sensitive superposition of ponderomotive and terahertz intersubband currents.

1. Introduction

Terahertz (THz) spectroscopy on semiconductor heterostructures has revealed new insight in low-energy excitations and their dynamics. A microscopic analysis of these experiments has to take into account the true THz transitions, but also the so-called ponderomotive current. This current results from the classical, electric-field induced charge acceleration according to $\hbar\dot{\mathbf{k}} = -e\,\mathbf{E}_{\mathrm{THz}}$ [1] that causes a wiggling motion of the carriers. In recent experiments the influence of the ponderomotive current could only be seen rather indirectly [2, 3].
Here, we study the intersubband transition of multi quantum wells via THz spectroscopy and directly observe signatures of the ponderomotive current [4]. In the differential transmission spectra we measure a characteristic Fano-like line shape originating from the superposition of ponderomotive and true THz intersubband currents. Usually, asymmetric Fano line shapes result from the interference between a dicrete level and a continuum of states [5, 6].

2. Experimental

Spectrally broadband THz pulses are generated in a 55 μm thin z-cut GaSe crystal (see Fig. 1(a)) by phase-matched difference frequency mixing [7] within ultrashort 12 fs optical pulses from a 78 MHz Ti:sapphire oscillator (Femtolasers: Femtosource Scientific sPro). The THz beam is focused on the multi quantum well (MQW) sample. The THz field has a strong component normal to the MQW plane to couple to the intersubband transition. Phase-matched electro-optic sampling [8] allows for field-resolved detection in a second 30 μm thin z-cut GaSe crystal.

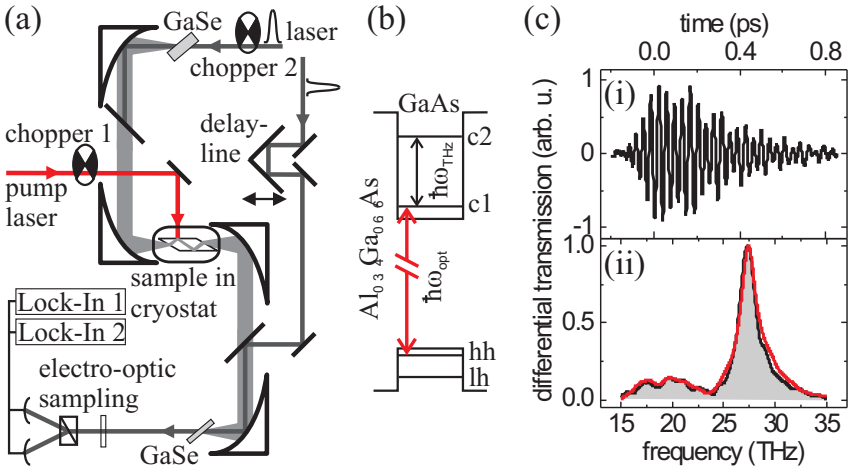

Figure 1. (a) Optical interband pump intersubband THz probe experiment. (b) THz pulses probe the c1-to-c2 transition after photoexcitation of the hh-c1 transition in the MQW. (c)(i) Time-resolved differential transmission after ps excitation. (c)(ii) Measured (shaded area) and computed (red line) spectral amplitude.

The MQW sample consists of 60 8.2-nm-thick undoped GaAs quantum wells, separated by 19.6-nm-thick barriers of $Al_{0.34}Ga_{0.66}As$. It was prepared as a 38-degree wedged waveguide and an $Al_{0.34}Ga_{0.66}As$ spacer layer of 300 nm thickness was grown on top for improved overlap of THz beam and MQWs. It was kept at a temperature of 6 K in a liquid He flow cryostat.

For photoexcitation (see Fig. 1(b)) an optical interband pump pulse either from a spectrally narrow 2.5 ps or a broad-band 100 fs 78 MHz laser (both Spectra Physics: Tsunami) excites the MQWs resonantly at the $1s$ heavy-hole exciton around $\hbar\omega_{opt} = 1.56$ eV. Only the first conduction subband is populated. The c1-to-c2 intersubband transition is then probed by THz pulses 25 ps after excitation. The photoexcited carrier density is around 2×10^{10} cm^{-2} per quantum well.

The transmitted THz transients with and without excitation are simultaneously measured. To this end both pump and THz probe beams are chopped at the same time at different frequencies. The first Lock-In amplifier locks on the modulation of the optical pump beam. Twice its signal yields the differential transmission $\Delta E(t)$, i.e. the pump-induced change in the transmitted THz field. The second Lock-In amplifier detects the mean value between transmission with and without excitation. The reference $E_{\rm ref}(t)$ without excitation follows by subtracting $\frac{1}{2}\Delta E(t)$.

3. Results

After ps photoexcitation the time-resolved differential transmission $\Delta E(t)$ shows a strong beating (Fig. 1(c)(i)), superimposed on the dephasing of a reradiated THz-induced intersubband polarization [9]. The beating is connected to a broad low-frequency peak around 20 THz in the spectral amplitude $|\Delta E(\omega)|$ (Fig. 1(c)(ii)) while the intersubband resonance at 27.3 THz displays a Fano-like asymmetry with an undershoot at the low-frequency side.

To explain our experimental findings, the THz transmission of a quantum well positioned at $z = 0$ is computed (z is the growth direction). The THz response follows from the wave equation $\left(\nabla^2 - (\frac{n_b}{c})^2 \frac{\partial^2}{\partial t^2}\right) E(\mathbf{r},t) = \mu_0 \delta(z) \frac{\partial}{\partial t} \left(J_{\rm A}(t) + J_{\rm THz}(t)\right)$ (n_b is the background refractive index). Here a delta function is used since the quantum well width is much smaller than the THz wavelength. On the right hand side of the equation the induced current density contains $J_{\rm THz}$, the current due to the intersubband transition, and $J_{\rm A}$, the THz field induced ponderomotive motion of the excited carriers. The solution yields the differential transmission $\Delta E \propto J_{\rm A} + J_{\rm THz}$, which can be interpreted as a field reemitted by the current density that is directly proportional to the induced current [10].

$J_{\rm A}$ is defined via $J_{\rm A} = -\sum_\lambda (e^2 n_\lambda / m_\lambda) A_{\rm THz}$ with the effective mass m_λ and the carrier density n_λ in band λ (λ includes both bulk-band index and subband index). The vector potential $A_{\rm THz}$ of the THz probe pulse is given by $E_{\rm THz} = -\frac{\partial}{\partial t} A_{\rm THz}$. Thus, $J_{\rm A}$ directly follows $A_{\rm THz}$ with an

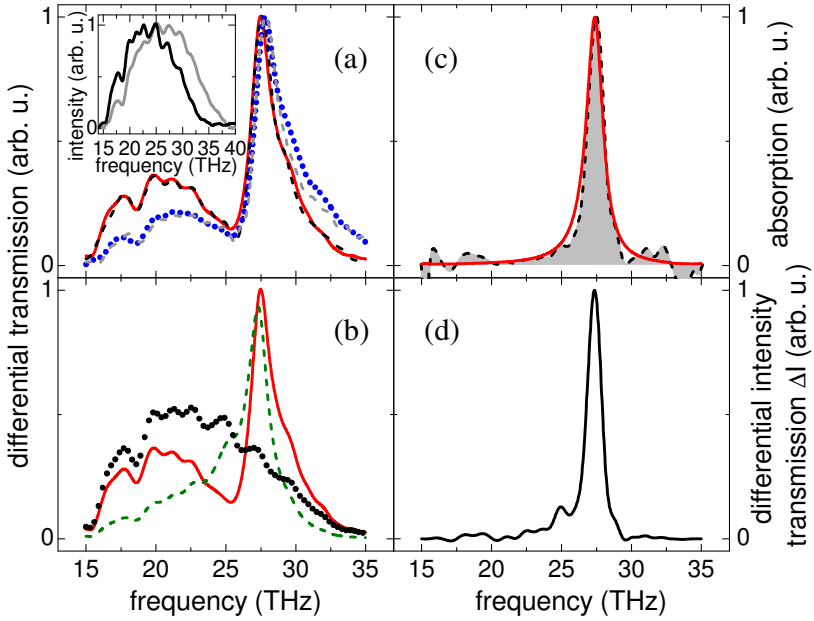

Figure 2. Experiment-theory comparison for fs excitation. (a) Measured (black and grey dashed line, resp.) and computed (red solid and blue dotted line, resp.) differential transmission for two different THz probe spectra (inset). (b) Decomposition of the computed current density (red solid line) into ponderomotive contribution $|J_{\mathrm{A}}|$ (black dotted line) and intersubband current $|J_{\mathrm{THz}}|$ (green dashed line). (c) Measured (shaded area) and computed (red line) THz absorption. (d) Simulated differential intensity change ΔI.

opposite phase. Since J_{A} leads to a real-valued linear susceptibility $\chi_{\mathrm{A}}(\omega) = -\omega_p^2/\omega^2$ (with the plasma frequency ω_p), it does not contribute to the absorption $\alpha(\omega) \propto \omega\,\mathrm{Im}[\chi(\omega)]$.

The THz current is given by $J_{\mathrm{THz}} = \frac{1}{S}\sum_{\lambda,l,l',\mathbf{k}} j^{\lambda}_{l',l}\, p^{\lambda}_{l,l',\mathbf{k}}$ with the quantization area S, the matrix elements $j^{\lambda}_{l,l'}$ and the microscopic intersubband polarization $p^{\lambda}_{l,l',\mathbf{k}}$ between subbands l and l' of bulk band λ. $j^{\lambda}_{l,l'} = -\frac{i\hbar e}{m_\lambda}\int \mathrm{dz}\, \xi^*_{\lambda,\mathrm{l}}(\mathrm{z})\, \frac{\partial}{\partial \mathrm{z}} \xi_{\lambda,l'}(\mathrm{z})$ is the intersubband matrix element with the confinement wave function of the carriers $\xi_{\lambda,l}(z)$. $p^{\lambda}_{l,l',\mathbf{k}}$ is computed microscopically with an equation-of-motion approach. Regarding only the c1-to-c2 transition, the sum is restricted to $\lambda = c$ and $l, l' \in \{1, 2\}$. In analogy to the semiconductor Bloch equations [11], one finds for $p^{c}_{1,2,\mathbf{k}}$: $i\hbar \frac{\partial}{\partial t} p^{c}_{1,2,\mathbf{k}} \approx \left(\tilde{\varepsilon}^{c}_{2,\mathbf{k}} - \tilde{\varepsilon}^{c}_{1,\mathbf{k}}\right) p^{c}_{1,2,\mathbf{k}} - i\gamma\, p^{c}_{1,2,\mathbf{k}} + (f^{c1}_{\mathbf{k}} - f^{c2}_{\mathbf{k}}) \left[j^{c}_{2,1} A_{\mathrm{THz}} - \sum_{\mathbf{q}\neq\mathbf{k}} V_{\mathbf{k}-\mathbf{q}}\, p^{c}_{1,2,\mathbf{q}}\right]$, with the renormalized single-particle energies $\tilde{\varepsilon}^{c}_{l,\mathbf{k}}$, the optically excited carrier distributions $f^{c,l}_{\mathbf{k}}$ in the conduction bands and the Coulomb matrix element $V_{\mathbf{q}}$. Optically excited interband coherences have already decayed and do not contribute. All scattering effects are modeled by a phenomenological dephasing constant γ to match the measured 440 fs decay.

We compute the single-particle energies via $\mathbf{k}\cdot\mathbf{p}$-perturbation theory. For the THz-response, we include the first two conduction subbands and the first heavy-hole and light-hole subband. The experimental THz reference transient serves as input for the time-dependent fields.

For ps excitation (Fig. 1(c)(ii)) the theoretical result (red line) as the absolute value of the computed current density, i. e. the differential transmission $|\Delta E(\omega)|$, is in excellent agreement with the measurement (shaded area). In the case of broadband fs excitation the low-frequency peak and the Fano-like asymmetry of the intersubband resonance are enhanced (Fig. 2(a), measured: black dashed line; computed: red solid line). These features are also affected by the THz probe spectrum. Shifting its center away from the previous 23.5 THz (Fig. 2(a) inset, black line) to 26.5 THz (inset, grey line) decreases the broad low-frequency peak while the asymmetry of the resonance increases (Fig. 2(a), measured: grey dashed line; computed: blue dotted line). In Fig. 2(b) the total current density for the low-frequency THz probe spectrum (red solid line) is broken up in its individual contributions, i. e. the ponderomotive current density J_{A} (black dotted line) and the intersubband current J_{THz} (green dashed line). J_{A} follows mainly the THz probe spectrum, while J_{THz} contains the intersubband resonance weighted with the THz probe

spectrum. The observed Fano-like line shape in the differential transmission results from a phase sensitive superposition of J_{A} and J_{THz}: $|J_{\mathrm{total}}| = |J_{\mathrm{A}} + J_{\mathrm{THz}}|$. Below the intersubband resonance both contributions partially compensate each other whereas they interfere constructively above. Thus, the resonance is narrowed at the low-frequency side and broadened at the high-frequency side, leading to an asymmetric Fano-like line shape. By shifting the THz probe spectrum mainly J_{A} is affected and shifted accordingly, explaining the observed behavior in Fig. 2(a). However, there is no Fano signature in the THz absorption $\alpha(\omega) = 2\mathrm{Im}[-\mathrm{i}\Delta\mathrm{E}(\omega)/\mathrm{E}_{\mathrm{ref}}(\omega)]$ (Fig. 2(c), shown for the low-frequency THz spectrum).

In the case of fs excitation we saw an enhanced ponderomotive contribution. The fs pulses are spectrally broader than the linewidth of the 1s exciton resonance and thus they are partially (46 %) transmitted through the quantum well film and absorbed in the GaAs substrate. Since the ponderomotive current J_{A} is proportional to the carrier density, J_{A} is increased, but not J_{THz}. Consequently the carrier density in the wells plus substrate is 1.85 times larger than in the wells alone, which can be modeled by increasing J_{A} relative to J_{THz} by 1.85.

It would be interesting to check whether the ponderomotive contribution could be seen in standard Fourier transform infrared (FTIR) spectroscopy while modulating the carrier density, e.g. by photoexcitation. Since FTIR spectroscopy detects only intensities one would record a differential intensity change $\Delta I(\omega)$ of the transmission without and with excitation, respectively, of the form $\Delta I(\omega) = I_{\mathrm{without\,exc.}}(\omega) - I_{\mathrm{with\,exc.}}(\omega) \propto |E_{\mathrm{ref}}(\omega)|^2 - |E_{\mathrm{ref}}(\omega) + \Delta E(\omega)|^2$. In the case of fs photoexcitation Fig. 2(d) presents the simulation of $\Delta I(\omega)$ based on our field-resolved data for $E_{\mathrm{ref}}(t)$ and $\Delta E(t)$. It turns out that the ponderomotive contribution has vanished almost completely compared to a field-resolved measurement.

4. Summary

In summary, we have observed strong Fano signatures in the differential transmission spectra of broadband THz pulses probing an undoped GaAs/AlGaAs multiple quantum well after resonant photoexcitation. In our microscopic theory, the Fano-like line shape of the intersubband resonance is unambiguously attributed to a phase sensitive interference of the sharp intersubband resonance with the effective continuum provided by the light-matter interaction through the ponderomotive contribution. Finally, the applied field-resolved method is better suited than intensity-based measurements for revealing the ponderomotive influence to the THz response.

Acknowledgments

The authors from Forschungszentrum Dresden-Rossendorf are grateful to Dr. Stephan Winnerl for critical discussions. The Marburg work is supported by the Quantum Optics in Semiconductors DFG Research Group. The Vienna group is supported by the Austrian FWF.

References

[1] Krieger J B and Iafrate G J 1986 *Phys. Rev.* B **33** 5494
[2] Danielson J R, Lee Y-S, Prineas J P, Steiner J T, Kira M and Koch S W 2007 *Phys. Rev. Lett.* **99** 237401
[3] Leinß S, Kampfrath T, Volkmann K v, Wolf M, Steiner J T, Kira M, Koch S W, Leitenstorfer A and Huber R 2008 *Phys. Rev. Lett.* **101** 246401
[4] Golde D, Wagner M, Stehr D, Schneider H, Helm M, Andrews A M, Roch T, Strasser G, Kira M and Koch S W 2009 *Phys. Rev. Lett.* **102** 127403
[5] Fano U 1961 *Phys. Rev.* **124** 1866
[6] Faist J, Sirtori C, Capasso F, Chu S-N G, Pfeiffer L N and West K W 1996 *Opt. Lett.* **21** 985
[7] Kaindl R A, Smith D C, Joschko M, Hasselbeck M P, Woerner M and Elsaesser T 1998 *Opt. Lett.* **23** 861
[8] Kübler C, Huber R, Tübel S and Leitenstorfer A 2004 *Appl. Phys. Lett.* **85** 3360
[9] Heyman J N, Kersting R and Unterrainer K 1998 *Appl. Phys. Lett.* **72** 644
[10] Kira M and Koch S W 2006 *Prog. Quantum Electron.* **30** 155
[11] Haug H and Koch S W 2004 *Quantum Theory of the Optical and Electronic Properties of Semiconductors* 5th ed. (Singapore: World Scientific)

Paper IX:
Proc. SPIE 7600, 76000F (2010)

Ultrafast terahertz response of optically excited semiconductor heterostructures

D. Golde, M. Kira, and S. W. Koch

Department of Physics and Materials Sciences Center, Philipps-University, Renthof 5, 35032 Marburg, Germany

ABSTRACT

A microscopic theory for the terahertz response of a semiconductor quantum well under coherent conditions is presented. It is shown that excitonic effects influence the intersubband absorption under certain conditions. For high-quality samples, one should be able to resolve both band-to-band and excitonic intersubband transitions in an terahertz absorption measurement. Due to the competition of intersubband transitions and classical field-induced carrier accelerations, an unexpected Fano feature is observed in the terahertz spectra. This result is in excellent agreement with recent measurements.

Keywords: THz response, Intersubband transitions, Fano resonance, quantum wells

1. INTRODUCTION

In recent years, terahertz (THz) spectroscopy has become a powerful tool to detect and analyze quasiparticle states[1–5] like excitons or plasmons in semiconductors. This technique has also been applied to analyze intersubband transitions[6–10] in systems with reduced dimensionality. The microscopic analysis of strong-field THz experiments[11,12] has shown that the THz response of semiconductor nanostructures is strongly influenced by field-induced accelerations[13] of the excited carriers. This contribution can often be neglected in optical spectroscopy but becomes important for low-energy excitations even at the lowest field intensities.

In this paper, we present our microscopic theory for the ultrafast linear THz response of an optically excited semiconductor quantum well (QW). We concentrate on ultrashort timescales directly after the optical excitation when the interband coherences are still present. It is shown that the THz field can interact in multiple ways with the electrons in the quantum well. In Sec. 3, we apply our theory to analyze excitonic effects in the intersubband transitions between the two lowest conduction subbands. For narrow absorption lines, two distinct resonances are obtained that can be attributed to free-carrier and excitonic transitions. In Sec. 4, a Fano-like resonance that is observed in the differential THz transmission is discussed. We show that this Fano feature occurs due to the interference of intersubband transitions and classical carrier accelerations. This situation is very similar to a typical Fano scenario where a transition continuum is coupled to a discrete transition that is energetically embedded in the continuum.

2. THEORY: THZ RESPONSE OF A MULTISUBBAND SYSTEM

In this section, we present a microscopic theory for the THz response and the optical excitation of a QW. In contrast to the bulk case, the QW electrons can move freely only in two dimension but are confined in one direction (the growth direction). In analog to the particle in a box problem, the motion in the confinement direction is quantized, i.e., the energy related to this motion takes only discrete values. This leads to a splitting of the energy bands into multiple subbands.[14] Hence, a QW Bloch state $|\lambda, n, \mathbf{k}\rangle$ is characterized by three quantum numbers: the so-called bulk band λ, the subband n, and the crystal momentum $\mathbf{k}$. All of these quantum numbers give rise to a light-matter interaction process as we will show in the following sections.

Further author information: (Send correspondence to D. Golde)
E-mail: daniel.golde@physik.uni-marburg.de

2.1 Hamiltonian

We start the presentation of our theory with a detailed discussion of the system Hamiltonian.[14,15] For the sake of clarity, we separate the Hamilton operator into three parts

$$H = H_0 + H_\mathrm{C} + H_\mathrm{l-m} \tag{1}$$

that contain the motion of the electrons in the crystal potential (H_0), the Coulomb interaction among the electrons (H_C), and the light-matter coupling ($H_\mathrm{l-m}$). In the light-matter interaction, we include both optical and THz excitations. In this paper, we do not account for other contributions like lattice vibrations or disorder effects.

As usual in semiconductor theory, we use the Bloch basis to express the operators in terms of creation and annihilation operators $a^\dagger_{\lambda,n,\mathbf{k}}$ and $a_{\lambda,n,\mathbf{k}}$, respectively. In this formalism, the explicit form of the free-particle Hamiltonian is given by

$$H_0 = \sum_{\lambda,\mathbf{k}} \varepsilon^\lambda_{n,\mathbf{k}}\, a^\dagger_{\lambda,n,\mathbf{k}} a_{\lambda,n,\mathbf{k}}, \tag{2}$$

where $\varepsilon^\lambda_{n,\mathbf{k}}$ are the single-particle energies of the electrons. The Coulomb interaction casts into

$$H_\mathrm{C} = \frac{1}{2} \sum_{\substack{\mathbf{k},\mathbf{k}',\mathbf{q}\neq 0 \\ \lambda,\lambda',n,n'}} V^{\lambda,\lambda'}_{n,n',\mathbf{q}}\, a^\dagger_{\lambda,n,\mathbf{k}} a^\dagger_{\lambda',n',\mathbf{k}'} a_{\lambda',n',\mathbf{k}'+\mathbf{q}} a_{\lambda,n,\mathbf{k}-\mathbf{q}} \tag{3}$$

with the Coulomb matrix element

$$V^{\lambda,\lambda'}_{n,n',\mathbf{q}} = \frac{e^2}{2\epsilon_0\epsilon_r \mathcal{S}|\mathbf{q}|} \iint_{-\infty}^{\infty} \mathrm{d}z\, \mathrm{d}z'\, |\xi_{\lambda,n}(z)|^2\, |\xi_{\lambda',n'}(z')|^2\, \mathrm{e}^{-|\mathbf{q}(z-z')|}. \tag{4}$$

Here, ϵ_r is the static background dielectric constant, $\mathcal{S}$ is the quantization area of the quantum well, and z is the spatial coordinate that points in growth direction. The so-called confinement functions $\xi_{\lambda,n}(z)$ are the z-dependent part of the envelope wave functions.

The coupling of the light field to the QW gives rise to various electronic transitions namely interband transitions between different bulk bands ($\lambda \leftrightarrow \lambda'$), intersubband transitions ($n \leftrightarrow n'$) within the same bulk band, and intraband transitions. Thus, we have three contributions to the light-matter Hamiltonian

$$H_\mathrm{l-m} = H_\mathrm{inter} + H_\mathrm{intersub} + H_\mathrm{intra}. \tag{5}$$

For typical III-IV semiconductors, the interband transitions are resonant to optical fields with photon energies of few eV while intersubband and intraband transitions have energies in the range of several meV. Since we want to study both optical and THz excitations, it is convenient to separate the total electric according to

$$\mathbf{E}(t) = \mathbf{E}_\mathrm{opt}(t) + \mathbf{E}_\mathrm{THz}(t), \tag{6}$$

such that E_opt enters only H_inter while E_THz contributes exclusively to H_intersub and H_intra. With these assumptions, the interband part of the Hamiltonian is given by

$$H_\mathrm{inter} = -E_\mathrm{opt}(t) \sum_{\substack{\lambda,\lambda',\mathbf{k} \\ n,n'}} d^{\lambda,\lambda'}_{n,n'}(\mathbf{k})\, a^\dagger_{\lambda,n,\mathbf{k}} a_{\lambda',n',\mathbf{k}}. \tag{7}$$

The dipole matrix element follows from the electronic wave functions via

$$d^{\lambda,\lambda'}_{n,n'}(\mathbf{k}) = \left(\int_{-\infty}^{\infty} \mathrm{d}z\, \xi^*_{\lambda,n}(z)\, \xi_{\lambda',n'}(z) \right) \int_\Omega \mathrm{d}^3 r\; u^*_{\lambda,n,\mathbf{k}}(\mathbf{r})\, (-e\, \mathbf{e}_\mathrm{P,opt} \cdot \mathbf{r})\, u_{\lambda',n',\mathbf{k}}(\mathbf{r}), \tag{8}$$

where $u_{\lambda,n,\mathbf{k}}(\mathbf{r})$ is the lattice-periodic Bloch function, Ω is the Volume of the unit cell, and $\mathbf{e}_\mathrm{P,opt}$ is the polarization vector of the optical field.

In order to model the THz excitations, we use the $\mathbf{p}\cdot\mathbf{A}$ picture of the light-matter interaction, i.e., we express the THz field via its vector potential $\mathbf{A}_{\mathrm{THz}}$ with $\mathbf{E}_{\mathrm{THz}} = -\frac{\partial \mathbf{A}_{\mathrm{THz}}}{\partial t}$ and $\nabla\cdot\mathbf{A}_{\mathrm{THz}} = 0$ (Coulomb gauge). In this representation, the intersubband Hamiltonian reads

$$H_{\mathrm{intersub}} = A_{\mathrm{THz}}(t) \sum_{\lambda,n,n',\mathbf{k}} \mu^{\lambda}_{n,n'}\, a^{\dagger}_{\lambda,n,\mathbf{k}} a_{\lambda,n',\mathbf{k}} \tag{9}$$

with the intersubband matrix element

$$\mu^{\lambda}_{n,n'} = -\frac{\mathrm{i}\hbar e}{m_{\lambda}} \left(\mathbf{e}_{\mathrm{P,THz}}\cdot\mathbf{e}_z\right) \int_{-\infty}^{\infty} \mathrm{d}z\, \xi^{*}_{\lambda,n}(z)\, \frac{\mathrm{d}}{\mathrm{d}z}\xi_{\lambda,n'}(z). \tag{10}$$

Obviously, only the z-component of the THz field can induce intersubband transitions. Finally, the intraband part is given by

$$H_{\mathrm{intra}} = -A_{\mathrm{THz}}(t) \sum_{\lambda,n,\mathbf{k}} j^{\lambda}_{n}(\mathbf{k})\, a^{\dagger}_{\lambda,n,\mathbf{k}} a_{\lambda,n,\mathbf{k}}\ , \tag{11}$$

where

$$j^{\lambda}_{n}(\mathbf{k}) = -\frac{e}{\hbar}\, \mathbf{e}_{\mathrm{P,THz}}\cdot\nabla_{\mathbf{k}}\varepsilon^{\lambda}_{n,\mathbf{k}} \tag{12}$$

is the intraband matrix element. The most prominent process of this part of the light-matter interaction are the intra excitonic transitions,[15–17] i.e., transitions from one excitonic state (e.g. $1s$) to another one (e.g. $2p$) within the same band.

2.2 THz response

The electrodynamic response of the quantum well to the THz field follows from Maxwell's equations. For homogeneous excitation and propagation perpendicular to the QW plane, the wave equation for the vector potential reads

$$\left[\frac{\partial^2}{\partial z^2} - \frac{n_b^2}{c^2}\frac{\partial^2}{\partial t^2}\right] A_{\mathrm{THz}}(z,t) = -\frac{1}{\epsilon_0 c^2} J(z,t), \tag{13}$$

where n_b is the background refractive index (assumed to be identical for the quantum well and the surrounding material), c is the speed of light, and $J(z,t)$ is the current density. Since only the quantum well is excited but not the barriers, the current density is nonzero in the quantum-well plane only. Due to the small QW width compared to the wavelength of the THz field, we can make the following ansatz for the z-dependence of the current density: $J(z,t) = \delta(z)\, J(t)$. Here, $J(t)$ is the expectation value of the QW current density operator. With this assumption, the wave equation, Eq. (13), can be solved analytically[15] and one finds for the reflected and transmitted electric fields at the quantum-well position

$$E_{\mathrm{R}}(\omega) = -\frac{1}{2n_b\epsilon_0 c}\, J(\omega), \tag{14}$$

$$E_{\mathrm{T}}(\omega) = E_0(\omega) - \frac{1}{2n_b\epsilon_0 c}\, J(\omega), \tag{15}$$

where E_0 is the incoming electric field. In linear response, we can introduce the susceptibility in the usual way $J(\omega) = -\mathrm{i}\epsilon_0\omega\chi(\omega)E_{\mathrm{T}}(\omega) = \epsilon_0\chi(\omega)\omega^2 A_{\mathrm{T}}(\omega)$ where A_{T} is the vector potential of the transmitted THz field. The total absorption of the quantum well can then be calculated via[15]

$$\alpha(\omega) = \frac{\omega}{n_b c}\, \mathrm{Im}[\chi(\omega)]. \tag{16}$$

The current density can be expressed in terms of carrier occupations $f^{\lambda}_{n,\mathbf{k}} = \langle a^{\dagger}_{\lambda,n,\mathbf{k}} a_{\lambda,n,\mathbf{k}}\rangle$ and microscopic intersubband polarizations $p^{\lambda}_{nn',\mathbf{k}} = \langle a^{\dagger}_{\lambda,n,\mathbf{k}} a_{\lambda,n',\mathbf{k}}\rangle$. For later reference, we split the total current into three parts

$$J = J_{\mathrm{intra}} + J_{\mathrm{intersub}} + J_{\mathrm{pond}} \tag{17}$$

with

$$J_{\text{intra}} = \sum_{\lambda,n,\mathbf{k}} j_n^{\lambda}(\mathbf{k})\, f_{n,\mathbf{k}}^{\lambda}, \tag{18}$$

$$J_{\text{intersub}} = -\sum_{\lambda,n,n',\mathbf{k}} \mu_{n,n'}^{\lambda} p_{nn',\mathbf{k}}^{\lambda}, \tag{19}$$

$$J_{\text{pond}} = -A_{\text{THz}} \sum_{\lambda,n} \frac{e^2 n_{\lambda,n}}{m_{\lambda,n}}, \tag{20}$$

where $n_{\lambda,n}$ is the carrier density in band λ, subband n and $m_{\lambda,n}$ is the effective mass of this band. The first two contributions to the current, Eqs. (18) and (19), are the responses from intraband and intersubband transitions. The third term, Eq. (20), is the so-called ponderomotive current that comes from the classical acceleration of the carriers in the THz field. Here, the (sub-) band sums include only partially filled bands.[18] For non-parabolic bands, the effective mass is $\mathbf{k}$-dependent and one has to use the generalized form $J_{\text{pond}} = -\frac{A_{\text{THz}}}{\mathcal{S}} \sum_{\lambda,n,\mathbf{k}} \frac{e^2 f_{n,\mathbf{k}}^{\lambda}}{m_{\lambda,n}(\mathbf{k})}$.

2.3 Equations of motion

According to Eqs. (18)-(20), the calculation of the THz response requires complete knowledge about the carrier occupations and the intersubband polarizations. We solve the dynamics of these quantities using an equation-of-motion approach.[14] This means that we evaluate Heisenberg's equation of motion

$$\mathrm{i}\hbar \frac{\mathrm{d}}{\mathrm{d}t} \langle \mathcal{O} \rangle = \langle [\mathcal{O}, H] \rangle \tag{21}$$

for all relevant quantities ($\mathcal{O}$ is an arbitrary operator). It turns out that the equations of motion for the occupations and the intersubband polarizations couple to interband polarizations $p_{nn',\mathbf{k}}^{\lambda,\lambda'} = \langle a_{\lambda,n,\mathbf{k}}^{\dagger} a_{\lambda',n',\mathbf{k}} \rangle$ via light-matter and Coulomb interaction. Furthermore, the Coulomb interaction couples these quantities to other quantities that consist of four creation and annihilation operators, and these again couple to six-operator quantities and so on. We truncate this infinite hierarchy of equations at Hartree-Fock level, i.e., we factorize all four-operator quantities into two-operator quantities to obtain a closed set of differential equations.[14]

In the analysis presented here, only three bulk bands are taken into account: one conduction band, the heavy-hole band, and the light-hole band. Each of these bands might have a formally arbitrary number of subbands. As usual, we derive the equations of motion in the electron-hole picture, i.e., instead of counting valence-band electrons, we count missing electrons in the valence bands, the so-called holes. Their occupation in hole band λ_h is given by $f_{n,\mathbf{k}}^{\lambda_h} = 1 - f_{n,\mathbf{k}}^{\lambda_v}$ where $f_{n,\mathbf{k}}^{\lambda_v}$ is the corresponding valence-band electron occupation. Apart from that, we have to introduce the energy of the holes $\varepsilon_{n,\mathbf{k}}^{\lambda_h} = -\varepsilon_{n,\mathbf{k}}^{\lambda_v}$ which implies a sign change in the intraband matrix elements, Eq. (12), as well. In all other quantities, we simply replace the valence-band index by a hole band index $\lambda_h \in \{hh, lh\}$. Additionally, the conduction band is denoted by index e. In this notation, the complete set of equations is given by

$$\begin{aligned}
\mathrm{i}\hbar \dot{p}_{mn,\mathbf{k}}^{\lambda_h,e} = {} & (\tilde{\varepsilon}_{n,\mathbf{k}}^{e} + \tilde{\varepsilon}_{m,\mathbf{k}}^{\lambda_h} - \mathrm{i}\gamma) p_{mn,\mathbf{k}}^{\lambda_h,e} - (1 - f_{n,\mathbf{k}}^{e} - f_{m,\mathbf{k}}^{\lambda_h}) \hbar\Omega_{mn,\mathbf{k}}^{\lambda_h,e} + \sum_{l \neq n} p_{ln,\mathbf{k}}^{e} \hbar\Omega_{ml,\mathbf{k}}^{\lambda_h,e} - \sum_{l \neq m} p_{ml,\mathbf{k}}^{\lambda_h} \hbar\Omega_{ln,\mathbf{k}}^{\lambda_h,e} \\
& - \sum_{l} p_{ml,\mathbf{k}}^{\lambda_h,\bar{\lambda}_h} \hbar\Omega_{ln,\mathbf{k}}^{\bar{\lambda}_h,e} - \sum_{l} p_{ln,\mathbf{k}}^{\bar{\lambda}_h,e} \sum_{\mathbf{q} \neq \mathbf{k}} V_{ml,\mathbf{k}-\mathbf{q}}^{\lambda_h,\bar{\lambda}_h} p_{ml,\mathbf{q}}^{\lambda_h,\bar{\lambda}_h} \\
& + \sum_{l \neq n} p_{ml,\mathbf{k}}^{\lambda_h,e} \left[\mu_{n,l}^{e} A_{\text{THz}}(t) - \sum_{\mathbf{q} \neq \mathbf{k}} V_{ln,\mathbf{k}-\mathbf{q}}^{e,e} p_{ln,\mathbf{q}}^{e} \right] + \sum_{l \neq m} p_{ln,\mathbf{k}}^{\lambda_h,e} \left[\mu_{l,m}^{e} A_{\text{THz}}(t) - \sum_{\mathbf{q} \neq \mathbf{k}} V_{ln,\mathbf{k}-\mathbf{q}}^{e,e} p_{ml,\mathbf{q}}^{e} \right] \\
& - j_{m,n}^{\lambda_h,e}(\mathbf{k})\, A_{\text{THz}}(t)\, p_{mn,\mathbf{k}}^{\lambda_h,e} \,,
\end{aligned} \tag{22}$$

$$
\begin{aligned}
\mathrm{i}\hbar\dot{p}^{\lambda_h,\bar{\lambda}_h}_{mn,\mathbf{k}} &= (\tilde{\varepsilon}^{\lambda_h}_{m,\mathbf{k}} - \tilde{\varepsilon}^{\bar{\lambda}_h}_{n,\mathbf{k}} - \mathrm{i}\gamma)p^{\lambda_h,\bar{\lambda}_h}_{mn,\mathbf{k}} + \sum_l (p^{\bar{\lambda}_h,e}_{nl,\mathbf{k}})^* \hbar\Omega^{\lambda_h,e}_{ml,\mathbf{k}} - \sum_l p^{\lambda_h,e}_{ml,\mathbf{k}} (\hbar\Omega^{\bar{\lambda}_h,e}_{nl,\mathbf{k}})^* \\
&\quad - \sum_{l\neq m} p^{\lambda_h}_{ml,\mathbf{k}} \sum_{\mathbf{q}\neq\mathbf{k}} V^{\lambda_h,\bar{\lambda}_h}_{ln,\mathbf{k}-\mathbf{q}} p^{\lambda_h,\bar{\lambda}_h}_{ln,\mathbf{q}} + \sum_{l\neq n} p^{\bar{\lambda}_h}_{ln,\mathbf{k}} \sum_{\mathbf{q}\neq\mathbf{k}} V^{\lambda_h,\bar{\lambda}_h}_{ml,\mathbf{k}-\mathbf{q}} p^{\lambda_h,\bar{\lambda}_h}_{ml,\mathbf{q}} \ , \\
&\quad + (f^{\lambda_h}_{m,\mathbf{k}} - f^{\bar{\lambda}_h}_{n,\mathbf{k}}) \sum_{\mathbf{q}\neq\mathbf{k}} V^{\lambda_h,\bar{\lambda}_h}_{mn,\mathbf{k}-\mathbf{q}} p^{\lambda_h,\bar{\lambda}_h}_{mn,\mathbf{q}} \\
&\quad + \sum_l p^{\lambda_h,\bar{\lambda}_h}_{ml,\mathbf{k}} \left[\mu^{\bar{\lambda}_h}_{n,l} A_{\mathrm{THz}}(t) - \sum_{\mathbf{q}\neq\mathbf{k}} V^{\bar{\lambda}_h,\bar{\lambda}_h}_{ln,\mathbf{k}-\mathbf{q}} p^{\bar{\lambda}_h,e}_{ln,\mathbf{q}} \right] - \sum_l p^{\lambda_h,\bar{\lambda}_h}_{ln,\mathbf{k}} \left[\mu^{\lambda_h}_{l,m} A_{\mathrm{THz}}(t) - \sum_{\mathbf{q}\neq\mathbf{k}} V^{\lambda_h,\lambda_h}_{ml,\mathbf{k}-\mathbf{q}} p^{\lambda_h}_{ml,\mathbf{q}} \right] \\
&\quad - j^{\lambda_h,\bar{\lambda}_h}_{m,n}(\mathbf{k}) A_{\mathrm{THz}}(t)\, p^{\lambda_h,\bar{\lambda}_h}_{mn,\mathbf{k}}
\end{aligned} \tag{23}
$$

$$
\begin{aligned}
\mathrm{i}\hbar\dot{p}^{e}_{mn,\mathbf{k}} &= (\tilde{\varepsilon}^{e}_{n,\mathbf{k}} - \tilde{\varepsilon}^{e}_{m,\mathbf{k}} - \mathrm{i}\gamma)p^{e}_{mn,\mathbf{k}} + \sum_{\lambda_h,l} p^{\lambda_h,e}_{ln,\mathbf{k}} (\hbar\Omega^{\lambda_h,e}_{lm,\mathbf{k}})^* - \sum_{\lambda_h,l} (p^{\lambda_h,e}_{lm,\mathbf{k}})^* \hbar\Omega^{\lambda_h,e}_{ln,\mathbf{k}} \\
&\quad + (f^{e}_{m,\mathbf{k}} - f^{e}_{n,\mathbf{k}}) \left[\mu^{e}_{n,m} A_{\mathrm{THz}}(t) - \sum_{\mathbf{q}\neq\mathbf{k}} V^{e,e}_{mn,\mathbf{k}-\mathbf{q}} p^{e}_{mn,\mathbf{q}} \right] \\
&\quad + \sum_{l\neq m} p^{e}_{ml,\mathbf{k}} \left[\mu^{e}_{n,l} A_{\mathrm{THz}}(t) - \sum_{\mathbf{q}\neq\mathbf{k}} V^{e,e}_{ln,\mathbf{k}-\mathbf{q}} p^{e}_{ln,\mathbf{q}} \right] - \sum_{l\neq n} p^{e}_{ln,\mathbf{k}} \left[\mu^{e}_{l,m} A_{\mathrm{THz}}(t) - \sum_{\mathbf{q}\neq\mathbf{k}} V^{e,e}_{ml,\mathbf{k}-\mathbf{q}} p^{e}_{ml,\mathbf{q}} \right] \\
&\quad - j^{e,e}_{n,m}(\mathbf{k}) A_{\mathrm{THz}}(t)\, p^{e}_{mn,\mathbf{k}} \ ,
\end{aligned} \tag{24}
$$

$$
\begin{aligned}
\mathrm{i}\hbar\dot{p}^{\lambda_h}_{mn,\mathbf{k}} &= (\tilde{\varepsilon}^{\lambda_h}_{m,\mathbf{k}} - \tilde{\varepsilon}^{\lambda_h}_{n,\mathbf{k}} - \mathrm{i}\gamma)p^{\lambda_h}_{mn,\mathbf{k}} + \sum_l (p^{\lambda_h,e}_{nl,\mathbf{k}})^* \hbar\Omega^{\lambda_h,e}_{ml,\mathbf{k}} - \sum_l p^{\lambda_h,e}_{ml,\mathbf{k}} (\hbar\Omega^{\lambda_h,e}_{nl,\mathbf{k}})^* \\
&\quad - \sum_l p^{\lambda_h,\bar{\lambda}_h}_{ml,\mathbf{k}} \sum_{\mathbf{q}\neq\mathbf{k}} V^{\lambda_h,\bar{\lambda}_h}_{nl,\mathbf{k}-\mathbf{q}} (p^{\lambda_h,\bar{\lambda}_h}_{nl,\mathbf{q}})^* + \sum_l (p^{\lambda_h,\bar{\lambda}_h}_{ml,\mathbf{k}})^* \sum_{\mathbf{q}\neq\mathbf{k}} V^{\lambda_h,\bar{\lambda}_h}_{nl,\mathbf{k}-\mathbf{q}} p^{\lambda_h,\bar{\lambda}_h}_{nl,\mathbf{q}} \\
&\quad + (f^{\lambda_h}_{n,\mathbf{k}} - f^{\lambda_h}_{m,\mathbf{k}}) \left[\mu^{\lambda_h}_{n,m} A_{\mathrm{THz}}(t) - \sum_{\mathbf{q}\neq\mathbf{k}} V^{\lambda_h,\lambda_h}_{mn,\mathbf{k}-\mathbf{q}} p^{\lambda_h}_{mn,\mathbf{q}} \right] \\
&\quad + \sum_{l\neq m} p^{\lambda_h}_{ml,\mathbf{k}} \left[\mu^{\lambda_h}_{n,l} A_{\mathrm{THz}}(t) - \sum_{\mathbf{q}\neq\mathbf{k}} V^{\lambda_h,\lambda_h}_{ln,\mathbf{k}-\mathbf{q}} p^{\lambda_h}_{ln,\mathbf{q}} \right] - \sum_{l\neq n} p^{\lambda_h}_{ln,\mathbf{k}} \left[\mu^{\lambda_h}_{l,m} A_{\mathrm{THz}}(t) - \sum_{\mathbf{q}\neq\mathbf{k}} V^{\lambda_h,\lambda_h}_{ml,\mathbf{k}-\mathbf{q}} p^{\lambda_h}_{ml,\mathbf{q}} \right] \\
&\quad - j^{\lambda_h,\lambda_h}_{m,n}(\mathbf{k}) A_{\mathrm{THz}}(t)\, p^{\lambda_h}_{mn,\mathbf{k}} \ ,
\end{aligned} \tag{25}
$$

$$
\hbar\dot{f}^{e}_{m,\mathbf{k}} = -2\mathrm{Im}\left[\sum_{\lambda_h,l} (p^{\lambda_h,e}_{lm,\mathbf{k}})^* \hbar\Omega^{\lambda_h,e}_{lm,\mathbf{k}} \right] - 2\mathrm{Im}\left[\sum_{l\neq m} p^{e}_{lm,\mathbf{k}} \left(\mu^{e}_{l,m} A_{\mathrm{THz}}(t) - \sum_{\mathbf{q}\neq\mathbf{k}} V^{e,e}_{ml,\mathbf{k}-\mathbf{q}} p^{e}_{ml,\mathbf{q}} \right) \right], \tag{26}
$$

$$
\begin{aligned}
\hbar\dot{f}^{\lambda_h}_{m,\mathbf{k}} &= -2\mathrm{Im}\left[\sum_{l} (p^{\lambda_h,e}_{ml,\mathbf{k}})^* \hbar\Omega^{\lambda_h,e}_{ml,\mathbf{k}} \right] + 2\mathrm{Im}\left[\sum_{l} p^{\lambda_h,\bar{\lambda}_h}_{ml,\mathbf{k}} \sum_{\mathbf{q}\neq\mathbf{k}} V^{\lambda_h,\bar{\lambda}_h}_{ml,\mathbf{k}-\mathbf{q}} (p^{\lambda_h,\bar{\lambda}_h}_{ml,\mathbf{q}})^* \right] \\
&\quad - 2\mathrm{Im}\left[\sum_{l\neq m} p^{\lambda_h}_{ml,\mathbf{k}} \left(\mu^{\lambda_h}_{m,l} A_{\mathrm{THz}}(t) - \sum_{\mathbf{q}\neq\mathbf{k}} V^{\lambda_h,\lambda_h}_{lm,\mathbf{k}-\mathbf{q}} p^{e}_{lm,\mathbf{q}} \right) \right],
\end{aligned} \tag{27}
$$

with the renormalized energies

$$
\tilde{\varepsilon}^{\lambda}_{n,\mathbf{k}} = \varepsilon^{\lambda}_{n,\mathbf{k}} - \sum_{\mathbf{q}\neq\mathbf{k}} V^{\lambda,\lambda}_{mm,\mathbf{k}-\mathbf{q}}\, f^{\lambda}_{m,\mathbf{q}} \tag{28}
$$

and the generalized Rabi frequencies

$$
\hbar\Omega^{\lambda_h,e}_{mn,\mathbf{k}} = d^{e,\lambda_h}_{nm,\mathbf{k}} E_{\mathrm{opt}}(t) + \sum_{\mathbf{q}\neq\mathbf{k}} V^{\lambda_h,e}_{mn,\mathbf{k}-\mathbf{q}}\, p^{\lambda_h,e}_{mn,\mathbf{q}}. \tag{29}
$$

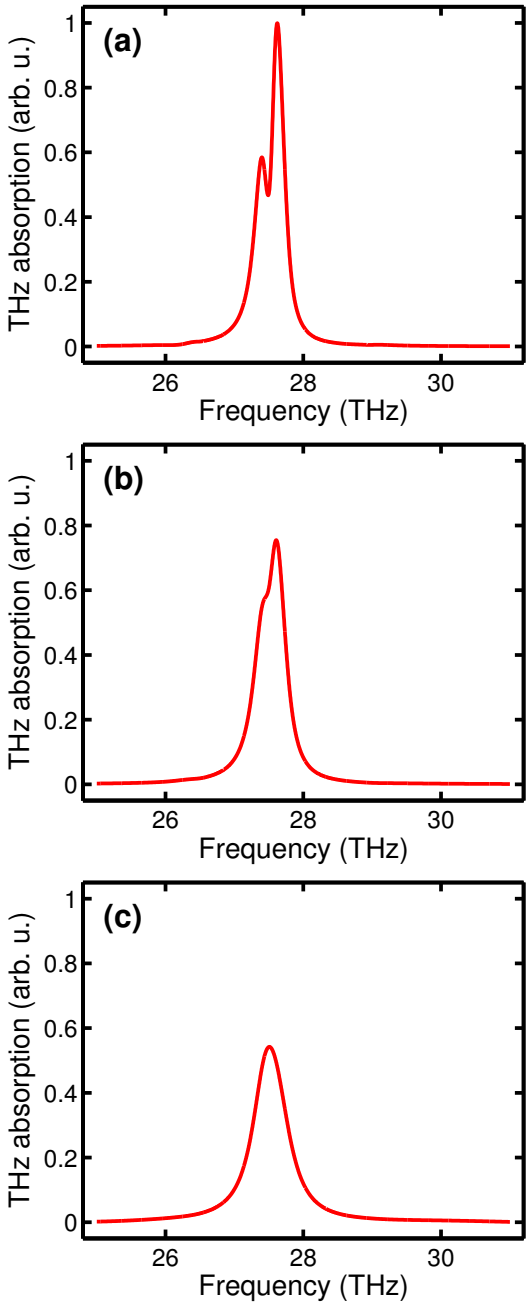

Figure 1. THz-intersubband absorption of a three-band system with one heavy-hole subband and two conduction subbands. The THz field probes the transition between $c1$ and $c2$ subbands. The figure illustrates the dependence on the phenomenological line width γ: (a) shows the absorption for $\gamma = 0.2\,\mathrm{meV}$, (b) for $\gamma = 0.3\,\mathrm{meV}$, and (c) for $\gamma = 0.7\,\mathrm{meV}$.

The band index $\bar{\lambda}_h$ denotes the other hole band than λ_h in each case. For the intraband transitions, we introduced combined matrix elements $j^{\lambda_h,e}_{m,n}(\mathbf{k}) = j^{\lambda_h}_m(\mathbf{k}) + j^e_n(\mathbf{k})$ and (for all other band combinations) $j^{\lambda,\lambda'}_{m,n}(\mathbf{k}) = j^{\lambda}_m(\mathbf{k}) - j^{\lambda'}_n(\mathbf{k})$. The dephasing of the polarizations has been modeled by the phenomenological damping constant γ. Equations (22)-(27) are generalizations of the semiconductor Bloch equations[14,19] for a multisubband system and with coupling to a THz field.

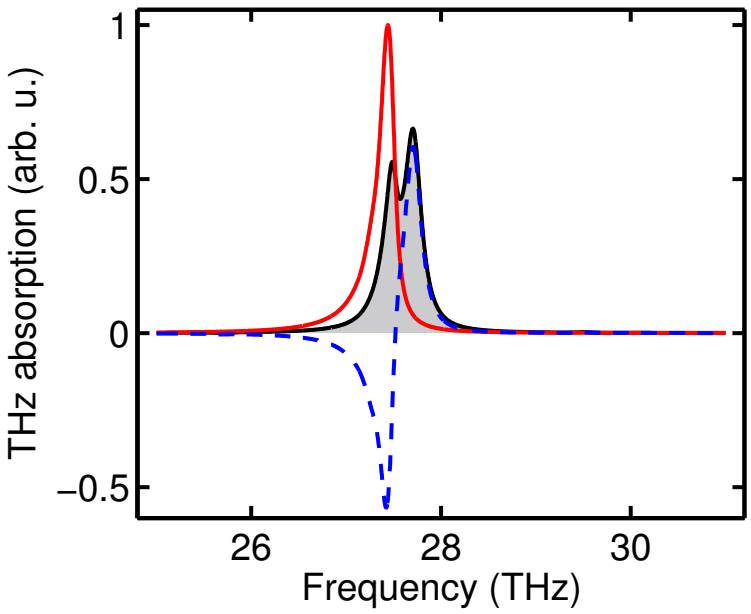

Figure 2. Contributions to the intersubband absorption. The total absorption (gray area) is decomposed into its two components namely the absorption from the occupations (red solid line) and that from the polarizations, i.e, the coherent excitons (blue dashed line).

3. EXCITONIC EFFECTS IN INTERSUBBAND TRANSITIONS

In order to study the intersubband absorption of an optically excited quantum well, we solve Eqs. (22)-(27) numerically. To keep the system as simple as possible, we restrict the analysis to one heavy-hole subband and two conduction subbands ($c1$ & $c2$). Furthermore, we omit the intraband terms in the equations of motion, i.e., we set $j_n^\lambda(\mathbf{k}) = 0$. The single particle energies $\varepsilon_{n,\mathbf{k}}^\lambda$ as well as the dipole matrix elements $d_{n,n'}^{\lambda,\lambda'}(\mathbf{k})$ are computed with standard $\mathbf{k}\cdot\mathbf{p}$ perturbation theory for an 8.3 nm thick GaAs/$Al_{0.34}Ga_{0.66}$As quantum well. The quantum well is assumed to be pumped resonantly at the $1s$ exciton transition belonging to the $c1$ subband. About 300 fs after the pump pulse, the THz pulse probes the system. On such an ultrafast timescale, the optically excited interband coherences have not decayed and the THz field reacts to both the excited carriers and the interband polarizations.

For such an scenario, the equation of motion for the intersubband polarization, Eq. (24), provides two sources for intersubband transitions. The most obvious source follows the second line of Eq. (24) that describes a simple free-carrier band-to-band transition as long as the electron distributions are different in the two subbands. This term clearly leads to a single peak at the (renormalized) $c1$-$c2$ transition frequency in the THz absorption spectrum. The second source for an intersubband transition is given by the last two terms of the first line of Eq. (24). Here, the optically excited hh-$c1$ interband polarization interacts with the THz induced hh-$c2$ polarization via Coulomb interaction. Since the both polarizations might oscillate with excitonic frequencies, this term describes transitions from an excitonic state that belongs to the $c1$ band to a state belonging to the $c2$ band as is shown below. Hence, a second peak might be expected in the absorption spectrum as long as the exciton binding energies are sufficiently different for the $c1$ and $c2$ bands.

Typical THz absorption spectra for intersubband transitions are shown in Fig. 1. For large line widths γ (Fig. 1(c)) only a single absorption peak is observed. When γ is decreased, however, this peak splits into two (see Figs. 1(b) and (a)). The final proof for the origin of these peaks is done by a switch-off analysis in Fig. 2. Here, the full absorption (gray area) is shown together with the contributions from the first source term (red solid line) and from the second source term (blue dashed line) for intersubband transitions. Obviously, the low-energy peak follows from band-to-band transitions while the high-energy peak is due to transitions between

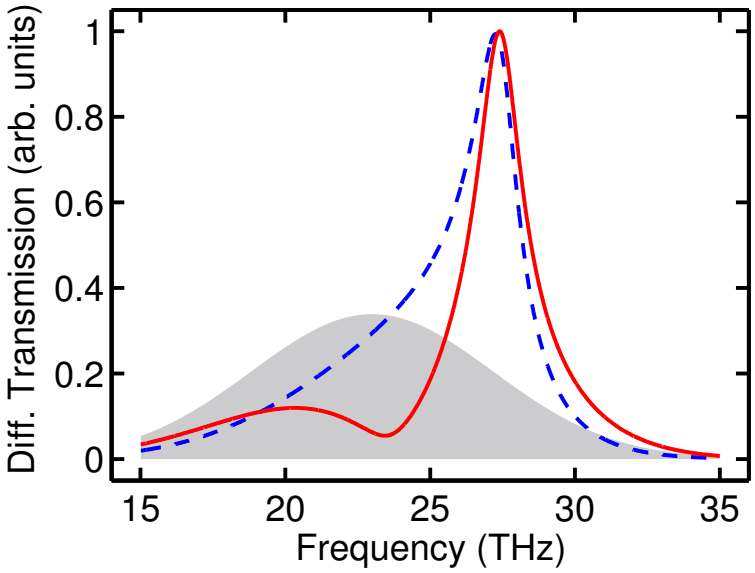

Figure 3. Computed spectral amplitude of the differential transmission ΔE_{THz}. The total result (red solid line) is shown together with its components the intersubband response (blue dashed line) and the ponderomotive part (gray area). The phenomenological dephasing constant is $\gamma = 1.65\,\mathrm{meV}$.

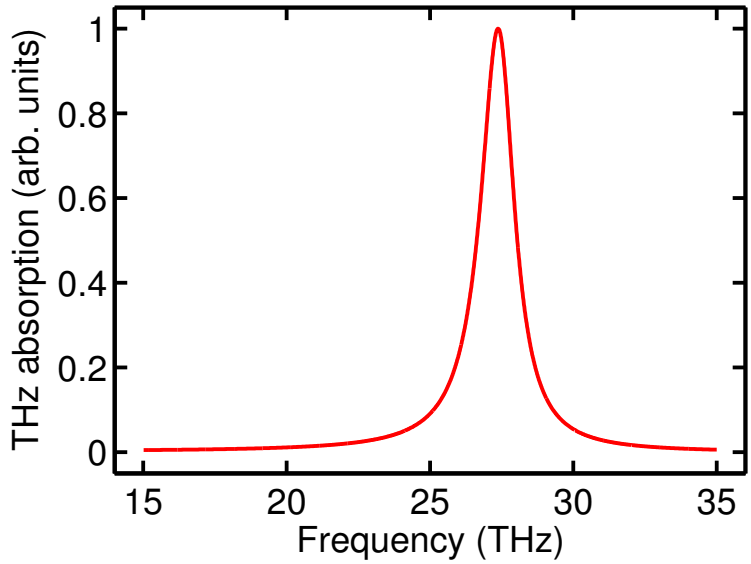

Figure 4. THz absorption for the same parameters as in Fig. 3.

(coherent) excitons that belong to different subbands. Further analysis reveals that this excitonic peak comes from a $1s$-to-$1s$ transition while the $1s$-to-$2s$ peak is two orders of magnitude smaller and cannot be seen here.

4. FANO FEATURES

Besides the excitonic contributions to the absorption spectrum, the THz intersubband response of a quantum well provides another interesting feature. The red line in Fig. 3 shows the spectral amplitude of the differential THz transmission, i.e., the difference between the transmitted and the incident THz electric fields. Besides the strong peak at about 27 THz, a broader spectral feature arises centered at roughly 20 THz. Furthermore, the

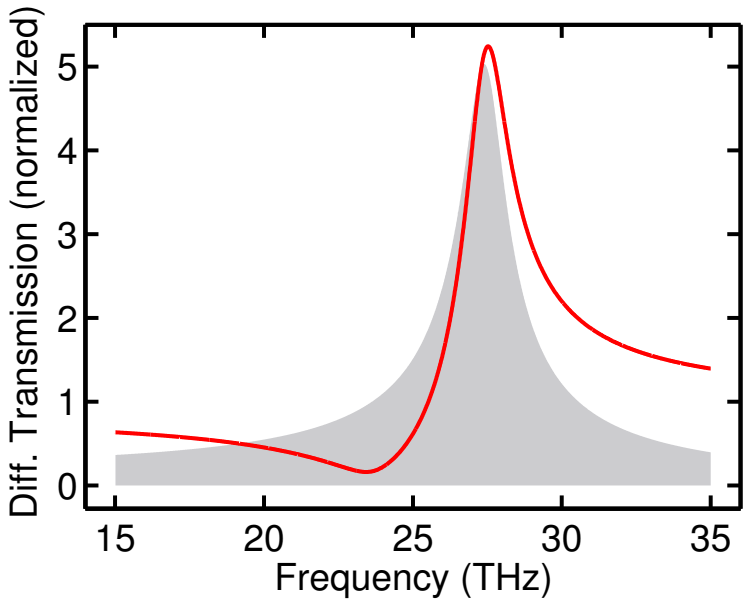

Figure 5. Spectral amplitude of the normalized differential transmission $\Delta E_{\mathrm{THz}}/E_{0,\mathrm{THz}}$. The red line shows the total result and the gray area is the contribution from intersubband transitions. The parameters are the same as in Fig. 3.

strong peak has a rather asymmetric line shape comparable to a Fano resonance.[20] The corresponding absorption spectrum (Fig. 4) shows that the broad contribution is not caused by an additional carrier transition.

To understand the origin of this special spectral structure we have to recall that the THz response consists not only of the intersubband contribution J_{intersub} but also of the ponderomotive current J_{pond}, Eq. (20). Figure 3 shows these two contributions separately in addition to the full result. As expected, the strong peak comes from the intersubband transition that is also visible in the absorption spectrum. The broad feature can clearly be attributed to the carrier accelerations via the ponderomotive response. The phase sensitive superposition of both contributions leads to constructive interference for frequencies larger than the $c1$-$c2$ transition frequency while they partially compensate each other for smaller frequencies. The Fano feature becomes even more prominent when plotting the normalized differential transmission, i.e., the differential transmission divided by the incident pulse (see Fig. 5). The results presented in this section are in great agreement with recent experiments.[21]

5. SUMMARY

We have presented a microscopic THz theory for a multisubband quantum well. The THz response has been computed by solving the generalized multisubband semiconductor Bloch equations numerically. As a first example, we analyzed excitonic effects in intersubband transitions. It turned out that high-quality samples with small line widths are needed to resolve both the band-to-band transition and the $1s$-to-$1s$ intersubband transition in GaAs quantum wells. We also discussed the Fano-like line shape of the THz response which was shown to result from a competition between true carrier transitions and the field-induced carrier acceleration. This analysis provides a tool to directly observe the ponderomotive response in linear THz spectroscopy. Indirect evidence for this contribution to the THz response has already been given by means of nonlinear THz spectroscopy.[11,12]

ACKNOWLEDGMENTS

We thank Martin Wagner, Dominik Stehr, Harald Schneider, and Manfred Helm from the Forschungszentrum Dresden-Rossendorf for fruitful discussion and collaboration. This work has been supported by the Quantum Optics in Semiconductors DFG Research Group.

REFERENCES

[1] Groeneveld, R. H. M. and Grischkowsky, D., "Picosecond time-resolved far-infrared experiments on carriers and excitons in gaas-algaas multiple quantum wells," *J. Opt. Soc. Am. B* **11**, 2502–2507 (1994).

[2] Cerne, J., Kono, J., Sherwin, M. S., Sundaram, M., Gossard, A. C., and Bauer, G. E. W., "Terahertz dynamics of excitons in GaAs/AlGaAs quantum wells," *Phys. Rev. Lett.* **77**, 1131–1134 (1996).

[3] Huber, R., Tauser, F., Brodschelm, A., Bichler, M., Abstreiter, G., and Leitenstorfer, A., "How many-particle interactions develop after ultrafast excitation of an electron-hole plasma," *Nature* **414**, 286–289 (2001).

[4] Kaindl, R. A., Carnahan, M. A., Hägele, D., Lövenich, R., and Chemla, D. S., "Ultrafast terahertz probes of transient conducting and insulating phases in an electron-hole gas," *Nature* **423**, 734–738 (2003).

[5] Galbraith, I., Chari, R., Pellegrini, S., Phillips, P. J., Dent, C. J., van der Meer, A. F. G., Clarke, D. G., Kar, A. K., Buller, G. S., Pidgeon, C. R., Murdin, B. N., Allam, J., and Strasser, G., "Excitonic signatures in the photoluminescence and terahertz absorption of a gaas/al[sub x]ga[sub 1 - x]as multiple quantum well," *Phys. Rev. B* **71**, 073302 (2005).

[6] Bonvalet, A., Nagle, J., Berger, V., Migus, A., Martin, J.-L., and Joffre, M., "Femtosecond infrared emission resulting from coherent charge oscillations in quantum wells," *Phys. Rev. Lett.* **76**, 4392 (1996).

[7] Heyman, J. N., Kersting, R., and Unterrainer, K., "Time-domain measurement of intersubband oscillations in a quantum well," *Appl. Phys. Lett.* **72**, 644–646 (1998).

[8] Kersting, R., Bratschitsch, R., Strasser, G., Unterrainer, K., and Heyman, J. N., "Sampling a terahertz dipole transition with subcycle time resolution," *Opt. Lett.* **25**, 272 (2000).

[9] Müller, T., Parz, W., Strasser, G., and Unterrainer, K., "Influence of carrier-carrier interaction on time-dependent intersubband absorption in a semiconductor quantum well," *Phys. Rev. B* **70**, 155324 (2004).

[10] Luo, C. W., Reimann, K., Woerner, M., Elsaesser, T., Hey, R., and Ploog, K. H., "Phase-resolved nonlinear response of a two-dimensional electron gas under femtosecond intersubband excitation," *Phys. Rev. Lett.* **92**, 047402 (2004).

[11] Danielson, J. R., Lee, Y.-S., Prineas, J. P., Steiner, J. T., Kira, M., and Koch, S. W., "Interaction of strong single-cycle terahertz pulses with semiconductor quantum wells," *Phys. Rev. Lett.* **99**, 237401 (2007).

[12] Leinß, S., Kampfrath, T., v. Volkmann, K., Wolf, M., Steiner, J. T., Kira, M., Koch, S. W., Leitenstorfer, A., and Huber, R., "Terahertz coherent control of optically dark para excitons in," *Phys. Rev. Lett.* **101**, 246401 (2008).

[13] Krieger, J. B. and Iafrate, G. J., "Time evolution of bloch electrons in a homogeneous electric field," *Phys. Rev. B* **33**, 5494–5500 (1986).

[14] Haug, H. and Koch, S. W., [*Quantum Theory of the Optical and Electronic Properties of Semiconductors*], World Scientific, Singapore, fifth ed. (2009).

[15] Kira, M. and Koch, S. W., "Many-body correlations and excitonic effects in semiconductor spectroscopy," *Prog. Quantum Electron.* **30**, 155–296 (2006).

[16] Kira, M., Hoyer, W., and Koch, S. W., "Microscopic theory of the semiconductor terahertz response," *phys. stat. sol. (b)* **238**, 443–450 (2003).

[17] Kira, M., Hoyer, W., and Koch, S. W., "Terahertz signatures of the exciton formation dynamics in non-resonantly excited semiconductors," *Sol. Stat. Comm.* **129**, 733–736 (2004).

[18] Steiner, J. T., *Microscopic Theory of Linear and Nonlinear Terahertz Spectroscopy of Semiconductors*, PhD thesis, Philipps-University Marburg (2008).

[19] Lindberg, M. and Koch, S. W., "Effective bloch equations for semiconductors," *Phys. Rev. B* **38**, 3342–3350 (1988).

[20] Fano, U., "Effects of configuration interaction on intensities and phase shifts," *Phys. Rev.* **124**, 1866 (1961).

[21] Golde, D., Wagner, M., Stehr, D., Schneider, H., Helm, M., Andrews, A. M., Roch, T., Strasser, G., Kira, M., and Koch, S. W., "Fano signatures in the intersubband terahertz response of optically excited semiconductor quantum wells," *Phys. Rev. Lett.* **102**, 127403 (2009).